ACS SYMPOSIUM SERIES 790

Film Formation in Coatings

Mechanisms, Properties, and Morphology

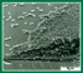

EDITED BY

odore Provder and Marek W. Urban

Downloaded by 89.163.34.136 on September 17, 2012 | http://pubs.acs.org
Publication Date: July 26, 2001 | doi: 10.1021/bk-2001-0790.fw001

ACS SYMPOSIUM SERIES **790**

Film Formation in Coatings

Mechanisms, Properties, and Morphology

Theodore Provder, Editor
Polymer and Coatings Consultants

Marek W. Urban, Editor
The University of Southern Mississippi

American Chemical Society, Washington, DC

In Film Formation in Coatings; Provder, T., et al.;
ACS Symposium Series; American Chemical Society: Washington, DC, 2001.

TA 418.76 .F54 2001 c. 1

Film formation in coatings :
mechanisms, properties,

Library of Congress Cataloging-in-Publication Data

Film formation in coatings : mechanisms, properties, and morphology / Theodore Provder, Marek W. Urban, editors.

p. cm.—(ACS symposium series, ISSN 0097–6156 ; 790)

Includes bibliographical references and index.

ISBN 0–8412–3712–3

1. Protective Coatings—Congresses. 2. Surfaces (Technology)—Congresses

I. Provder, Theodore, 1939- II. Urban, Marek W., 1953- III. Series.

TA418.76 .F54 2001
667′.9—dc21 2001016046

The paper used in this publication meets the minimum requirements of American National Standard for Information Sciences—Permanence of Paper for Printed Library Materials, ANSI Z39.48–1984.

Copyright © 2001American Chemical Society

Distributed by Oxford University Press

All Rights Reserved. Reprographic copying beyond that permitted by Sections 107 or 108 of the U.S. Copyright Act is allowed for internal use only, provided that a per-chapter fee of $20.50 plus $0.75 per page is paid to the Copyright Clearance Center, Inc., 222 Rosewood Drive, Danvers, MA 01923, USA. Republication or reproduction for sale of pages in this book is permitted only under license from ACS. Direct these and other permission requests to ACS Copyright Office, Publications Division, 1155 16th St., N.W., Washington, DC 20036.

The citation of trade names and/or names of manufacturers in this publication is not to be construed as an endorsement or as approval by ACS of the commercial products or services referenced herein; nor should the mere reference herein to any drawing, specification, chemical process, or other data be regarded as a license or as a conveyance of any right or permission to the holder, reader, or any other person or corporation, to manufacture, reproduce, use, or sell any patented invention or copyrighted work that may in any way be related thereto. Registered names, trademarks, etc., used in this publication, even without specific indication thereof, are not to be considered unprotected by law.

PRINTED IN THE UNITED STATES OF AMERICA

American Chemical Society
Library
1155 16th St., N.W.
Washington, D.C. 20036

Downloaded by 89.163.34.136 on September 17, 2012 | http://pubs.acs.org
Publication Date: July 26, 2001 | doi: 10.1021/bk-2001-0790.fw001

Foreword

The ACS Symposium Series was first published in 1974 to provide a mechanism for publishing symposia quickly in book form. The purpose of the series is to publish timely, comprehensive books developed from ACS sponsored symposia based on current scientific research. Occasionally, books are developed from symposia sponsored by other organizations when the topic is of keen interest to the chemistry audience.

Before agreeing to publish a book, the proposed table of contents is reviewed for appropriate and comprehensive coverage and for interest to the audience. Some papers may be excluded to better focus the book; others may be added to provide comprehensiveness. When appropriate, overview or introductory chapters are added. Drafts of chapters are peer-reviewed prior to final acceptance or rejection, and manuscripts are prepared in camera-ready format.

As a rule, only original research papers and original review papers are included in the volumes. Verbatim reproductions of previously published papers are not accepted.

ACS Books Department

Downloaded by 89.163.34.136 on September 17, 2012 | http://pubs.acs.org
Publication Date: July 26, 2001 | doi: 10.1021/bk-2001-0790.fw001

In Film Formation in Coatings; Provder, T., et al.;
ACS Symposium Series; American Chemical Society: Washington, DC, 2001.

Downloaded by 89.163.34.136 on September 17, 2012 | http://pubs.acs.org
Publication Date: July 26, 2001 | doi: 10.1021/bk-2001-0790.pr001

Preface

Coatings technologies are still heavily influenced by the "Clean Air Act" of 1990 and its subsequent updates that keep reducing the volatile organic content (VOC) of coatings. The continuing development of high solids, powder, waterborne and radiation-curable coating technologies is highly focused on reducing the emission of VOCs while maintaining and/or improving product properties in a cost-effective manner. Understanding the film formation process is one of the key enablers in the further development of these coatings technologies. This understanding involves continued elucidation of film formation mechanisms, the evolution of film properties during film formation, and the resultant morphology and structure of the films. The film formation knowledge base continues to grow facilitated by advances in instrumentation that has been applied to this area of investigation, as well as progress made in modeling various aspects of the film formation process.

The first section of this book focuses on aspects of the mechanism of film formation including the modeling of drying of polymer colloids, modeling and understanding capillary forces and stress involved in drying latex coatings, and understanding the effect of molecular weight and molecular interactions on film formation. Instrumental methods such as fluorescence decay spectroscopy, Fourier transform infrared spectroscopy (attenuated total reflectance and photoacoustic), atomic force microscopy (AFM), ellipsometry, and thermogravimetric analysis have contributed to our understanding of various aspects of film formation. The second section focuses on film properties developed during the film formation process for waterborne thermoplastic and cross-linkable systems as well as radiation curable systems. The focus on property development in this section involves the use of dynamic mechanical analysis, dielectric spectroscopy, and swelling measurements. The third section focuses on the morphology and film structure resulting from the film formation process. This is a very active area of study utilizing advanced morphological instrumentation, such as transmission electron microscopy, cryogenic scanning electron microscopy (SEM), confocal microscopy, environmental SEM, AFM, as well as routine measurements of gloss and film porosity. The instrumentation used in these studies also facilitates the determination of unique and novel film structures in some of these studies.

We hope this book will encourage and foster continued studies to further our understanding of the scientifically challenging and commercially relevant issue of film formation in waterborne coatings.

In Film Formation in Coatings; Provder, T., et al.;
ACS Symposium Series; American Chemical Society: Washington, DC, 2001.

Downloaded by 89.163.34.136 on September 17, 2012 | http://pubs.acs.org
Publication Date: July 26, 2001 | doi: 10.1021/bk-2001-0790.pr001

Acknowledgments

We are grateful to the authors for their effective oral and written communications and to the reviewers for their critiques and constructive comments. We also gratefully acknowledge the American Chemical Society Division of Polymeric Materials: Science and Engineering, Inc. and ICI PLC for their financial support of the symposium on which this book is based.

Theodore Provder
Polymer and Coatings Consultants
26567 Bayfair Drive
Olmsted Falls, OH 44138

Marek W. Urban
School of Polymers and High Performance Materials
Shelby F. Thames Polymer Science Research Center
The University of Southern Mississippi
Hattiesburg, MS 39406

Downloaded by 89.163.34.136 on September 17, 2012 | http://pubs.acs.org
Publication Date: July 26, 2001 | doi: 10.1021/bk-2001-0790.ch001

Chapter 1

Drying Modes of Polymer Colloids

Y. Holl[1], J. L. Keddie[2], P. J. McDonald[2], and W. A. Winnik[3]

[1]Institut de Chimie des Surfaces (CNRS), B.P. 2488, 68057 Mulhouse, France
[2]Department of Physics, University of Surrey, Guildford, Surrey GU 5XH, United Kingdom
[3]Department of Chemistry, University of Toronto, 80 St. George Street, Toronto, Ontario M5S 3H6, Canada

This chapter reviews the complex step of drying in the latex film formation process. Drying modes have a profound effect on drying rates and on the final properties of films, primarily through their influence on film morphology and the distribution of water-soluble species. Three distinct drying modes (acting separately, successively or together) can be defined, namely *homogeneous drying* (in which the water concentration remains uniform in the sample throughout the drying process), *drying normal to the surface* (where a dry layer of increasing thickness develops from the air surface of the latex coating); and *lateral drying* (where dry areas increase in size in a direction parallel to the substrate). Details are given on the current knowledge and understanding of these drying modes. The last section of the chapter considers the main parameters controlling the drying modes, i.e. thickness and geometric effects, the structure and rheology of the dispersion, particle viscoelasticity, and the overall rate of water loss.

Environmental and health regulations are causing the manufacturers of coatings and paints to develop new formulations. One important strategy for coatings that are friendly to the environment is based on waterborne colloidal dispersions of polymers. As industry is confronted with the need to replace coatings formulated in organic solvents, more coatings are converted from being based on polymers dissolved in solvent to those based on colloidal dispersions in water. This is the reason why waterborne film formation mechanisms are becoming increasingly

In Film Formation in Coatings; Provder, T., et al.;
ACS Symposium Series; American Chemical Society: Washington, DC, 2001.

important and relevant to product design. A number of useful reviews of latex film formation have recently been published (*1*, *2*, *3*). The film formation process is commonly divided into 3 steps. As water evaporates from the dispersion, the polymer particles become more and more concentrated and come into proximity (step 1). When the forces accompanying drying exceed the mechanical (both elastic and viscous) resistance of the particles, particle deformation occurs to yield a void free film that is still mechanically weak (step 2). In the final stage of film formation, polymer diffusion occurs across the interparticle boundaries to provide the entanglements that give strength to the film (step 3). These steps are not always well separated, and within each step subtle features operate that often differ from system to system. In certain cases, additional steps can be observed in the film formation process. Some factors (such as uniform particle size and low ionic strength) promote ordering of the dispersion in the liquid state. The disorder to order transition can be considered as an additional step (*4*). Furthermore, all latex particles have surface polar or ionic groups that provide colloidal stability. In some systems, this polar layer is sufficiently thick that it forms a continuous phase called a membrane in the freshly formed film (*5*). Break-up of this membrane becomes an important step in bringing the particles cores into intimate contact so that interdiffusion can occur (*6*).

This chapter focuses on the drying modes of polymer colloids. Drying encompasses step 1 and part of step 2 in the above description of the latex film formation. The mechanism of water loss from latex dispersions is surprisingly complex. This stage of film formation is, at present, the least understood (*1*).

Drying modes are very important for several reasons. They determine drying rates which are of technological importance. Perhaps the most important example of the need for rapid drying, which to our knowledge has not been described at all in the open literature, is waterborne road paints. These paints must dry within minutes of application to a road surface so that the painting process does not impede traffic. For some other applications, one would like to slow down the drying process to increase the “open time.” The open time is the time available for the "touch up" of flaws in a coating to be made without permanent disturbance of the surface. Once the open time is over, the surface cannot be “re-worked” or smoothed out. Solvent borne paints normally have much longer open times than waterborne paints. The classic example involves alkyd coatings. Solvent borne alkyd coatings have long open times whereas water-borne emulsified alkyd resins are much more difficult to rework (*7*). We lack a mechanistic understanding of the factors that control open time. However, the viscosity of the formulation is likely to play an important role. The viscosity of polymer solutions increases monotonically as the solvent evaporates and the polymer becomes more concentrated. Polymer molecular weight has a large effect on the solution viscosity. In colloidal dispersions, the viscosity is low at modest concentrations, but rises abruptly as the solids content reaches values above 55 to 65 vol %, depending upon the size distribution of the particles. Above a critical value of viscosity, the surface cannot be smoothed out, but more important, addition of fresh coating at lower solids content may not be able to redisperse latex particles

Downloaded by 89.163.34.136 on September 17, 2012 | http://pubs.acs.org
Publication Date: July 26, 2001 | doi: 10.1021/bk-2001-0790.ch001

which have coalesced on the substrate. Furthermore, the user of a paint judges the "amount of dryness" by examining the air surface. It is the viscosity at the surface of a coating that most heavily influences perceptions of open time. The distribution of water within a layer, and not the overall average water concentration, is thus the more important parameter. The exact drying mode will determine the distribution of water within a drying layer, and so theoretical and experimental investigations of drying are certainly warranted.

Another important issue is that drying implies transport of water in the latex dispersion. This transport can involve diffusion of water molecules through a continuous polymer phase, percolation of water through interstitial spaces in the film, or water fluxes in the wet regions of the drying film. The fluxes are particularly interesting because they can transport polymer particles, pigment, and water-soluble species from wet regions to the boundary to adjacent dry regions of the film. Transport of particles will influence the array of particles and thus the morphology of the film. On the other hand, transport of water-soluble species, such as surfactants or soluble oligomers, will influence the final distribution of such species in the dry film (*8*). Both the morphology and the distribution of water-soluble species have a profound influence on the properties of latex films.

Downloaded by 89.163.34.136 on September 17, 2012 | http://pubs.acs.org
Publication Date: July 26, 2001 | doi: 10.1021/bk-2001-0790.ch001

From a phenomenological point of view, one can distinguish three distinct drying modes (and these can act separately or together) for a latex dispersion on a non porous solid substrate. Depending on the authors, they are referred to by different terms. Therefore, let us first clarify the vocabulary. The first mode is *homogeneous drying*. This means that the water concentration remains uniform in the system throughout the drying process. The tendency to dry homogeneously is very general. All drying systems tend to compensate for heterogeneous water concentrations. Dilute latices start drying homogeneously. However, once a certain solids content has been reached, which depends on the particular system and drying conditions, heterogeneities in the distribution of water can appear. Heterogeneities occur when the rate of water loss is too high, and the equilibration of water inside of the system does not have time to take place. Examples of real homogeneous drying in latex dispersions, in which homogeneity is retained throughout the drying process, are very rare and this case will not be developed much in the following text.

The second mode is *drying normal to the latex dispersion surface*. In this case, the heterogeneity in the distribution of water is such that the top of the latex coating (the air side) is drier than the bottom, on the substrate side. Drying proceeds by a movement in a direction normal to the surface of a drying front separating a top dry region from a bottom wet region. Systems drying like this, in which the dry region undergoes particle coalescence, are sometimes called "skin forming systems".

Drying fronts can also propagate in a lateral direction, parallel to the substrate. This mode is called *lateral drying*. Very often drying occurs inward from the outer edges and thus the center of the specimen is the last region to dry. This final region to dry has been called the "last drop". It can have special characteristics, such as high concentration of water-soluble species and special morphology, as has been found recently (*9*). Later in this chapter, we will mention factors, such as the addition of thickeners or high-solids dispersion (both of which raise the dispersion viscosity), which are expected to suppress lateral drying. Normal and lateral drying modes are depicted in Figure 1.

This chapter will consider four main topics: normal drying; lateral drying; mixed modes of drying; and in the final section, the parameters that determine the drying modes.

Drying Normal to the Surface

Downloaded by 89.163.34.136 on September 17, 2012 | http://pubs.acs.org
Publication Date: July 26, 2001 | doi: 10.1021/bk-2001-0790.ch001

When a latex dispersion dries normal to the surface, a dry layer of increasing thickness builds up from the top downwards. Water has to diffuse through this top layer in order to leave the film. If the diffusion through this layer is the slow step in the drying process, then the drying rate is not constant, but it decreases progressively. If the water content in the film is plotted versus the square root of time, a straight line is obtained, the slope of which can be related to the diffusion coefficient of water through the dry top layer (*10*). An example of this behavior was found in the case of the drying of a concentrated (84 wt% solids), reactive (crosslinking upon drying), polydimethylsiloxane emulsion (*11*). However, diffusion through the top layer is not always a slow step and the global rate of water loss can be constant over a large period of time in normal drying (*12*).(By global, we mean the overall rate, as compared to the water loss rate in a local region within the coating.) It is the tendency of the system to equilibrate the concentration of water between the top and the bottom which drives water from the bottom to the top and is responsible for the drying of the whole film.

A possible consequence of this mode is that water soluble species, which tend to remain in water as much as possible, are driven to the film-substrate interface. Accumulation of such species, like surfactants, at this interface can strongly affect the properties of the film, especially adhesion (*13*). In studies of the distribution of surfactants in latex films by Urban and coworkers (*14*) and Holl and coworkers (*15*), such a mode is invoked to explain the high concentration of surfactants often observed at the film/substrate interface. However, in certain cases, more subtle transport mechanisms for surfactants have to be taken into account like osmotic and capillary pressure gradients occurring near the interface (*11*).

Classical Models for Normal Drying

Traditional models for the drying process are based upon measurements of the rate of water loss from latex dispersions. Almost all the experiments on which the classical models were based involve dispersions stabilized by surfactants. Water

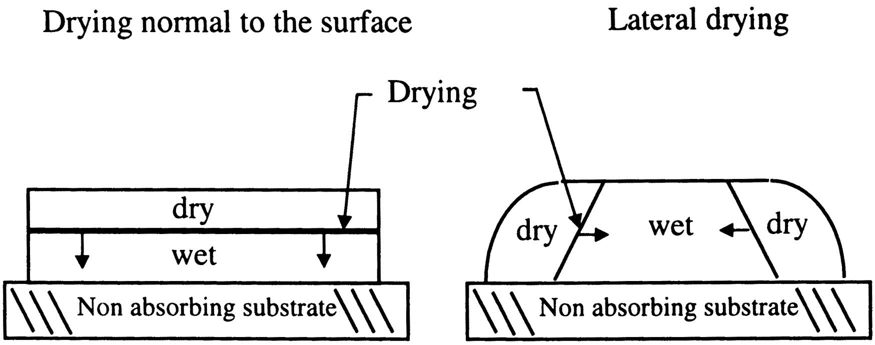

Figure 1 : Schematic diagram showing two possible drying modes for latices, namely normal and lateral drying.

is lost initially at a constant rate, and then the rate slows down until water loss is complete. The three main models are due to Sheetz (*16*), Vanderhoff (*17*), and Croll (*12*, *18*).

Sheetz 1965

Sheetz (*16*) proposed that very early in the drying process, a dry skin of coalesced particles forms on top of the latex dispersion. Further evaporation of water then occurs by diffusion through this skin. In fact, the main emphasis of his work was not drying modes but particle deformation. He made an analogy to a piston in which the coalesced surface layer exerts pressure on the wet layer underneath. His work was primarily theoretical, based on his limited experimental study of acrylic latices.

Vanderhoff 1973

In Vanderhoff *et al.*'s model (*17*), drying is described as a three stage process. In stage 1, water evaporates at its normal rate from the surface of the dilute dispersion, in which the particles remain separated. Stage 2 commences as the particles come into close contact and protrude at the latex dispersion-air interface. As the area of the water-air interface is reduced, the evaporation rate slows. Eventually, coalescence leads to the closing of the surface. In stage 3, the loss of the last traces of water is very slow because the water now must diffuse through a layer comprising continuous polymer at the surface. This last suggestion may be correct under certain circumstances. For example, there is some evidence that near the end of the drying process, the rate of water loss is consistent with Fickian diffusion of water through the solid polymer (*19*, *20*, *21*). On the other hand, when the latex particles have sufficient polar material in their shell that it forms a continuous hydrophilic phase in the film as it dries, water diffusion through this phase may be the most favorable route and may predominate.

Downloaded by 89.163.34.136 on September 17, 2012 | http://pubs.acs.org
Publication Date: July 26, 2001 | doi: 10.1021/bk-2001-0790.ch001

This model has an appealing simplicity and had a strong influence on many researchers over the years. However, it made an implicit claim for generality which is unjustified as it is obviously not applicable in the most frequent cases of lateral drying.

Croll 1986

Croll (*12*, *18*) conducted one of the more significant experimental and theoretical works on the topic of latex dispersion drying. Based on his experimental work, he proposed a two-stage process, unlike Vanderhoff *et al.* 's three stage model. He compared the rate of water evaporation from latex dispersions to that of pigment suspensions (clay, mica) where coalescence is not possible, and found remarkable similarities. Both the latex dispersions and the pigment suspensions exhibited a loss of water that was linear with time over much of the drying process, independent of film thickness, and in each instance, this rate was 85% of that of water itself. In the first stage of this model, particles form a flocculated phase at the air interface. The surface from which water evaporates recedes into this phase, leaving a dry porous layer. This phase is initially thin and becomes thicker as the drying proceeds. Beneath the evaporative surface is a "transition layer" of closely packed particles immersed in water on top of a liquid phase containing mobile particles. Croll describes the dry top phase in terms of a percolation network of voids which permits water vapor to pass. Since the top layer does not constitute a real barrier to the transport of water vapor, the rate of water loss is constant during the first stage, whatever the thickness of the layer. The second stage starts when the water evaporation rate begins to slow down. This corresponds to the time where the transition layer reaches the substrate and the concentration of water in the wet region decreases. Then, the flux of evaporating water decreases eventually to zero. In a subsequent paper (*18*), Croll developed a mathematical model to describe drying during latex film formation with an emphasis on thermal aspects of the drying process which had not been previously investigated much in the literature. He considered the temperature decrease due to the endothermic drying process, which in turn decreases the drying rate. His model made use of values of thermal conductivity, thermal expansivity and viscosity of the latex dispersion. Croll's model is then more quantitative than Vanderhoff *et al.*'s one but has the same drawback: it is not general as it does not account for lateral drying. This model, slightly modified, was used by Eckersley and Rudin (*20*) to fit their results on skin forming systems.

Whereas the above models for normal drying capture certain features of the drying process, they are neither general nor complete. In the last section of this chapter, we will review recent ideas used to predict when normal drying will occur. Let us now discuss the case of lateral drying.

Downloaded by 89.163.34.136 on September 17, 2012 | http://pubs.acs.org
Publication Date: July 26, 2001 | doi: 10.1021/bk-2001-0790.ch001

Lateral Drying

Lateral drying, as defined in the introduction of this chapter, was observed and reported in the literature a long time ago. In 1964, Hwa (*22*) reported lateral nonuniformity during the drying of a film forming acrylic latex dispersion. He observed three regions with different appearances: a central wet region that was turbid; a peripheral dry region that was optically clear; and a region between the other two that was partly cloudy. The central turbid region decreased in area as drying proceeded. Hwa proposed that the intermediate region consisted of flocculated particles that could not be redispersed in water. In the same year, Myers and Schultz (*23*) published ultrasonic measurements of the lateral drying of latex films. Okubo *et al.* (*24*) constructed a description of drying similar to that of Hwa, with the additional observation of a skin forming on top of the central wet region. We will comment further on this work by Okubo *et al.* later in the chapter.

More recently, Chevalier *et al.* (*5*) followed the drying of latex dispersions using Small Angle Neutron Scattering. The particular latex dispersion studied had a hydrophobic core with a hydrophilic shell. They found that the spacing of particles in the central wet region of a drying film remained roughly constant, even though the global volume fraction of polymer, Φ, increased because of water evaporation. At a particular point in time, the spacing of the particles decreased abruptly and Φ approached 1. They associated this collapse with the passing of a "coalescence front" through the spot being irradiated by the neutron beam. They postulated that a coalescence front moved inward from the edges by the action of the particles in the central wet region colliding with and sticking to it. Even though it was proposed that particles were transported from the central regions outward toward the edges, Φ stayed roughly constant because of evaporative loss of water. This concept of a central region with a constant polymer concentration is incorporated into the so-called "shape models" of drying that will be discussed in the next section.

In some ways, this work of Chevalier *et al.* describes the same process observed by Hwa (*22*) and like the work of Okubo *et al.* (*24*), it shows that the water content in the central wet region remains high, but it is low in the flocculated and dry regions. Somewhat earlier, the same group (*4*) had also observed a dry region surrounding a central wet region in a surfactant containing latex dispersion during drying. They found as evaporation proceeded that the central region increased in thickness and decreased in surface area. They suggested a different mechanism in which "water is expelled from the drying film into the wet area". This later view of water expelled from a water-poor region into a water-rich region is inconsistent with the predictions of thermodynamics but can have some equivalence in phase separation phenomena occurring in emulsions. However, to our knowledge, this idea was never developed any further in the literature.

It is surprising to note that lateral drying was observed by researchers like Sheetz (*16*) and Croll (*12*) who did not take it into account in their models. Interestingly, Croll attributed the observation of latex films becoming optically

Downloaded by 89.163.34.136 on September 17, 2012 | http://pubs.acs.org
Publication Date: July 26, 2001 | doi: 10.1021/bk-2001-0790.ch001

clear near their edges first to the belief that air was drier there and allowed faster evaporation. Another possible explanation will be presented in the next section. Nevertheless, some authors (*25*) still use Croll's normal drying model or the version modified by Eckersley and Rudin (*20*) to fit their drying data even when they observe lateral drying (*26*).

General Considerations about Lateral Drying

In almost all observed cases of lateral drying in laboratory specimens (in which there is a convex shape of the dispersion layer), drying fronts move inward (from the edges toward the center). The opposite case also exists (drying from the center toward the edges) but only when the thickness of the central region is initially thinner. In the following, lateral drying will be considered as occurring from the edges inward.

Downloaded by 89.163.34.136 on September 17, 2012 | http://pubs.acs.org
Publication Date: July 26, 2001 | doi: 10.1021/bk-2001-0790.ch001

Lateral Transport of Water

All authors who have studied lateral drying have come to the conclusion that when a latex dispersion dries laterally, water moves in a lateral direction, i.e. parallel to the interface with the substrate. The problem is often discussed by considering the drying of drops of aqueous dispersions on solid non absorbing substrates since this situation neatly encapsulates many of the open questions. Two possible causes of lateral transport of water have been proposed.

One is based on the fact that at the beginning of the drying process, in a convex drop of emulsion, even if the water concentration is constant over all of the volume, the absolute amount of water is lower near the edges where the drop is thin than in the center where it is thick. If the water evaporation rate is uniform across the surface (neglecting effects of surface curvature), the water will be depleted first near the edges. Soon, a gradient of concentration of water appears oriented from the central part of the drop towards the edges. This lateral gradient will subsequently cause a diffusive flux of water from regions of high concentration to low concentration. The same argument holds for initial shapes other than drops. Large planar films have edges often thinner than the central part, and at these edges, the time for full drying is expected to be shorter. Even in the coating of very large areas, there are usually regions of thinner application, such as caused by brush strokes. As there will almost always be thinner regions in a wet coating, lateral transport of water is usually relevant in the drying process.

Another possible cause of lateral transport of water is the fact that the convex drop tries to maintain a particular shape. One assumes a dominance of surface energies in determining the drop profile. First, the drop keeps the shape of a spherical cap because of its surface tension. Second, at the edges, the drop can either retain a constant contact angle or a constant base (more details will be given later). With uniform evaporation of the drop at the air-liquid interface, the relative change in drop height is greatest at the thin edges, and the flow (from the center to the edges) seeks to rectify the consequent shape changes. These kind of shape models were mainly developed by Parisse and Allain (*27*, *28*) and Deegan et al. (*29*).

Lateral Transport of Particles and Water Soluble Species

Lateral water fluxes in latex dispersions drying laterally can carry particles toward the edges. A famous example is the case of the drying coffee drop elegantly treated by Deegan et al. (*29*). It is an everyday observation that a dry coffee stain always exhibits a dark border due to coffee particles being driven to the edges by the lateral water flux during drying. Dilute poly(styrene) latices were used by the authors as model systems in which the lateral transport of particles could be clearly followed (Figure 2). According to the authors, this phenomenon can influence processes such as printing, washing and coating.

Another piece evidence in support of particle transport is the observation of a thick rim surrounding a flat center in a film resulting from the drying of a latex dispersion that contains a surfactant (*30*). Here a film with a coated circular area 18 mm in diameter and 45 µm thick in the center, was surrounded by a rim 60 µm high.

Routh and Russel (*31*) have performed an experiment which nicely confirms the above considerations. In this experiment, certain regions of a latex dispersion were covered during the drying process. The water loss rate was therefore non-uniform laterally. In regions in which evaporation took place, water concentration was lower, and so there was a lateral flow of water and particles to replace it. In the dried film, the uncovered regions were significantly thicker as a result of this lateral transport.

In the lateral drying mode, a drying front recedes toward the center. As a consequence, the last region of the film to dry is the central part. This laterally moving drying front can have the effect of driving water soluble species toward the center. Thus, in the dry film, a higher concentration can be observed in the center. Indeed, Juhue et al. (*9*) observed by Atomic Force Microscopy a large amount of surfactant at the surface in the central part of a film after drying of a poly(butyl methacrylate) latex dispersion.

Downloaded by 89.163.34.136 on September 17, 2012 | http://pubs.acs.org
Publication Date: July 26, 2001 | doi: 10.1021/bk-2001-0790.ch001

Recent Contributions to the Understanding of Lateral Drying

We will next consider the recent contribution of Winnik and coworkers (*1*, *3*) at the University of Toronto to the understanding of lateral drying. According to these authors, a dry region forms first at the thinnest portion of the wet film. Where this occurs depends upon the shape of the meniscus, which in turn depends upon the contact angle of the dispersion with the substrate. If the contact angle is significantly smaller than 90°, the meniscus is convex, and the dispersion at the edges is thinner than at the center. Drying commences then at the edges of the dispersion. The dry portion at the edge is separated from the wet dispersion by a transition or boundary region (Figure 3).

Downloaded by 89.163.34.136 on September 17, 2012 | http://pubs.acs.org
Publication Date: July 26, 2001 | doi: 10.1021/bk-2001-0790.ch001

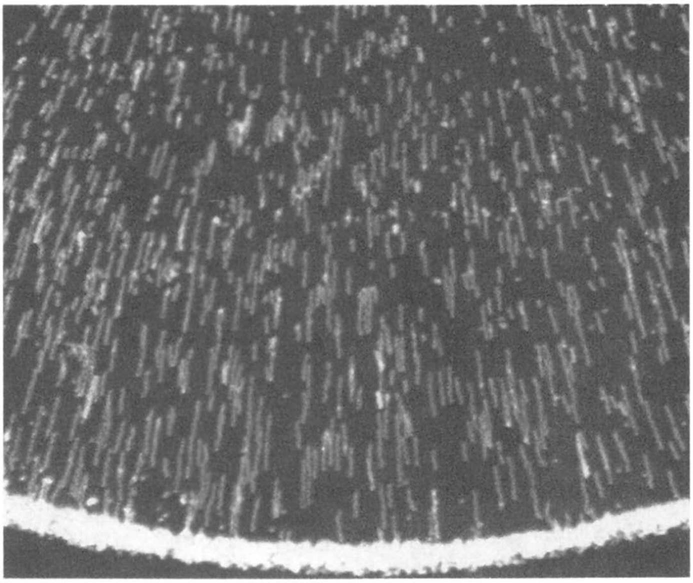

Figure 2 : Poly(styrene) particles in a dilute dispersion in water being driven to the edges during evaporation. Multiple exposures are superimposed to indicate the motion of the particles. Reproduced with permission from reference 29. Copyright 1997 Macmillan Magazines Ldt.

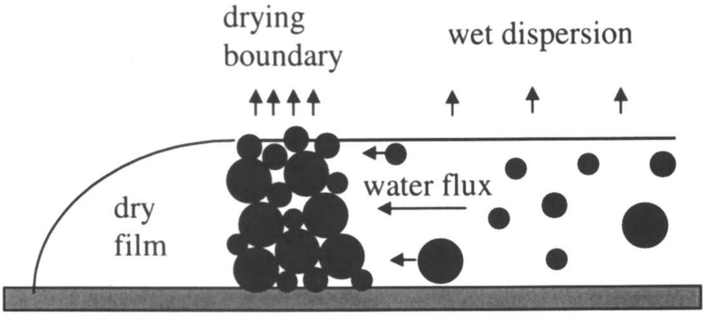

Figure 3: Representation of the drying front for a latex dispersion. Adapted, with permission, from Winnik and Feng (37). Copyright Federation of Societies for Coatings Technology 1996.

The structure and properties of this transition region plays a major role in the drying process. The boundary region is formed of particles in contact constituting a porous medium in which water is constantly wicked through by capillary forces. The water-air interfacial area will be very high and evaporation will take place rapidly in this zone. Thus water evaporates more rapidly from the boundary region than from the water surface above the wet dispersion. This can explain the classical observation of a constant global drying rate even as the wet zone shrinks in size. The high evaporation rate in the drying boundary creates a flux of water and particles from the wet central region to the boundary. The drying front propagates in the direction opposite to that of the water flux. As drying proceeds, the dry film grows in size and the wet dispersion contracts in area. Scriven and coworkers (*32*, *33*) examined rapidly frozen dip-coated films by cryo-scanning electron microscopy to observe particle packing in the boundary region. They called the wet side of the drying boundary the compaction front, and the dry side the pore-emptying front. Voids can persist at the dry side of the drying boundary and, at times, even in the optically clear dry film itself. The time scale for full densification of the dry film can be hours or days (*34*). The forces which operate in the drying boundary in thin layers, and which affect particle packing morphology in monolayers, have been investigated by Denkov et al. (*35*, *36*).

Winnik and coworkers (*37*) also reported some rather surprising results on the kinetics of the drying process of latex blends which can be quite well understood by considering the structure of the drying boundary. Whereas previous studies of drying by gravimetry have mainly considered the total mass loss, this work considered the area of the wet region and thereby estimated the local solids fraction. This approach is much more appropriate in cases where there is lateral drying. They found that the change in solids content over time was faster in dispersions of hard particles than in similar dispersions of soft particles and also that blends of the two dried even more slowly. Measurements of drying rate versus blend composition indicated that there is a composition near a 1:1 number ratio that dries at the lowest rate. Another striking observation is that in the presence of surfactant, the difference in the drying rate of hard and soft latex dispersions disappears. All of these dispersions dry as a laterally moving front. Unlike previous experiments which measured the drying rate from concentrated dispersions, here the dispersions were first diluted to 5 wt% solids. For each film, the loss of water, the time of formation of the dry edge and the contracting area of the wet portion of the film were monitored. The water evaporation rate remained constant long after the appearance of the dry edge at the periphery of the film. This dry edge grew to 60 % of the surface area of the film before a noticeable decrease in the rate of water loss occurred, an observation that established that the dry boundary layer must play an important role in the drying process.

From the previously mentioned point of view, the reason that dispersions of hard particles dry faster than those of similar sized soft particles is related to the magnitude of the capillary transport of water at the wet-dry interface. Latex particles with a high glass transition temperature do not deform during drying at room temperature. The pore structure that remains can conduct water from the wet

Downloaded by 89.163.34.136 on September 17, 2012 | http://pubs.acs.org
Publication Date: July 26, 2001 | doi: 10.1021/bk-2001-0790.ch001

domain into the high surface area region of the film. Deformation of the soft latex particles will lead to smaller capillaries and reduced flow of water. When surfactant is present, it would form a continuous hydrophilic phase and this would have a larger effect on the capillaries of the soft latex dispersion than on the larger pores formed when the hard latex dispersions dry.

In latex blends, the soft particles can deform to fill the spaces between the hard particles. At low values of the volume fraction of hard spheres, the hard particles act as obstacles to the diffusion of water through the capillaries of the soft polymer matrix. Obstacles decrease the diffusion or capillary flow by increasing the tortuosity of the path (*38*). At high values of the volume fraction of hard spheres, the soft polymer plugs the pores between the hard particles. This produces obstacles to water flow, and the drying rate is slower than for the hard particle dispersion itself.

Downloaded by 89.163.34.136 on September 17, 2012 | http://pubs.acs.org
Publication Date: July 26, 2001 | doi: 10.1021/bk-2001-0790.ch001

Most Recent Experimental Studies and Modeling of Lateral Drying

Shape Models

These models have already been mentioned above. It is assumed that surface energies are critical in determining the profile of the drying drop and that maintenance of a prescribed shape in the face of evaporation is critical. The two shape models due to Parisse and Allain (*27*, *28*) envisage an outer drop region in which the particles have gelled at a critical solids fraction and a liquid central region. The outer region is termed the foot. Water evaporates from the whole of the drop surface including the foot. Indeed, it is the flow of matter to the foot that drives its further formation. In both cases, the shape of the central region is that of a spherical cap. The first model assumes that the contact angle at the foot-liquid region boundary is constant (constant contact angle model) whereas the second assumes that the extended spherical cap base is constant (constant base model). Parisse and Allain monitored shape changes of drying drops using optical microscopy. They found that the constant base model better described their observations of drop shape over time than the constant angle model. However, lacking spatially resolved composition data, they were unable to fully test the models.

The model by Deegan et al. (*29*) is another typical example of a shape model. These authors consider that the shape of the drop is always a spherical cap and stress the importance of the pinning of the edges to the substrate. Contact-line pinning is produced by surface irregularities and is much stronger when there are particles in the liquid. The particles deposited at the edges by the initial water flow can create surface unevenness as well as augment the surface imperfections that produced the initial pinning. Pinning of the contact line of the drying drop ensures that part of the liquid evaporating from the edge is replenished by liquid from the interior.

Lateral flow and diffusion models

In the model developed by Routh and Russel (*31*), surface-tension-driven horizontal flow plays a major role. They have analyzed the problem of lateral drying fronts during the drying of latex layers. In particular, they predicted that particles build up at the edge of a latex layer in a close-packed array with a volume fraction of polymer of Φ_m. A particle front is defined as separating the central region of the dispersion from the edge where the particles are packed together. At later times, there is a drying front that recedes from the sample edges, and it separates the dry outer region (with air between the particles) from the region in which water fills the space between the close-packed particles (with $\Phi = \Phi_m$). Routh and Russel have predicted the time required for the water to recede from the edges of the layer, t_{dry}, as a function of a dimensionless capillary pressure, P_{cap}. This single parameter greatly influences the drying behavior and can be used as a predictive tool. It is the strength of the capillary force that determines how long water will remain at the edges of a drying layer and thereby determine the extent of lateral drying. In a dispersion layer of thickness H containing particles of radius a, the dimensionless capillary pressure is given as:

Downloaded by 89.163.34.136 on September 17, 2012 | http://pubs.acs.org
Publication Date: July 26, 2001 | doi: 10.1021/bk-2001-0790.ch001

$$P_{cap} = \frac{20}{75}\left(\frac{3\gamma\eta_0}{\dot{E}}\right)^{1/2} \frac{a(1-\Phi_m)^2}{\mu\Phi_m^2 H}$$

where γ is the water/air interfacial tension, η_0 is the zero-shear rate viscosity of the dispersion, $\dot{E}$ is the evaporation rate, Φ_m is the fraction of solids when there is close packing, and μ is the solvent viscosity. They found that t_{dry} increases with increasing P_{cap}. As an example, they predict that if P_{cap} increases by a factor of 10 (from 12 to 120), then t_{dry} will also increase by about an order of magnitude. The value of P_{cap} can be tuned via the control of several parameters. We see that faster evaporation rates (such as at higher temperatures or in lower humidities) and thicker layers, will cause a lower P_{cap}. A higher surface tension, dispersion viscosity or particle size, on the other hand, will increase P_{cap}. Thickeners (modifiers to viscosity) and surfactants (modifiers to surface tension) are predicted to influence the open time. The amount of particle ordering regulates the value of Φ_m, which also has a large influence on P_{cap}. Thus, this theoretical work identifies factors of a latex dispersion that will influence its drying characteristics.

It is instructive to consider the values of P_{cap} typically encountered in latex dispersions. For the purposes of illustration, let $\gamma = 0.035$ N/m, $\eta_0 = 0.1$ Pa s, $\mu = 10^{-3}$ Pa s, and $\Phi_m = 0.64$ (corresponding to random close-packing). A large P_{cap} value of ~ 430, and hence a long open time, will be obtained with a relatively slow evaporation rate (in still air, $\dot{E}$ is about 4 x 10^{-6} g cm^{-2} s^{-1} or 4 x 10^{-8} m s^{-1}) (*18, 34*), big particles (a = 0.3 μm), and a thin film (H = 30 μm). A small P_{cap} value of about 0.7, on the other hand, and a corresponding short open time, will be obtained with a relatively fast evaporation rate ($\dot{E} = 4 \times 10^{-7}$ m s^{-1}), small particles (a = 25 nm), and a thick film (H = 500 μm).

MRI Experimental Studies and Modeling of Lateral Drying

As pointed out earlier, it is the position of water within a coating (vertically and laterally) that determines its open time and its performance characteristics. Hence, there is a need for non-invasive techniques suitable for the study of waterborne coatings as they dry. The use of vacuum-based techniques, such as electron microscopies, ion beam analysis, Secondary Ion Mass spectrometry, Electron Spectroscopy for Chemical Analysis, etc., is generally not feasible. [However, the use of a cryogenic stage has enabled Scanning Electron Microscopy on film cross sections in order to reveal water concentration profiles and particularly the interface between wet and dry regions (*32*, *33*).] Secondly, polymer and colloidal systems are often chemically and mechanically fragile during their processing, and so, in many techniques, artefacts and often outright damage develop. The technique of Magnetic Resonance Imaging (MRI) overcomes both difficulties. MRI can be performed in the ambient atmosphere on wet samples, and it is a truly non-invasive technique as it only radiates the sample with radiofrequency pulses.

MRI has gained wide acceptance in medicine where it is frequently the imaging modality of choice. Within the last decade, it has been used increasingly more often to tackle problems in materials science. For instance, the group at the University of Surrey has employed MRI to visualize solvent ingress into polymers (*39*, *40*), including water transport in natural polymers (*41*, *42*), to probe the ingress and efficacy of hydrophobic coatings on cements and other building materials (*43*, *44*), to determine the kinetics of creaming in thin layers of oil-in-water emulsions (*45*), to probe the effect of flocculation in emulsions (*46*), and to monitor water concentration profiles during the film formation of alkyd emulsions (*47*).

MRI offers several capabilities that are highly relevant to the study of coatings. It provides compositional profiles of selected elements (such as ^{1}H, which is most often studied) in one or two dimensions. Beyond this, however, it provides information on the mobility of chemical species, as indicated in spatially-resolved measurements of T_1 and T_2 relaxation times and self-diffusivities. Polymer dynamics are of scientific interest, and they are directly relevant to technological processes such as polymerization, curing, melting, dissolution and weathering. It is this second capability that makes MRI stand out among other techniques. Moreover, the capability of profiling both composition and polymer dynamics makes the technique particularly suited for coating/substrate systems. In cases where there is a large chemical shift between the signals from water and from a polymer, it is possible to obtain images of both components. Quantitative information can be obtained from the images. The technique builds on the principles of nuclear magnetic resonance spectroscopy. By introducing a magnetic field gradient, resonant frequency is used to encode spatial position in a sample.

Downloaded by 89.163.34.136 on September 17, 2012 | http://pubs.acs.org
Publication Date: July 26, 2001 | doi: 10.1021/bk-2001-0790.ch001

In a 2D MRI microscope image of a drying aqueous dispersion, the intensity can be related to the mass of water at a particular position. By careful analysis of images (such as shown in Figure 4), the group at Surrey (*47*) has measured the water loss rates as a function of radial position in drops of alkyd emulsions and latex dispersions.

They found that the local water loss is faster at the center and slower at the edges. This is due to the lateral flux of water from the center to the edges. This result is fully explained and supported by the predictions of a master equation describing the lateral flux of water, given below. The result is also consistent with the predictions of Routh and Russel (*31*).

The master equation predicts the water concentration, ϕ, as a function of time, t, and radial position, r, in a drop with a height of h(r). The expression consists of two terms. The first one describes the lateral diffusive flux of water from the center of a drop to the edges. The second term describes the water loss because of evaporation with a rate of E (mass loss per second per unit area):

$$\frac{\partial\phi}{\partial t} = \frac{1}{r\,h(r)}\frac{\partial}{\partial r}\left[r\,h(r)(1-\phi)\phi^{1/2}D_0\frac{\partial\phi}{\partial r}\right] + \frac{(1-\phi)}{h(r)\rho_w}E$$

Here, ρ_w is the density of water. The mutual diffusion coefficient, D_m, is given by $D_0(1-\phi)\phi^{1/2}$, where D_0 is the self diffusion coefficient of water. This expression for D_m takes into account the fact that at higher concentrations of polymer, there is a greater tortuosity and reduced diffusive flow, and hence there is a $\phi^{1/2}$ term. In addition, if the shape of the convex layer does not change as a result of diffusion but only because of evaporation, which it is usually found to do, then there must be a back-flow of the dispersion for volume conservation. Hence, there is a $(1-\phi)$ term in the mutual diffusion coefficient.

Current experimental work is exploring the effects of the influence of the particles on the drying behavior. Particle size and coating thickness affect the reduced capillary pressure, which in turn influences the drying time, t_{dry}. The degree of ordering of the particles will influence the fraction of solids in the dry region of the film (Φ_m in the notation defined above). Similarly, the polydispersity in the size of the particles will influence the volume fraction of polymer in a close-packed array of particles, and so it too will affect Φ_m.

Mixed Modes of Drying

The drying modes presented so far are not always well separated in real systems. In a dilute dispersion, where particles are at large mean distances, drying starts homogeneously, the volume fraction of water remains homogeneous for a while. Then, quite often, a dry edge can appear which progresses inward laterally. What happens in the meantime in the central region of the latex dispersion? In the description of lateral drying reviewed above, it is assumed that the polymer

Downloaded by 89.163.34.136 on September 17, 2012 | http://pubs.acs.org
Publication Date: July 26, 2001 | doi: 10.1021/bk-2001-0790.ch001

Downloaded by 89.163.34.136 on September 17, 2012 | http://pubs.acs.org
Publication Date: July 26, 2001 | doi: 10.1021/bk-2001-0790.ch001

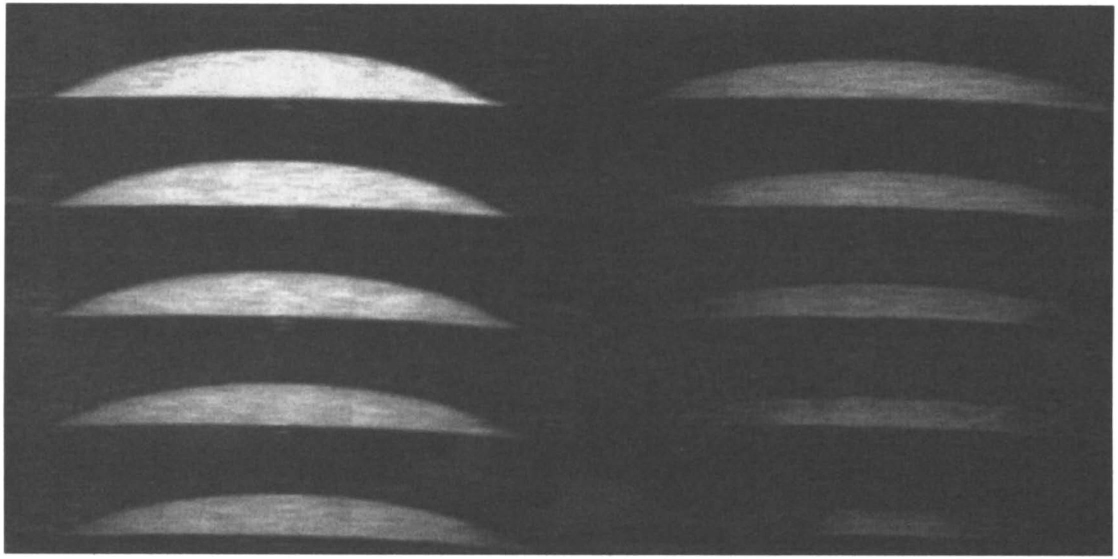

Figure 4: A series of MR images obtained from a drop of a latex dispersion with a bimodal size distribution. Time is increasing in 34 min. intervals starting from the top left and moving downwards. The intensity of the image can be related to the local water concentration. The initial drop diameter is about 1 cm. Over time both the diameter and height of the drop decrease. A water concentration gradient is seen in the radial direction, but there is not an abrupt step in concentration between the "dry" edge and "wet" central region.

concentration stays constant over time. In real systems, however, two drying fronts can coexist in the system, one moving laterally, the other one moving in a direction normal to the surface. This situation is depicted in Figure 5, in which two distinct drying fronts are shown. The drying fronts are also expected to reflect the geometry of the dispersion layer, so that in a convex drop, the drying front might be more like an "onion skin" growing in thickness over time.

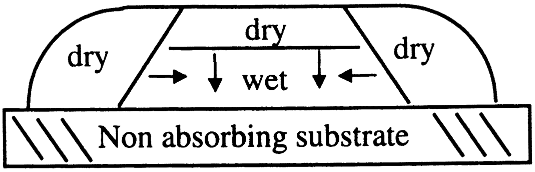

Figure 5: Normal and lateral drying modes occurring at the same time, giving rise to two drying fronts moving simultaneously.

An interesting example of this case is given in the paper by Okubo *et al.* already quoted above (*24*). In the central part of a laterally drying acrylic latex dispersion, a skin was observed on top of the wet region, as shown in Figure 6.

Van Tent and Nijenhuis (*48*, *49*) reported a series of experiments in which they monitored the turbidity (UV-visible transmission) of latex dispersions and weight loss simultaneously. The dispersions had a very narrow particle size distribution and were stabilized by a limited amount of anionic surfactant. The films dried as a front moving inward from the edge, and the transmission measurements probed the center of the samples. Below film forming temperature, as water evaporated, turbidity decreased except at a particular wavelength where optical interference due to particle ordering led to a peak with reduced transmission. As the dispersion dried further, the interference peak shifted to lower wavelengths, consistent with a decrease in particle separation. Then, a second peak appeared which was interpreted as reflecting the formation of a flocculated phase at the latex dispersion-air interface, equivalent to the skin mentioned above in Okubo et al.'s work. The thickness of this phase progressively increased upon further drying. This image of the drying process has similarities to that presented by Croll (*12*), described earlier in this chapter.

As a side remark, let us briefly address here a somewhat different issue, namely ordering in the center of laterally drying latices. Juhué et al. (*9*) used Atomic Force Microscopy to observe ordering of poly(butyl methacrylate) particles in dispersions containing sodium dodecyl sulfate. One can speculate that there are lateral forces due to the drying front affecting the packing of particles in the last spot to dry, and the symmetry of the forces promotes strong ordering in this region.

Downloaded by 89.163.34.136 on September 17, 2012 | http://pubs.acs.org
Publication Date: July 26, 2001 | doi: 10.1021/bk-2001-0790.ch001

Downloaded by 89.163.34.136 on September 17, 2012 | http://pubs.acs.org
Publication Date: July 26, 2001 | doi: 10.1021/bk-2001-0790.ch001

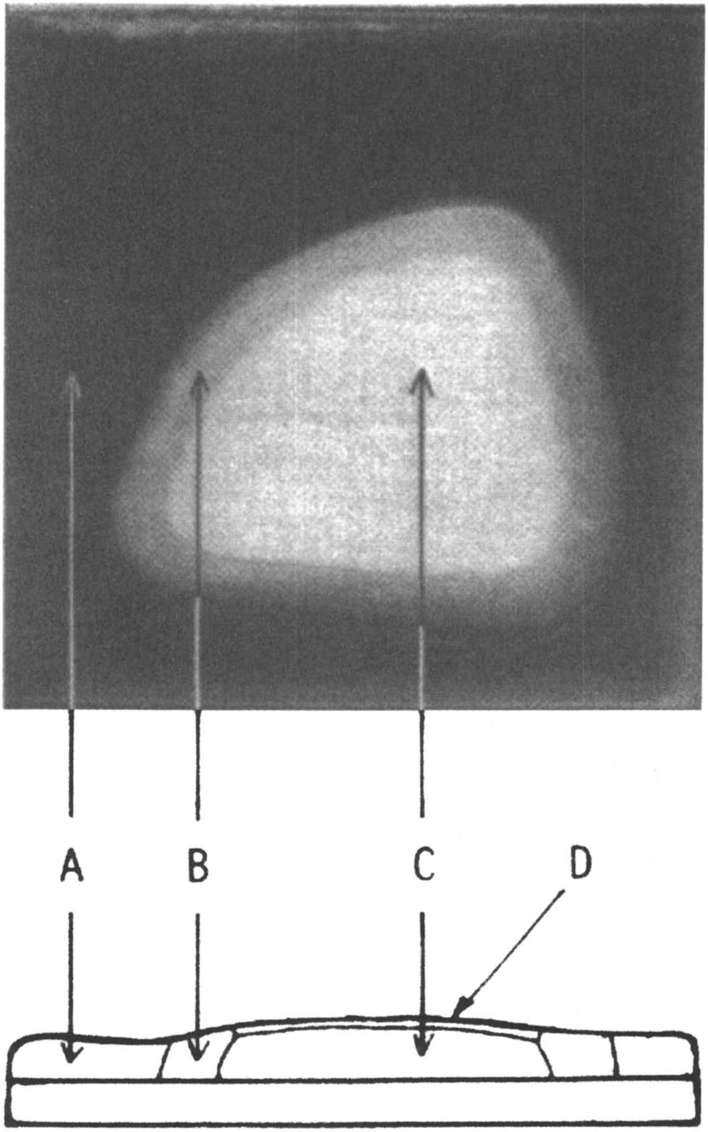

Figure 6: Optical micrograph (top view) and schematic diagram (side view) of an unstable acrylic latex dispersion drying on a glass plate. A transparent "dry" polymer is seen at the perimeter (region A); a turbid wet emulsion is in the sample center (C); and a "flocculated zone" (B) is between these two regions. On top of the wet region, a skin is present (D). Adapted, with permission, from reference 24. Copyright John Wiley & Sons 1981.

Downloaded by 89.163.34.136 on September 17, 2012 | http://pubs.acs.org
Publication Date: July 26, 2001 | doi: 10.1021/bk-2001-0790.ch001

A very clear example of a mixed mode of drying was given recently by Scriven and coworkers (*50*). They used Cryogenic Scanning Electron Microscopy (cryo-SEM) to examine the distribution of polystyrene and poly(butyl methacrylate) latex particles during the early stages of drying of waterborne suspensions. The particles of both latices were narrowly distributed around 500 nm. Apparently, these systems dried laterally. The boundary region between the dry edges and the wet center was disordered when the ionic strength of the medium was high but was ordered in deionized latices. Away from the edges, in the central part, very early in the drying process, clusters of particles formed at the surface and grew in size. As the water was drawn upward by evaporation and capillarity, particles were driven by this flux and lodged in a consolidation front (on top of the latex dispersion) that was parallel to the surface and advanced downward into the coating. This front advanced downward, not laterally along the coating surface. In contrast, the front at the thin edge does advance laterally. According to the authors, the underlying mechanism for both fronts is the same except that the downward pace of the consolidation front was much slower than the lateral pace of the front at the edges, where drying was much faster.

A consequence of the mixed mode of drying is that water soluble species tend to accumulate in the central part of the film, at the film-substrate interface. This behavior was indeed observed by Belaroui et al. (*51*) in their study of the distribution of the highly water soluble sulfate ion in dry poly(butyl acrylate-co-acrylic acid) latex films by Raman Confocal Spectroscopy (Figure 7).

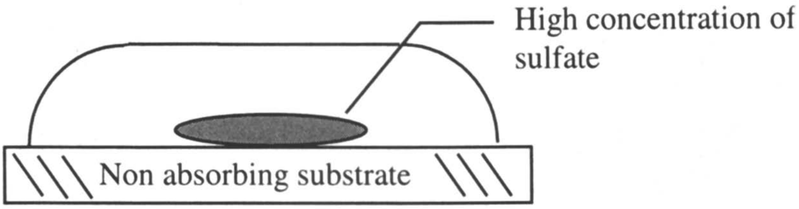

Figure 7: Accumulation of SO_4^{2-} in the center of a film along the interface with the substrate following a mixed mode of drying.

Although there are clear examples in the literature of systems drying in a pure lateral mode (e.g. the system described above of alkyd emulsions (*47*) in which no vertical heterogeneity of water concentration was detected), the mixed mode of drying discussed in this section is perhaps the more general case.

Normal versus Lateral Drying: the Controlling Parameters

Whether a particular coatings system dries from the air surface or from the sample edge is an important technological question. It is also a topic that causes confusion and that stirs debate among researchers. Based on the arguments presented already, we suggest that in layers that are thinner at the edges, a drying front will eventually proceed inward from the edge. The exact time when this occurs, as considered by Routh and Russel (*31*), is a function of the reduced capillary pressure, which is a function of several parameters.

Routh and Russel (*52*, *54*) have also considered what determines vertical homogeneity during drying. They proposed that a convenient predictive tool is the ratio of the rate of vertical convection over the diffusion coefficient of particles, D, given as $H\dot{E}/D$, where H is the layer thickness and $\dot{E}$ is the evaporation rate (given in units of distance per time). If this ratio is much less than 1, then diffusion is dominant and particle transport will ensure vertical homogeneity. If it is significantly greater than 1, then diffusion is slow in comparison to vertical convection, and a drying front will be seen to recede from the surface at an early stage. In this latter case, soft particles are prone to form a "skin" at the surface. It is highly worthwhile to consider what parameters influence D, which can be expressed according to the Stokes-Einstein equation as:

$D = kT/6\pi a\mu$,

using the same symbols defined above. Thus, we see that the relative values of layer thickness, evaporation rate, particle size, temperature, and solvent viscosity will all play a part in influencing whether there is drying normal to the surface. (Particle sedimentation will also lead to non-homogeneity in the vertical direction, of course.) The gauge can then be expressed as:

$$\frac{kT}{6\pi\mu aH\dot{E}}$$

If this expression is much greater than one, the layer will be uniform vertically. Thus we see that the relative values of layer thickness, evaporation rate, particle size, temperature, and solvent viscosity will play a part in influencing whether there is drying normal to the surface. With this gauge, quick calculation for a given dispersion will be able to predict if drying should occur normal to the surface. We will next consider specific examples of how lateral and normal drying is influenced by thickness (H) and geometric effects, structure and rheology of the dispersion and solvent (μ), polymer particle viscoelasticity, and the global rate of water loss ($\dot{E}$).

Thickness and geometric effects

The importance of thickness effects was already stressed in the preceding sections. More precisely, differences in thickness in the cast dispersion are crucial. In thinner parts of the layer, the water concentration decreases faster and

Downloaded by 89.163.34.136 on September 17, 2012 | http://pubs.acs.org
Publication Date: July 26, 2001 | doi: 10.1021/bk-2001-0790.ch001

this, in turn, provokes a water flux in order to compensate for concentration gradients. Water fluxes can carry particles as discussed at length previously.

The most common origin of thickness differences is a surface tension effect. At the edge of a latex dispersion cast on a substrate, the interfacial tensions in play (dispersion-air, dispersion-substrate, and substrate-air) determine the curvature of the meniscus formed by the dispersion. A convex meniscus gives rise to a thin edge and this will lead to a system drying laterally inward. On the other hand, a concave meniscus will lead to the opposite case of lateral drying from the center outward. This latter situation might be found when coating large areas with varying surface energy. As shown in the theoretical development of Routh and Russel, the geometry of a layer at its edge (e.g. curved or square), which defines the initial boundary conditions, has a profound influence on the open time and progression of the lateral drying fronts. The geometry is also expected to influence the amount of mixing of the lateral and vertical modes. Finally, in very thick layers, the Routh and Russel gauge will be less than 1, and so homogeneity in the vertical direction is not expected.

In large samples, the coating procedure can also lead to thinner regions which will be the origin of laterally moving drying fronts. An interesting question to investigate is the relative thickness difference at which the effect starts, in conjunction with the evaporation rate. Current work at the University of Surrey is developing MRI technology to image large, planar coatings in which the meniscus is negligible.

Downloaded by 89.163.34.136 on September 17, 2012 | http://pubs.acs.org
Publication Date: July 26, 2001 | doi: 10.1021/bk-2001-0790.ch001

Structure and rheology of the dispersion

For lateral drying to occur, fluxes within the wet portion of the drying film transport latex particles to the dry-wet boundary layer. The rate of this flux is sensitive to the viscosity of the wet droplet. Under normal circumstances, when the particle size distribution is broad or when particles only weakly repel each other, the dispersion will remain fluid. Such a system is expected to be very sensitive to thickness effects.

On the other hand, if the latex dispersion is able to form a colloidal crystal (i.e. it has a narrow particle size distribution and strong interparticle repulsion), the particles no longer have the possibility to move freely in the liquid. The flux will be suppressed, and drying will occur homogeneously with an uniform decrease of the interparticle distance until particles come in contact. Afterwards, thickness effects should be much less pronounced and drying is more likely to occur as a front moving normal to the surface.

An analogous situation should happen in latex dispersions where the continuous phase is highly viscous (containing water-soluble polymers or thickeners, for instance) or when the drying process is started with a very concentrated dispersion. Feng et al. (*53*) reported that addition of small amounts of diamines to PBMA latex dispersions changed the drying mode from lateral to normal. They reasoned that weak flocs formed in the dispersion opposed lateral fluxes in the wet film, and as a consequence, no dry edge appeared. The concentrated (84 wt% solids), reactive, polydimethylsiloxane emulsion already cited (*11*) is an example of a system exhibiting the normal mode of drying, despite marked thickness variation across the coated layer. Moreover, the viscosity of the continuous phase and the viscosity of the dispersion were both identified as influences on the open time in the modeling of Routh and Russel (31). In addition, the solvent viscosity will influence particle diffusion, which in turn, affects vertical homogeneity.

Polymer Particle Viscoelasticity

There have been various attempts over the years to determine if particle deformation influences the water loss rate of water in drying dispersions. Clearly, in the early stages, the particles should have no effect on the drying rate. In the later stages, a global slowing down in water loss rate is often observed and which is often attributed to the effects of particle deformation and coalescence. As already mentioned, Sheetz (16) proposed the concept of skin formation at the air surface leading to a slowing down of drying. The difference in drying rate, described in reference 37 for dispersions of hard and soft latex particles, was explained in terms of soft particle deformation to narrow the capillary pores at the dry-wet boundary of the drying film. Routh and Russel (*54*) have recently considered the various driving forces for particle deformation and identified conditions when skin formation is likely. They concluded that the polymer viscosity is the dominant property in influencing whether skin formation occurs. At temperatures well above the glass transition temperature, where viscosity is lower, skin formation is encouraged.

Global rate of water loss

Qualitatively, it can be argued that a slow rate of evaporation (as caused by low temperature, high relative humidity, or static air) favors uniform drying (because the water concentration has more time to equilibrate within the coating) or lateral drying. Conversely, a fast rate of evaporation will lead to a rapid elimination of water in the top region of the drying layer all over the surface and lead to the normal drying mode.

This is neatly illustrated in Ciampi *et al.*'s paper (*47*). In the case of a hard sphere latex dispersion, the rate limiting conditions have a pronounced influence on the water profile during drying. With static air, when diffusion of the water vapor away from the sample is the rate-controlling step, drying profiles are seen to move in from the thinner edges. Under flowing nitrogen, when free evaporation of

Downloaded by 89.163.34.136 on September 17, 2012 | http://pubs.acs.org
Publication Date: July 26, 2001 | doi: 10.1021/bk-2001-0790.ch001

the water is allowed, the sample dries near its surface first, forming a skin, in what can be considered to be a different mode of drying. In terms of the Routh and Russel "gauge", we suggest that when E was faster, $kT \ll 6\pi a\mu H E$, and so vertical homogeneity was lost, leading to drying normal to the surface.

Concluding Remarks

It is clear now that drying modes of polymer colloids still hold mysteries, even if the understanding of the underlying processes has much improved over the last decade. There are still further aspects which were not discussed above like the effect of the chemical nature of the particles (*55*) or the case where water is absorbed into a porous substrate (such as paper).

An improvement in the understanding of the relative importance of the parameters which determine the drying modes is required if better control and predictions are to be achieved. This is certainly possible through a continuing effort in experimental studies as well as in theoretical modeling. New promising techniques to study drying have appeared, like Raman Confocal Spectroscopy and Magnetic Resonance Imaging, but still further improvements would be desirable, especially if one wants to get valuable information about ultra-fast drying processes of major technological importance.

Downloaded by 89.163.34.136 on September 17, 2012 | http://pubs.acs.org
Publication Date: July 26, 2001 | doi: 10.1021/bk-2001-0790.ch001

Literature cited

1. Winnik, M.A.; *Current Opinion in Colloid Interface Sci.* **1997**, 2, 192-199.
2. Keddie, J.L.; *Mat. Sci. Eng.* **1997**, R21, 101-170.
3. Winnik, M.A. in *Emulsion Polymerization and Emulsion Polymers*; Lovell P.A. & El-Aasser M.S., Eds; John Willey: New York, 1997; pp 467-518.
4. Joanicot, M.; Wong, K.; Maquet, J.; Chevalier, Y.; Pichot, C.; Graillat, C.; Lindner, P.; Rios, L.; Cabane, B.; *Prog. Colloid Polym. Sci.* **1990**, 81, 175.
5. Chevalier, Y.; Pichot, C.; Graillat, C.; Joanicot, C.; Wong, K.; Maquet, J.; Lindner, P.; Cabane, B.; *Colloid Polym Sci.* **1992**, 270, 806-821.
6. Joanicot, M.; Wong, K.; Richard, J.; Maquet, J.; Cabane, B.; *Macromolecules* **1993**, 26, 3168-3175.
7. Beetsma, J., *Pigment Resin Technol.* **1998**, 27, 12.
8. Holl, Y.; Macromol Symp. **2000**, 151, 473.
9. Juhué, D.; Wang, Y.; Lang, J.; Leung, O.M.; Goh, M.C.; Winnik, M.A.; *J Polym Sci Part B Polym Phys.* **1995**, 33, 1123.
10. Crank, J.; *The Mathematics of Diffusion*; Clarendon: Oxford, **1975**.
11. Guigner, D.; Fischer, C.; Holl, Y.; *Langmuir* (submitted).
12. Croll, S.G.; *J Coating Technol.* **1986**, 58 (734), 41-49.
13. Charmeau, J.Y.; Gerin, P.; Vovelle L.; Schirrer, R.; Holl, Y.; *J Adhesion Sci Technol.***1999**, 13, 203 & 217.

14. Tebelius, L.K.; Urban, M.; *J Appl Polym Sci.* **1995**, 56, 387.
15. Kientz, E.; Holl, Y.; *Coll Surf.* **1993**, 78, 255.
16. Sheetz, D.P.; *J Appl. Polym Sci.* **1965**, 9, 3759.
17. Vanderhoff, J.W.; Bradford E.B.; Carrington, W.K.; *J Polym Sci: Polym Symp.* **1973**, 41, 155-174.
18. Croll, S.G.; *J Coating Technol.* **1987**, 59 (751), 81-92.
19. Sullivan, D.A.; *J Coating Technol.* **1973**, 47 (610), 60.
20. Eckersley, S.T.; Rudin, A.; *Prog Org Coating.* **1994**, 23, 387.
21. Eckersley, S.T.; Rudin, A.; *J Appl Polym Sci.* **1994**, 53, 1139.
22. Hwa, J.C.H.; *J Polym Sci.* **1964**, A2, 785.
23. Myers, R.R.; Schultz, R.K.; *J Appl Polym Sci.* **1964**, 8, 755.
24. Okubo, M.; Takeya, T.; Tsutsumi, Y.; Kadooka, T.; Matsumoto, T; *J Polym Sci Polym Chem Ed.* **1981**, 19, 1.
25. Jackson, M.L.; Love, B.J.; *Proceedings of the American Chemical Society, Div Polym Mat Sci Eng.* **1999**, 81, 415.
26. Jackson, M.L. *personal communication.*
27. Parisse, F.; Allain, C.; *J Phys II France* **1996**, 68, 39.
28. Parisse, F.; Allain, C.; *Langmuir* **1997**, 8, 3598.
29. Deegan, R.D.; Bakijin, O.; Dupont, T.F.; Huber, G.; Nagel, S.R.; Witten, T.A.; *Nature* **1997**, 389, 827.
30. Feng, J.; Winnik, M.A.; Shivers, R.R.; Clubb, B.; *Macromolecules* **1995**, 28, 7671.
31. Routh, A.F.; Russel, W.B.; *AIChE J.* **1998**, 44, 2088-2098.
32. Sheehan, J.G.; Takamura, K.; Davis, H.T.; Scriven, L.E.; *Tappi J.* **1993**, 76, 93.
33. Ming, Y.; Takamura, K.; Davis, H.T.; Scriven, L.E.; *Tappi J.* **1995**, 78, 151.
34. Keddie, J.L.; Meredith, P.; Jones, R.A.L.; Donald, A.M.; *Macromolecules* **1995**, 28, 2673-2682.
35. Denkov, N.D.; Velev, O.D.; Kralczevsky, P.A.; Ivanov, I.B.; Yoshimura, H.; Nagayama, K.; *Langmuir* **1992**, 8, 3183-3190.
36. Denkov, N.D.; Velev, O.D.; Kralczevsky, P.A.; Ivanov, I.B.; Yoshimura, H.; Nagayama, K.; *Nature* **1993**, 361, 26.
37. Winnik, M.A.; Feng, J.; *J Coating Technol.* **1996**, 68 (852), 39-50.
38. Mackie, J.S.; Meares, P.; *Proc R Soc London A* **1955**, 232, 498.
39. Lane, D.M.; McDonald,P.J.; *Polymer* **1997**, 38, 2329.
40. Lane, D.M.; McDonald, P.J.; Keddie, J.L.; *Spatially Resolved Magnetic Resonance*; Wiley-VCH, 1998; p 241.
41. Hopkinson, I.; Jones, R.A.L.; Black, S.; Lane, D.M.; McDonald, P.J.; *Carbohydrate Polym.* **1997**, 34, 39.
42. Hart, T.D.; Chamberlain, A.H.L.; Lynch, J.M.; Newling, B.; McDonald, P.J.; *Enzyme Microbial Technol.* **1999**, 24, 339.
43. Bohris, A.J.; Goerke, U.; McDonald, P.J.; Mulheron, M.; Newling, B.; LePage, B., *Magnetic Resonance Imaging*, **1998**, 16, 455.
44. Bohris, A.J.; McDonald, P.J.; Mulheron, M., *J Mat Sci.* **1996**, 31, 5859.

Downloaded by 89.163.34.136 on September 17, 2012 | http://pubs.acs.org
Publication Date: July 26, 2001 | doi: 10.1021/bk-2001-0790.ch001

45. Newling, B.; Glover, P.M.; Keddie, J.L.; Lane, D.M.; McDonald, P.J., *Langmuir* **1997**, 13, 3621.
46. McDonald, P.J.; Ciampi, E.; Keddie, J.L; Heidenreich, M.; and Kimmich, R., *Phys Rev E* **1999**, 59, 879.
47. Ciampi, E.; Goerke, U.; Keddie, J.L.; McDonald P.J.; *Langmuir* **2000**, 16, 1057.
48. Van Tent, A.; te Nijenhuis, K.; *J Coll Interface Sci.* **1992**, 150, 97.
49. Van Tent, A.; te Nijenhuis, K.; *Prog Org Coating* **1992**, 20, 459.
50. Sutanto, E.; Ma, Y.; Davis, H.T.; Scriven, L.E.; *Proceedings of the American Chemical Society, Div Polym Mat Sci Eng.* **1999**, 81, 181.
51. Belaroui, F.; Grohens, Y.; Boyer, H.; Holl, Y.; *Polymer* **2000**, (in press).
52. A.F. Routh and W.B. Russel, *Proceedings of the American Chemical Society, Div Polym Mat Sci Eng.* **1999**, 81, 209.
53. Feng, J.; Pham, H. H.; Macdonald, P. M.;. Winnik M. A.; Geurts, J. M.; Zirkzee, H.; van Es, S.; German A. L.; *J. Coat. Technol.* **1998** 70 (881), 57.
54. Routh, A.F.; Russel, W.B.; *Langmuir* **1999**, 15, 7762.
55. Tang, J.; Dimonie, V.L.; Daniels, E.S.; Klein, A.; El-Aasser, M.S.; *Proceedings of the American Chemical Society, Div Polym Mat Sci Eng.* **1999**, 80, 567.

Downloaded by 89.163.34.136 on September 17, 2012 | http://pubs.acs.org
Publication Date: July 26, 2001 | doi: 10.1021/bk-2001-0790.ch001

Downloaded by NORTH CAROLINA STATE UNIV on September 17, 2012 | http://pubs.acs.org
Publication Date: July 26, 2001 | doi: 10.1021/bk-2001-0790.ch002

Chapter 2

On Capillary Forces and Stress in Drying Latex Coating

L. A. Pekurovsky and L. E. Scriven

Department of Chemical Engineering and Materials Science and Center for Interfacial Engineering, University of Minnesota, 421 Washington Avenue, S.E., Minneapolis, MN 55455–0132

In drying latex coating particles come to contact under capillary forces at curved menisci. The same menisci compress all of the particles beneath, and the particles contacts flatten. They continue flattening under capillary forces generated by menisci of pendular rings around interparticle contacts, and adhesion forces between close particle interfaces. This research focuses on the role of capillary forces on compaction and deformation of latex particles, and development of stresses throughout the coating. The net in-plane stress is compressive or tensile, depending on whether the particles are in wet or moist stage, and the out-of-plane stress changes from compressive to zero, whereas the local stresses in contacts may be so large that yielding and plastic flow occur there.

In latex coating a layer of aqueous suspension of micron- or sub-micron scale polymer particles stabilized against flocculation is deposited on a substrate, and then dried and transformed into a continuous, adhering polymer film — or, in some cases, a film of controlled porosity. Of the stages into which the transformation can be divided (Figure 1), this research concerns the wet and moist stages of particle compaction and deformation. The actions of surface tension directly and through capillary pressure difference ("Laplace pressure") across curved gas-liquid menisci in the coating are evaluated. As water dries from the surface of the suspension, the particle concentration rises until the particles at the surface start clustering and are driven together into a consolidated layer (1). As this happens, the water that has evaporated leaves the particles

In Film Formation in Coatings; Provder, T., et al.;
ACS Symposium Series; American Chemical Society: Washington, DC, 2001.

of the surface layer protruding, with menisci between them that are concave to the air (provided the particles are not hydrophobic). The capillary pressure of these menisci sucks liquid from beneath to replace that which evaporates; the arriving liquid carries still more particles into the consolidated layer until that layer grows all the way to the substrate. The fully consolidated coating with menisci still at its top surface is here called the *wet stage* (Figure 2(a)). In it the particles are put into compression by the surface tension force that acts directly at the contact lines on the protruding surface particles, and by the capillary pressure acting over the protruding cross-section of surface particles (i.e. the difference between ambient air pressure and the lower pressure of the liquid within the coating). Under the compression, neighboring particles flatten against each other in patterns that depend strongly on the density and regularity of particle packing. As drying proceeds and water is depleted from the coated layer, the menisci between the particles at the surface advance into the constricted passages, or pore-throats, between particles. They advance until they become so sharply curved that they are unstable and move forward, more or less abruptly depending on the liquid's viscosity, by Haines' jumps, which empty pore bodies of liquid except for pendular rings around particle-particle contacts. The coating with its porespace filled with air except for the pendular rings of liquid is here called the *moist stage* (Figure 2(b)). The menisci of the pendular rings are sharply curved and cause capillary pressure that, together with surface tension's force at the contact circles, flattens the particles against each other. Adhesion forces between adjoining particle surfaces can flatten them too, although these were not considered in the work reported here. Actually in the course of drying, a front of menisci advancing by Haines' jumps descends into the coating. Behind the front is an expanding moist zone; ahead of it is a contracting wet zone. As it passes a particle, the latter changes from a state of compression, both perpendicular to the plane of the coating, or *out-of-plane*, and parallel to it, or *in-plane*, to a more complicated state. That state is no net stress *out-of-plane*, and net tensile stress *in-plane*; at contacts the tensile stress must be balanced by the local compressive contribution from the pendular ring (as long as it remains), or else an adhesion force must make up the difference.

Downloaded by NORTH CAROLINA STATE UNIV on September 17, 2012 | http://pubs.acs.org
Publication Date: July 26, 2001 | doi: 10.1021/bk-2001-0790.ch002

Forces that Act on Particles

A particle in a consolidated coating can be acted on by four forces (Figure 2):

$$(i) \quad \textit{liquid pressure force} = -\int_{S_{wet}} p_l \mathbf{n}\, dS \qquad (1)$$

S_{wet} here is the wetted sphere surface, $\mathbf{n}$ is its unit normal (outward), and p_l is the local liquid pressure. Here that pressure is taken to be uniform (e.g. negligible effect of gravity – buoyancy – and negligible pressure gradient to drive viscous flow toward evaporating menisci) and therefore set by the capillary pressure difference ("Laplace pressure") at bounding menisci, here taken to all have the same curvature (e.g. slow enough evaporation for hydrostatic equilibrium to be closely approached). Thus $p_a - p_l = 2H\sigma$, where H is the meniscus mean curvature and σ is the air-water surface tension; here the liquid is taken as wetting

Downloaded by NORTH CAROLINA STATE UNIV on September 17, 2012 | http://pubs.acs.org
Publication Date: July 26, 2001 | doi: 10.1021/bk-2001-0790.ch002

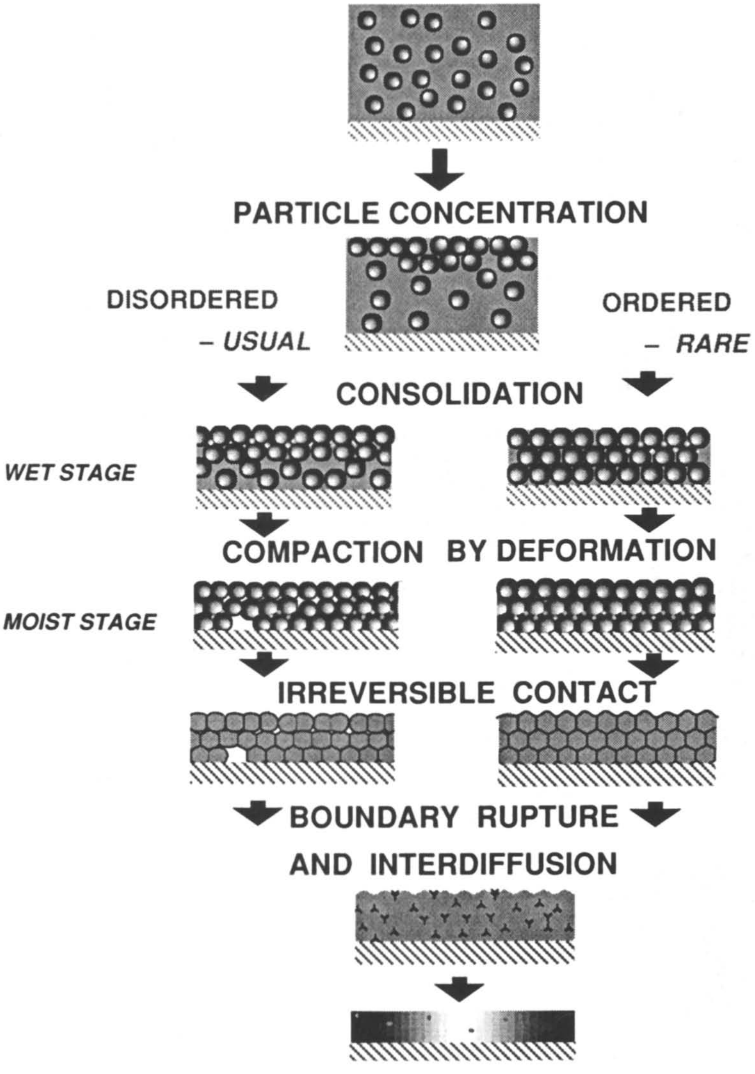
PARTICLE CONCENTRATION
DISORDERED
- USUAL
ORDERED
- RARE
CONSOLIDATION
WET STAGE
COMPACTION BY DEFORMATION
MOIST STAGE
IRREVERSIBLE CONTACT
BOUNDARY RUPTURE
AND INTERDIFFUSION

FIGURE 1. Scenario of film formation and coalescence by drying of a latex suspension.

Downloaded by NORTH CAROLINA STATE UNIV on September 17, 2012 | http://pubs.acs.org
Publication Date: July 26, 2001 | doi: 10.1021/bk-2001-0790.ch002

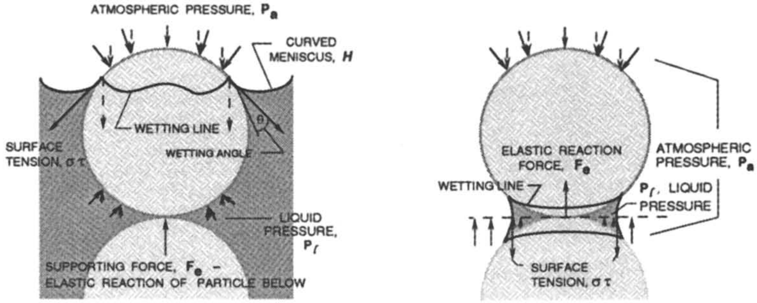
ATMOSPHERIC PRESSURE, P_a
CURVED MENISCUS, H
WETTING LINE
θ
SURFACE TENSION, σ τ
WETTING ANGLE
LIQUID PRESSURE, P_ℓ
SUPPORTING FORCE, F_e - ELASTIC REACTION OF PARTICLE BELOW
ELASTIC REACTION FORCE, F_e
WETTING LINE
ATMOSPHERIC PRESSURE, P_a
P_ℓ, LIQUID PRESSURE
SURFACE TENSION, σ τ

(a) wet stage

(b) moist stage

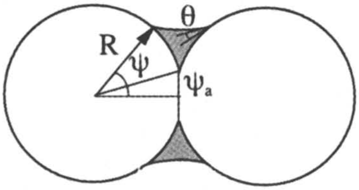

(c) pendular ring geometry: ψ is filling angle; ψ_a is flattening angle

FIGURE 2. Forces on partly wetted particles.

the particles sufficiently well (low enough contact angle) that menisci between particles are (net) concave toward air ($H > 0$). Thus the pressure in the liquid is less than atmospheric (and can be greatly so).

$$(ii) \quad \textit{gas pressure force} = -\int_{S_{dry}} p_a \mathbf{n}\, dS \tag{2}$$

S_{dry} is the dry portion of a sphere surface (which may in fact bear a thin wetting film which in turn contacts the gas), and p_a is the local gas pressure, which is here taken to be uniform and atmospheric, or ambient (e.g. negligible pressure gradient to drive air and vapor from evaporating menisci or to retreating menisci).

$$(iii) \quad \textit{surface tension force} = \oint_{C} \sigma \mathbf{m}\, ds \tag{3}$$

C is the air-water-particle contact line, or wetting line, a closed curve on any particle a meniscus intersects, σ is the local surface tension, which is here taken to be uniform (e.g. negligible surface tension gradients from solute concentration gradients), and $\mathbf{m}$ is the unit vector in the direction in which surface tension acts at a contact line, namely perpendicular to the local tangent to the line and tangential to the meniscus there.

$$(iv) \quad \textit{elastic contact force} = \int_{S_{cont}} \mathbf{T} \cdot \mathbf{n}\, dS \tag{4}$$

S_{cont} is the area of particle-particle contact or contacts (or particle-substrate contact), $\mathbf{n}$ is the unit normal to the area (here taken to be flat) and points outward from the particle under consideration, and $\mathbf{T}$ is the stress state (a dyadic or tensor) in the solid contacted, here taken to be elastic. Moreover, elastic stress here is positive when tensile (the usual convention).

If surface tension were zero, the stress everywhere in the solid would be isotropic and equal to atmospheric, or ambient, pressure, and the force at contacts would be

$$\textit{datum contact force} = -\int_{S_{cont}} p_a \mathbf{n}\, dS \tag{5}$$

The resultant of the first three forces, with this deducted, can be called the (net) force of capillarity on a sphere:

$$\mathbf{F}_c \equiv -p_l \int_{S_{wet}} \mathbf{n}\, dS - p_a \int_{S_{dry}} \mathbf{n}\, dS - p_a \int_{S_{cont}} \mathbf{n}\, dS + \sigma \oint_{C} \mathbf{m}\, ds \tag{6}$$

Downloaded by NORTH CAROLINA STATE UNIV on September 17, 2012 | http://pubs.acs.org
Publication Date: July 26, 2001 | doi: 10.1021/bk-2001-0790.ch002

Downloaded by NORTH CAROLINA STATE UNIV on September 17, 2012 | http://pubs.acs.org
Publication Date: July 26, 2001 | doi: 10.1021/bk-2001-0790.ch002

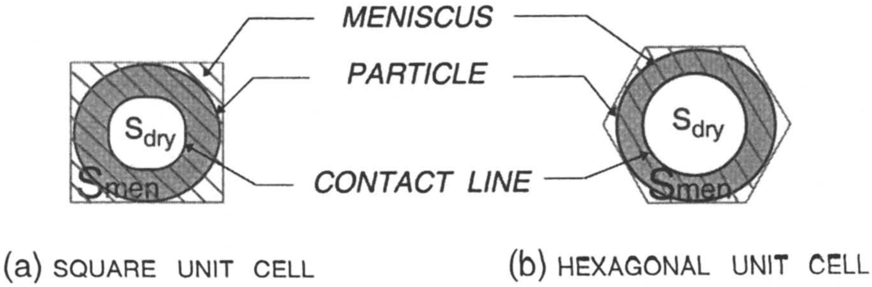

FIGURE 3. A unit cell viewed from above contains the normal projections of the meniscus area S_{men} and the sphere area S_{dry}.

The elastic contact force, Eq. (4), with the datum contact force, Eq. (5), deducted, can be called the (net) elastic reaction force – in reaction to the force of capillarity:

$$\mathbf{F_e} \equiv \int_{S_{cont}} (\mathbf{T} + p_a\mathbf{I}) \cdot \mathbf{n} dS \tag{7}$$

where $\mathbf{I}$ is the unit isotropic dyadic, or tensor. Unless a particle is being accelerated it is in mechanical equilibrium, that is the forces on it must balance. Thus the (net) force of capillarity plus the (net) elastic reaction force must equal zero:

$$\mathbf{F_c} + \mathbf{F_e} = \mathbf{0} \tag{8}$$

What follows is an examination of consequences of this physical principle in simple models of two stages of drying a consolidated, ordered coating of monodisperse (i.e. equal diameter) latex spheres.

Net Force of Capillarity: Wet Stage

In the wet stage the only menisci are among the particles in the top rank, or layer, of the coating. In any regular (planar) array, or packing, of that rank, the (net) force of capillarity on a particle acts perpendicular to the plane of that rank, as a consequence of the symmetry of the packing. With $\mathbf{e_z}$ the direction perpendicular to the plane and away from the coating, the force is $\mathbf{F_c} = \mathbf{e_z} F_c$, F_c being its magnitude:

$$F_c = -(p_a - 2H\sigma) \int_{S_{wet}} \mathbf{n} \cdot \mathbf{e_z}\, dS - p_a \int_{S_{dry}+S_{cont}} \mathbf{n} \cdot \mathbf{e_z}\, dS + \sigma \oint_C \mathbf{m} \cdot \mathbf{e_z}\, ds. \tag{9}$$

Because $S_{wet} + S_{dry} + S_{cont}$ is the total surface of the sphere, over which $\int \mathbf{n}\, dS$ vanishes, the contribution of atmospheric, or ambient, pressure vanishes. It can be shown that

$$F_c = -2H\sigma(S_{cell} - S^*{}_{cont}), \quad S^*{}_{cont} \equiv \int_{S_{cont}} \mathbf{n} \cdot \mathbf{e_z}\, dS. \tag{10}$$

Thus the force of capillarity on a sphere in the top rank of a wet coating is independent of the length and shape of the contact line and is completely determined by the meniscus mean curvature H, the projections of the contact areas, and the area of the symmetry cell (Figure 3). The last is $S_{cell} = 4R^2$ in the square arrayand $2\sqrt{3}R^2$ in the hexagonal array; R is the sphere radius. The force balance, Eq.(8), reduces to

$$-2H\sigma(S_{cell} - S^*{}_{cont}) + \int_{S_{cont}} \mathbf{e_z} \cdot (\mathbf{T} + p_a\mathbf{I}) \cdot \mathbf{n} dS = 0, \tag{11}$$

With a meniscus concave upward, the mean curvature H is positive and the force of capillarity presses the sphere downward against its neighbors beneath. As the liquid volume per top particle (i.e. in the particle's unit cell) falls the mean curvature rises to a maximum.

When departure of liquid by evaporation has raised the meniscus mean curvature to the maximum, the meniscus is unstable with respect to Haines' jumps that carry it to a new set of mechanical equilibrium locations in or about the second layer of spheres. In the course of the jumps, liquid around the intersphere contacts is detached from the main meniscus passing by and takes the form of isolated, axisymmetric pendular rings. Air invades behind the jumps. With further drying come successive rounds of jumps behind which the moist zone enlarges until the entire porespace is full of air (and water vapor) except for the pendular rings. The moist stage of drying ensues.

Downloaded by NORTH CAROLINA STATE UNIV on September 17, 2012 | http://pubs.acs.org
Publication Date: July 26, 2001 | doi: 10.1021/bk-2001-0790.ch002

Net Force of Capillarity: Moist Stage

In the moist stage all intersphere contacts are encircled by pendular rings, and by hypothesis they all share the same mean curvature H. Hence the liquid pressure in each is $p_l = p_a - 2H\sigma$. Because the rings are axisymmetric, the (net) force of capillarity exerted on a sphere by a ring acts along the axis of symmetry and therefore perpendicular to the plane of the contact. With $\mathbf{e_z}$ the axial direction away from the sphere, the force is $\mathbf{F_c} = \mathbf{e_z}F_c$ and its magnitude, according to Eq. (6), is

$$F_c = -(p_a - 2H\sigma) \int_{S_{wet}} \mathbf{n} \cdot \mathbf{e_z}\, dS - p_a \int_{S_{dry}+S_{cont}} \mathbf{n} \cdot \mathbf{e_z}\, dS + \sigma \oint_C \mathbf{m} \cdot \mathbf{e_z}\, ds. \tag{12}$$

The contribution of atmospheric, or ambient, pressure again vanishes. The contact line is a circle, its location on the sphere being marked by the filling angle ψ; see Figure 2. The contact angle there, measured through the liquid, is θ. It can be shown that the magnitude of the force of capillarity adjacent to a contact in the moist stage is

$$F_c = 2\pi\sigma\left(HR^2(\sin^2\psi - \sin^2\psi_a) + R\sin\psi\sin(\psi+\theta)\right) \tag{13}$$

where ψ_a is the flattening angle $\psi_a = \arcsin(a/R)$ and a is the radius of the contact disk. The mean curvature of a pendular ring is uniform (apart from quite negligible effect of gravity) and can be found as a function of R, ψ, ψ_a, and θ from the Young-Laplace equation, which requires solving a two-point boundary-value problem. Although solutions are available a convenient approximation is (2)

$$H \simeq \frac{1}{2R}\left(\frac{\cos(\theta+\psi)}{\cos\psi_a - \cos\psi} - \frac{\sin(\theta+\psi)}{\sin\psi}\right). \tag{14}$$

Combining Eqs. (13) and (14) and employing trigonometric identities leads to a useful approximation to the force of capillarity exerted on a (flattened) sphere by a single pendular ring:

$$F_c \simeq \pi\sigma R\left(\cos(\theta+\psi)\,\cos\psi_a + \cos\theta + \frac{\sin(\theta+\psi)\,\sin^2\psi_a}{\sin\psi}\right). \tag{15}$$

In the limit as the pendular ring shrinks, as by evaporation, $\psi \to \psi_a$, the force tends to a non-zero value:

$$F_{c,limit} = \pi R\sigma(\cos(\psi_a - \theta) + \cos\theta)) \tag{16}$$

If the sphere is not flattened at the contact, $\sin\psi_a = 0$; in the limit as the pendular ring around a point contact shrinks, $\psi \to 0$ and the force rather than vanishing tends to a non-zero value:

$$F_{c,limit} = 2\sigma\pi R\cos\theta. \tag{17}$$

This confirms that traces of residual liquid in the form of minute pendular rings can exert forces of capillarity comparable to – indeed, greater than – those of larger rings.

In every case, the force of capillarity exerted on a (flattened) sphere by a single pendular ring is positive, which means it tends to press the sphere against its neighbor in the contact the ring encircles. Hence the normal stress (relative to ambient pressure) in the contacts tends to be compressive; whether it actually is depends on the collective behavior of the contacts and spheres in the compacting coating.

Downloaded by NORTH CAROLINA STATE UNIV on September 17, 2012 | http://pubs.acs.org
Publication Date: July 26, 2001 | doi: 10.1021/bk-2001-0790.ch002

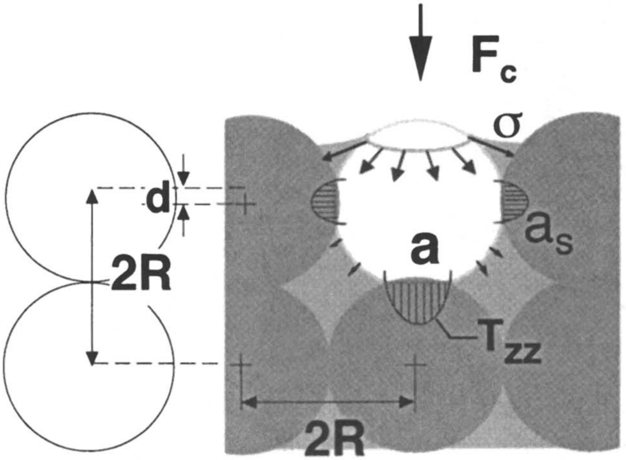

FIGURE 4. In the wet stage, spheres are pressed together by capillary force loading of the top layer, and are squeezed against each other laterally.

Sphere Deformation: Wet Stage

In the wet stage, particles are compressed perpendicular to the substrate by capillary pressure and surface tension loading of the top layer. The loading rises as liquid evaporates and the menisci curve more. (Contact angle affects their curvature, so that loading falls somewhat as particles are made less wettable and contact angle rises.) The interlayer contacts flatten until the compressive stress at them balances the loading (as in the simple packing shown in Figure 4). This compression squashes the particles against their in-plane neighbors and those intralayer contacts flatten under compressive stress too, because once particles are close-packed their centers cannot move in-plane. The elastic stresses at the two types of contacts are not the same nor are they uniform (Figure 5). On each interparticle contact is an evolving distribution of both compressive and tensile local stresses. (Local stress can grow so large that the polymer yields plastically, a likelihood excluded here.) The *wet-stage mean in-plane stress* is *compressive.*

Sphere Deformation: Moist Stage

By assumption the sphere deformations are small enough for contact theory from linear elasticity to apply. Stresses, deformation and flattening can therefore be analyzed by breaking the boundary-value problem of elasticity into three basic ones already solved, and then superposing their solutions (Figure 6). The first is Boussinesq's: contact of two spheres over a circular area governed by distant force on the spheres (3). The second is the problem of distant loading to maintain

Downloaded by NORTH CAROLINA STATE UNIV on September 17, 2012 | http://pubs.acs.org
Publication Date: July 26, 2001 | doi: 10.1021/bk-2001-0790.ch002

Downloaded by NORTH CAROLINA STATE UNIV on September 17, 2012 | http://pubs.acs.org
Publication Date: July 26, 2001 | doi: 10.1021/bk-2001-0790.ch002

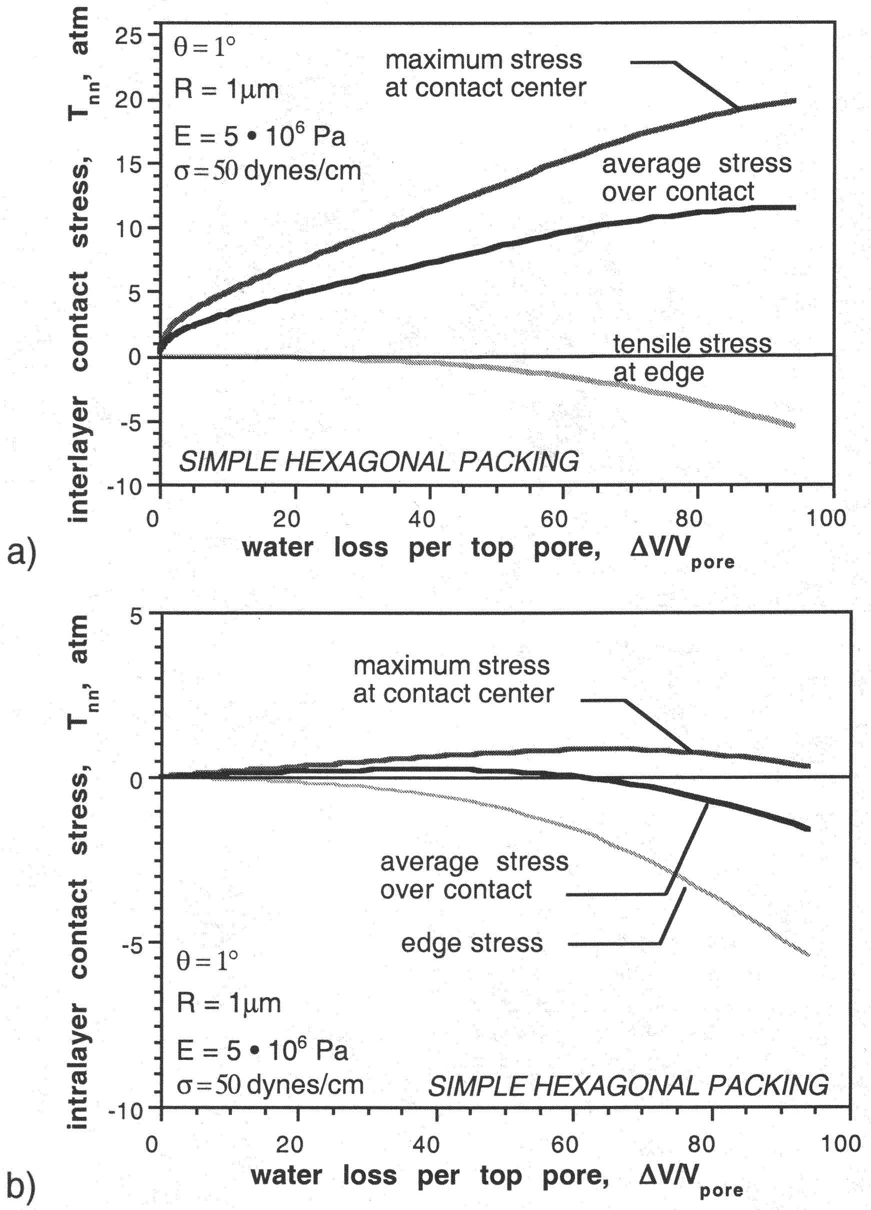

FIGURE 5. Wet-stage stresses (compressive) in a simple hexagonal packing, at (a) interlayers contacts, and (b) intralayer contacts, versus water loss from the top layer. T_{nn} is normal stress, $\Delta V/V_{pore}$ (%) is volume of water evaporated from a top particles's unit cell divided by pore volume in that cell, σ is surface tension, θ is wetting angle, E is Young's modulus, and R is undeformed particle radius.

Downloaded by NORTH CAROLINA STATE UNIV on September 17, 2012 | http://pubs.acs.org
Publication Date: July 26, 2001 | doi: 10.1021/bk-2001-0790.ch002

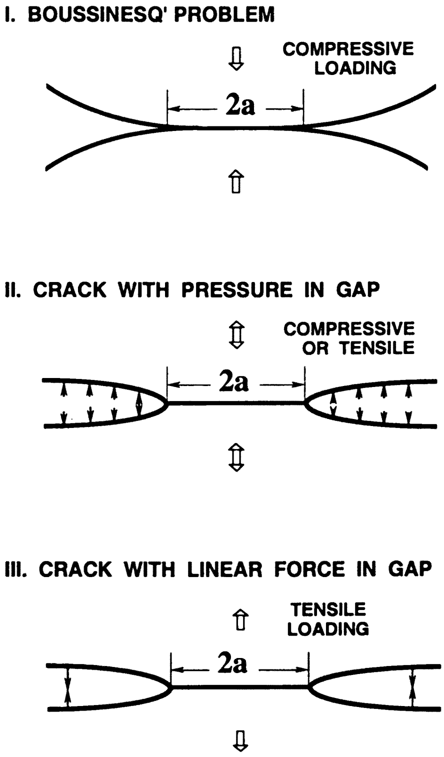
I. BOUSSINESQ' PROBLEM
COMPRESSIVE LOADING
2a
II. CRACK WITH PRESSURE IN GAP
COMPRESSIVE OR TENSILE
2a
III. CRACK WITH LINEAR FORCE IN GAP
TENSILE LOADING
2a

FIGURE 6. The three relevant basic cases of axisymmetric elastic contact and crack equilibrium.

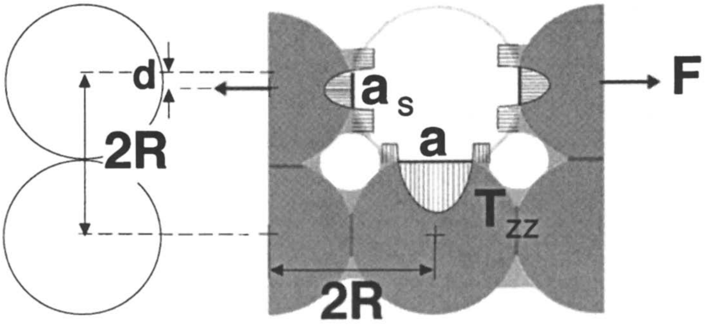

FIGURE 7. In the moist stage spheres are drawn together by pendular rings that produce capillary force loading at each contact.

the same area intact when the planar, external crack surrounding it contains liquid under lowered pressure, as in a pendular ring (4). The third is the same problem without liquid pressure but with surface tension force acting around a circle, as at the contact line of a pendular ring.

In the moist stage, the particles are no longer compressed toward the substrate because no menisci span the porespace and so there is no loading in that direction. Nevertheless they are flattened against every neighbor by the local compression in response to the capillary pressure and surface tension force in each pendular ring (Figure 7). Perpendicular to the substrate no stress opposes this flattening; the net out-of-plane stress is zero; particle centers move toward the substrate and the entire assemblage — the coating — shrinks in that direction. But parallel to the substrate the coating cannot shrink, because particle centers cannot move in-plane. The ultimate reason is that the coating adheres to the virtually rigid substrate. Hence within each particle must arise in-plane extension and tensile stress that prevent its center from moving parallel to the substrate. On each interparticle contact the distribution of both compressive and tensile local stresses changes abruptly at the end of the wet stage and then continues to evolve (Figure 8). The mean normal stress between out-of-plane neighbors becomes and remains zero. That between in-plane neighbors changes from compressive to tensile when, or soon after, the pendular rings form. So with the possible exception of the beginning of the moist stage, the *moist-stage mean in-plane stress* is *tensile.* If the tension exceeds the developing adhesion strength of a flattened contact, the drying coating cracks there; such microcracks may multiply into 'mud-cracking.' Otherwise the coating remains in in-plane tension until that stress state is relieved by relaxation mechanisms, by curl, or by delamination (which is no different than drying of polymer solutions).

As contacts flatten, the porespace between particles decreases. Provided the particles are incompressible, the decrease in porespace is precisely the shrinkage

Downloaded by NORTH CAROLINA STATE UNIV on September 17, 2012 | http://pubs.acs.org
Publication Date: July 26, 2001 | doi: 10.1021/bk-2001-0790.ch002

Downloaded by NORTH CAROLINA STATE UNIV on September 17, 2012 | http://pubs.acs.org
Publication Date: July 26, 2001 | doi: 10.1021/bk-2001-0790.ch002

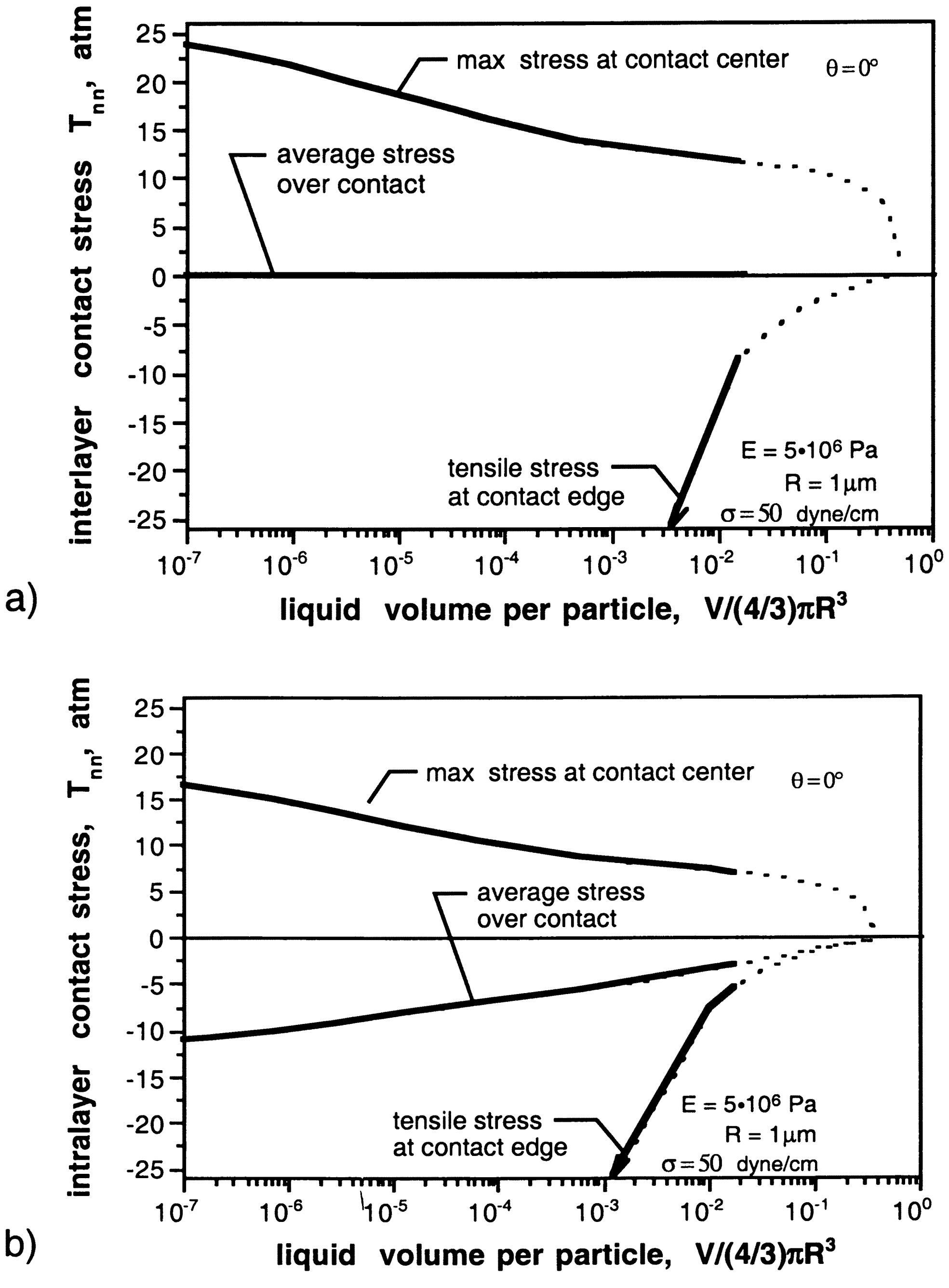

FIGURE 8. Moist-stage at (a) interlayer contacts, and (b) intralayer contacts. Broken curves pertain to fuller pendular rings than are left by Haines' jumps.

of the coating, i.e. the descent of the coating's top surface toward the substrate. That descent is accompanied by movement of particle centers in the same direction and concomitant bulging of particles into what was porespace. The narrowest parts, the pore throats, are occluded and sooner or later are closed off. Then normal drying ceases. The theoretical analysis indicates that this outcome can be brought about by capillary force loading during drying, for instance in the surface layers when they are the first to reach the moist stage, and the particles' modulus is low. This would be a kind of 'skinning' — blockage of water evaporation from deeper in the coating.

Closure

Capillary forces — capillary pressure from surface tension in curved menisci, and surface tension at contact lines — can dominate the stressing, deformation, and flattening of latex particles as they compact in a drying latex coating. A remarkable prediction is that capillarity-induced in-plane stress is compressive in the wet stage of drying before it turns tensile in the moist stage. A critical issue to be considered is the development in contacts of adhesive strength that can withstand the in-plane tensile stress and prevent cracking. The essence of the analysis here of simply ordered particle packings seems likely to carry over to disordered packings, which are more common. A fuller account and further results are to appear elsewhere (5).

References

1. Sutanto, E.; Ma, Y.; Davis, H. T.; Scriven, L. E. In *ACS International Symposium on Latex Film Formation, New Orleans, LA, Aug. 1999*; Urban, M.; Provder, T., Eds,; American Chemical Society: Washington, DC; this volume.
2. Orr, F. M.; Scriven, L. E.; Rivas, A. P. *J. Fluid Mech.*,**1975**, *67*, 723-742
3. Johnson, K. L. *Contact Mechanics*; Cambridge University Press: New York, NY, 1985; Ch. 3, p 59.
4. Sneddon, I. N.; Lowengrub, M. *Crack Problems in the Classical Theory of Elasticity*; John Wiley & Sons, Inc.: New York, NY, 1969; Ch. 3, p 173.
5. Pekurovsky, L. A.; Scriven, L. E. *J. Coll. and Interface Sci.*; in review.

Downloaded by NORTH CAROLINA STATE UNIV on September 17, 2012 | http://pubs.acs.org
Publication Date: July 26, 2001 | doi: 10.1021/bk-2001-0790.ch002

Chapter 3

Mobility and Molecular Interactions during Latex Film Formation

Yaqiu Zhao and Marek W. Urban*

School of Polymers and High Performance Materials, Shelby F. Thames Polymer Science Research Center, The University of Southern Mississippi, Hattiesburg, MS 39406

Downloaded by COLUMBIA UNIV on September 17, 2012 | http://pubs.acs.org
Publication Date: July 26, 2001 | doi: 10.1021/bk-2001-0790.ch003

This chapter outlines factors that may affect latex coalescence as well as provides fundamental principles of spectroscopic probes allowing multi-dimensional analysis of surfaces and interfaces. Using attenuated total reflectance (ATR), photoacousitc (PA), and infrared imaging Fourier transform infrared spectroscopy (FT-IR) these studies show that surfactant stratification can be affected by numerous factors such as surfactant-copolymer interactions, substrate surface tensions, particle and suspension composition, coalescence and glass transition temperatures, and the particle size. Furthermore, the presence of additives also affects film properties due to a non-homogeneous distribution of individual latex components. This process is amplified by exposure to elevated temperatures and enhanced relative humidity.

Introduction

While the ongoing quest for new environmentally compliant polymeric coatings is driven by two goals: to achieve desirable film properties and to minimize volatile organic content (VOC), an ultimate goal is to understand mechanisms governing film formation. Because behavior of macromolecules near surfaces and interfaces of polymeric films and organic coatings is responsible for numerous coating properties and applications,[1,2] understanding of molecular level processes affecting durability, adhesion, mechanical strength, and other properties is of particular importance. This knowledge will allow us not only to enhance properties of existing films and coatings, but also develop new materials. In an effort to achieve this task it is necessary to utilize methods that are non-destructive, sensitive, and quantitative, because minute

---

*Author to whom all correspondence should be addressed (Marek.Urban@usm.edu)

In Film Formation in Coatings; Provder, T., et al.;
ACS Symposium Series; American Chemical Society: Washington, DC, 2001.

changes in coatings compositions or formulations may result in significant macroscopic property changes. Although there are numerous sensitive techniques utilized in polymer surface analysis, many require high vacuum operating conditions or elaborative sample preparation often altering properties. As a result, the scope of analysis is often limited or obscured. However, certain Fourier transform infrared (FT-IR) techniques offer unique surface sensitivity and selectivity without vacuum limitations and broader scope of analysis and applications. Such techniques, especially with current advances in attenuated total reflection (ATR),[3,4,5] reflectance-absorbance (R-A),[6] continuous or step-scan photoacoustic (SS-PA),[7,8,9] rheo-photoacoustic (RPA) Fourier transform infrared (FT-IR) spectroscopy, and chemical IR/Raman imaging measurements allow 3-dimensional and multi-component analysis of complex polymeric systems.[10] One of the chemically and physically complex systems are latex suspensions typically produced by the emulsion polymerization process.

This chapter focuses on the last decade highlights of surface-interfacial developments in latexes and the factors that govern their film formation. From the historical prospective we have gotten into this field through the back doors, as the first paper published in 1990 aimed at understanding of the mobility of surfactants in latexes, not necessarily forecasting that this information can be used to monitor latex film formation.[11] However, at that time, there was virtually no data even indicating that a number of factors may so effectively influence and control latex film formation. Today, with a significant degree of experience and developments of necessary analytical tools such as quantitative analysis using ATR FT-IR,[12] enhanced sensitivity of SS-PA FT-IR detection, and the ability of chemical IR/Raman surface imaging,[13] we are in position to provide a better picture of chemically and spatially complicated polymeric films. Due to quite useful features of spectroscopic multi-dimensional analysis, before we discuss factors affecting latex film formation, let us briefly outline the principles, advantages, and disadvantages of the key techniques that can be utilized in the film formation studies.

Surface/Interfacial Spectroscopic Methods

In an ATR FT-IR experiment schematically depicted in Figure 1, an infrared beam is directed at an incident angle through a crystal of refractive index n_1 onto a sample of refractive index n_2. The passage of IR light through the ATR crystal depends on the critical angle (θ_c), which is defined as $\sin^{-1}n_2/n_1$. Due to the different refractive indices of the ATR crystal and sample, light reflects inside the crystal and infrared signal, carrying molecular information to the detector. The internal reflection element and physical principles of ATR forms the basis of numerous configurations from which a wide variety of coatings samples can be studied.[12]

Downloaded by COLUMBIA UNIV on September 17, 2012 | http://pubs.acs.org
Publication Date: July 26, 2001 | doi: 10.1021/bk-2001-0790.ch003

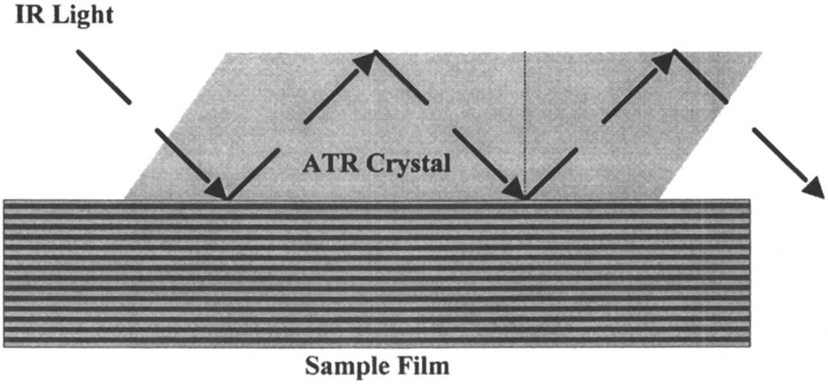

Figure 1. A schematic diagram of an attenuated total reflectance experiment.

It should be pointed out that this technique allows surface depth profiling through the use of the Urban-Huang step-wise approach described elsewhere.[5] While the major advantages of ATR are the ability to quantitatively analyze surfaces with a high spatial resolution, the ability to analyze layers ranging from monolayers up, and a non-destructive nature of measurements, disadvantages come from the fact that it is a contact method allowing to analyze from surface depths no greater than 3-4 μm.

Unlike ATR, photoacoustic spectroscopy is based on the direct detection of the energy absorbed by the sample and does not require contact with an optical element. As a result, this technique provides a means of analysis for opaque specimens of essentially any shape or morphology in a non-destructive manner. The photoacoustic effect is a result of absorption of modulated radiation, producing corresponding temperature fluctuations at the sample surface. The coupling gas phase above the sample surface will undergo modulated pressure changes, producing a periodic acoustic signal. This acoustic response is measured with a sensitive microphone, and the obtained electrical signal is Fourier-transformed, giving the PA spectra.[7] This process is illustrated in Figure 2.

While quantitative surface depth profiling can be accomplished using ATR FT-IR spectroscopy, more advanced analysis that utilizes a photoacoustic effect is capable of phase rotational analysis from significantly greater depths. The utility of rheo-photoacoustic FT-IR allows detection of the work of adhesion.[14]

Reflectance-absorbance theory and practical applications of this method are well documented[15] and Figure 3 illustrates a schematic diagram of a typical R-A measurement configuration, where IR light hits the surface of a metal substrate and reflects off. In R-A experiments, only molecular entities aligned with the electric vector of the incident light will interact with the light, resulting in an absorption band and providing information about macromolecules at a surface.

While the obvious advantages of RA FT-IR come from the ability of detecting metal-coating interfaces and mono-layer sensitivity, the main disadvantage is that only highly reflective and smooth surfaces can be used.

Downloaded by COLUMBIA UNIV on September 17, 2012 | http://pubs.acs.org
Publication Date: July 26, 2001 | doi: 10.1021/bk-2001-0790.ch003

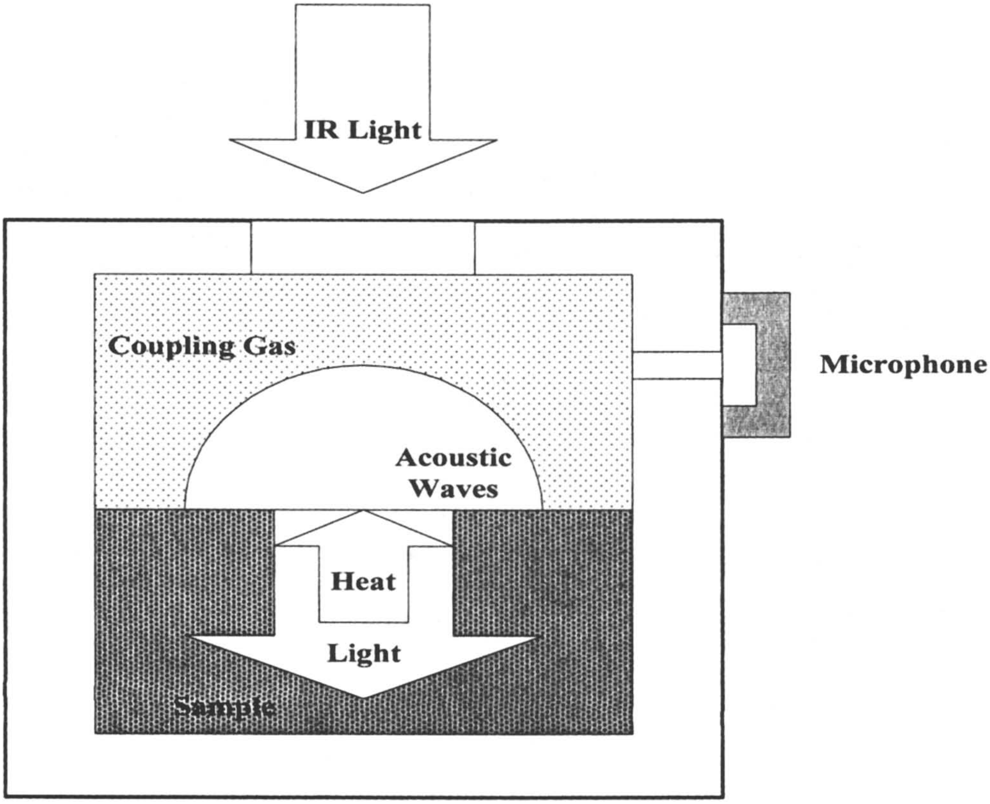
IR Light
Coupling Gas
Microphone
Acoustic Waves
Heat
Light
Sample

Figure 2. A schematic diagram of a step-scan photoacoustic experiment.

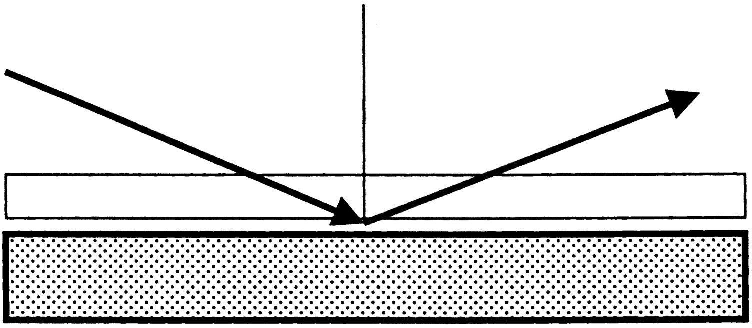

Figure 3. A schematic diagram of the reflectance-absorbance (R-A) experiment.

Downloaded by COLUMBIA UNIV on September 17, 2012 | http://pubs.acs.org
Publication Date: July 26, 2001 | doi: 10.1021/bk-2001-0790.ch003

IR imaging is an advanced technique to generate high-contrast, high-spatially resolved (3 μm in XY horizontal direction) spectral images that add a new perspective in analysis of surfaces.[16,17] This approach implements an array of 4096 mercury-cadmium-telluride (MCT) detectors aligned in a 64 x 64 matrix which are 'looking' at 400 x 400 μm area. Each detector generates a pixel that represents one spectrum of a small area of a given species. Furthermore, the analyzed surface area can be represented as distribution of a given wavenumber due to specific chemical entities present in the analyzed area. This is accomplished not only be utilizing an array of IR detectors, but applying a step-scan mode of an IR spectrometer, allowing obtaining the images of a given wavenumber. Unlike ATR, R-A, or PA FT-IR experiments, which generate an average of chemical species present in a given area, IR chemical imaging combines spectroscopy's chemical identification and quantitative abilities with a high spatial resolution. A schematic diagram of infrared imaging experiment is illustrated in Figure 4, and the later sections provide examples how this approach can be utilized in latex analysis. In the context of other imaging methods, IR/Raman imaging represents the frontiers of analytical methods, because unlike atomic force microscopy, it is capable of generating molecular information and images. Thus, the imaging combined with ATR and PA allow non-destructive characterization of polymeric films and coatings, making possible understanding of such processes as crosslinking kinetics and reactions, stratification of individual coatings components and film formation, diffusion and mobility, organic-inorganic interactions, corrosion, molecular level adhesion, and surface depth-profiling.

Downloaded by COLUMBIA UNIV on September 17, 2012 | http://pubs.acs.org
Publication Date: July 26, 2001 | doi: 10.1021/bk-2001-0790.ch003

Latex Film Formation

As indicated in the Introduction, processes leading to the film formation are significantly more complex than anticipated in the past. Transformation of liquid colloidal dispersions into solid films may be affected not only by latex particle composition,[18] but other numerous properties associated with particle stabilization,[19,20,21,22] particle glass transition and film coalescence temperatures,[23,24,25] particle composition and size,[26,27,28,29,30,31,32] coalescence conditions,[33,34] and other properties.[35,36,37,38,39,40,41] In essence, interactions of all components as well as minor compositional/processing changes may effectively influence a number of macroscopic properties. With this background in mind let us consider how surfactant-copolymer interactions, substrate surface tension, latex copolymer and blend composition, coalescence and glass transition temperature, particle size and additives will affect coalescence.

Surfactant-Copolymer Interactions

The most direct method for monitoring molecular interactions is to measure vibrational energy changes resulting from molecular entities responsible for these interactions. For example, if the environment of a sulfonate group is disturbed by the presence of acid groups and water, the S-O stretching energies will shift, and the magnitude of the energy changes will vary, depending on the strength of these interactions. It was demonstrated that when sodium dioctylsulfosuccinate (SDOSS) is used as a surfactant in copolymerization of ethyl acrylate/methacrylic acid (EA/MAA) latexes, the S-O stretching band at 1050 cm^{-1} splits to two bands at

Downloaded by COLUMBIA UNIV on September 17, 2012 | http://pubs.acs.org
Publication Date: July 26, 2001 | doi: 10.1021/bk-2001-0790.ch003

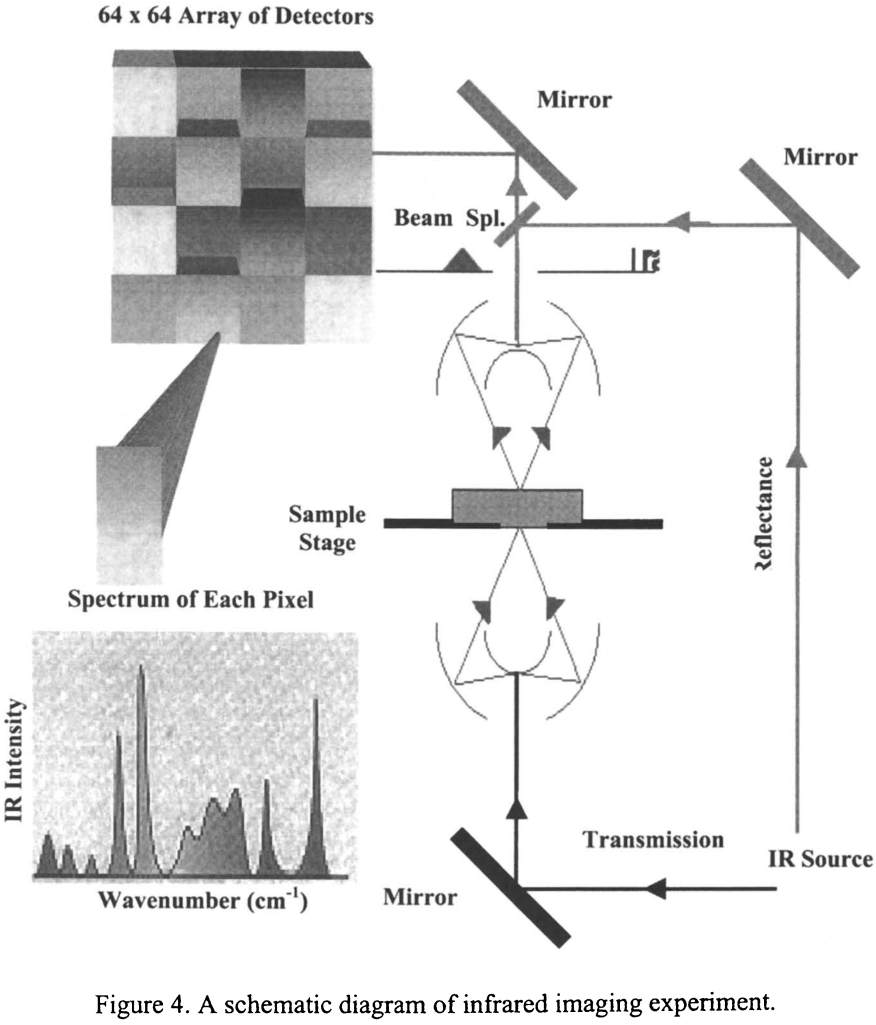
64 x 64 Array of Detectors
Mirror
Mirror
Beam Spl.
Sample
Stage
Reflectance
Spectrum of Each Pixel
IR Intensity
Wavenumber (cm^{-1})
Transmission
IR Source
Mirror

Figure 4. A schematic diagram of infrared imaging experiment.

1046 and 1056, which are due to $COOH\cdots SO_3^-Na^+$ and $H_2O\cdots SO_3^-Na^+$ interactions, respectively.[11] In addition, other bands at 1240 and 1216 cm^{-1} also split as a result of local $SO_3^-Na^+$ changes. Furthermore, temperature and humidity studies indicated that the formation of SDOSS-H_2O and SDOSS-COOH interactions is strongly affected by environmental conditions.[31] For example, at 10% and 50% relative humidity (RH) both interactions are present, but when coalescence is conducted at 80% RH, SDOSS-COOH interactions are not detected. The fact that the SDOSS-H_2O interactions are still present at 10% RH indicates that perhaps due to its more hygroscopic nature, SDOSS will not readily dehydrate under ambient conditions, even in the absence of atmospheric water vapor.

The Effect of Substrate Surface Tension

Although one would not anticipate that the surface tension of a substrate may possibly have some effect on migration of individual components in latexes, and indeed our earlier studies indicated that for the majority of non-ionic surfactants do not exhibit mobility in ethyl acrylate/methacrylic acid (EA/MAA) latexes due to their higher degree of compatibility, most of the ionic surfactants may migrate. As demonstrated in our earlier studies,[11,42] EA/MAA latex films prepared on polytetrafluoroethylene (PTFE), glass, and Hg showed that the magnitude of surfactant migration depends on the substrate-latex interactions. As shown in Figure 5, EA/MAA deposited on PTFE exhibits moderate exudation of SDOSS to the film-substrate (F-S) interface in order to lower the interfacial surface tension between the copolymer of PTFE. However, the same films prepared on glass exhibit minimal or no exudation to the F-S interface. This is because copolymer is able to wet the substrate, thus lowering the driving forces for SDOSS exudation to this interface. When latex films are deposited and allowed to coalesce on Hg, the enhancement of surfactant exudation to the F-S interface occurs, which is attributed to the fact that a liquid will only wet a high energy surface. Therefore, if the latex is deposited on a liquid Hg substrate, there are two liquids in contact with each other, and initial surfactant enrichment may occur to lower the surface tension at the liquid-liquid interface. As the coalescence progresses, water evaporates, leaving the copolymer film in contact with Hg and forming a solid (latex film)-liquid (Hg) interface. Because Hg has a high surface energy, a high interfacial surface tension exists at this interface, providing sufficient driving forces for surfactants to exude to this interface. One can envision numerous substrates that are not suitable for latex applications because the surface tension difference is so high that prohibits film formation.

One issue that should be addressed is the competing forces between surface tension difference and water flux. During coalescence, as water molecules evaporate out of the latex, they carry surfactant molecules to the F-A interface. However, when the interfacial surface tension difference between substrate and liquid latex film is high, this excessive interfacial energy will dominate the process. A series of studies performed on Sty/n-BA/MAA latexes indicated that when this latex was deposited on Hg, enrichment of surfactant was observed near the F-A interface. This behavior is attributed to a composite of Sty/n-BA/MAA latex particles and SDOSS compatibility. Although one would suggest that the presence of Sty diminishes SDOSS compatibility with the latex copolymer, later studies showed that this is not the case unless latex films are coalesced above the p-Sty glass transition (T_g) temperature.[18]

Downloaded by COLUMBIA UNIV on September 17, 2012 | http://pubs.acs.org
Publication Date: July 26, 2001 | doi: 10.1021/bk-2001-0790.ch003

American Chemical Society
Library
1155 16th St., N.W.
Washington, D.C. 20036

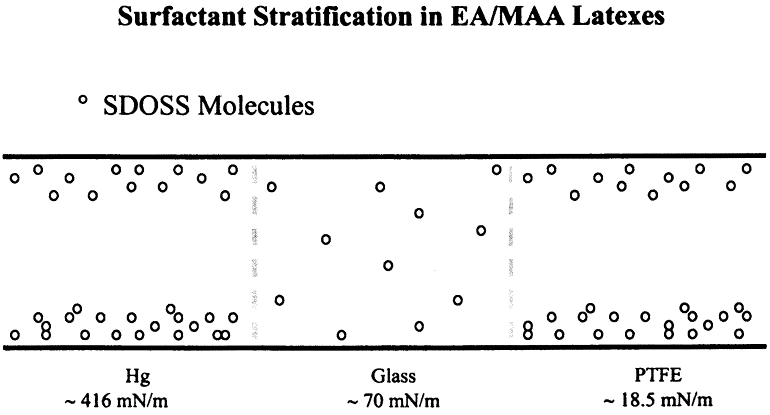

Figure 5. A schematic representation of the distribution of surfactant molecules as a function of substrate surface tension (Adopted from ref. 21).

Downloaded by COLUMBIA UNIV on September 17, 2012 | http://pubs.acs.org
Publication Date: July 26, 2001 | doi: 10.1021/bk-2001-0790.ch003

Latex Copolymers and Blends

While latex blends can be prepared by mixing independently polymerized particles in a form of polymeric microspheres dispersed in an aqueous phase, latex copolymers are synthesized by semi-continuous polymerization of individual monomers to form particle that may exhibit various morphologies. Both processes may lead to certain advantages or disadvantages, but more importantly, there is a significant difference between latex blends and copolymers surfaces. For example, Figure 6, a and b, illustrate optical images from the F-A interfaces of 50/50% Sty/n-BA copolymer and p-Sty/p-nBA blend films, respectively. As seen, aggregates are detected at the F-A interface of copolymer latex, whereas the F-A interface of latex blend appears to be uniform.

In an effort to determine composition of aggregates detected in Figure 6 (a), ATR micro-analysis was performed, which was accomplished by recording spectra using an ATR crystal on the surface area of 50 ~ 100 μm. Marked circles in Figures 6 (a) and (b) indicate spectral acquisition areas at the F-A interfaces of copolymer and blended latex films, and Figures 6 (c) and (d) illustrate a series of spectra that correspond to points A, B, C, D, and E of Figures 6 (a) and (b), respectively. As seen in Figure 6 (c), the band at 1159 cm^{-1} due to the C-O-C stretching modes of p-nBA does not change its intensity, but the intensities of the 1056 and 1046 cm^{-1} bands due to SDOSS increase while moving an IR beam from points A through E. These results show that the observed aggregates in Figure 6 (a) are mainly composed of water-soluble SDOSS islands. In contrast to the Sty/n-BA copolymer latex, SDOSS exhibits different behavior in p-Sty/p-nBA latex blends. As shown in Figure 6 (d), only traces of SDOSS are detected and the F-A interface (Figure 6 (b)) appears to have uniform morphology.

Downloaded by COLUMBIA UNIV on September 17, 2012 | http://pubs.acs.org
Publication Date: July 26, 2001 | doi: 10.1021/bk-2001-0790.ch003

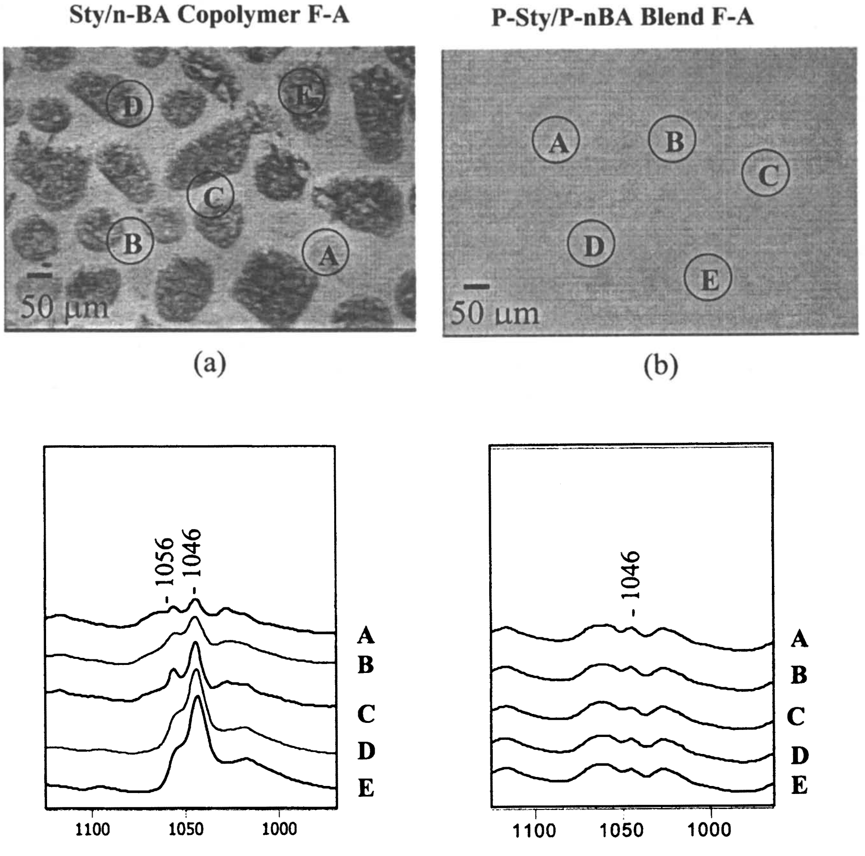

(a) (b)

(c) (d)

Figure 6. (a) Optical image of 50/50% Sty/n-BA copolymer latex F-A interface; (b) optical image of 50/50% p-Sty/p-nBA blended latex F-A interface; (c) ATR FT-IR spectra in the 1130-960 cm^{-1} region of 50/50% Sty/n-BA copolymer latex; (d) ATR FT-IR spectra in the 1130-960 cm^{-1} region of 50/50% p-Sty/p-nBA blended latex (Reproduced with permission from ref. 18; Copyright: American Chemical Society).

Coalescence and Glass Transition Temperature

The Sty and n-BA phase behavior affects SDOSS mobility, and for latex copolymers and latex blends SDOSS mobility exhibits significant differences during film formation. As a matter of fact, dynamic mechanical thermal analysis (DMTA) analysis indicated that one glass transition temperature (T_g) at 20°C of Sty/n-BA randomly copolymerized is present, and for p-Sty and p-nBA latex blend two T_gs are detected at –35°C and 110°C, which are due to phase separation of p-nBA and p-Sty, respectively.

In an effort to elucidate the effect of coalescence temperature (T_c) and the actual T_g of the latex copolymer and latex blend films were coalesced at 4°, 25°, 50°, 75°, 90°, and 120°C, followed by cooling to 25°C. It appears that there is a significant difference between these systems, and the T_c-T_g difference also influences migration of SDOSS. As shown in Figure 7, for latex copolymer, SDOSS migration is hardly observed when $T_c = 4$°C. However, as the T_c increases to 25°C, SDOSS concentration levels significantly increase. SDOSS concentration levels are almost constant when $T_c > T_g$, indicating that for 50/50% Sty/n-BA latex copolymer, significant SDOSS migration is observed when $T_c > T_g$. For 50/50% p-Sty/p-nBA latex blend, as the T_c increases from 4 to 90°C, SDOSS concentration levels slightly increase. However, at 120°C, significant SDOSS migration is observed, which indicates that SDOSS is released from the p-Sty particles when coalescence temperatures are above the T_g of p-Sty phase.

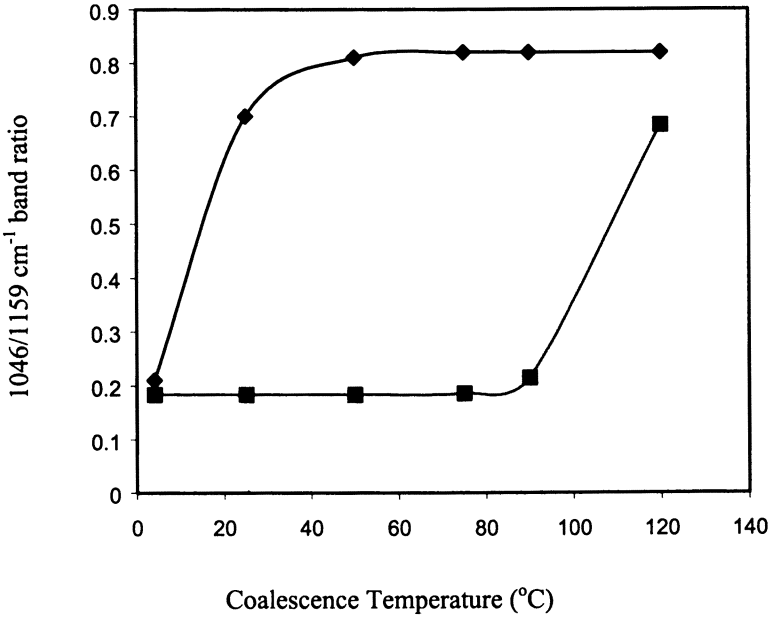

Figure 7. 1046/1159 cm^{-1} band ratio as a function of T_c for copolymer and blended latexes.

Downloaded by COLUMBIA UNIV on September 17, 2012 | http://pubs.acs.org
Publication Date: July 26, 2001 | doi: 10.1021/bk-2001-0790.ch003

Downloaded by COLUMBIA UNIV on September 17, 2012 | http://pubs.acs.org
Publication Date: July 26, 2001 | doi: 10.1021/bk-2001-0790.ch003

SDOSS migration is significantly affected by the temperature difference between the coalescence temperature T_c and the actual T_g of latex particles, this is also observed in Sty/n-BA/MAA core/shell latexes. Sty/n-BA/MAA latex films were coalesced at 25°, 30°, 40°, 50°, and 60°C for 2 hours, followed by cooling to 25 °C, and recording ATR FT-IR spectra from the F-A interface. A plot of the amount of SDOSS migration to the F-A interface as a function of $T_c - T_g$ is shown in Figure 8. It is quite apparent that when $T_c - T_g$ is negative ($T_c < T_g$), concentration levels of SDOSS increase at higher rates which is represented by the slope of the line A. When $T_c - T_g$ crosses zero ($T_c = T_g$) and becomes positive ($T_c > T_g$), the slope changes and the rate at which SDOSS migrates to the F-A interface is slow, but the amount of SDOSS is high. These results also indicated that SDOSS migration is affected by the extent of latex particle coalescence because the particle coalescence is significantly affected by the temperature difference between T_c and T_g.

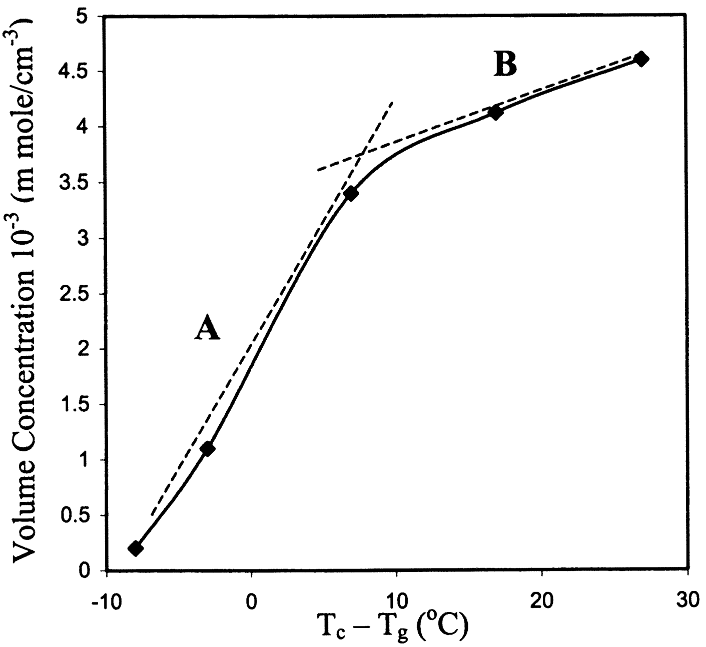

Figure 8. SDOSS volume concentration changes as a function of $T_c - T_g$ for 50/50% Sty/n-BA/MAA core/shell latex.

The Particle Size Effect

Since the T_c - T_g difference has a significant effect on the migration of SDOSS molecules in 50/50% Sty/n-BA latex blend and significant SDOSS migration is observed when $T_c > T_g$ of p-Sty. If this is the case, p-Sty particle in latex blend may affect SDOSS migration because of particle surface area differences. Latex blend films were coalesced at 50, 75, 90, and 120°C for 2 hours, followed by cooling them down to 25°C. Such films were analyzed using ATR FT-IR to quantitatively determine the surface content changes at the F-A interface as a function of exposure temperature. As previously reported model studies showed,[28] the first step in this analysis is to determine an absorption coefficient of the bands of interest, which for the 1046 cm^{-1} band due to SDOSSH_2O interactions is 0.017 l/mol·cm, whereas for the 1056 cm^{-1} band resulting from the SDOSSCOOH entities is 0.14 l/molcm.[1] Using a double KKT approach,[12] it is then possible to determine SDOSS volume concentration changes as a function of temperature. These results are shown in Figure 9 for p-Sty particle sizes of 61, 77, and 102 nm (Curves A, B, and C, respectively). As seen, curves A, B, and C, as T_c increases from 25 to 90°C, SDOSS concentration levels slightly increase. However, at 120°C, the band due to SDOSS significantly increases, and it appears that for 61, 77, and 102 nm p-Sty particles in latex blends, volume concentration levels at approximately 1.9 μm near the F-A interface 3.2 x 10^{-3}, 2.50 x 10^{-3}, and 1.90 x 10^{-3} mmol/cm^3, respectively. Thus, exudation of SDOSS in latex blends above the T_g of p-Sty is quite pronounced. Furthermore, as illustrated in Figure 9, higher concentration levels of SDOSS for smaller p-Sty particles provide a source for expelling larger amounts of SDOSS. This behavior indicates that the majority of SDOSS detected at the F-A interface comes from the p-Sty phase.

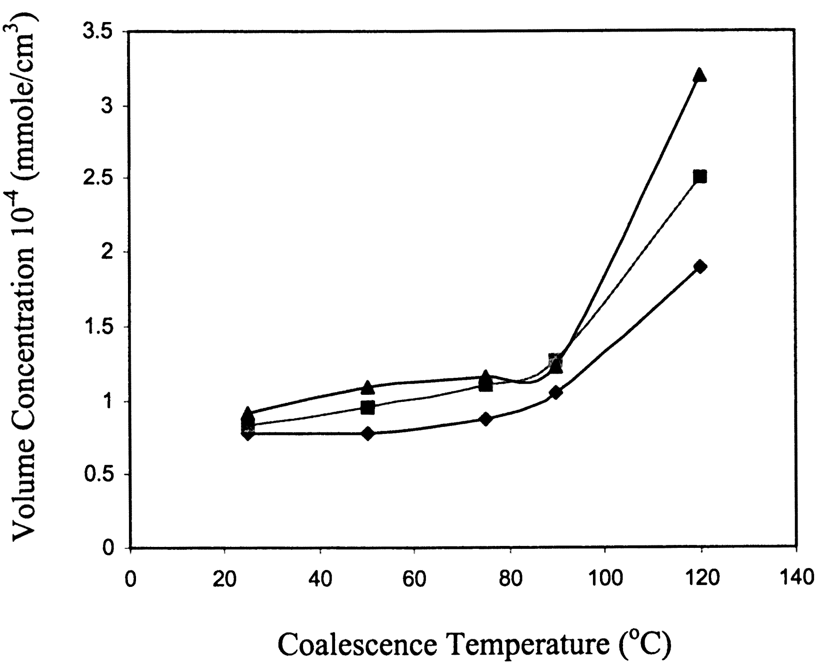

Figure 9. SDOSS volume concentration as a function of T_c for 50/50% p-Sty/p-nBA blended latex.

Downloaded by COLUMBIA UNIV on September 17, 2012 | http://pubs.acs.org
Publication Date: July 26, 2001 | doi: 10.1021/bk-2001-0790.ch003

What's Underneath the Surface

While ATR FT-IR studies have shown that SDOSS molecules of Sty/n-BA copolymer latex exude to the F-A interface, and stratify near the surface forming non-uniformly distributed islands, it is also of interest to determine the relative distribution of SDOSS molecules in the direction perpendicular to the F-A and F-S interfaces. For that purpose step-scan (SS) PAS and phase rotation analysis can be utilized. SS-PAS magnitude spectra provide information from estimated depths for a particular modulation frequency, whereas phase rotational analysis using I and Q spectra enhances spatial resolution for a given penetration depth.[7-9] Using a digital signal processor (DSP) to precisely control mirror position, the in-phase and in-quadrature components of the signal can be simultaneously acquired and used to obtain the phase signal. The spectra obtained at 0° phase shifted (I) and 90° phase shifted (Q) with respect to the incident radiation; I spectra represent molecular information closer to the surface, whereas the Q spectra evolve primarily from the specimen bulk.[7] A combination of ATR FT-IR, SS-PAS and SS-PAS phase rotation analysis data allowed us to construct Figure 10, which schematically illustrates distribution of SDOSS molecules and their interactions across the Sty/n-BA copolymer latex film thickness.

The presence of SDOSS-H_2O below 7 μm from the F-S interface indicates there is a transition zone from the wet dry stage of coalescence, and at this zone, polymer particles are not completely inter-diffused. However, in the case of the F-A interface, the presence of water in the surrounding atmosphere allows diffusion into the film, which affects kinetics of the coalescence process, resulting in significantly larger amounts of SDOSS-H_2O associations at 11 μm depths. Nonbonded SDOSS molecules are detected from about 9 ~ 13 μm from the surface.

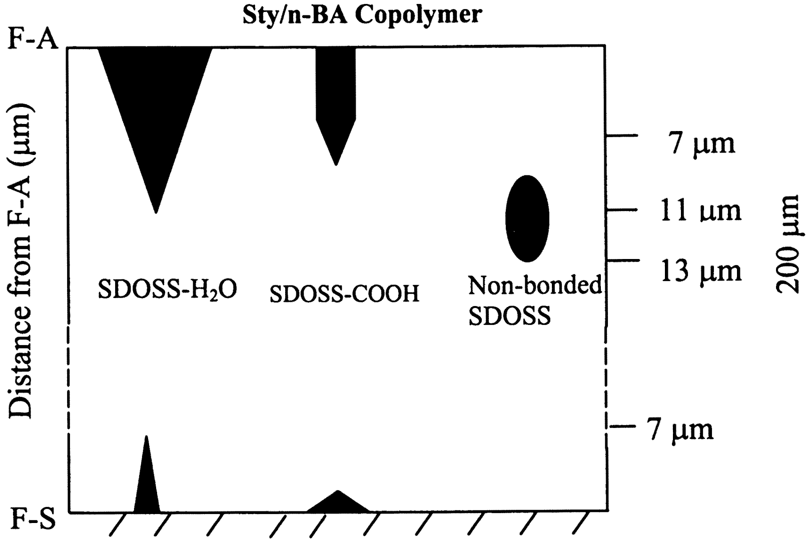

Downloaded by COLUMBIA UNIV on September 17, 2012 | http://pubs.acs.org
Publication Date: July 26, 2001 | doi: 10.1021/bk-2001-0790.ch003

Figure 10. Schematic diagram of relative quantities of SDOSS associated with H_2O, COOH, and non-bonded SDOSS as a function of the depth of penetration from 50/50% Sty/n-BA copolymer interfaces.

Additives

Many latex systems contain additives that are utilized for various justifiable reasons. For example, if tackiness is one of the desired properties, molecular entities enhancing this property are added. The question is, however, how such additives behave, especially upon exposure to various conditions. Since distribution of theses species is typically non-homogeneous, and the majority of surface selective probes provide average information, thus not providing true representation of surface/interfacial regions, there is need for an approach that would "count" all molecules. This approach removes averaging and allows distribution that contains significantly more value, especially for non-homogeneous polymeric coatings. Infrared chemical imaging is one of the newer approaches in determining chemical heterogeneity and surface/interfacial microstructures. Figure 11 illustrates how drying conditions may affect a tackifier distribution in ethylhexyl acrylate/methyl methacrylate (EHA/MMA) latex. While one set of these adhesives was dryied at 25°C and 50% relative humidity (climc condition), another was kept at 35°C and 75% RH for 7 days, and IR chemical images from 400 μm x 400 μm sample area were collected. The 1697 cm^{-1} band is attributed to the C=O stretching bands of tackifier. As seen, when EHA/MMA latex is exposed to elevated temperature and humidity conditions, distribution of tackifier becomes non-uniformed. Although the origin of this behavior is yet to be determined, these studies show that conditions can significantly affect the individual component distribution in adhesive latexes. At climatic conditions, tackifier is uniformly distributed on the adhesive surface, but its distribution becomes non-uniform at high temperature and humidity conditions. In summary, this chapter provided a snap-shot of issues that are needs to consider and deal with when trying to understand film formation and coalescence.

Downloaded by COLUMBIA UNIV on September 17, 2012 | http://pubs.acs.org
Publication Date: July 26, 2001 | doi: 10.1021/bk-2001-0790.ch003

Conclusions

The attempt of this chapter was to summarize the highlights of the current and past advances in latex film formation and to identify factors that affect stratification processes and non-homogeneous distribution of individual components. Although one can depict latex coalescence as a simple three-stage process (water evaporation, close particle packing, and particle deformation followed by inter-diffusion), in reality coalescence processes are quite complex and each of the individual components may significantly influence film formation, and therefore film properties. It is apparent that further studies are needed to understand particle coalescence processes.[43]

Downloaded by COLUMBIA UNIV on September 17, 2012 | http://pubs.acs.org
Publication Date: July 26, 2001 | doi: 10.1021/bk-2001-0790.ch003

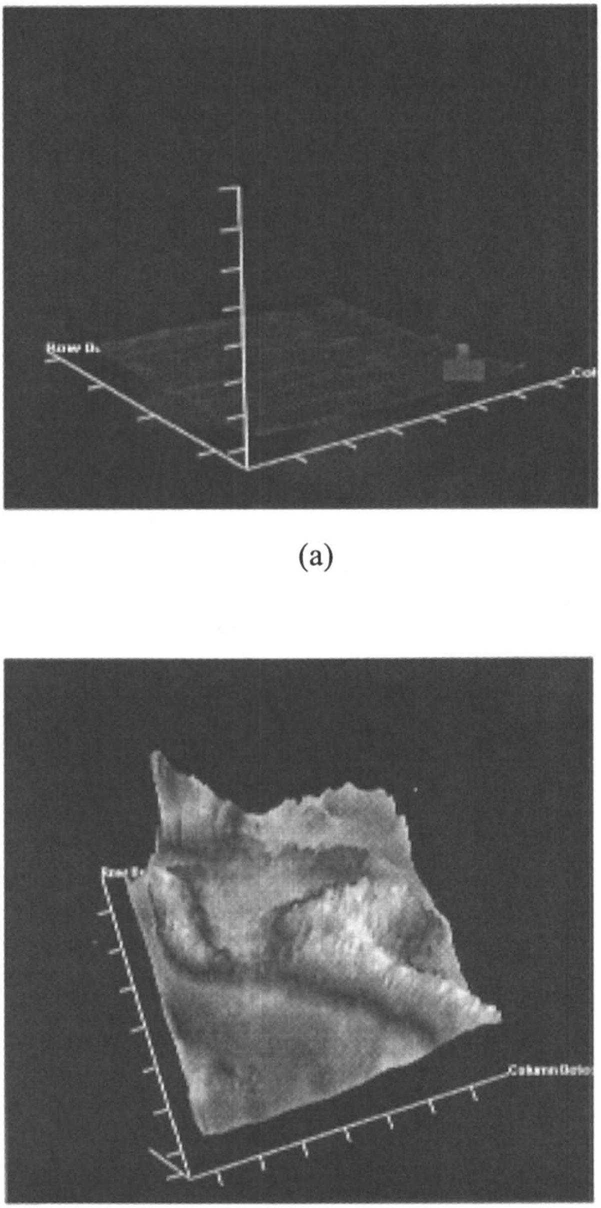

(a)

(b)

Figure 11. IR imaging of tackifier distribution in EHA/MMA latex: (a) climatic condition; (b) after aging for 7 days; 35°C, 75% RH).

Acknowledgments

The authors are thankful to the National Science Foundation, Industry/University Cooperative Research Center in Coatings at the University of Southern Mississippi and Eastern Michigan University for support of these studies.

References

1. M.W.Urban, *Laboratory Handbook of Organic Coatings,* Global Press, Chicago, IL, 1997.
2. R.A.Ryntz, Adhesion to Plastics; Molding and Paintability, Global Press, Chicago, IL, 1998.
3. Urban, M. W.; Stewart, M. T.; J. Appl. Polym. Sci., 1990, 39, 265.
4. Morra, M.; Occhielo, E.; Marloa, R.; Garbassi, F.; Humphrey, P.; Johnson, D., J. Coll. Int. Sci., 1990, 137, 11.
5. Huang J. B.; Urban, M. W.; Appl. Spectrosc., 1992, 46, 1666.
6. Urban, M. W.; Vibrational Spectroscopy of Molecules and Macromolecules on Surfaces, Wiley-Interscience Publication, New York, 1993.
7 Rosencwaig, A.; *Photoacoustics and Photoacoustic Spectroscopy*, Wiley-Interscience Publication, New York, 1980.
8. Jones, R. W.; Mcclelland, J. F.; Appl. Spectrosc., 1996, 50, 1258.
9. Jiang, E. Y.; Palmer, A. P.; Barr, N. E.; Appl. Spectro., 1997, 51, 1238-1244.
10. Kim, H.; Urban, M.W., Langmuir, 2000, in press.
11. Urban, M.W., Evanson, Polymer Comm., 1990, 31, 279.
12. Urban, M.W., *Attenuated Total Reflectance Spectroscopy of Polymers; Theory and Practice,* American Chemical Society, Washington, DC, 1996.
13. Bio-Rad, Cambridge, 1999, MA.
14. Pennington, B.P, Urban, M.W., J.Adhesion Sci.Techn., 1999, Vol. 13, 19.
15. Claybourn, M., *Reflectance Spectroscopy of Polymers,* Polymer Surfaces and Interfaces Series, Global Press, Chicago, IL, 1998.
16. Lewis, E. N.; Treado, P. J.; Reeder, R. C.; Story, G. M.; Dowrey, A. E.; Marcott, C.; Levin, I. W.; Anal. Chem., 1995, 67, 3377.
17. Lewis, E. N.; Gorbach, A. E.; Levin, I. W.; Applied Spectroscopy, 1996, 50, 263.
18. Zhao, Y.; Urban, M. W.; Macromolecules, 2000, 33, 2184.
19. Joanicot, M.; Wong, K.; Richard, J.; Maquet, J.; Cabane, B.; Macromolecules, 1993, 26, 3168.
20. Kim, H.-B.; Wang, Y.; Winnik, M. A; Polymer, 1994, 35, 1779.
21. Evanson, K. W.; Thorstenson, T. A.; Urban, M. W.; J. Appl. Polym. Sci., 1991, 42, 2297.
22. Thorstenson, T. A.; Urban, M. W.; J. Appl. Polym. Sci., 1993, 47, 1381.
23. Niu, B. –J.; Urban, M. W.; J. Appl. Polym. Sci., 1995, 56, 377.
24. Niu, B. –J.; Urban, M. W.; J. Appl. Polym. Sci., 1996, 60, 371.
25. Zhao, Y.; Urban, M. W.; Macromolecules, 2000, in press.
26. Thorstenson, T. A.; Urban, M. W.; J. Appl. Polym. Sci., 1993, 47, 1387.
27. Thorstenson, T. A.; Urban, M. W.; J. Appl. Polym. Sci., 1993, 50, 1207.
28. Niu, B. –J.; Urban, M. W.; J. Appl. Polym. Sci., 1996, 60, 389.

Downloaded by COLUMBIA UNIV on September 17, 2012 | http://pubs.acs.org
Publication Date: July 26, 2001 | doi: 10.1021/bk-2001-0790.ch003

29. Evanson, K. W.; Urban, M. W.; J. Appl. Polym. Sci., 1991, 42, 2287.
30. Kunkel, J. P. W.; Urban, M. W.; J. Appl. Polym. Sci., 1993, 50, 1217.
31. Tebelius, L. K.; Urban, M. W.; J. Appl. Polym. Sci., 1995, 56, 387.
32. Zhao, C. L.; Holl, Y.; Pith, T.; Lambla, M.; Coll. and Polym. Sci., 1987, 265, 823.
33. Niu, B. -J.; Urban, M. W.; J. Appl. Polym. Sci., 1996, 60, 379.
34. Kim, H.-B.; Winnik, M. A; Macromolecules, 1995, 28, 2033.
35. Eisenberg, A.; Macromolecules, 1970, 3, 147.
36. Arora, A.; Daniels, E. S.; El-Aasser, M. S.; J. Appl. Polym. Sci. 1995, 58, 301.
37. Thorstenson, T. A.; Evanson, K. W.; Urban, M. W.; Polym. Mater. Sci. Eng., 1991, 64, 195.
38. Thorstenson, T. A.; Tebelius, L. K.; Urban, M. W.; J. Appl. Polym. Sci., 1993, 49, 103.
39. Evanson, K. W.; Thorstenson, T. A.; Urban, M. W.; J. Appl. Polym. Sci., 1991, 42, 2309.
40. Thorstenson, T. A.; Evanson, K. W.; Urban, M. W.; *Advances in Chemistry Series #236*, Urban, M. W.; Craver, C. D.; Ed., American Chemical Society: Washington, D.C., 1993.
41. Evanson, K. W.; Urban, M. W.; *Surface Phenomena and Fine Particles in Water-based Coating and Printing Technology*, Sharma, M. K.; Micale, F. J.; Ed., Plenum: New York, 1991.
42. Martin, L. R.; Urban, M. W.; J. Appl. Polym. Sci., 1996, 62, 1893.
43. Zhao, Y.; Urban, M.W., Macromolecules, 2000, in press.

Downloaded by COLUMBIA UNIV on September 17, 2012 | http://pubs.acs.org
Publication Date: July 26, 2001 | doi: 10.1021/bk-2001-0790.ch003

Downloaded by UNIV MASSACHUSETTS AMHERST on September 17, 2012 | http://pubs.acs.org
Publication Date: July 26, 2001 | doi: 10.1021/bk-2001-0790.ch004

Chapter 4

Molecular Weight Effects on the Film Formation of Latex and on Surfactant Distribution and Morphology

A. Tzitzinou[1], J. L. Keddie[1], J. L. Geurts[2], M. Mulder[2], R. Satguru[2], and K. E. Treacher[3]

[1]School of Physics and Chemistry, University of Surrey, Guildford, Surrey GU2 7XH, United Kingdom
[2]Avecia BV, P.O. Box 123, Sluisweg 12, Waalwijk 5140 AC, The Netherlands
[3]Avecia Ltd., P.O. Box 42, Hexagon House, Blackley, Manchester M9 8ZS, United Kingdom

It is well known that viscosity, self-diffusion coefficient and glass transition temperature are a strong function of molecular weight (MW). Here we report the film formation characteristics of an acrylic (BMA/MMA/MAA) latex as a function of its average MW, considering four molecular weights ranging from 7,500 to 705,000 Daltons. As a means of taking into account the lower glass transition temperature and viscosity expected in the lower MW latices, we compare the film formation behaviours at the same temperature increment above their respective minimum film formation temperatures (MFT). We find that the lower MW latices form a film with a lower void concentration and lower surface roughness in comparison to the higher MW latices at the same temperature relative to the MFT. Non-invasive analysis of the film formation using ellipsometry finds evidence for void formation in the high MW latex (M_w = 705, 000 Daltons) up to 30 °C above MFT. In contrast, the lowest MW latex (M_w = 7,500 Daltons) forms a dense film with few, if any, voids immediately upon the evaporation of water and at temperatures as low as 5 °C above MFT. These differences can be partly attributed to varying degrees of plasticization by water. In addition, the film morphology at the polymer/air interface was investigated using atomic force microscopy. Surface features were attributed to the presence of surfactant. A low MW latex shows surfactant features at a lower film formation temperature (relative to the MFT) and/or a shorter film-formation time in comparison to the high MW latex.

In Film Formation in Coatings; Provder, T., et al.;
ACS Symposium Series; American Chemical Society: Washington, DC, 2001.

Downloaded by UNIV MASSACHUSETTS AMHERST on September 17, 2012 | http://pubs.acs.org
Publication Date: July 26, 2001 | doi: 10.1021/bk-2001-0790.ch004

Introduction

There are ever-increasing demands on waterborne coatings for applications that require mechanical properties ranging from being hard and elastic (e.g. protective coatings) to being soft and viscoelastic (e.g. adhesives). Formulation scientists have developed a variety of compositions — ranging from vinyls to acrylics to urethanes — to meet particular requirements. In some instances, there might be a particular restriction on the polymer composition used. In such a case, a volatile coalescent can be used to aid film formation, a plasticizer can be used to soften the coating, or a crosslinker can be used to make the coating harder. When there is also a need to reduce the volatile organic content (for environmental and health reasons), another means must be used to control the coating's mechanical properties. One potentially cost-effective approach is to vary the molecular weight of the polymer. It is the influence of this last parameter on the film formation of an acrylic latex that is the topic of this investigation.

It is well-established that the glass transition temperature, Tg, of a glassy polymer decreases with decreasing molecular weight. [1] Previous study of the film formation of a series of acrylic latices with varying Tg values[2] has revealed that the film formation behaviour is strongly related to the magnitude of difference between the film formation temperature and the Tg. When the film formation temperature is well above the Tg, then water evaporation and particle coalescence occur simultaneously. There is a single drying and coalescence front. Water evaporation is the rate-limiting step in film formation. When the temperature is near the Tg, on the other hand, then deformation occurs after completion of water evaporation. A separate coalescence front is observed immediately after the drying front.[3] In this later case, particle deformation is the rate-limiting step.

There are usually both elastic and viscous contributions to particle deformation during film formation.[4] Some models of film formation consider elastic deformation of particles to be the dominant contribution, whereas other models consider the viscous flow of the polymer leading to closure of interparticle voids. It is well known[5] that both the elasticity and the viscosity of a polymer are a function of its molecular weight, M. Specifically, above the critical molecular weight, Mc, the shear modulus and the recoverable shear compliance reach a plateau value with increasing M, whereas they are linearly related to M below Mc. Also above Mc, the zero shear rate viscosity, η_o, usually increases with M to a power of 3.2 to 3.6. Below Mc, η_o varies as M. Molecular weight, therefore, is expected not only to determine the mechanical behaviour of a coating, but it should also influence the relative contributions of elastic and viscous particle deformation on the film formation mechanisms.

This work aims to compare the efficiency of film formation in latices with the same nominal composition but with varying molecular weight. In an attempt to take into account the fact that a lower latex molecular weight leads to a lower T_g, lower η_o

and possibly lower modulus, we compare the film formation at equivalent increments above the minimum film-formation temperature[4] (MFT) for each of the latices. We have also explored how the polymer molecular weight influences the behaviour of the surfactant during film formation.

Experimental Work

Latex Polymerisation and Characteristics

The latex used here is based on a copolymer of 10 wt. % methyl methacrylate (MMA), 85 wt. % butyl methacrylate (BMA) and 5 wt. % methacrylic acid (MAA) prepared by standard procedures[6] of emulsion polymerization. Ammonium dodecyl benzene sulphonic acid was used as the stabilising surfactant. A conventional mercaptan chain transfer agent was used to reduce the molecular weight. Further details of the latex synthesis can be found elsewhere. [6] The characteristics of the four different molecular MW latices used can be found in Table 1. For ease of discussion, these are referred to as very-low, low, medium and high MW samples. The glass transition temperatures of the polymers decrease with decreasing molecular weight, as expected from the Flory-Fox equation. [1]

Variable-Angle Ellipsometry

Ellipsometry was performed using a Woollam variable angle spectroscopic ellipsometer (VASE), which incorporates a rotating-analyser configuration.[7] Ellipsometry is a non-invasive optical technique that measures the change in the state of polarisation of light upon reflection from an optical system (i.e. a sample with one or more planar, parallel interfaces)[8]. Well established in the study of semiconductors, ellipsometry has more recently been used extensively to study polymer surfaces and interfaces.[9] Ellipsometry has been used previously to probe latex film formation, and this particular application of the technique has been described elsewhere. [2,3]

An ellipsometry measurement determines the angles, Ψ and Δ. These define the ellipticity, ρ, which is equal to the ratio of the Fresnel reflection coefficients, R_p and R_s, for the parallel and the perpendicular (senkrecht) component of the polarisation, respectively, as follows:

$$\rho = \frac{R_p}{R_s} = \tan\Psi \quad e^{i\Delta} . \tag{1}$$

The Fresnel reflection coefficients, in turn, are functions of the refractive indices of the media at the interface.

Downloaded by UNIV MASSACHUSETTS AMHERST on September 17, 2012 | http://pubs.acs.org
Publication Date: July 26, 2001 | doi: 10.1021/bk-2001-0790.ch004

Two types of ellipsometric analysis were used here: variable-angle and dynamic scans. In a variable-angle scan, which takes approximately 2 min to perform, we measured ψ and Δ as a function of the angle-of-incidence of light, ϕ_o, from a film immediately after the onset of optical clarity and at subsequent times thereafter. Variable-angle scans provide sufficient data to determine with certainty the nano-void concentration and surface roughness of a latex film, as will be explained later. In a dynamic scan, we determined Ψ and Δ at a fixed wavelength of light and fixed ϕ_o at time intervals of 15.6 sec. during the course of latex film formation, starting with a wet dispersion and finishing with a polymer film. The dynamic scans were initiated with a time delay of approximately 5 min. after the deposition of the dispersion onto the substrate. Typically scans were obtained with light in the visible region (500 or 600 nm) with ϕ_o of 56°, corresponding to the Brewster angle of a dry film, where greatest sensitivity is obtained.

To prepare samples for ellipsometry, 0.5 ml of a latex dispersion was cast on the rough surface of a silicon single crystal substrate (4 cm x 4 cm) using a Meyer Bar. Samples were heated in air at various temperatures (5, 10, 15, 20, 30 and 40 °C above their MFT) using a heating stage (Linkam, Surrey, UK). This heating stage was placed on the ellipsometer when performing dynamic scans. Dispersions were cast at room temperature, then heated at 90 °C/min to the film formation temperature and the measurement was commenced.

Atomic Force Microscopy

Atomic force microscopy was performed with a Nanoscope III instrument (Digital Instruments) in the tapping mode. Scans were performed using ultra-sharp Si tips with a spring constant of 0.07-0.29 N/m. Phase contrast images, obtained simultaneously with topographical images, are sensitive to surface features without significant topographical contrast (such as water-soluble species), which are clearly revealed because of their viscoelastic characteristics being distinctively different than the polymer surface. Latex films for AFM analysis were cast on silicon surfaces and film-formed on the heating stage, as used for ellipsometry analysis. The analysis was usually performed within one day of film formation.

Thermal Gravimetric Analysis

A high resolution thermogravimetric analyser (TA Instruments, TGA 2950) was used to analyse films prepared from high and low MW latex dispersions. Latex dispersions were cast on card and film-formed in an oven at 10 °C above their MFT. When optical clarity was achieved, the sample was left in the oven as it cooled to room temperature. A small piece (approximately 20 mg) of the film was peeled from the substrate for TGA analysis after the films had been stored at room temperature

Downloaded by UNIV MASSACHUSETTS AMHERST on September 17, 2012 | http://pubs.acs.org
Publication Date: July 26, 2001 | doi: 10.1021/bk-2001-0790.ch004

and room humidity for one day. During the analysis, samples were heated to 300 °C at a rate of 5 °C/min.

Results and Discussion

Downloaded by UNIV MASSACHUSETTS AMHERST on September 17, 2012 | http://pubs.acs.org
Publication Date: July 26, 2001 | doi: 10.1021/bk-2001-0790.ch004

Void Content and Surface Roughness Films

Interpretation of ellipsometry data requires the construction of models to describe the sample. In previous work, we showed that latex films can be described as consisting of nanometer-size voids dispersed in a polymer matrix and having a surface with roughness on the particle level[10]. This model is shown schematically in Figure 1.

The refractive index of film that is composed of polymer and air voids can be described with an Effective Medium Approximation (EMA).[11,12,13] According to the EMA model, the fraction of voids, f_v, in a latex film is related to the refractive index of the film, n:

$$f_v = \frac{n^2 - n_p{}^2}{n^2 + 2n_p{}^2} \; \frac{n_v{}^2 + 2n_p{}^2}{n_v{}^2 - n_p{}^2} \tag{2}$$

where n_v is the index of air voids ($n_v = 1$), and n_p is the index of the fully-dense polymer. The value of n_p was determined independently from measurements of the latex polymer spin-coated from a toluene solution. The rough surface layer of a latex film is described in the EMA model as consisting of 50 vol. % air voids and 50 vol.% polymer.

Figure 2a illustrates the effect of surface roughness on the ellipsometric angles (Ψ and Δ) obtained from a simulation of an angular scan. As is shown, in data obtained from a smooth film, Ψ has a characteristic V-shape and reaches a minimum at the Brewster angle, the position of which is a function of the refractive index of the substrate. For the same surface, Δ is a step function going from 180° to 0° at the Brewster angle. As the surface roughness increases, the minimum in Ψ also increases, and the step in Δ becomes more gradual. Figure 2b illustrates the effect of voids on the ellipsometric angles. It is apparent that an increase of void volume concentration causes a shift of both Ψ and Δ to the left (and to a lower Brewster angle). Thus, while an increase of surface roughness causes rounding of the V-shape of Ψ and a more gradual step in Δ around the *same* value of Brewster angle, an increase of voids causes a *decrease* in the Brewster angle. These simulations indicate that the ellipsometry analysis is robust, as the two fitting parameters (surface roughness and void concentration) are not strongly correlated. In fitting a model to the experimental data, they each can be independently determined with certainty.

Downloaded by UNIV MASSACHUSETTS AMHERST on September 17, 2012 | http://pubs.acs.org
Publication Date: July 26, 2001 | doi: 10.1021/bk-2001-0790.ch004

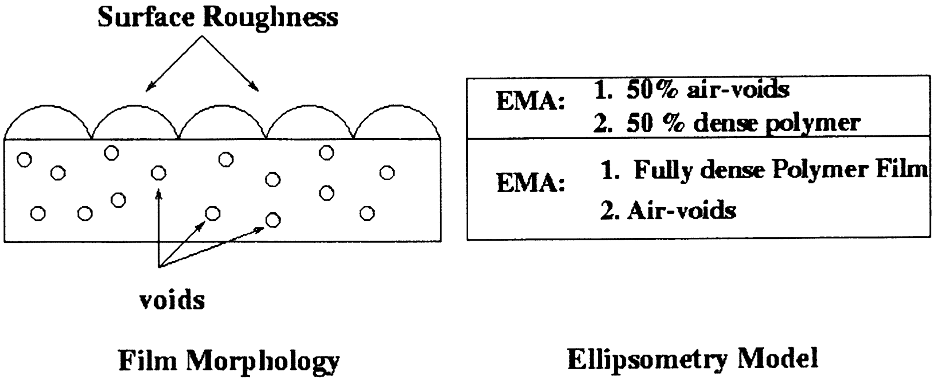
Surface Roughness
voids
Film Morphology
EMA: 1. 50% air-voids
2. 50 % dense polymer
EMA: 1. Fully dense Polymer Film
2. Air-voids
Ellipsometry Model

Figure 1. *Schematic representation of the model to fit the experimental data acquired by ellipsometry.*

Downloaded by UNIV MASSACHUSETTS AMHERST on September 17, 2012 | http://pubs.acs.org
Publication Date: July 26, 2001 | doi: 10.1021/bk-2001-0790.ch004

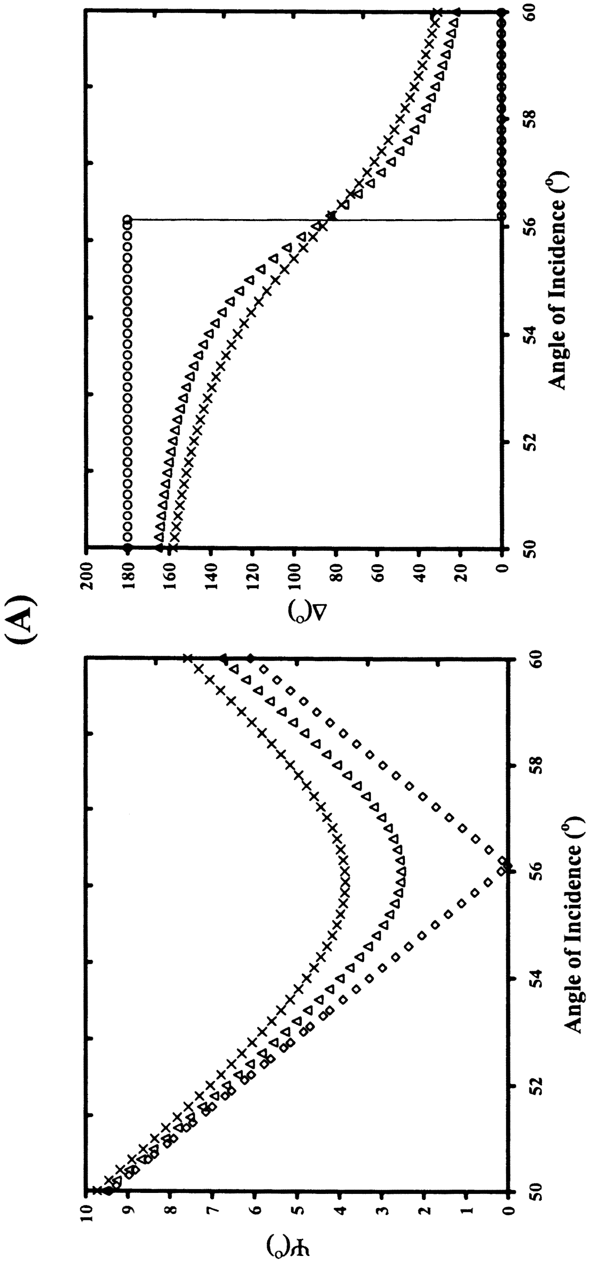

Downloaded by UNIV MASSACHUSETTS AMHERST on September 17, 2012 | http://pubs.acs.org
Publication Date: July 26, 2001 | doi: 10.1021/bk-2001-0790.ch004

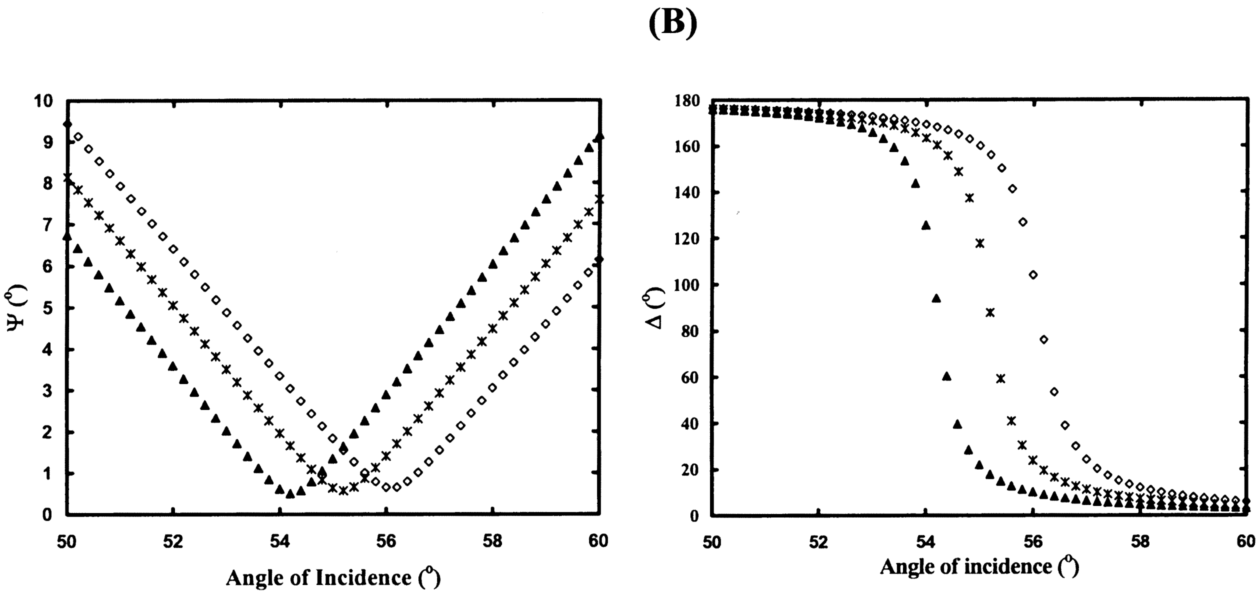

Figure 2. *(A) Simulated ellipsometry spectra showing Ψ (left) and Δ (right) for a transparent substrate with $n = 1.488$ and for surface roughness that equals to 0 (◊), 20 nm (Δ) and 30 nm (X). The minimum value of Ψ increases and Δ becomes less step-like with increasing surface roughness. (B) Simulated ellipsometry spectra for the same system but with surface roughness of 10 nm. The void concentration varies from 20% (▲) to 10% (✳) and finally to 0% (◊). Both Ψ and Δ shift to the right with decreasing void volume concentration.*

Angular scans were performed on each of the latex samples during film formation. Figure 3 presents measurements of surface roughness and void volume fraction obtained by fitting the data to the model shown in Figure 1. Measurements were made at regular time intervals, with time zero corresponding roughly to the point after completion of water evaporation and the onset of optical clarity. The temperature of film formation for each sample was 10 °C above the particular MFT to enable easy comparison.

These ellipsometry data indicate that there is a decrease with passing time in both void content and surface roughness of the films prepared from each and every of the different MW latices. These changes are consistent with what is expected during latex particle coalescence, which causes the closure of the voids and the formation of a denser and smoother film. Figure 3 also reveals that films prepared from the high MW latex show much higher surface roughness and voids percentage in comparison to films prepared from all the other MW latices investigated. Moreover, reduction of both measured parameters occurs much faster in high MW films than in the medium and low. Note that no significant change in surface roughness and void volume concentration was observed in films prepared from the *very-low* MW latex, which indicates that these films acquire their maximum density immediately after water evaporation.

Likewise, when the very-low MW latex films were heated for 6 min at various temperature increments above the MFT, no significant reduction of surface roughness and void volume concentration was observed with increasing temperature, as shown in Figure 4. This finding indicates that very-low MW latex films acquire their maximum density at a film-forming temperature as low as 24 °C (i.e. 5 °C above the MFT). In contrast, when films prepared from low, medium and high MW latices are formed at comparable temperatures (5, 10, 20, 30 and 40 °C above their respective MFT values), both bulk void content and surface roughness decrease with increasing temperature. There is more extensive particle coalescence and surface smoothing at higher temperatures, which is consistent with previous investigations. As also shown previously in Figure 3, roughness and voids concentration (for a given temperature relative to the MFT) increase with increasing molecular weight.

The lower MW latices are more efficient in film formation, according to measurements of void content, in comparison to higher MW ones. We note, however, that the presence of surfactant features at the latex air surface (to be discussed in Section 5.4), in some cases, obscures the measurement of surface roughness due to the polymer alone. Nevertheless, the measurements of the overall observed trends in latex roughness should be valid.

Downloaded by UNIV MASSACHUSETTS AMHERST on September 17, 2012 | http://pubs.acs.org
Publication Date: July 26, 2001 | doi: 10.1021/bk-2001-0790.ch004

Downloaded by UNIV MASSACHUSETTS AMHERST on September 17, 2012 | http://pubs.acs.org
Publication Date: July 26, 2001 | doi: 10.1021/bk-2001-0790.ch004

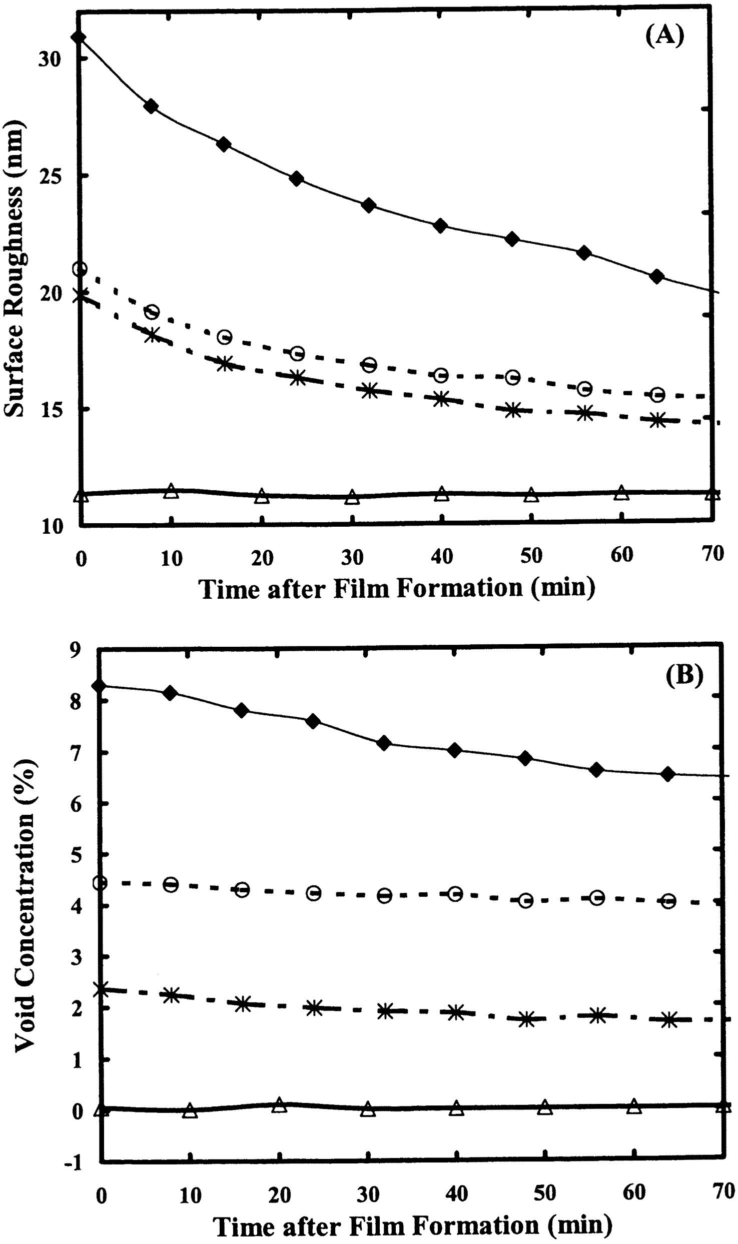

Figure 3. (A) Surface roughness and (B) bulk void concentration as a function of time after latex film formation for high (◆), medium (O), low (✳) and very low (Δ) MW latex. All the films were heated at 10 °C above their MFT.

Downloaded by UNIV MASSACHUSETTS AMHERST on September 17, 2012 | http://pubs.acs.org
Publication Date: July 26, 2001 | doi: 10.1021/bk-2001-0790.ch004

Dynamic Ellipsometry Measurements of Film Formation

Until this point, we have reported the analysis of films *after* their formation. We have additionally probed the morphological changes that occur *during* film formation for films prepared from the different MW latices. Figure 5 shows the raw ellipsometry data that were acquired during the film formation of a low MW latex film film-formed at 10 °C above the MFT. After gradual changes in ψ and Δ over time in the beginning of the scan, there are large changes corresponding to the onset of optical clarity (which is usually associated with film formation). Note that additional changes in Ψ and Δ continue to occur after this point.

Since only single (Ψ,Δ) pairs are measured during a dynamic scan, it is not possible to determine reliably the surface roughness and void content. Data, such as shown in Figure 5, however, can be inverted to obtain the complex pseudo-refractive index, <N>, as a function of time. The pseudo-refractive index is obtained directly from the ellipticity, ρ:

$$<N> = <N_o> \tan\phi_o \left[1 - \frac{4\rho}{(1+\rho)^2} \sin\phi_o^2\right]^{1/2} , \qquad (3)$$

where $<N_o>$ is the complex pseudo-refractive index of the ambient medium, which in our case is air with $<N_o> = 1$. <N> corresponds to the refractive index of the semi-infinite medium leading to the measured ellipticity. The real component of the pseudo-refractive index, <n>, will increase with increasing film density and with decreasing void size as occurs with particle coalescence. A large imaginary component, <k>, usually indicates a rough surface[14] and will therefore decrease as the film becomes smoother. The value of <k> in a dense, optically-clear film with a smooth surface is 0. Thus the pseudo-refractive index of a latex provides qualitative information on the evolution of surface roughness and bulk air voids as influenced by particle deformation during the process of film formation.

We now will consider the film formation of each of the latices, starting with the lowest MW. Figure 6 reports the evolution of <n> acquired from films prepared from the very low MW latex at three different film formation temperatures, all above the MFT. At each temperature, the <n> increases continuously as the water evaporates and reaches a maximum plateau value of about 1.48, which corresponds to the index of the fully-dense polymer. (Prior to this measurement, the refractive index of the dense polymer was determined by ellipsometry measurements of thin films that had been deposited onto silicon substrates by spin-coating from toluene solution. The films were heated at temperatures well above their T_g value to allow an equilibrium polymer conformation and density to be obtained.) The plateau value *does not* increase with film formation temperature. Thus even at the lowest temperature (24 °C, which is just 5 °C above the MFT) the maximum density is obtained immediately upon the evaporation of water. This finding is in agreement with the previous analysis, where both surface roughness and void content of the very

Downloaded by UNIV MASSACHUSETTS AMHERST on September 17, 2012 | http://pubs.acs.org
Publication Date: July 26, 2001 | doi: 10.1021/bk-2001-0790.ch004

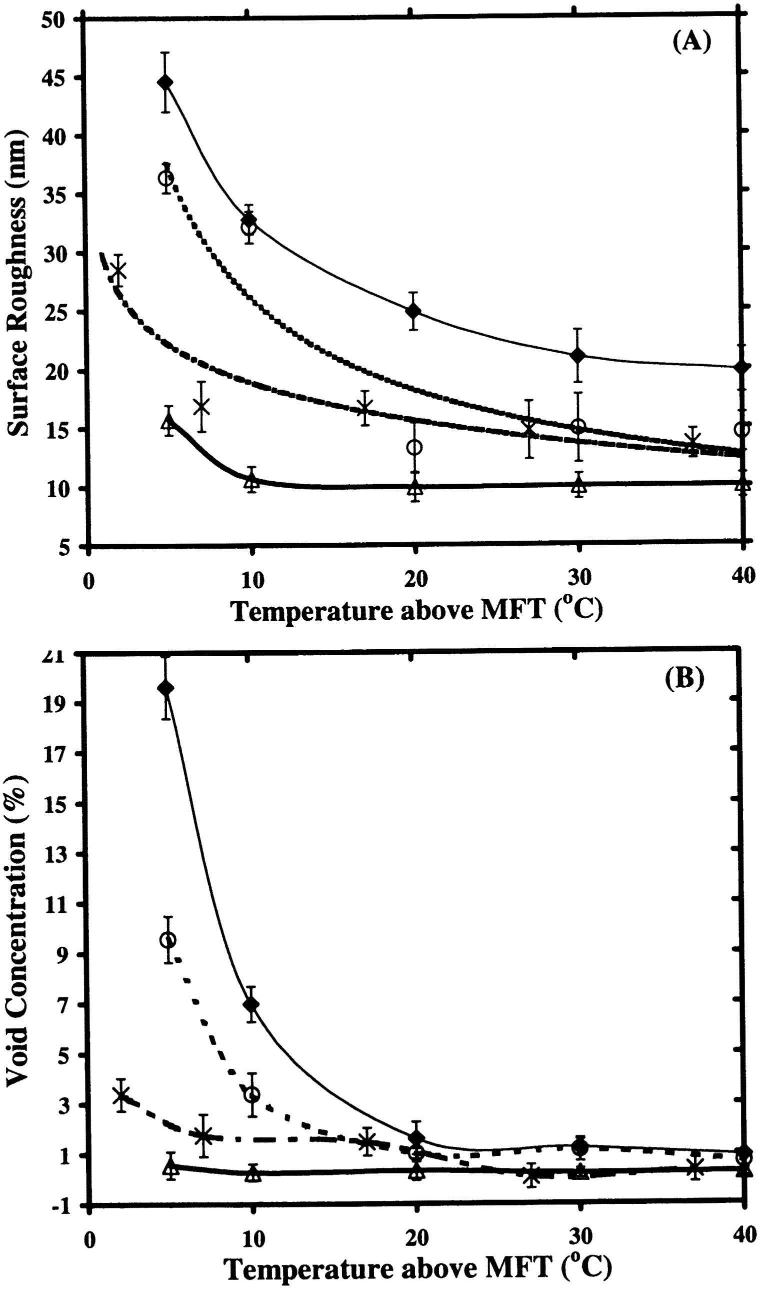

Figure 4. *(A) Surface roughness and (B) bulk void concentration as a function of film formation temperature above MFT after 6 min of film-formation for high (◆), medium (O) low (X) and very low (Δ) MW latex. The lines are a guide to the eye.*

Downloaded by UNIV MASSACHUSETTS AMHERST on September 17, 2012 | http://pubs.acs.org
Publication Date: July 26, 2001 | doi: 10.1021/bk-2001-0790.ch004

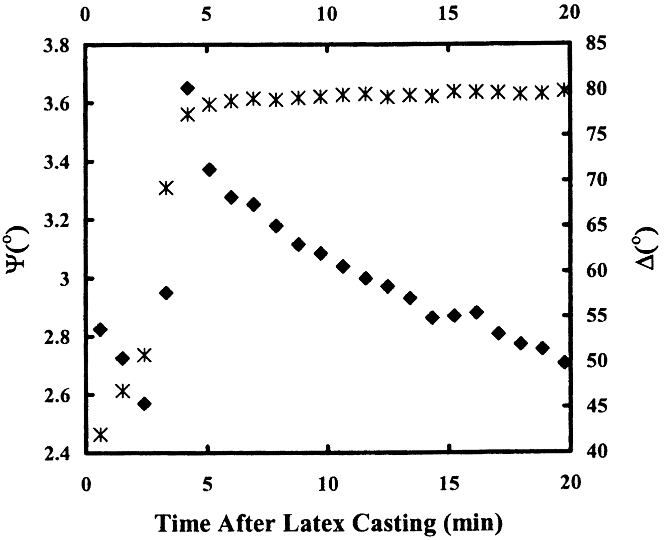

Figure 5. *A typical dynamic ellipsometry scan of a film prepared from a low MW latex dispersion at 10 °C above the MFT. The ellipsometry parameters, Ψ (◆) and Δ (✱), are plotted versus time after latex casting (as film formation proceeds). Data were obtained using a wavelength of 500 nm and* ϕ_o *of 56 °.*

Downloaded by UNIV MASSACHUSETTS AMHERST on September 17, 2012 | http://pubs.acs.org
Publication Date: July 26, 2001 | doi: 10.1021/bk-2001-0790.ch004

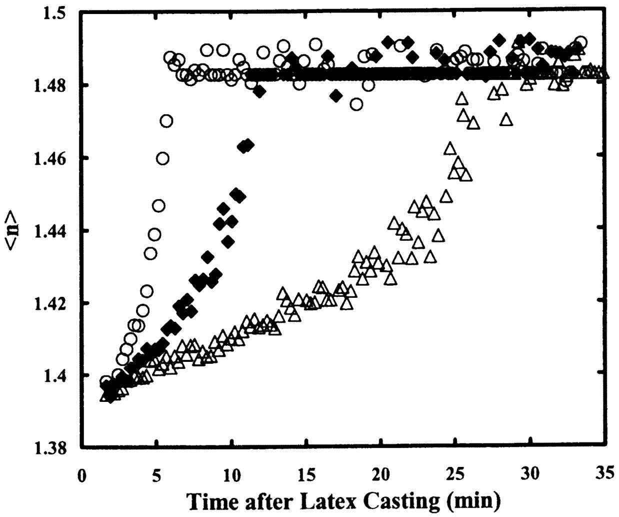

Figure 6. *Dynamic evolution of <n> acquired from very low MW latex films prepared at 5 °C (Δ), 10 °C (◆), and 20 °C (O) above the MFT.*

Downloaded by UNIV MASSACHUSETTS AMHERST on September 17, 2012 | http://pubs.acs.org
Publication Date: July 26, 2001 | doi: 10.1021/bk-2001-0790.ch004

low MW latex film were lower than the other MW films and were constant with increasing film-forming temperature and time.

Figure 7 shows <n> and <k> dynamic data for the low MW latex at three different temperatures. At 5 °C above the MFT, <n> initially increases during film formation but then experiences a sudden drop as the film dries. The <n> then increases slowly over time. It takes on the order of two hours for the closure of all voids and for <n> to attain a value of 1.48. When the same latex was prepared at 10 °C and 20 °C above the MFT, the <n> shows a distinctively different shape. There is no indication of a reduction in the <n>. Instead <n> increases continuously with time until it starts to approach a plateau value. At 10 °C above MFT, there is still a slight upward slope, which is indicative of further particle coalescence. At the highest temperature, <n> is stable with time at the plateau value (1.48) once drying is completed.

The pseudo-extinction coefficient (<k>) is also shown (Figure 7B). At the highest temperature, <k> changes very little over time, suggesting that there is not significant surface roughening or void formation. At the two lower temperatures, the <k> initially increases, which is attributed to the increase of surface roughness with the evaporation of water. <k> reaches a maximum value when all the water is evaporated and then decreases, probably because of a decrease in surface roughness and void content accompanying further particle coalescence. This effect is more dominant at the lowest film formation temperature. This result is similar to what it has been observed previously[3], where particle coalescence proceeds much faster at elevated temperatures.

Figure 8 compares the film formation of very-low, low and medium MW latices, each at 10 °C above their respective MFT values. The arrows indicate the points where the films become optically clear and where most of the water has evaporated. At higher temperatures of film formation, this point occurs after shorter times (because evaporation is faster at elevated temperatures, of course). After this point, the <n> of the medium MW latex decreases to a minimum and then gradually increases again. These optical changes are consistent with the formation of air voids upon water loss (which would cause a decrease in index) followed by gradual particle coalescence (which would cause an index increase). The lower MW latices have a different behaviour, with the very-low MW latex showing no change in <n> once drying and film formation are complete. The <n> of the low MW latex increases slightly with time and is lower than the value of *ca.* 1.48 obtained in the very-low MW film. Thus, in the low MW film there is evidence for some void content after drying, but much less than in the medium MW film.

Figure 9 compares the <n> acquired from films prepared from very-low and high MW latices film-formed at 20 °C above their respective MFT values. The <n> of the high MW film shows a small drop (which is reproducible in replicate scans) after about 4 min (corresponding to the completion of drying), indicating that a small fraction of air voids develops.[15] There is an immediate increase in <n>, however,

Downloaded by UNIV MASSACHUSETTS AMHERST on September 17, 2012 | http://pubs.acs.org
Publication Date: July 26, 2001 | doi: 10.1021/bk-2001-0790.ch004

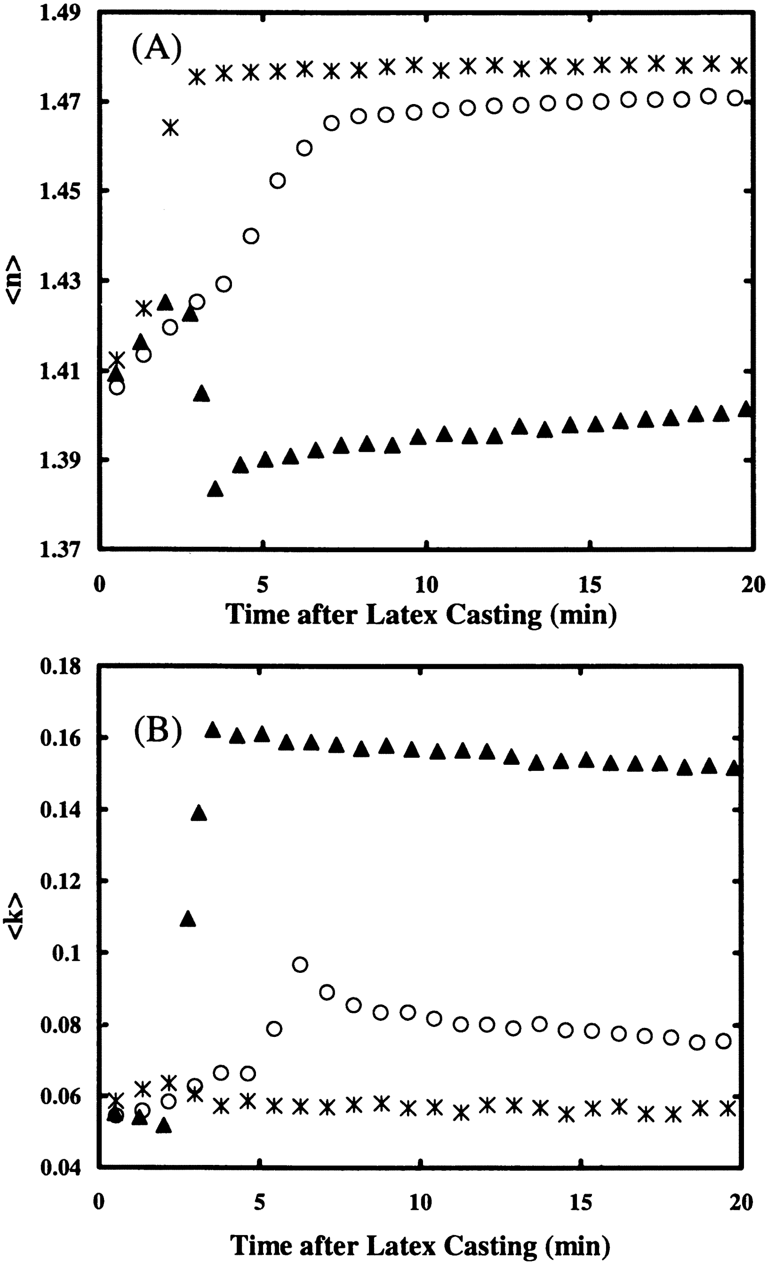

Figure 7. *Dynamic evolution of the pseudo-refractive index (<n>) and the pseudo-extinction coefficient (<k>) for films prepared from low MW latex at 5 ° C (▲), 10 °C (○) and 20 °C (✱) above the MFT.*

Downloaded by UNIV MASSACHUSETTS AMHERST on September 17, 2012 | http://pubs.acs.org
Publication Date: July 26, 2001 | doi: 10.1021/bk-2001-0790.ch004

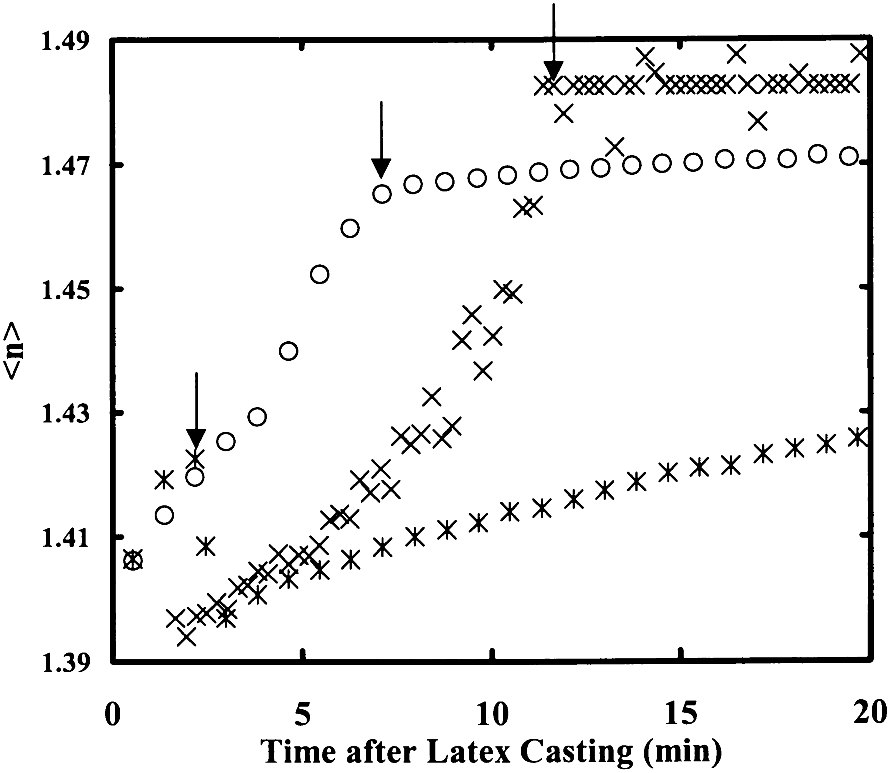

Figure 8. *Dynamic evolution of <n> acquired from films of very low (X), low (O) and medium (✱) MW latices prepared at 10 °C above their MFT values. The arrows indicate the points where the films become optically clear. Their relative positions reflect the slower evaporation time of water at lower temperatures.*

Downloaded by UNIV MASSACHUSETTS AMHERST on September 17, 2012 | http://pubs.acs.org
Publication Date: July 26, 2001 | doi: 10.1021/bk-2001-0790.ch004

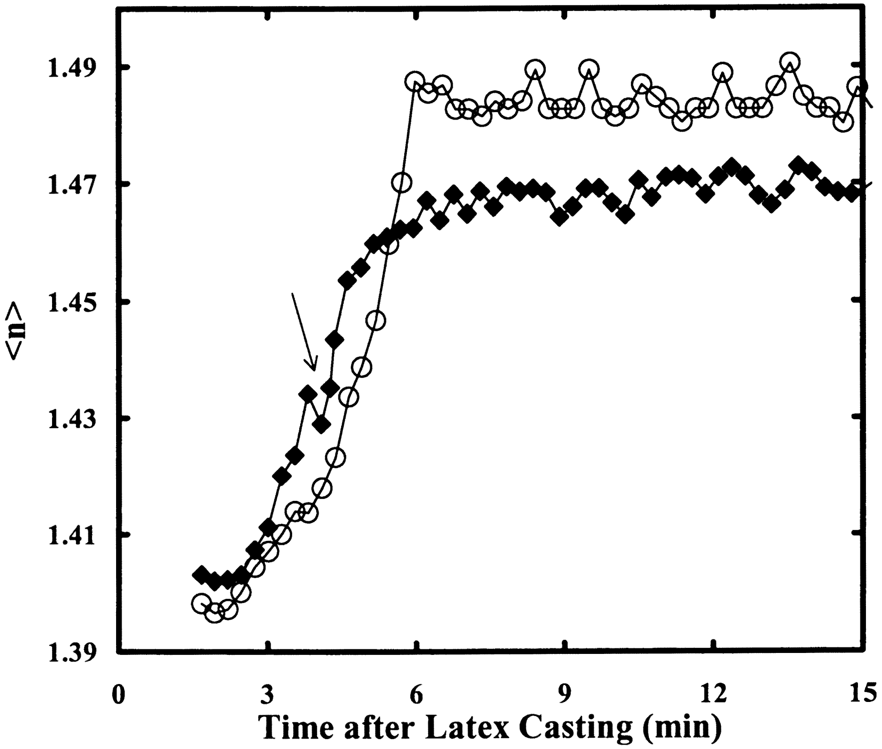

Figure 9*. Dynamic evolution of <n> and <k> acquired from films of very low (○) and high (◆) MW latices prepared at 20 °C above their MFT values. High MW shows a small drop in <n> and <k>, indicated by the arrows. A separate drying and coalescence front are indicated. The very low MW latex shows a continuous drying front.*

which is consistent with fast particle coalescence at this elevated temperature. The film reaches an <n> of *ca.* 1.47, which is close to what is measured in a fully-dense (spun-cast) film. In comparison, in the very low MW film, a plateau value of *ca.* 1.48 (corresponding to low or no air voids) is obtained *immediately* upon water evaporation.

Thus, the experimental evidence in Figures 3 through 9 suggests that the efficiency of film formation is strongly related to the MW of the latex as well as to the temperature and time of film formation. At a given value above the MFT, the lower MW latices form films with lower void content and surface roughness, in comparison to the higher MW materials. At elevated temperatures (over 30 °C above MFT), the higher MW latices form smooth, dense films immediately upon water evaporation in a way that is similar to the lower MW latices at temperatures very close to their MFT. Not only does film formation occur at lower absolute temperatures in the low MW latex, but it is more efficient.

Downloaded by UNIV MASSACHUSETTS AMHERST on September 17, 2012 | http://pubs.acs.org
Publication Date: July 26, 2001 | doi: 10.1021/bk-2001-0790.ch004

Surfactant Morphology and Concentration at the Latex Air Surface

We next report the surfactant morphology and concentration at the polymer/air interface of very-low and low MW latex films. Figure 10 shows the polymer/air interface of the very-low MW latex film after formation at 24 °C (5 °C above the MFT). It is apparent that the individual latex particles have lost their identity because of the process of interdiffusion. There is no topographical evidence for particle/particle boundaries, but these are slightly apparent in the phase contrast image. This smooth, void-free surface is consistent with our previous measurements of ellipsometry that indicated full particle coalescence in this very-low MW latex. The phase contrast image reveals the existence of small island-like regions (without significant topographical contrast), which we suggest are composed of thin layers of surfactant and water-soluble species. These species are apparent at the polymer/air interface, even though the film was prepared at such a relatively low temperature. In stark contrast, previous study[6] of the high MW latex films has found that surfactant features appear at the surface only when the film is formed at elevated temperatures or for longer times. Note that acidic monomers and water-soluble oligomers (resulting from the emulsion polymerization) might be expected at the latex surface. RBS analysis,[6] however, finds a high concentration of sulphur at the surface, which is attributed to surfactant and would not be found in high concentrations in other species.

In a low MW latex film, AFM analysis (shown in Figures 11 through 13) likewise reveals separate features apparent at the surface under all conditions of film formation. The morphology of these features depends on the film-forming temperature and time. At temperatures only slightly above MFT (6 °C above MFT), Figure 11 shows that individual particles are evident, but they are partially covered by a thin layer of a second phase, which is apparent in the phase contrast image, but

Downloaded by UNIV MASSACHUSETTS AMHERST on September 17, 2012 | http://pubs.acs.org
Publication Date: July 26, 2001 | doi: 10.1021/bk-2001-0790.ch004

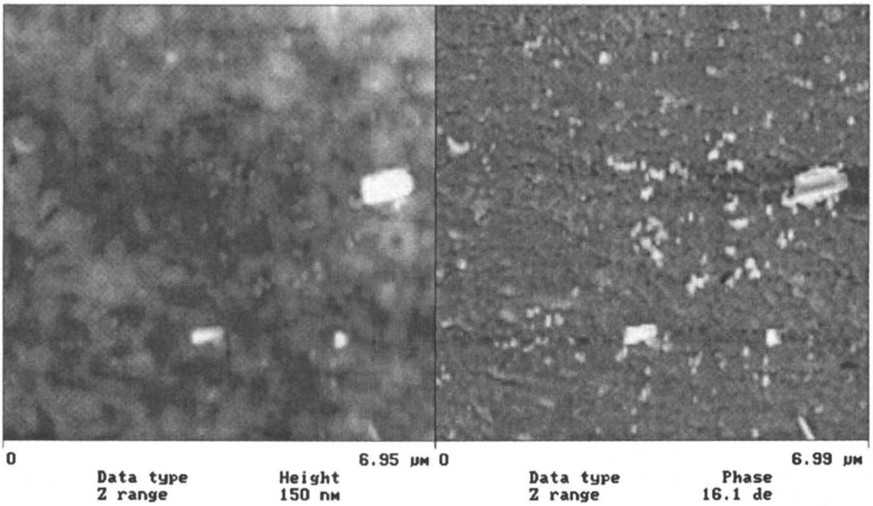
0
6.95 µm
Data type Height
Z range 150 nm
0
6.99 µm
Data type Phase
Z range 16.1 de

***Figure 10**. AFM images (topography on the left and phase contrast on the right) of the polymer/air interface of a film prepared from the very low MW latex dispersion. The film was formed at 24 °C (5 °C above the MFT). The scan was performed immediately after the film was optically clear.*

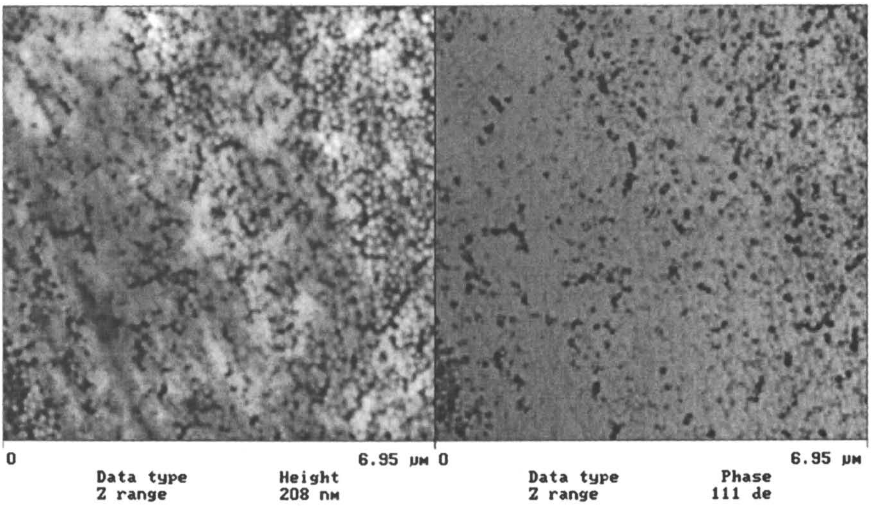
0
6.95 µm
Data type Height
Z range 208 nm
0
6.95 µm
Data type Phase
Z range 111 de

***Figure 11**. AFM images of the polymer/air interface of films prepared from a low MW latex dispersion. The film was formed at 43 °C (6 °C above the MFT) for 15 min., which is the minimum time required at this temperature to achieve film clarity. Area of images is 6.95 µm x 6.95 µm.*

which does not have topographical contrast. It probably consists of surfactant and perhaps other water-soluble species.

After film formation at a higher temperature (15 °C above MFT) for 10 min, the surface morphology is distinctly different. In Figure 12A, there are features that appear clearly in the phase-contrast images but that do not provide topographical contrast. These features have an undulating contour that is similar to the so-called "finger-like" morphology observed previously at the surface of the high MW latex cast from six-month old dispersions.[6] This finger-like morphology might result from the break-up of the thin "blanket" observed at a lower temperature. Figure 12B clearly shows a second phase at the surface with a distinctive morphology. In some areas, there are pits or holes in the surface, perhaps resulting from voids between the underlying particles. These tiny pits are surrounded by a second phase with a colour contrast similar to that in the larger, finger-like regions. We interpret these phases as consisting of surfactant. Indeed, previous studies of this latex have indicated that surfactant features appear brighter in phase mode. We will discuss these observations further in the next section.

A further increase of the film formation temperature to 57 °C leads to the formation of separate hemispherical drops with diameters between about 300 and 500 nm at the surface of the low MW latex (Figure 13). These features might be the result of further de-wetting of the latex surface, driven by the minimisation of surface energy. Also in the phase contrast image of Figure 13B, tiny pits are again seen to be surrounded by a second phase.

A similar pattern of morphologies – thin layers then undulating "fingers" then hemispherical domes (or "blobs") – was reported previously[6] in films prepared from the high-MW acrylic latex film. In those experiments, higher temperatures and/or longer film formation times were required to obtain the various morphologies. With this low MW latex, the morphologies develop immediately upon water evaporation and at lower temperatures relative to the MFT. Previously[6] it was determined that the changes in surfactant morphology are caused by de-wetting and minimization of surface energy. There was no evidence for exudation of surfactant over time but only a re-arrangement of surfactant already at the surface. (Incidentally, in the previous studies of the high MW latex, the dispersion had been stored in a partially open container for over six months. This storage resulted in water evaporation, pH decrease, and a surface tension decrease. Studies of freshly-prepared dispersions, described elsewhere[16], have found no evidence for surfactant at the surface.)

Further Discussion

This work has two primary results, which we will now consider in greater depth, regarding molecular weight effects on the efficiency of film formation and on surfactant behaviour.

Downloaded by UNIV MASSACHUSETTS AMHERST on September 17, 2012 | http://pubs.acs.org
Publication Date: July 26, 2001 | doi: 10.1021/bk-2001-0790.ch004

Downloaded by UNIV MASSACHUSETTS AMHERST on September 17, 2012 | http://pubs.acs.org
Publication Date: July 26, 2001 | doi: 10.1021/bk-2001-0790.ch004

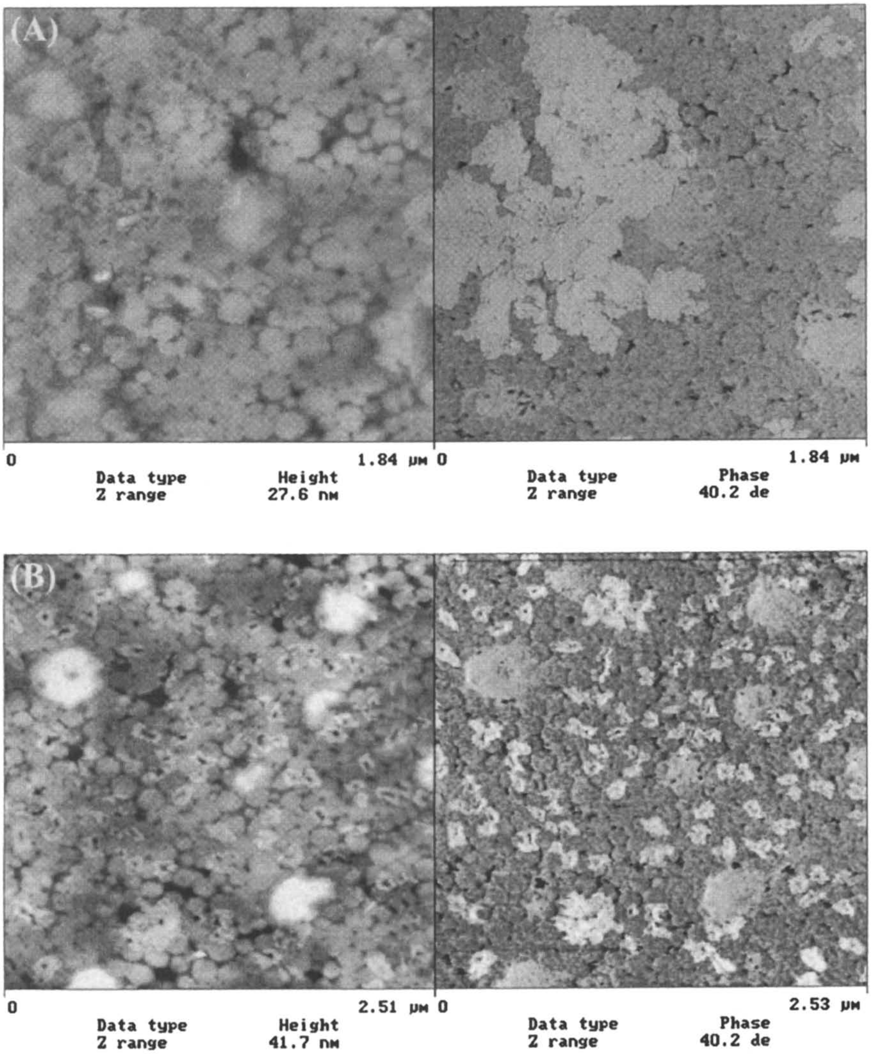
(A)
0
1.84 µm
0
1.84 µm
Data type
Z range
Height
27.6 nm
Data type
Z range
Phase
40.2 de
(B)
0
2.51 µm
0
2.53 µm
Data type
Z range
Height
41.7 nm
Data type
Z range
Phase
40.2 de

Figure 12. *AFM images (topographic on the left and phase image on the right) of the polymer/air interface of a film prepared from a low MW latex dispersion at 52 °C (15 °C above the MFT) for the minimum film formation time of 10 min. (A) 1.84 µm x 1.84 µm and (B) 2.53 µm x 2.53 µm. Surfactant de-wetting is apparent in A.*

Downloaded by UNIV MASSACHUSETTS AMHERST on September 17, 2012 | http://pubs.acs.org
Publication Date: July 26, 2001 | doi: 10.1021/bk-2001-0790.ch004

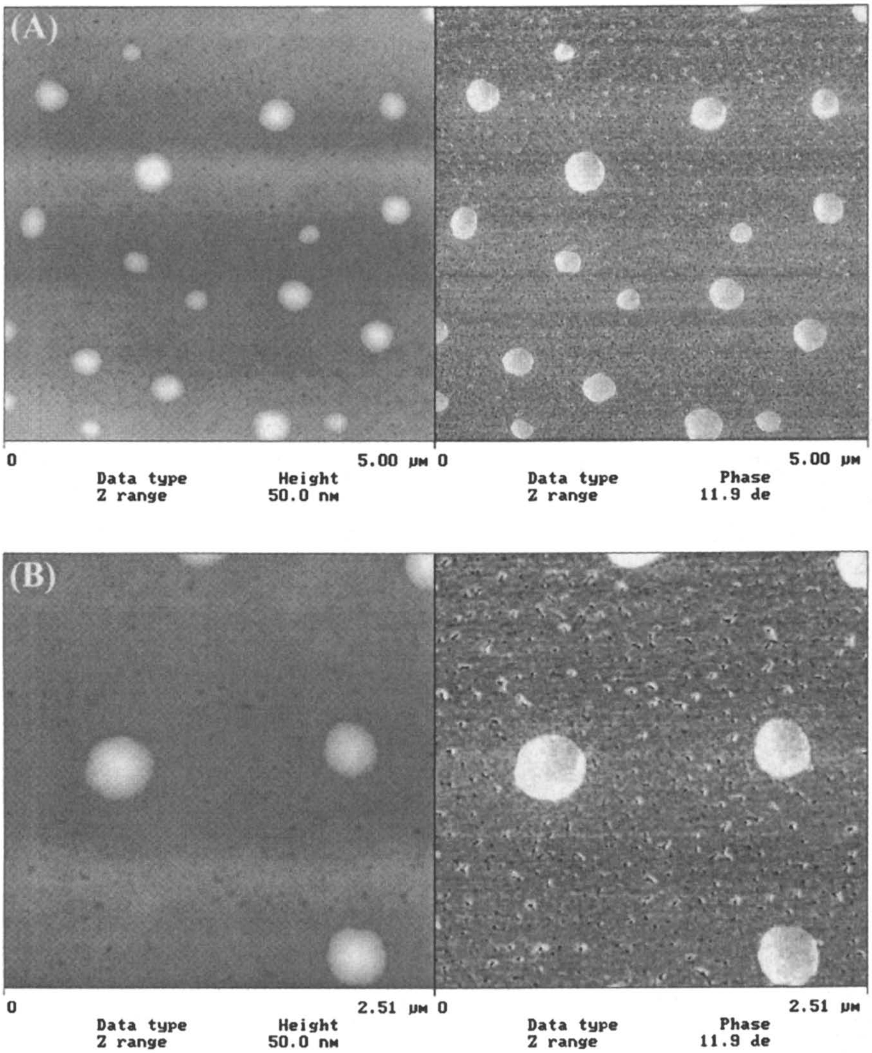
(A)
0
5.00 µm
0
5.00 µm
Data type
Height
Z range
50.0 nm
Data type
Phase
Z range
11.9 de
(B)
0
2.51 µm
0
2.51 µm
Data type
Height
Z range
50.0 nm
Data type
Phase
Z range
11.9 de

***Figure 13**. AFM images (topographic on the left and phase image on the right) indicating dome-shaped surfactant features at the polymer/air interface of a low-MW acrylic latex film prepared at 57 °C (20 °C above the MFT) for the minimum film formation time of 8 min. (A) 5 µm x 5 µm and (B) 2.51 µm x 2.51 µm. Small holes can be seen in the topographical images at the particle interfaces. In the phase images, a separate species, possibly surfactant, is observed around these holes.*

First, we consider the film formation, starting with a review of the results. The dynamic ellipsometry scans provide insight into the origins of these observed differences. Figure 6 shows that in a very low MW latex the index rises continuously during water evaporation. This behaviour is consistent with the concept of particle coalescence occurring simultaneously with the evaporation of water. There is a single drying and coalescence front during film formation at the higher temperatures. Only at a relatively low temperature (5 °C above the MFT) is there evidence for voids remaining after a drying front has receded.

In comparison, the medium MW latex film shows evidence for void formation after drying when film-formed at 5 and 10 °C above MFT. Only when it is film-formed at temperatures greater than 20 °C above MFT is there evidence for a single film formation front in which drying and complete particle deformation occur simultaneously. At lower temperatures the presence of voids causes a coalescence front to follow the drying front. The high MW latex films require film formation at 30 °C above MFT to achieve this same behaviour.

As Figure 9 illustrates, at 20 °C above MFT, the very low MW latex has little if any void formation upon water evaporation, leading to a smooth increase in <n> during film formation. The high MW shows a distinctly different behaviour. There is a rise in <n> during drying, but with passing of the drying front, the <n> decreases as an apparent result of void formation. There follows a gradual increase in <n> with subsequent particle coalescence. The differences observed in the final films correlated with the MW clearly have their origins in these differing characteristics of film formation.

Now we seek to explain these observations of film formation that presumably reflect differences in the mechanical properties of the polymer with varying MW. Examination of the values in Table I reveals that in all cases MFT occurs at temperatures below the T_g of the dry polymer. Deformation and coalescence of the polymer particles below their T_g, when they would otherwise be glassy, requires plasticization. The differences between the T_g and MFT values, listed in Table I, reveals an increase with decreasing molecular weight. The very low MW latex apparently undergoes the greatest amount of plasticization. There are several examples in the literature[4] in which water is attributed to acting as a volatile plasticizer. In an acrylic latex made hydrophilic by the introduction of methacrylic acid, such as used here, water plastization is expected.

As a means of studying this possible effect of water further, TGA curves of the low and high MW latices were compared. Figure 14 shows that over temperatures ranging from room temperature to 150 °C, the low MW film loses a greater amount of weight than does the high MW latex. This difference in weight loss can be attributed to a greater amount of weakly-bound water in the low MW films. This idea is consistent with most of the weight loss occurring while heating up to 100 °C, which is also suggested by the greater amount of observed plasticization.

Downloaded by UNIV MASSACHUSETTS AMHERST on September 17, 2012 | http://pubs.acs.org
Publication Date: July 26, 2001 | doi: 10.1021/bk-2001-0790.ch004

Table I. Characteristics of the MMA/BMA/MAA Latex

	Very-Low MW	*Low MW*	*Medium MW*	*High MW*
M_w (Daltons)	7,500	15,130	29,000	704,000
M_w/M_n	1.70	1.86	1.95	2.34
pH	7	7	7	7
Percent of Solids	38.7	38.2	38	39.8
Particle Size (nm)	165	150	146	144
MFT (°C)	19	37	49	59
Glass Transition Temperature (°C)*	43	60	68	73
T_g-MFT (°C)	24	23	19	14

* Determined using dynamic mechanical thermal analysis at 1 Hz on dried films.

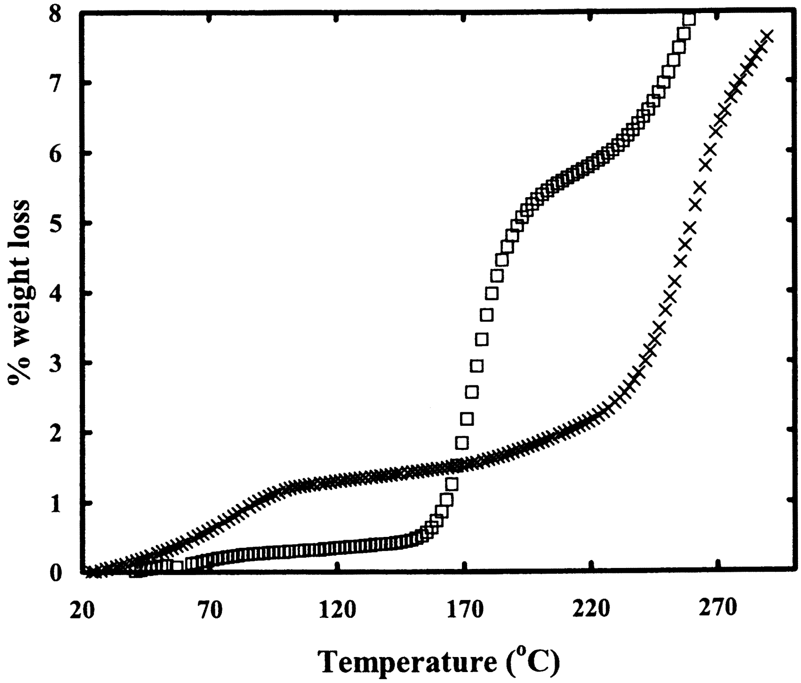

Figure 14. Mass loss, according to TGA, from heating films prepared from high (□) and low (x) MW latex dispersions.

Downloaded by UNIV MASSACHUSETTS AMHERST on September 17, 2012 | http://pubs.acs.org
Publication Date: July 26, 2001 | doi: 10.1021/bk-2001-0790.ch004

The presence of water has been shown elsewhere to alter latex mechanical properties, as studied with dynamic mechanical thermal analysis.[17] Of particular relevance here is work by Eckersley *et al*[18],[19] on a latex copolymer of BMA/MMA/MAA in which the presence of water causes a significant decrease in the modulus of latex. Accordingly, the variation of water content with varying latex molecular weight should influence the film formation of the latex studied here. By comparing film formation at comparable temperatures in relation to MFT, however, one could naively argue that the effects of water plastization should thereby be taken into account. Another factor to consider, though, is that the water loss rate of the latex will be increased at higher temperatures. Thus, by virtue of the fact that the high MW latex is film-formed at elevated temperatures, water loss will be faster and perhaps more complete in the high MW latex. The effects of plasticization might therefore be dominant in the lower MW latices (film-formed at lower absolute temperatures) for a significantly longer time. Further complicating the issue is the possibility that high coalescence at the film surface could trap water within the film. Thus, more extensive particle coalescence in the low MW latex might inhibit water evaporation, which would then prolong the effects of water plasticization.

We next consider surface morphologies. In Figure 12B, neck formation between low MW particles is already apparent in some areas, which would cause smoothening of the surface. AFM analysis of the high MW latex film (shown in Figure 15), which was found by ellipsometry analysis to be rougher and to contain voids, clearly shows the boundaries of individual particles. Particles have deformed but have not coalesced.

Our AFM studies (and Rutherford Backscattering Spectrometry analysis, reported elsewhere[6,16]) of low MW latex provides evidence for surfactant at the latex/air surface for all temperatures of film formation. This result is in contrast to our previous study of the high MW latex in which extended film formation times and/or higher temperatures were required to create similar surfactant structures.[6] (Note, for instance, that Figure 15 shows no second phases at the high MW latex surface.) What is the cause of these differences? The surfactant behaviour might be directly influenced by the relative deformability of the latex particles. That is, the more efficient film formation of the low MW latex might encourage the transport of surfactant to the air surface. Support for this idea comes from recent work by Du Chesne *et al.*[20] They investigated the behaviour of surfactant in a poly(vinyl acetate) latex and in a latex based on a copolymer of methyl methacrylate and butyl acrylate. When either type of latex is film-formed at temperatures greater than MFT, then the emulsifier formed separate domains both at the surface and in the bulk. On the other hand, when the samples were annealed at temperatures below MFT, the surfactant was presumably retained at the surface of the latex particles as a thin "possibly monomolecular layer."[20] The authors conclude that particle deformation, which only occurs above MFT, contributes to the process of expelling of surfactant from the latex surfaces and into the serum. During further film formation and particle packing, some of this surfactant in the serum is deposited at the air surface.

Downloaded by UNIV MASSACHUSETTS AMHERST on September 17, 2012 | http://pubs.acs.org
Publication Date: July 26, 2001 | doi: 10.1021/bk-2001-0790.ch004

Downloaded by UNIV MASSACHUSETTS AMHERST on September 17, 2012 | http://pubs.acs.org
Publication Date: July 26, 2001 | doi: 10.1021/bk-2001-0790.ch004

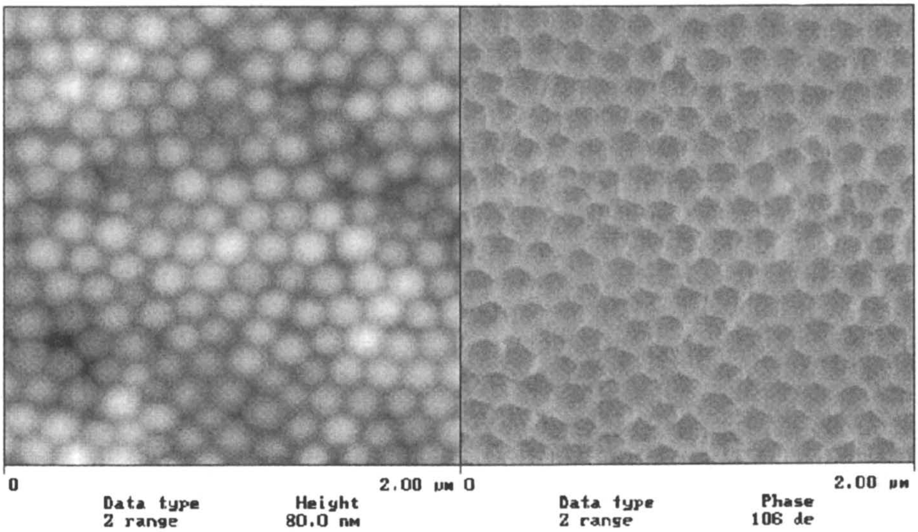
0
2.00 μm
Data type
Z range
Height
80.0 nm
0
2.00 μm
Data type
Z range
Phase
106 de

***Figure 15.** AFM images (topographic on the left and phase image on the right) of a latex film obtained from a freshly-prepared, high MW latex dispersion. The films were film-formed at 89 °C (30 °C above the MFT) for 90 min. Area of images is 2.51 μm x 2.51 μm.*

Downloaded by UNIV MASSACHUSETTS AMHERST on September 17, 2012 | http://pubs.acs.org
Publication Date: July 26, 2001 | doi: 10.1021/bk-2001-0790.ch004

Finally, we comment on the interesting ring-like features observed in Figures 12B and 13. Larger regions exist of a second phase, presumably surfactant. Tiny rings of this surfactant phase are also present around pits or holes that are associated with interparticle voids. What is the origin of these features? A study of the phase equilibria of a surfactant similar to the one used here, sodium dodecyl benzene sulfonate, offers some insight.[21] Depending on the surfactant and salts concentrations, a rich variety of phases are found, most notably large vesicles. In particular, vesicles are favoured at higher concentrations. As the water evaporates in the latex studied here, higher concentrations of both surfactant and salt are obtained. Drawing upon knowledge of the Na-analogue, one might expect vesicles to develop during the later stages of film formation. The large features found in Figure 13C might be such collapsed vesicles.

The tiny rings observed in our work are quite similar in appearance to features observed by Du Chesne *et al.*,[20] which they attributed to surfactant micelles at particle interstices. In our case, formation of these rings is even more noticeable and numerous, although their size is on the order of 100 nm in comparison to the 30 nm features observed by Du Chesne *et al.*. Building on the ideas proposed by Chevalier *et al.*,[22] it was proposed that these structures are inverted surfactant micelles, containing small amounts of bound water, and which are formed after desorption from the particle surfaces.[20] Although our analytical techniques cannot confirm the composition of the ring-like features, their appearance is consistent with this notion of trapped micelles. Moreover, the latex studied here and the one used by Du Chesne *et al.* are both acrylic polymers containing methacrylic acid, which produces a hydrophilic particle surface, and so similar behaviour might be expected.

Notably, surfactant rings were *not* found at the surface of high MW latex films. Because the high MW latex is film-formed at higher temperatures leading to faster water loss rates, there is less time available for surfactant desorption and re-organisation into micelles. As the low MW latex is film-formed at lower temperatures, there is more time available for these processes.

Summary

The main conclusion from these experiments is that lower MW latex not only forms films at lower temperatures compared to higher MW latex, but that film formation is more efficient. At comparable temperatures and times, low MW latex films are denser (lower voids volume concentration) and smoother (smaller surface roughness). Higher temperature and/or longer film-forming times are required for the high MW latex to close up all the voids in the bulk of the film and to minimise the surface roughness. This result reflects the complex interplay between MW, polymer viscoelasticity and temperature. Additionally, since the low MW latex is film-formed at lower temperatures, it will lose water at a slower rate, and so it might be more prone to water plasticization in comparison to the high MW latex.

These results indicate the attractiveness of low MW latex, but we also report a consequence. In low MW films, surfactant is found at higher concentrations at the air surface, under all conditions of film formation. It was shown that surfactant tends to de-wet the surface of the polymer particles with increasing temperature and/or time. Similar surfactant concentrations and morphologies are observed in high MW latex films only when the dispersion is aged (via evaporation of water) prior to casting.

Downloaded by UNIV MASSACHUSETTS AMHERST on September 17, 2012 | http://pubs.acs.org
Publication Date: July 26, 2001 | doi: 10.1021/bk-2001-0790.ch004

References

[1] T.G. Fox and P.J. Flory, *J. Appl. Phys.*, **21**, 581 (1950).

[2] J.L. Keddie, P. Meredith, R.A.L. Jones and A.M. Donald, *Macromolecules*, **28**, 2673 (1995).

[3] J.L. Keddie, P. Meredith, R.A.L. Jones, and A.M. Donald, in *Film Formation in Waterborne Coatings (ACS Symposium Series)*, **648**, T. Provder, M.A. Winnik and M.W. Urban, Ed., ACS, Washington DC, 1995, Ch. 21, p. 332-348.

[4] J.L. Keddie, *Mat. Sci. Eng. Reports*, **R21**, 101 (1997).

[5] G. Strobl, *The Physics of Polymers, 2nd ed.*, Springer, Berlin, 1997, p. 217-230.

[6] A. Tzitzinou, P.M. Jenneson, A.S. Clough, J.L. Keddie, J.R. Lu, P. Zhdan, K.E. Treacher, and R. Satguru, *Prog. Org. Coatings*, **35**, 89 (1999).

[7] Snyder, P. G.; Rost, M. C.; Bu-Abbud G. H.; Woollam, J. A., *J. Appl. Phys.,* **60**, 3293 (1986).

[8] R. M. A. Azzam and N.M. Bashara, *Ellipsometry and polarised light*, North-Holland, Amsterdam, 1977, p. 153-416.

[9] D.A. Styrkas, S.J. Doran, V. Gilchrist, J.L. Keddie, J.R. Lu, E. Murphy, R. Sackin, T.-J. Su and A. Tzitzinou in *Polymers at Surface and Interfaces III*, R.W. Richards and S.K. Peace, Ed., John Wiley, Chichester, 1999, chap. 1.

[10] A. Tzitzinou, J. L. Keddie, J. M. Geurts, A. C. I. A. Peters and R. Satguru, *Macromolecules*, **33**, 2695 (2000).

[11] D. E. Aspnes, J. B. Theeten and F. Hottier, *Phys. Rev. B*, **20**, 3293 (1979).

[12] D. Roennow, S. K. Anderson and G. A. Niklasson, *Optical Materials*, **4**, 851 (1995).

[13] S-M.F. Nee, *Appl. Optics*, **27**, 2819 (1988).

[14] F.K.Urban III, P. Ruzakowski Athey and Md. S. Islam, *Thin Solid Films,* **253**, 326 (1994).

[15] In other high MW latex studied previously, such as in references 2, 3, and 10, even greater decreases in <n> have been observed.

[16] A. Tzitzinou, PhD thesis, University of Surrey, Guildford (UK), 1999.

[17] A. Arora, E.S. Daniels, and M.S. El-Aasser, *J. Appl. Polym. Sci.*, **58**, 301 (1995).

[18] S. T. Eckersley, A. Rudin, *J. Appl. Pol. Sci.*, **48**, 1369 (1993).

[19] S. T. Eckersley and A. Rudin, *J. Appl. Pol. Sci.*, **53**, 1139 (1994).

[20] A. Du Chesne, B. Gerhard, and G. Lieser, *Polym. Internat.*, **43**, 187 (1997).

[21] A. Sein and J.B.F.N. Engberts, *Langmuir*, **11**, 455 (1995).

[22] Y. Chevalier, C. Pichot, C. Graillat, M. Joanicot, K. Wong, J. Maquet, P. Lindner and B. Cabane, *Colloid Polym. Sci.*, **270**, 806 (1992).

Downloaded by UNIV MASSACHUSETTS AMHERST on September 17, 2012 | http://pubs.acs.org
Publication Date: July 26, 2001 | doi: 10.1021/bk-2001-0790.ch004

Downloaded by OHIO STATE UNIV LIBRARIES on September 17, 2012 | http://pubs.acs.org
Publication Date: July 26, 2001 | doi: 10.1021/bk-2001-0790.ch005

Chapter 5

Film Formation from Blends of Carbodiimide and Carboxylic Acid-Functional Latex

Hung H. Pham and Mitchell A. Winnik*

**Department of Chemistry, University
of Toronto, Toronto, Ontario M5S 3H6, Canada
*Corresponding author: mwinnik@chem.utoronto.ca**

Anthracene-labeled poly(2-ethylhexyl methacrylate) copolymer latex particles containing carbodiimide groups and corresponding phenanthrene-labeled particles containing carboxylic acid groups were synthesized. We employed fluorescence energy transfer experiments to follow polymer diffusion rates in these films, and FTIR measurements to follow the carbodiimide group reaction rates. The -COOH- and -N=C=N-containing polymers have limited miscibility. During film formation from the aqueous dispersions at 22 °C some branched polymer is formed by the reaction of the carbodiimide and carboxylic acid groups. As the films are annealed, further reaction occurs, and polymer diffusion leads to full mixing of the two polymers. The formation of branches promotes polymer miscibility but retards the rate of polymer diffusion. While the rate of polymer diffusion at 60 °C is on the whole faster than the rate the chemical reaction between the -N=C=N- and -COOH groups, it is still substantially slower than the polymer diffusion rate in PEHMA latex films lacking the reactive groups.

Latex dispersions are widely employed as binders in waterborne coatings. The largest markets, such as architectural coatings, employ thermoplastic latex. Formulations based upon thermoplastic latex polymers combine convenient use and clean up, typical of most waterborne formulations, with useful final film performance properties such as adhesion and toughness. Although latex coatings reduce the amount of volatile organic emissions compared to solvent-based coatings and display excellent performance in many areas of applications, thermoplastic latex films lack tensile strength, abrasion resistance, chemical resistance, and general durability. These film properties can be greatly improved by introducing crosslinks in the

In Film Formation in Coatings; Provder, T., et al.;
ACS Symposium Series; American Chemical Society: Washington, DC, 2001.

systems.[1] As a consequence, increasing attention is being paid to utilizing reactive latex polymers to form crosslinkable films for their applications in water-borne paints, coatings, and adhesives.

Among the strategies one can consider for thermoset latex systems, one of the most attractive involves packaging the reactive functional groups into separate latex particles. In this approach, one synthesizes two similar types of latex, each bearing one of the reactive groups. If the reactive functionality is chosen appropriately, the reactive groups will remain stable in the aqueous dispersion. When the coating is applied to a substrate and allowed to dry, particles containing the two reactive groups come into contact. As polymer diffusion takes place in the binder film, these groups are brought together and react. In this way one obtains the advantages of a two-pack formulation premixed in a single container.[2]

An important goal for novel latex-based coatings is to be able to cure the films at ambient temperature. This requires very reactive crosslinking functional groups. One candidate for rapid crosslinking is the carbodiimide (-N=C=N-) group. Taylor and Bassett[3] have shown that carbodiimides react rapidly with carboxylic acid groups to form N-acyl ureas. Union Carbide has commercialized a water-dispersible polycarbodiimide as a crosslinking agent for carboxylated latex.[4]

In this paper, we consider a blend of two types of latex based upon poly(2-ethylhexyl methacrylate) (PEHMA), one containing -N=C=N- groups; and the other, -COOH groups. The former latex was prepared using either t-butylcarbodiimidoethyl methacrylate (t-BCEMA) or cyclohexylcarbodiimidoethyl methacrylate (CCEMA) as the functional comonomer. The latter was prepared using methacrylic acid (MAA) as the functional comonomer. Blends were prepared by mixing the two dispersions, after carefully adjusting the pH of the MAA-containing latex to 8 with aqueous ammonia. When this blend is drawn down on a substrate and allowed to dry, tough elastomeric films are formed which undergo crosslinking on a time period of days. Crosslinking occurs more rapidly if the films are annealed at 60 °C.

The system described above is unusual in that in the initial film, the reactive groups are located in different cells. Only at the boundary between the cells can the reaction between the -N=C=N- and -COOH groups occur. Polymer diffusion is necessary to bring the two reactive groups together. Thus reaction is coupled to diffusion. One also has to realize that the chemical reaction affects the rate of polymer diffusion. The first covalent bond formed converts a linear polymer into a branched polymer. Branched polymers diffuse much more slowly than linear polymers from which it was formed. Thus the branching reaction should

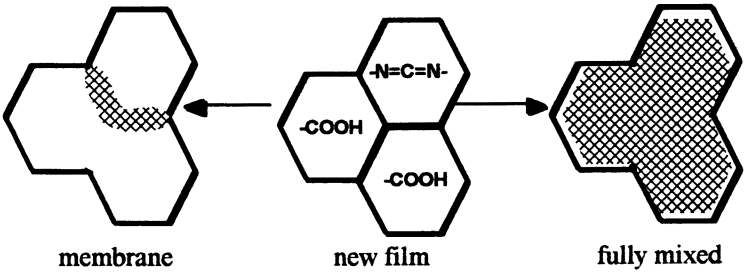

Downloaded by OHIO STATE UNIV LIBRARIES on September 17, 2012 | http://pubs.acs.org
Publication Date: July 26, 2001 | doi: 10.1021/bk-2001-0790.ch005

substantially slow the rate of polymer diffusion and reticulation should bring the diffusion rate to a stop. The properties of the system may be expected to depend sensitively on the relative rates of polymer diffusion and the chemical reaction.

We conceptualize this competition in the drawing above. In the initially formed latex film, some of the interfaces will be between two similar types of latex polymer. No reaction will occur at this interface. Other interfaces separate the -N=C=N- and -COOH groups. If the chemical reaction is much faster than the rate of polymer diffusion, a crosslinked membrane will form at this interface. One imagines that this membrane will suppress further diffusion of polymer molecules across the membrane. On the other hand, if the polymer diffusion step is much more rapid, complete intermixing of the two polymers will occur before a substantial amount of reaction takes place. One expects, under these circumstances to obtain the same type of uniformly crosslinked polymer film that one would obtain from a solution of the two polymers.

Downloaded by OHIO STATE UNIV LIBRARIES on September 17, 2012 | http://pubs.acs.org
Publication Date: July 26, 2001 | doi: 10.1021/bk-2001-0790.ch005

Experimental

Latex Synthesis: All latex particles were prepared by seeded two-stage emulsion polymerization at 80 °C, with reactive and/or fluorescent monomers being introduced only in the second stage under monomer-starved conditions. In all of the particles, the seed represents approximately 8 wt % of the total polymer. Full details are reported elsewhere. [5,6] PBMA seed particles were used to prepare carbodiimide-containing PBMA latex particles, and PEHMA seed particles were used to prepared carbodiimide- and methacrylic acid (MAA)-containing PEHMA latex particles. For labeled particles, we prepared only PEHMA latex. The carbodiimide-containing latex were labeled with anthracene (An), whereas the MAA-containing particles were labeled with phenanthrene (Phe). Each recipe includes 1 wt % of chain transfer reagent (1-dodecyl mercaptan, DM). Typical recipes are given in Table 1.

Particle sizes were determined by dynamic light scattering at an angle of 90° and at 22 °C, employing a Brookhaven BI-90 Particle Sizer. Molecular weights and molecular weight distribution were measured by gel permeation chromatography (GPC) at 30 °C, using an instrument equipped with two Styragel® columns (HR 3 and 4), and tandem refractive index and fluorescence detectors. Linear poly(methyl methacrylate) standards were used to calibrate the columns.

Film preparation. Studies of -N=C=N- group stability during emulsion polymerization, storage of the dispersion, and film formation used unlabeled latex.[5,6] We used labeled latex for the investigation of polymer miscibility, [5,7] polymer diffusion and the disappearance of -N=C=N- groups during the crosslinking reaction.[5,8] Films were prepared on CaF_2 disks for Fourier transform infrared (FTIR) measurements and on quartz plates for energy transfer (ET) measurements. Latex films were prepared by casting an aliquot of the latex dispersion onto the substrate and allowing the water to evaporate. In films formed from blends that included an MAA-containing latex, the dispersion was first neutralized to pH 8 with aqueous ammonia before mixing the dispersion with its partner. This step is essential for preventing reaction of -N=C=N- groups in its blends with MAA-containing latex.

Table 1. Typical recipes to prepare labeled latex particles.

reactants	*PEHMA-D*	*D-MAA-11*	*A-tBCEMA-5*	*A-CCEMA-4.6*
seed [a] (g)	60.0	120.0	60.0	60.0
EHMA (g)	35.0	66.5	33.1	33.1
MAA (g)	--	3.50	--	--
t-BCEMA (g)	--	--	1.92	--
CCEMA (g)	--	--	--	1.92
PheMMA (g)	0.49	0.77	--	--
AnMA (g)	--	--	0.47	0.47
DM [b] (g)	0.32	0.61	0.32	0.32
KPS (g)	0.06	0.12	0.07	0.07
SDS [c] (g)	0.70	1.29	0.70	0.70
$NaHCO_3$ (g)	--	--	0.31	0.31
H_2O (g)	27.0	55.0	27.1	27.1
temperature (°C)	80	80	80	80

[a] PEHMA dispersion, 5 wt % solids; [b] 1-dodecyl mercaptan; [c] sodium dodecyl sulfate

Downloaded by OHIO STATE UNIV LIBRARIES on September 17, 2012 | http://pubs.acs.org
Publication Date: July 26, 2001 | doi: 10.1021/bk-2001-0790.ch005

Latex films were often prepared by casting a latex dispersion onto a substrate and then allowing the water to evaporate at 22 °C at high humidity over 5 – 7 h. To minimize the extent of polymer diffusion during film formation, some films were prepared in a cold room at 4 °C. Drying took 2 - 3 days. These films were kept cold and transferred to the sample chamber of the fluorescence decay apparatus, also cooled to 4 °C. For subsequent measurements, they were then heated to the annealing temperature. Solvent-cast films were prepared by taking freeze-dried samples of the same mixture of Phe- and An-labeled latex dispersions, dissolving the in tetrahydrofuran (THF), and then rapidly casting an aliquot of the solution onto the substrate. Here drying took only a few minutes at 22 °C.

Energy transfer (ET) experiments. Quartz plates containing polymer films were annealed for various amounts of time in a pre-heated oven. They were then removed, cooled to room temperature for donor fluorescence decay measurements, and then returned to the oven for further annealing. Donor decay measurements were carried out using the single photon timing technique,[9] with λ_{ex} = 300 nm, and the emission measured through an interference filter at 350 ± 5 nm.

To characterize the extent of miscibility of PEHMA copolymers, we employ the quantum efficiency of energy transfer, Φ_{ET}, which is defined as [10]

$$\Phi_{ET}(t_n) = 1 - \frac{\int_0^\infty I_{DA}(t_n,t)dt}{\int_0^\infty I_D(t_n,t)dt} = 1 - \frac{area_{DA}(t_n)}{area_D} \qquad (1)$$

where $area_{DA}(t_n)$ is the area under the normalized decay curves of donor fluorescence in the presence of acceptor after an annealing time t_n, and $area_D$ is the area under the

Downloaded by OHIO STATE UNIV LIBRARIES on September 17, 2012 | http://pubs.acs.org
Publication Date: July 26, 2001 | doi: 10.1021/bk-2001-0790.ch005

normalized decay curves of the donor fluorescence in the absence of acceptor. Since Phe is quite stable under examined conditions, the area$_D$ is not a function of t_n.

To obtain the area under a donor fluorescence decay curve, we fit each decay curve to the empirical equation (2) and then evaluate the integral from the magnitude of the fitting parameters.

$$I_{DA}(t) = A_1 \exp\left[\left(-\frac{t}{\tau_D}\right) + \beta\left(-\frac{t}{\tau_D}\right)^{1/2}\right] + A_2 \exp\left(-\frac{t}{\tau_D}\right) \qquad (2)$$

We characterize the diffusion process in terms of the fraction of mixing f_m, which represents the fractional growth in energy transfer efficiency due to polymer diffusion.

$$f_m = \frac{\Phi_{ET}(t_n) - \Phi_{ET}(t_0)}{\Phi_{ET}(t_\infty) - \Phi_{ET}(t_0)} = \frac{area_{DA}(t_0) - area_{DA}(t_n)}{area_{DA}(t_0) - area_{DA}(t_\infty)} \qquad (3)$$

where $[\Phi_{ET}(t_n) - \Phi_{ET}(t_0)]$ is the change in energy transfer efficiency of the freshly prepared film and of the same film annealed for a time (t_n). $[\Phi_{ET}(t_\infty) - \Phi_{ET}(t_0)]$ is the difference in energy transfer efficiency between the fully mixed film and the newly formed film. Area$_{DA}(t_0)$ is the area under the fluorescence decay curve of a newly formed film. Since the dispersions take several hours to dry, we define t_0 as 1 h after the "wet spot" visible in the center of the film disappeared. Area$_{DA}(t_n)$ represents the corresponding quantity determined from the same film annealed for a time t_n. Area$_{DA}(t_\infty)$ represents the area under the decay curve of a fully mixed film. For PEHMA itself, the area$_{DA}(t_\infty)$ was obtained from a newly formed solvent-cast film. Upon further annealing of the film, the area under the decay curve did not change.

For films containing MAA- and carbodiimide-functionalized copolymers, the area$_{DA}(t_\infty)$ was obtained also from solvent-cast films, but these films needed to be annealed for sufficiently long times until the area of these films reached its limiting value, similar to that of the PEHMA film itself. This point is discussed in more detail below.

Fourier Transform infrared (FTIR) experiments. The -N=C=N- content of carbodiimide-containing latex dispersions and films, [5,6] and the reaction between the carboxylic acid and carbodiimide groups,[5,8] were monitored by FTIR. To determine the carbodiimide content of a carbodiimide-containing latex dispersion, a portion of the dispersion was freeze-dried, dissolved in $CHCl_3$ solvent and then transferred to a 1 mm NaCl cell. Latex and solvent-cast films were examined on CaF_2 disks. Each disk was mounted on an FTIR holder. The disk plus holder were placed in a temperature-controlled oven, and annealed for various amounts of time. They were removed periodically, cooled to room temperature for FTIR measurements, and then returned to the oven. All FTIR measurements were carried out with a Perkin Elmer FTIR Spectrum 1000 Spectrometer with a resolution of 4.0 cm^{-1}.

To follow the crosslinking reaction, we compare the intensity of the -N=C=N- band [11] at 2125 - 2130 cm^{-1} to the band at 1380 cm^{-1} from the polymer. In equation

(4), $\left(I_{-N=C=N-}/I_{1380}\right)_{t_0}$ and $\left(I_{-N=C=N-}/I_{1380}\right)_{t_n}$ are the intensity ratios of a nascent film (t_0) and of the same film annealed for time t_n.

$$\text{-N=C=N- remaining (\%)} = \left(1-\frac{\left(I_{-N=C=N-}/I_{1380}\right)_{t_n}}{\left(I_{-N=C=N-}/I_{1380}\right)_{t_0}}\right)\times 100 \qquad (4)$$

Results and Discussion

In the sections below, we will examine film formation, polymer diffusion, and crosslinking reactions in latex films prepared from a blend of carbodiimide- and carboxylic acid-containing latex particles. The formation of uniformly crosslinked polymer films requires that the polymer diffusion rate be greater than the rate of reaction between the -COOH groups and the -N=C=N- groups. If the diffusion rate is slower than the reaction rate, crosslinking will occur in a boundary region between cells in the film containing the reactive pairs. A more subtle issue is the miscibility of the two different functional polymers. Incorporation of a polar monomer like -COOH into PEHMA may affect the magnitude of the Flory Huggins χ-parameter between the two copolymers and limit their miscibility.

To study miscibility and polymer diffusion in latex films, we label one set of particles with a fluorescent dye (phenanthrene, Phe) which can act as a donor in a non-radiative energy transfer (ET) experiment. The other latex is labeled with an acceptor dye (anthracene, An). This type of experiment for the study of polymer blends was pioneered by Herbert Morawetz and his students.[12,13] Our approach differs only in that we use fluorescence decay measurements of the donor decay profiles ($I_{DA}(t)$) instead of measurements of the steady-state donor and acceptor intensities to determine the extent of ET in a polymer. The information obtained from ($I_{DA}(t)$) is in principle identical to that obtained from steady-state measurements, but is subject to fewer artifacts.

To be useful in coatings applications, carbodiimide-containing latex must satisfy four important requirements. First, the -N=C=N-containing monomer must be incorporated in high yield into the latex during emulsion polymerization. Second, it must survive extended storage. Third, it must not hydrolyze under typical conditions of film formation. Finally, it must react to form crosslinks in blend films in which the second component contains -COOH groups. We first consider the stability of the -N=C=N- group to hydrolysis.

Stability of -N=C=N- functionality. Carbodiimide groups are very sensitive to acid. [14] When -N=C=N-containing monomers are copolymerized with BMA or EHMA in unbuffered reaction media, all of the -N=C=N- groups are hydrolyzed during the reaction.[5,6] The hydrolysis reaction is strongly suppressed in the presence of excess $NaHCO_3$ buffer. [5,6] Under these circumstances, three other factors become important. These are the hydrophobicity of the base polymer (EHMA vs. BMA), the steric bulk of the substituent on the -N=C=N- moiety (t-BCEMA vs. CCEMA), and the temperature of the reaction. Examples are given in Table 2.

Downloaded by OHIO STATE UNIV LIBRARIES on September 17, 2012 | http://pubs.acs.org
Publication Date: July 26, 2001 | doi: 10.1021/bk-2001-0790.ch005

For reactions carried out at pH 8, incorporation of carbodiimide groups is favored by the more hydrophobic latex polymer. For example, the cyclohexylcarbodiimide group undergoes about 32% hydrolysis when copolymerized at 80 °C with BMA but only 14% hydrolysis when EHMA is the base monomer. Even greater protection against hydrolysis is provided by the t-butyl substituent. Here we obtain 91% survival of the -N=C=N- groups in the reaction with BMA and 92% survival with EHMA. If the reaction temperature is lowered to 60 °C, the incorporation of carbodiimide into the latex is virtually quantitative.

The same factors affect the pot life of the dispersions stored at room temperature. For the PEHMA latex containing the t-butylcarbodiimide, nearly 90% of the -N=C=N- groups survive storage for one year at 23 °C. [5,6]

Characterization of labeled PEHMA latex. All the latex particles, labeled and unlabeled, were prepared using common seed particles and almost identical reaction conditions. As a consequence, they have almost identical characteristics. These characteristics include particle size and size distributions, solids content, and polymer molecular weight and molecular weight distributions. In Table 3 we summarize the characteristics of the labeled latex. The abbreviated names for each functional latex in Table 3 contains information about the dye, the nature of the functional comonomer and its mol % in the polymer. Thus D-MAA-11 refers to a donor (Phe)-labeled PEHMA latex containing 11 mol % MAA. PEHMA-D and PEHMA-A refer to the labeled latex containing only PEHMA and no reactive monomer.

Miscibility of PEHMA copolymers. The quantum efficiency of energy transfer, Φ_{ET}, is a useful parameter to characterize the extent of interdiffusion in latex films. In this section we show that Φ_{ET} measurements on solvent-cast films provides a very important measure of miscibility for PEHMA copolymers.

We prepare films from 1:1 mixtures of Phe- and An-labeled latex. When these dispersions are spread on a substrate and water is allowed to evaporate, continuous transparent films are formed. In the newly formed film, before any interparticle diffusion has occurred, the Phe- and An-labeled polymers should be still confined within their own cells. Φ_{ET} is small because only cross-boundary energy transfer can occur. If the sample is then allowed to stand at room temperature, or heated to increase the polymer diffusion rate, polymers will diffuse from one cell to the adjacent cells, bringing the Phe and An groups into proximity. Φ_{ET} increases and evolves to its maximum value. If the polymers in adjacent cells are fully miscible, this maximum value should correspond to that obtained from films prepared from a solution of the same polymer blend in an organic solvent. In a solvent like THF, the Phe- and An-labeled polymers are homogeneously mixed because THF is a good solvent for the PEHMA copolymers. For homopolymers that differ only in their fluorescent label, the two types of polymers are miscible in the bulk state. The homogeneous mixture in the solution will carry forward into the films when the solvent is evaporated. For solvent-cast films of other pairs of miscible polymers with the same extent of labeling, the same maximum Φ_{ET} value should be obtained, and the magnitude of Φ_{ET} should not change when the film is annealed.

Downloaded by OHIO STATE UNIV LIBRARIES on September 17, 2012 | http://pubs.acs.org
Publication Date: July 26, 2001 | doi: 10.1021/bk-2001-0790.ch005

Downloaded by OHIO STATE UNIV LIBRARIES on September 17, 2012 | http://pubs.acs.org
Publication Date: July 26, 2001 | doi: 10.1021/bk-2001-0790.ch005

Table 2. The percentage of carbodiimide remaining under various polymerization conditions

latex	*pH of dispersion*	*T (°C)*	*feed rate (mL/min)*	*-N=C=N- survival (%)*[a]
P(BMA-co-CCEMA)	3-5	80	0.062	0
P(BMA-co-CCEMA)	8	80	0.062	68
P(BMA-co-tBCEMA)	8	80	0.062	91
P(EHMA-co-CCEMA)	8	80	0.062	86
P(EHMA-co-tBCEMA)	8	80	0.062	92
P(EHMA-co-tBCEMA)	8	60	0.056	98

[a] Determined by FTIR in $CHCl_3$ solution, assuming that the extinction coefficient is the same for the monomer as it is for the polymer [t-BCEMA, $\varepsilon_{-N=C=N-}$ = 1342 L mol^{-1} cm^{-1}; CCEMA, $\varepsilon_{-N=C=N-}$ = 2134 L mol^{-1} cm^{-1}].[5,6]

Table 3. Characteristics of the labeled latex polymers.

	particle diameter (nm)	*solids content (%)*	M_w, M_w/M_n	*pH*	*-N=C=N- content (%)*
PEHMA-D[a]	98	30.9	39 000, 2.44	5	--
PEHMA-A[b]	97	31.1	56 000, 2.07	5	--
D-MAA-11[c]	101	31.2	41 000, 1.95	5	--
D-MAA-20[d]	113	31.0	50 500, 2.35	5	--
A-tBCEMA-5[e]	106	31.9	63 000, 3.15	8	98
A-tBCEMA-11[f]	102	31.7	45 500, 2.39	8	98
A-CCEMA-4.6[g]	107	32.1	86 000, 2.05	8	80

[a] P(EHMA-co-PheMMA): 1 mol % PheMMA; [b] P(EHMA-co-AnMA): 1 mol % AnMA; [c] P(EHMA-co-PheMMA-co-MAA): 1 mol % PheMMA, 11 mol % MAA; [d] P(EHMA-co-PheMMA-co-MAA): 1 mol % PheMMA, 20 mol % MAA; [e] P(EHMA-co-AnMA-co-tBCEMA): 1 mol % AnMA, 5 mol % tBCEMA; [f] P(EHMA-co-AnMA-co-tBCEMA): 1 mol % AnMA, 11 mol % tBCEMA; [g] P(EHMA-co-AnMA-co-CCEMA): 1 mol % AnMA, 4.6 mol % CCEMA.

Immiscible polymer pairs should behave differently. In films prepared from latex blends, one expects Φ_{ET} to increase, accompanying some segment mixing across the interface between adjacent cells. The limiting value of Φ_{ET} should be significantly less than that for the fully mixed film. For films prepared by solvent casting, some polymer demixing will occur as the solvent evaporates. Some further segregation may occur as the solid film is annealed. In this case, Φ_{ET} will decrease from the initial value.

PEHMA-D + PEHMA-A. As the first example, we examine the miscibility of PEHMA itself (PEHMA-D + PEHMA-A) and then use this as the control experiment for films prepared from other copolymers. Aside from the label, these polymers are chemically identical. In a newly formed solvent-cast film prepared at 22 °C from a mixture of an equal amount of PEHMA-D and PEHMA-A dissolved in THF, we obtain $\Phi_{ET} = 0.52$. When the same film is annealed at 60 °C for various amounts of time, Φ_{ET} remains at 0.52 ± 0.01. This result indicates that when the Phe- and An-labeled PEHMA polymers are fully mixed in the freshly prepared film, and that no changes occur when the film is annealed for various amounts of time at 60 °C. For films freshly prepared at 4 °C from a dispersion containing the same mixture of labeled latex particles, we obtain $\Phi_{ET} = 0.06$. We believe that little polymer diffusion occurs at this temperature and that cross-boundary ET is the major contribution to this value. When the same film is annealed at 60 °C, Φ_{ET} increases to 0.38 over 2 min, and then to 0.49 over 12 min. This result indicates that diffusion leading to polymer mixing has occurred. The value of Φ_{ET} at 0.49 signifies that the mixing between PEHMA-D and PEHMA-A polymers is nearly complete and will reach completion if the film is annealed for a sufficiently long time. The Φ_{ET} values obtained from the dispersion-cast and THF-cast films at different times are plotted in Figure 1A. We take the value $\Phi_{ET} = 0.52$ as that for fully mixed films, and use this value as the reference to compare to that of other blends.

PEHMA-D + A-tBCEMA-5. Similar results (Figure 1B) are found for films prepared from a blend of PEHMA-D and A-tBCEMA-5 polymers. For the THF-cast film, Φ_{ET} remains at 0.52 for films with and without annealing. For the dispersion-cast film, $\Phi_{ET} = 0.04$ in the newly formed film, and evolves to a value of 0.52 when the same film is annealed.

D-MAA-11 and D-MAA-20 + PEHMA-A. In contrast to the results described above, blends of PEHMA with MAA-containing copolymers exhibit the behavior expected for a blend of polymers with limited miscibility. The first of two examples of this type of blend we consider consists of equal amounts of D-MAA-11 and PEHMA-A latex polymers. We prepared dispersion- and THF-cast films from a mixture of D-MAA-11 and PEHMA-A polymers, and annealed these films at 60 °C. The Φ_{ET} data obtained from these films are shown in Figure 1C. In the latex film formed at 4 °C, $\Phi_{ET} = 0.03$. When this film is annealed, the Φ_{ET} values increase to 0.21 over 10 min, and then slowly increase to 0.24 over 1 h. The increase in Φ_{ET} signifies that polymer mixing occurs. The limiting value is significantly less than 0.52, the value expected for complete mixing. We take this result to indicate that the two polymers have only limited miscibility.

Downloaded by OHIO STATE UNIV LIBRARIES on September 17, 2012 | http://pubs.acs.org
Publication Date: July 26, 2001 | doi: 10.1021/bk-2001-0790.ch005

Further evidence to support the limited miscibility of these latex polymers is obtained from the solvent-cast film. A freshly formed film prepared from a THF solution of the same blend exhibits Φ_{ET} = 0.40. This result indicates that the D-MAA-11 copolymer and PEHMA-A homopolymer demix during THF evaporation. When this film is annealed at 60 °C, Φ_{ET} decreases to 0.25 over 20 min, indicating that further demixing takes place, leading to increased separation of the Phe- and An-labeled polymers. At longer annealing time (e.g., 4 h), Φ_{ET} decreases to 0.23, a value similar to that obtained from the annealed latex film.

An increase in the amount of MAA from 11 to 20 mol % further reduces the limited miscibility of PEHMA (Figure 1D). In the freshly formed film prepared at 4 °C from D-MAA-20 + PEHMA-A latex dispersions, Φ_{ET} = 0.03. When this film is annealed at 60 °C, Φ_{ET} increases to 0.14 over 1 h, and then to a maximum value of only 0.16 over 7 h. When a film of the same mixture of polymers is freshly prepared from THF solution, we obtain Φ_{ET} = 0.23, smaller than that (0.40) obtained for the solvent-cast film prepared from D-MAA-11 + PEHMA-A. Here we infer that the polymers segregate substantially as the solvent evaporates. When this film is

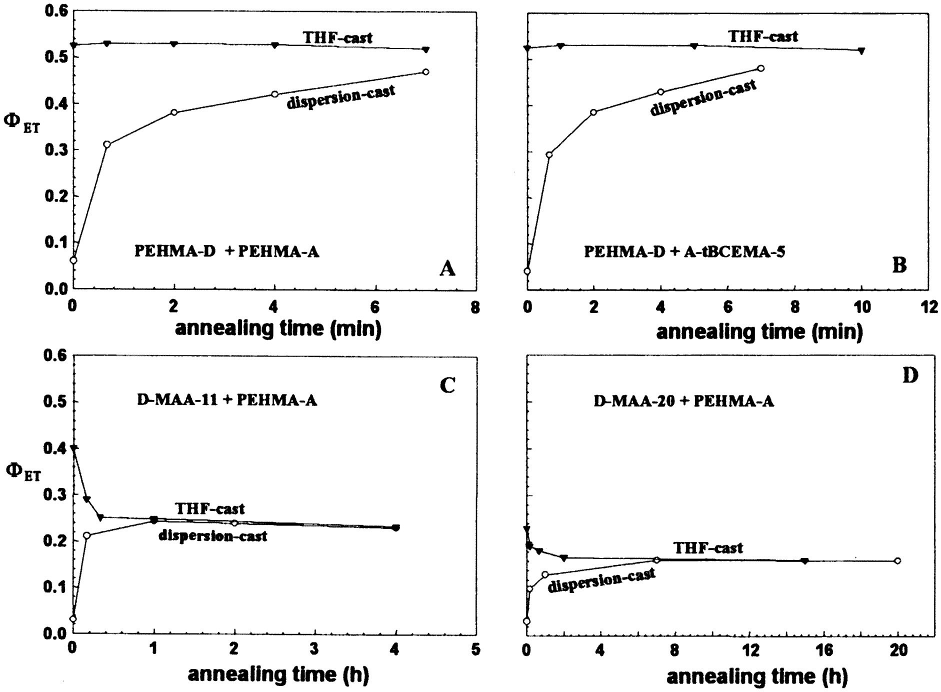

Figure 1. Plots of the Φ_{ET} vs. annealing time for four pairs of latex films. In each example, the upper curve refers to a film cast from a mixture of the two polymers dissolved in THF. The lower curve refers to a film prepared from a mixed dispersion of the two types of latex in water. All films were annealed at 60 °C.

Downloaded by OHIO STATE UNIV LIBRARIES on September 17, 2012 | http://pubs.acs.org
Publication Date: July 26, 2001 | doi: 10.1021/bk-2001-0790.ch005

annealed, Φ_{ET} decreases and approaches 0.16 over 15 h, a value close to that obtained from the annealed latex film.

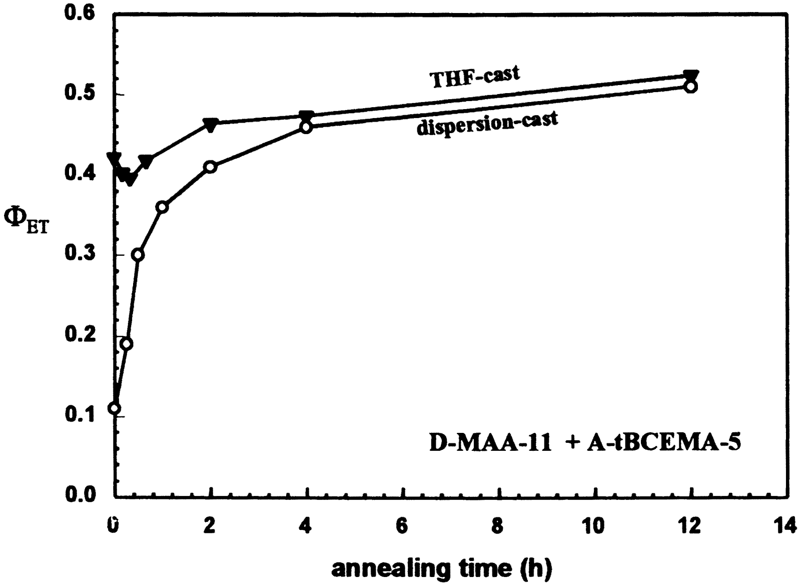

Figure 2. A plot of Φ_{ET} vs. annealing time at 60 °C for blends of D-MAA-11 + A-tBCEMA-5. The upper curve refers to a film cast from THF solution; the lower curve to a latex film formed at 22 °C.

D-MAA-11 + A-tBCEMA-5. The blend of D-MAA-11 + A-tBCEMA-5 constitutes a reactive system in which the two polymers contain functional groups that can react to produce a graft copolymer initially, and eventually a crosslinked network. The reaction is that of the carbodiimide group of the A-tBCEMA-5 with the carboxylic acid group of the D-MAA-11 to form an N-acyl urea.[3] The film contains an equal number of the two particles but a 2:1 ratio of -COOH to -N=C=N- groups. When we examine a film freshly prepared at room temperature from this latex blend, Φ_{ET} = 0.11. It is likely that both cross-boundary ET and local interdiffusion contribute to this value, since this film is formed at 22 °C, not 4 °C. When the film is annealed at 60 °C, Φ_{ET} increases to 0.36 over 1 h, and then to 0.52 over 12 h. The data are plotted in Figure 2. This is, for us, a very satisfying result, because it indicates that a fully mixed film is obtained. We note, however, that it takes hours for the polymers of this blend to mix completely, whereas for the polymers of the PEHMA-D/PEHMA-A blend (Figure 1A), full mixing occurs on the time scale of minutes.

In the D-MAA-11 + A-tBCEMA-5 blend examined here, polymer diffusion and the crosslinking reaction are coupled. The polymer chain length and the extent of branching increase as the reaction proceeds.

Downloaded by OHIO STATE UNIV LIBRARIES on September 17, 2012 | http://pubs.acs.org
Publication Date: July 26, 2001 | doi: 10.1021/bk-2001-0790.ch005

For comparison, we examine the Φ_{ET} vs. time curve obtained for the blend of these polymers from a THF-cast film. This curve is plotted as the filled triangles in Figure 2. This curve shows several interesting aspects. In the newly formed film, Φ_{ET} = 0.42, a value lower than 0.52. This result indicates that segregation of D-MAA-11 and A-tBCEMA-5 polymers has occurred as the THF evaporates. When this film is annealed at 60 °C, Φ_{ET} decreases to 0.40 over the first 20 min. Demixing of the polymers contributes to a decrease in Φ_{ET}. Upon longer annealing, Φ_{ET} begins to increase, an indication that polymer mixing occurs. We imagine that the reaction between -N=C=N- groups and -COOH groups produces *in situ* polymer compatibilizers [15] which enhance miscibility of the -COOH- and the -N=C=N-containing polymers. At long times, Φ_{ET} reaches 0.52, indicating that the polymers in the film are fully mixed, at least on the scale of the energy transfer distance R_o.

Polymer interdiffusion vs. crosslinking. The competition between polymer diffusion and the crosslinking reaction in the latex films prepared from PEHMA copolymers is a complex process. Polymer diffusion is necessary to bring the functional groups into close enough proximity for them to react. In return, the formation of branches and the increase in polymer molecular weight reduce the rate of further polymer diffusion. In addition, polymer miscibility, as seen above, changes as the reaction proceeds. The presence of -COOH groups in the PEHMA polymer limits the miscibility of these copolymers with PEHMA polymer containing -N=C=N- groups. This limited miscibility hinders polymer diffusion across the particle interfaces at early stages of the healing process. However, when the reaction between the -COOH and the -N=C=N- groups occurs, generating N-acylurea bonds, the branched polymers formed become compatibilizers, produced *in situ* by the chemical reaction. In a simple picture of this process, the domains containing the branched polymers (and even crosslinked polymers) provide regions for the mobile MAA-containing polymers and tBCEMA-containing polymers to mix. As a benchmark, we calculate f_m values for the (PEHMA-D + PEHMA-A) latex film (c.f., Figure 1A) and plot the data in Figure 3A. We see that f_m increases rapidly to 0.64 in 2 min and then to 0.9 over 7 min. Polymer interdiffusion for PEHMA itself is very rapid, and, for this sample, is nearly complete on time scale of a few minutes.

D-MAA-11 + A-tBCEMA-5 and A-CCEMA-4.6. A plot f_m (•) vs. time for a (D-MAA-11 and A-tBCEMA-5) latex films annealed at 60 °C is presented in Figure 3B. We see that f_m increases to 0.45 over 30 min, to 0.60 over 1 h, and then to 0.96 over 12 h. This is the same film shown in Figure 2, and confirms the conclusion reached previously that full mixing due to diffusion takes place, and is complete on the time scale of 12 h. In this system, where crosslinking competes with diffusion, the polymer interdiffusion occurs on a much longer time scale than in the film prepared from unreactive latex.

We next compare these results to the case where we replace tBCEMA with CCEMA as the reactive comonomer. One should note that the CCEMA and tBCEMA comonomers differ only in the substituent attached to the "other end" of the -N=C=N- group, the cyclohexyl group vs. the t-butyl group. One of the differences between the two comonomers is that the CCEMA group undergoes

Downloaded by OHIO STATE UNIV LIBRARIES on September 17, 2012 | http://pubs.acs.org
Publication Date: July 26, 2001 | doi: 10.1021/bk-2001-0790.ch005

Downloaded by OHIO STATE UNIV LIBRARIES on September 17, 2012 | http://pubs.acs.org
Publication Date: July 26, 2001 | doi: 10.1021/bk-2001-0790.ch005

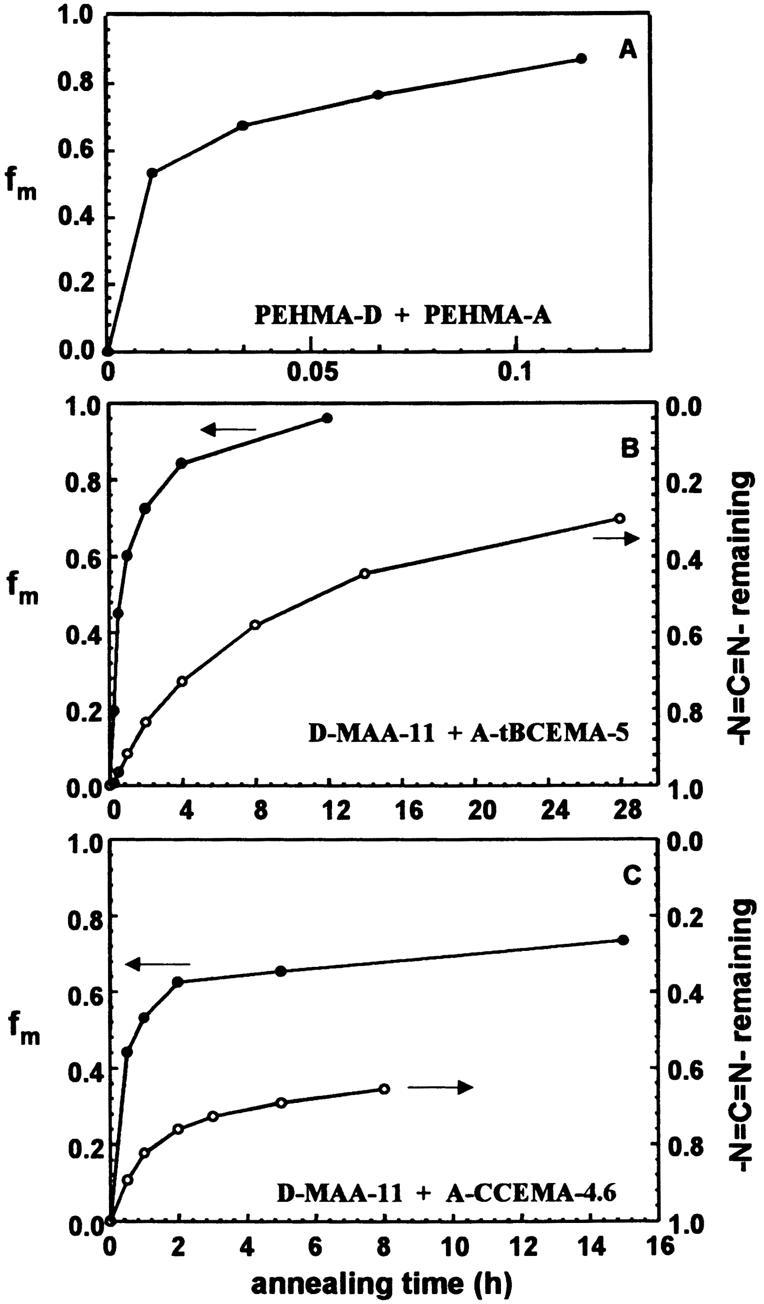

Figure 3. Plots of f_m and fraction of carbodiimide remaining vs. annealing time at 60 °C for three latex films. A refers to a PEHMA film with no reactive functionality. All of the polymers have similar molecular weights.

PEHMA homopolymer latex films. The polymers in both types of films have similar molecular weights. First, the glass transition temperature of the methacrylic acid copolymer (-3 °C) is slightly higher than that of PEHMA itself (-10 °C)[16]. Thus the annealing temperature of 60 °C corresponds to a slightly lower value of (T – Tg) for the carboxylic acid-containing films. Second, the two reactive polymers have only limited miscibility. The chemical reaction is necessary to induce full mixing between the two polymers. Third, the reaction leads initially to the formation of branched polymers. Because of their higher molecular weight and branched architecture, these polymers have a slower diffusion rate. [17,18] Finally, a significant fraction of the carbodiimide groups react during the drying process to form the films. In this process, a weakly crosslinked membrane may be formed between cells in the film. Polymer diffusion in the dry film may have to pass through this phase for mixing to occur.

Downloaded by OHIO STATE UNIV LIBRARIES on September 17, 2012 | http://pubs.acs.org
Publication Date: July 26, 2001 | doi: 10.1021/bk-2001-0790.ch005

Summary

We synthesized methacrylate copolymer latex particles containing carbodiimide groups. Hydrolysis of the carbodiimide function during emulsion polymerization is favored by lower reaction temperature (60 °C vs. 80 °C), steric hindrance of the other carbodiimide substituent (t-butyl vs. cyclohexyl), and the hydrophobic nature of the methacrylate base polymer poly(2-ethylhexyl methacrylate) vs. poly(butyl methacrylate).

Anthracene-labeled carbodiimide-containing PEHMA latex were mixed at pH 8 in a 1:1 ratio with phenanthrene-labeled methacrylic acid-containing PEHMA and cast into films. We employed energy transfer experiments to follow polymer diffusion rates in these films, and FTIR measurements to follow the rate of carbodiimide group reaction. Films were formed at room temperature and then annealed at 60 °C. While the rate of polymer diffusion at 60 °C is on the whole faster than the rate the chemical reaction between the -N=C=N- and -COOH groups, it is still substantially slower than the polymer diffusion rate in PEHMA latex films lacking the reactive groups. A number of factors affect the diffusion rate. The most important are the limited miscibility between the -COOH- and -N=C=N-containing polymer, and the formation of branched chains through reaction of the two copolymers. Some branched polymer is formed by reaction of the carbodiimide groups during film formation; and further reaction occurs as the films are annealed.

Acknowledgments

The authors thank NSERC Canada and ESTAC Canada for their support of this research.

References

[1] (a) Bufkin. B G., Grawe, J R *J. Coatings Technol.* **1978**, 50(641), 41-55; (b) Grawe, J R, Bufkin. B G. *J. Coatings Technol.* **1978**, 50(643), 67-83; (c) Bufkin. B G., Grawe, J. R.: *J. Coatings Technol.* **1978**, 50(644), 83-109; (d) Grawe, J R, Bufkin. B G. *J. Coatings Technol.* **1978**, 50(645), 70-100; (e) Bufkin. B G., Grawe, J R, *J. Coatings Technol.* **1978**, 50(647), 65-96.

[2] (a) Guerts, J. M., Ph.D. thesis, Eindhoven University, 1998. (b) Guerts, J. M., van Es, J. J. G. S., German, A. L. *Prog. Organic Coatings* **1996**, 29, 107-115.

[3] Taylor J. W.; Bassett D. R., *Technology of Waterborne Coatings* J. Edward Glass, Ed., ACS Symposium Series 666, American Chemical Society, Washington DC, 1997, 137.

[4] UCARLNK XL29SE, Union Carbide Corporation

[5] Pham, H. H. Ph.D. thesis, University of Toronto, Toronto, Canada, 1999.

[6] Pham, H. H. and Winnik, M. A. *J. Polym. Science Part A-Polymer Chemistry* **2000**, 38, 855.

[7] Pham, H. H.; Jose, P. S. Farinha J. P. S.; Winnik M. A., submitted to *Macromolecules.*

[8] Pham, H. H. and Winnik, M. A. *Macromolecules* **1999**, 32, 7692.

[9] O'Connor, D.; Phillips, D. *Time-Resolved Single-Photon Counting*; Academic Press, New York , 1984.

[10] Wang, Y.; Zhao, C.-L.; Winnik, M. A. *J. Chem. Phys.* **1991**, 95, 2143.

[11] Dolphin, D.; Wick, A. *Tabulation of Infrared Spectral Data A*; Wiley-Interscience Publication, 1977.

[12] (a) Morawetz, H. *Science* **1979**, 203, 405; (b) Morawetz, H. *Science* **1988**, 240, 172; (c) Morawetz, H. *J. Polym. Science Part A-Polymer Chemistry* **1999**, 37, 1725.

[13] Morawetz, H. and Amrani F. *Macromolecules* **1978**, 11, 281.

[14] Williams, A. and Ibrahim, T. I. *Chem. Rev.* **1981**, 81, 589.

[15] For a review of polymer compatibilizers, including those formed through *in situ* reactions, see Bonner, J. G. and Hope, P. S. In *Polymer Blends and Alloys: Compatibilisation and Reactive Blending*; Editor, Folkes M. J.; Hope P.S; Chapman & Hall, 1993, 46.

[16] Brandrup J. and Immergnt E. H. eds., "Polymer Handbook", 3rd eds., John Wiley & Sons, 1989.

[17] Doi, M. and Edwards, S. F. *The Theory of Polymer Dynamics*; Oxford University Press, New York, 1986.

[18] Kausch, H. H.; Tirrell, M. *Annu. Rev. Mater. Sci.* **1989**, 19, 341.

Downloaded by OHIO STATE UNIV LIBRARIES on September 17, 2012 | http://pubs.acs.org
Publication Date: July 26, 2001 | doi: 10.1021/bk-2001-0790.ch005

Downloaded by UNIV MASSACHUSETTS AMHERST on September 17, 2012 | http://pubs.acs.org
Publication Date: July 26, 2001 | doi: 10.1021/bk-2001-0790.ch006

Chapter 6

Dynamic Mechanical Analysis of Property Development during Film Formation

Loren W. Hill

Resins Division, Solutia Inc., 730 Worchester Street, Springfield, MA 01151

Dynamic mechanical analysis (DMA) reveals many details about the film forming process. For coatings films formed from thermoplastic binders, DMA can be used to determine the glass transition temperature, T_g. For films from thermosetting binders, DMA is used to follow molecular weight build up and crosslinking. Recent papers indicate that crosslink density can also be obtained for films formed by coalescence of waterborne latex systems in which one of the monomers contains two double bonds. When coalescence is not complete, the latex particle boundaries persist and in some cases are believed to form a continuous structure. In the US this particle boundary continuous phase material has been called "honeycomb structure" whereas in Europe the term "particle membranes" has been used. If the membrane or honeycomb material is continuous, it contributes more strongly to DMA response than expected from its content (i. e. weight percentage) in the film. Therefore, if the structure collapses from continuous to unconnected small domains, changes occur in the DMA response. Details of latex film structure are still emerging, and many different methods, including DMA, are making significant contributions to understanding.

DMA Methods and Definitions

In dynamic testing, an oscillating strain is applied and the resulting oscillating stress is measured, or conversely an oscillating stress is applied and the resulting oscillating strain is measured (*1-3*). Definitions and mathematical treatments do not depend on which of these modes of operation is used. Relationships between strain, stress and time are sketched in Figure 1 for tensile DMA with application of strain and measurement of stress. The maximum applied strain is ε_o. The maximum resulting stress is σ_o. The oscillation is carried out as a sine wave as shown in

In Film Formation in Coatings; Provder, T., et al.;
ACS Symposium Series; American Chemical Society: Washington, DC, 2001.

Figure 1. The sample is held under sufficient tension so that it remains taut (not slack) even when the oscillating strain is at a minimum.

The sine waves for strain and stress have the same frequency, but for viscoelastic samples the waves are out of phase by an amount, δ, called the phase lag. Theoretically and experimentally, δ is zero for an ideal (Hookean) elastic solid. If an ideal (Newtonian) liquid could be tested in this way, δ would be 90°. For viscoelastic materials, δ lies between 0 and 90°, and the value of δ is a rather direct indication of viscoelastic character (*1, 2*).

In many cure studies (*2-13*), films are fully cured on test panels and removed from the substrate before being analyzed as a free film in a DMA instrument. In this approach film formation takes place before analysis, and DMA serves to characterize the final film essentially after film formation. However, DMA has also been used to follow property development as it takes place during cure (*14-16*). With this approach an uncured sample is placed on a support (i.e. thin metal shim or metal spring) or impregnated into a supporting material (i.e. glass braid, cloth or paper support). The supported sample is then placed in an oven and dynamic properties are determined as a function of time as cure takes place.

Modulus Definitions with Tensile Deformation

Definitions of dynamic properties depend on the concept of resolving the stress wave of Figure 1 into two waves, one which is in phase with strain and one which is 90° out-of-phase with strain. The resolved plot that is in-phase represents elastic response, and the resolved plot that is 90° out-of-phase represents viscous response. In terms of modulus, the separated responses result in the following definitions:

$$\text{Tensile Storage Modulus} = E' = (\sigma_o \cos \delta)/\varepsilon_o \qquad (1)$$

$$\text{Tensile Loss Modulus} = E'' = (\sigma_o \sin \delta)/\varepsilon_o \qquad (2)$$

$$\text{Loss Tangent} = E''/E' = \text{Tan}\,\delta \qquad (3)$$

The term "storage" is associated with the elastic part of the response, E', because mechanical energy input to elastic materials is "stored" in the sense of being completely recoverable. The term "loss" is associated with the viscous part of the response, E", because mechanical energy input to ideal liquids is totally lost through viscous heating. The ratio E"/E' is viscous response expressed relative to elastic response. This ratio reduces to sin δ / cos δ which is Tan δ. Thus, the name "loss tangent" is appropriate.

Tensile deformation is convenient for fully cured films that need no support. Often free films of normal coating thickness (about 25 μm ≅ 1.0 mil) can be analyzed under oscillating tension. The maximum tensile strain during

Downloaded by UNIV MASSACHUSETTS AMHERST on September 17, 2012 | http://pubs.acs.org
Publication Date: July 26, 2001 | doi: 10.1021/bk-2001-0790.ch006

Downloaded by UNIV MASSACHUSETTS AMHERST on September 17, 2012 | http://pubs.acs.org
Publication Date: July 26, 2001 | doi: 10.1021/bk-2001-0790.ch006

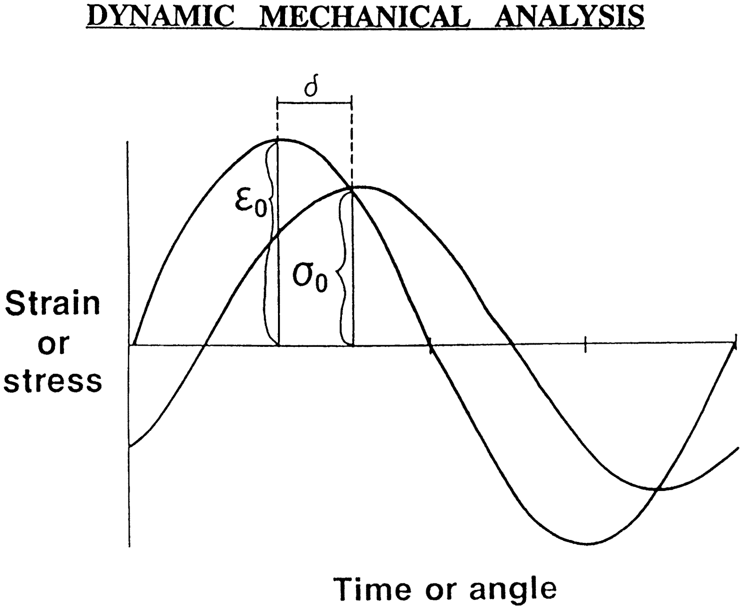
DYNAMIC MECHANICAL ANALYSIS
δ
ε0
σ0
Strain or stress
Time or angle

Figure 1. Sine wave plot of applied strain in DMA showing maximum strain, ε_0, and the plot for resulting stress showing maximum stress, σ_0. The lag in peak stress behind peak strain is called the phase lag, δ. (Reproduced from reference 4. Copyright 1987 Federation of Societies for Coating Technology.)

oscillation, ε_o, is kept very small, typically about 1 x 10^{-3} cm which corresponds to about 0.05 % strain. In this way the sample neither breaks nor yields, and properties can be obtained continuously on a single sample as temperature is scanned while oscillation frequency is held constant. Some DMA instruments are designed to permit taking data at several frequencies during a single temperature scan. Another mode of operation is to scan the oscillating frequency while temperature is held constant (*1- 3*).

Downloaded by UNIV MASSACHUSETTS AMHERST on September 17, 2012 | http://pubs.acs.org
Publication Date: July 26, 2001 | doi: 10.1021/bk-2001-0790.ch006

Modulus Definitions with Shear Deformation

If the film sample requires support, testing can be carried out in shear. Two circular parallel plates are often used. One plate is stationary with shear stress detectors attached. The other plate is moveable. It is rotated back and forth through a small angle to generate oscillatory shear strain. The sine wave forms of Figure 1 are still appropriate, but tensile strain (ε_o) would be replaced by shear strain (γ_o). The symbols used for dynamic properties obtained in shear tests are G' and G" as defined in equations (4), (5) and (6):

$$\text{Shear Storage Modulus} = G' = (\sigma_o \cos \delta)/\gamma_o \qquad (4)$$

$$\text{Shear Loss Modulus} = G'' = (\sigma_o \sin \delta)/\gamma_o \qquad (5)$$

$$\text{Loss Tangent} = G''/G' = \text{Tan}\ \delta \qquad (6)$$

In general, the relationship between E' and G' depends on Poisson's ratio, μ (*1*):

$$E' = 2G'(1+\mu) \qquad (7)$$

For materials that do not undergo change in volume when exposed to moderate tensile elongation, $\mu = 1/2$. Inserting this μ value into eq. (7) results in $E' = 3\,G'$.

Film Formation from Thermoset Formulations

Determination of Extent of Cure by DMA

DMA has been used extensively to determine the extent of cure of solvent borne thermoset industrial coatings. An example (*6*) is shown in Figure 2 for an unpigmented thermoset film prepared from a polyester polyol and an etherified melamine formaldehyde (MF) crosslinker. The formulation was applied using a drawdown bar with a 6 mil (150 μm) gap on a tinplated metal panel. The coated

Downloaded by UNIV MASSACHUSETTS AMHERST on September 17, 2012 | http://pubs.acs.org
Publication Date: July 26, 2001 | doi: 10.1021/bk-2001-0790.ch006

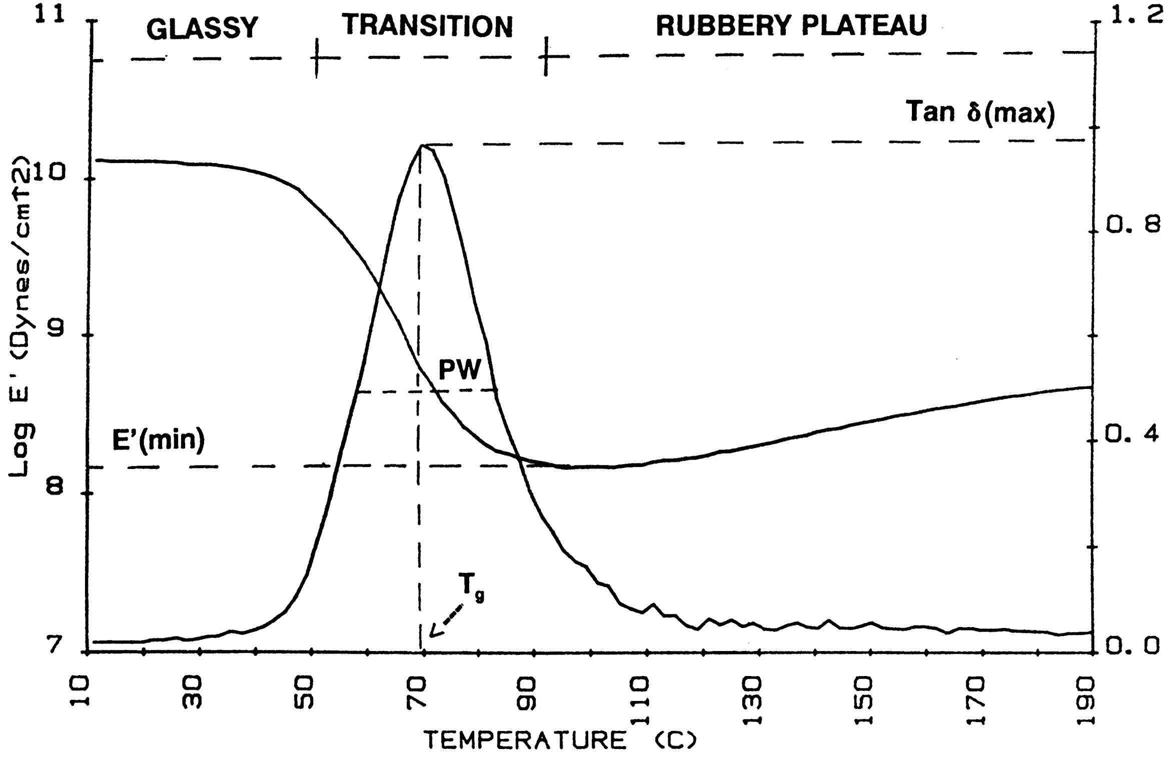

Figure 2. DMA plots of storage modulus, E', and loss tangent (Tan Delta) versus temperature for an unpigmented, highly crosslinked coating. (Reproduced from reference 6. Copyright 1997 Division of Polymeric Materials Science and Engineering, American Chemical Society.)

panel was cured in a electrically heated convection oven for 30 minutes at 220 °F (104.4 °C). Dry film thickness was 1.4 mil (35 μm). The film was easily removed following amalgamation of the tinplating on the substrate (*2*). A 0.4 x 3.5 cm strip of free film was mounted in the grips of an Autovibron™ instrument (Imass Inc,), and tensile DMA was carried out at an oscillating frequency of 11 cycles/second. The temperature scan rate was 2 °C/minute, and the computer controlled data acquisition system took data points at one minute intervals.

The full range of polymer network properties is exhibited in Figure 2: glassy behavior on the left, transition behavior in the center and rubbery plateau behavior at the right. The storage modulus, E', is about the same for all amorphous, unpigmented network polymers in the glassy region (approximately 2 to 4 x 10^{10} dynes/cm^2). E' drops sharply in the transition region. For uncrosslinked, high molecular weight polymers, E' drops by more than three orders of magnitude. Crosslinking reduces the magnitude of the drop in E'. In Figure 2, the value of E'(min) is 1.47 x 10^8 dynes/cm^2. Cure studies of model coating formulations have shown that E'(min) is proportional to crosslink density (*2-6*). Therefore, the value of E'(min) increases as extent of cure increases, and E'(min) can be used as a measure of the extent of cure. In Figure 2, various measures of the extent of cure are indicated by dashed lines.

At higher temperatures in the rubbery plateau, E' rises for two reasons. A small increase in E' is expected due to the effect of temperature on the rate of segmental motion. Rubber retractive forces increase with increasing rate of segmental motion (*2*). A larger increase in E' is expected due to additional curing during the temperature scan. With a scan rate of 2°/ minute, the sample represented in Figure 2 experiences temperatures that are higher than the original cure temperature for more than 40 minutes in the rubbery plateau region. Often E'(min) indicates original crosslink density, and E' values at higher scan temperatures indicate crosslink density as modified by additional curing that takes place during the temperature scan.

The Tan δ plot shows a strong maximum in the transition region. The peak height, referred to as Tan δ (max), is also a sensitive measure of extent of cure. Tan δ (max) decreases as extent of cure increases because cure causes a decrease in liquid-like character of the sample. The point on the temperature axis where Tan δ reaches a maximum is often taken as the glass transition temperature, T_g as indicated in Figure 2. As extent of cure increases T_g also increases. The peak width at half height (PW in Figure 2) is an indication of network uniformity. PW is also useful as an indication of property change during the scan. If additional cure takes place before the minimum in E' is reached, the Tan δ peak is not symmetrical and PW increases accordingly.

The measures of extent of cure identified in Figure 2 have been used to characterize cure of acrylic and polyester polyols with several types of crosslinkers such as MF resins (*2-6*), isocyanates (*7*) and blocked isocyanates (*8, 9*). DMA has also been used extensively for epoxy systems to test models for the curing process

Downloaded by UNIV MASSACHUSETTS AMHERST on September 17, 2012 | http://pubs.acs.org
Publication Date: July 26, 2001 | doi: 10.1021/bk-2001-0790.ch006

(*10, 11*) and to determine the effects of rubber (*12*) or thermoplastic modifier (*13)* on mechanical properties.

Following Property Development During Cure

Details of cure behavior are revealed by determination of changes in dynamic properties in real time as cure takes place. Provder (*14*) analyzed thermoset formulations of electrodeposition binders and blocked isocyanate formulations using woven fiberglass braids to support the starting formulations. Relative shear storage modulus was determined as samples were heated at a rate of 5 °C/min. The initial G' signal reflects the properties of the support material because liquids have negligible modulus. When the cure reaction has proceeded far enough to first form a three dimensional network structure (i.e. the gel point), G' begins to rise rapidly reflecting increasing solid-like characteristics. For the binder types described (*14*), rather high cure temperatures are used, and glass formation (vitrification) does not interfere with continued conversion. For such systems, complete conversion of functional groups is possible. As complete conversion is approached the rise in modulus becomes slower, and eventually the G' plot becomes flat. Provder (*14*) describes how to extract kinetic data from the modulus versus temperature plot. After the first scan to high temperatures, the sample is completely cured. Subsequent plots of modulus versus temperature are similar in shape to the one shown in Figure 2. For supported samples, however, relative rather than absolute modulus values are usually given because contributions from the support are not easily subtracted out.

For thermoset systems that react rather rapidly at moderate cure temperatures, vitrification is often observed before functional group conversion is complete. Gillham (*15*) has analyzed the interplay between functional group conversion and vitrification for amine-cured bisphenol-A epoxy resins on time-temperature-transformation (TTT) cure diagrams. TTT diagrams provide insight for understanding isothermal cure in terms of different material states encountered. Data for constructing TTT diagrams is obtained by torsional braid analysis (TBA) in which the uncured liquid sample is impregnated on an inert multifilamented glass braid. An automated torsion pendulum is used to determine dynamic properties as isothermal cure proceeds. Two separate and distinct Tan δ peaks are observed with increasing cure time. The earlier peak gives "time to gel" and the later peak gives "time to vitrify." Isothermal cure is repeated at numerous cure temperatures, T_c, and time to gel and time to vitrify are determined for each T_c. Connection of gel time points and vitrification time points on the TTT diagram results in the lines of demarcation between different material states. For example, at short times the sample is a liquid. As time passes functional groups react, and eventually the sample gels. Now the material state of the sample is sol/gel rubber. Sol is the term used for material that has not yet reacted into the network. There is a lot of segmental mobility in the sol/gel rubber which facilitates continued functional group conversion. Continued reaction may eventually result in complete conversion, in

Downloaded by UNIV MASSACHUSETTS AMHERST on September 17, 2012 | http://pubs.acs.org
Publication Date: July 26, 2001 | doi: 10.1021/bk-2001-0790.ch006

which case the new material state is gel rubber. The sol is all gone. In some cases, however, continued conversion in the sol/gel rubber will not result in complete conversion because the sample will vitrify before the sol is gone. In this case, the new material state is sol/gel glass.

Gillham (*15*) has emphasized the importance of the glass transition temperature of thermoset polymers at complete conversion of functional groups, $T_{g\infty}$. If the T_c selected is below $T_{g\infty}$, the sample will vitrify before complete conversion. If the T_c selected is above $T_{g\infty}$, complete conversion is possible without vitrification. Examples of complete TTT cure diagrams are mainly published for epoxy resins cured with various types of amine functional crosslinkers, but the concepts are useful more generally for thermoset coatings. Most formulations that contain crosslinkers that require relatively high cure temperatures such as MF resins and blocked isocyanates will conform to the condition, $T_c > T_{g\infty}$. For these, complete conversion is possible given sufficient cure time. For more reactive crosslinkers that have the capability to cure at lower temperatures, it is quite likely that cure temperatures will be selected so that $T_c < T_{g\infty}$. For these, the ultimate fate of unconverted functional groups should be considered. Values of T_g have been observed to rise above T_c by about 50 °C in some cases, and this finding has been quoted as evidence for continued reaction (but at a at a very slow rate) in the glassy state (*15, 16*). Cure diagrams for non-isothermal heating and the realtionship between T_g and functional group conversion have also been presented (*16*).

Film Formation from Waterborne Systems

There are several types of waterborne coating systems, and each type has important issues to consider for optimizing the film formation. DMA has been used for understanding film formation more fully for some waterborne systems. A desired result of this review is increased use of DMA for understanding film formation. As expected, DMA results have been most revealing when combined in a creative way with other characterization methods such as advanced microscopic methods, particle scattering methods, numerous types of spectroscopy and other instrumental methods for chemical analysis.

DMA of Films From Water Reducible Binders

Polyester or acrylic polyols that have served well as binders for thermoset solvent borne industrial coatings have been modified for use in water. Carboxylic acid groups are incorporated in the polymer structure a moderate levels to increase miscibility with water. Neutralization of the carboxylic acid groups with low molecular weight amines increases miscibility further. Hill et al (*17, 18*) used DMA to compare cure response of solvent borne and waterborne formulations of the same binder with MF resins as crosslinker. DMA plots for waterborne films of this type

Downloaded by UNIV MASSACHUSETTS AMHERST on September 17, 2012 | http://pubs.acs.org
Publication Date: July 26, 2001 | doi: 10.1021/bk-2001-0790.ch006

are very similar to those of solvent borne films. The measures of extent of cure defined in Figure 2 could be used without modification to describe cure response of films from water reducible binders.

The effects on cure response of variation in structures of amine neutralizers has been determined. Crosslink density determinations by DMA have shown that amino alcohols containing primary amine groups function as auxiliary crosslinkers whereas amino alcohols with tertiary amine groups do not (*17*). Primary amines have also been shown to react with formaldehyde evolved from MF resins during cure (*18*).

Downloaded by UNIV MASSACHUSETTS AMHERST on September 17, 2012 | http://pubs.acs.org
Publication Date: July 26, 2001 | doi: 10.1021/bk-2001-0790.ch006

DMA of Films from Aqueous Polyurethane Dispersions

Several different types of polyurethane polymers have been dispersed in water for use as coating binders. All of these could be included under the term aqueous polyurethane dispersions (PUDs), but the discussion below pertains to PUDs of the type described by Satguru et al (*19*). These PUDs are prepared by the prepolymer mixing process in several steps:

(1) Prepare an isocyanate terminated oligomeric prepolymer that contains carboxylic acid groups from dimethylolpropionic acid (DMPA),
(2) Neutralize the acid groups with a tertiary amine,
(3) Add water with agitation to form a dispersion and simultaneously add smaller amounts of hydrazine (H_2NNH_2) for chain extension.

Films cast from PUDs prepared in this way have been characterized by DMA (*19*). Tan delta plots showed only one very broad peak with a low value of Tan δ (max). The authors concluded that DMA was not able to detect phase separation. However, no determination of peak width (PW) was reported. The approximate value of PW from the published plot (*19*) is 83 °C. This very large value is indicative of heterogeneity. For comparison, the value of PW for the more homogeneous film of Figure 2 is 25 °C. Heterogeneous systems will not exhibit two Tan delta peaks if the domain boundaries are very diffuse. Small angle X-ray scattering (SAXS) results indicated phase separation (*19*). PUD films had very low minimum film forming temperature (MFFT), but good hardness after water loss. Low MFFT was attributed to plasicization of PUD particles by absorbed water before and during the initial stages of film formation. Hardness was attributed to loss of water late in the film forming process and to the presence of hard domains.

Films were prepared by drawdown from commercial PUD's in our laboratory and were cured 30 minutes at 100 °C. DMA on the Autovibron at 11 cycles per second with a scan rate of 2 °C resulted in the plots shown in Figure 3. The value of E' at the beginning of the scan (-40 °C) is already below that of a glassy polymer indicating that part of the sample has very low T_g. The drop in E' with increasing temperature is very gradual indicating a heterogeneous structure in which different domains are undergoing transition at different temperatures. The gradual E' drop in Figure 3 differs greatly from the sharp E' drop in Figure 2. In this case, the Tan δ

Downloaded by UNIV MASSACHUSETTS AMHERST on September 17, 2012 | http://pubs.acs.org
Publication Date: July 26, 2001 | doi: 10.1021/bk-2001-0790.ch006

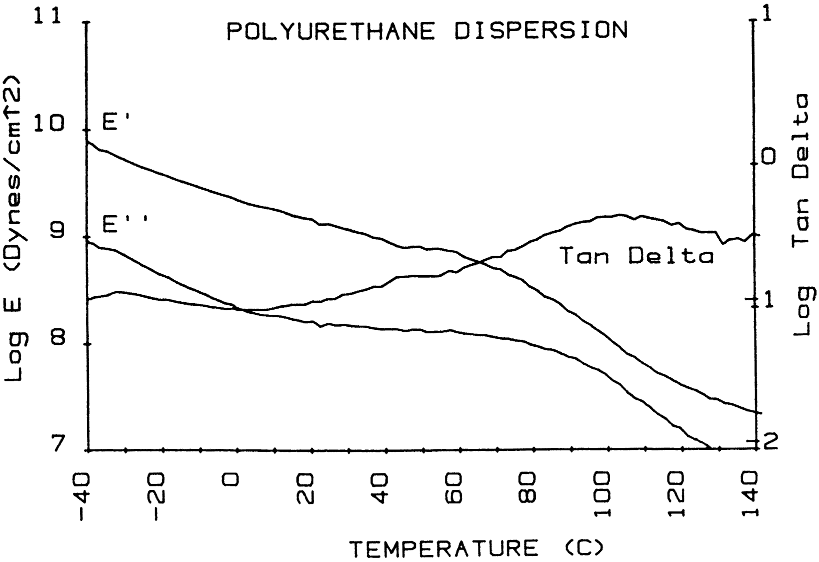

Figure 3. DMA plots of storage modulus, E', loss modulus, E", and loss tangent, (Tan Delta) versus temperature for an unpigmented coating prepared from an aqueous polyurethane dispersion.

plot has two peaks, but the low temperature peak at 25 °C is just barely detectable. The higher temperature peak occurs at about 105 °C. The sample is again revealed to be very heterogeneous with part of the sample having a very low T_g and part having a high T_g. It appears that the heterogeneous nature of films from PUD's is not widely recognized in the coatings field.

PUD films are not at all like polyurethane coating films prepared from polyols and isocyanates. Thermoset polyol/isocyanate coating films exhibit one narrow glass transition (*7*) indicating a homogeneous structure. Some coating chemists appear to believe that polyurethane coating films have separate domains of hard and soft segments, but this segmented polyurethane structure is characteristic of polyurethane elastomers (*20*), not coatings. In elastomers the weight percentage of the soft polyol portion (compared to the isocyanate portion) is much higher than for coatings. The higher polyol content, lower T_g of the polyol and lower crosslink density all favor phase separation of a soft domain in polyurethane elastomers.

PUD films are also not very similar to polyurethane elastomers. Tan δ plots and E' plots for polyurethane elastomers show two distinct transitions (*20*) in contrast to the very broad features of Figure 3 for PUD films. The difference is believed to result from the sharp domain boundaries in elastomers versus very diffuse domain boundaries for PUD films.

Downloaded by UNIV MASSACHUSETTS AMHERST on September 17, 2012 | http://pubs.acs.org
Publication Date: July 26, 2001 | doi: 10.1021/bk-2001-0790.ch006

DMA Study of Film Formation from Waterborne Latices

In concept the formation of uncrosslinked films by coalescence of latex particles is simple, but in practice the process can be quite complicated due to highly developed core/shell or multi-lob particle structure. Usually DMA is used along with other characterization methods to help prove that designed variations in composition or structure are having the desired effects on film formation and on the final properties of films.

Hard/Soft Latex Blends

Eckersley and Helmer (*21*) describe blends of hard latex and soft latex with control of particle size as well. Latices are identified by a two-letter code with the first letter indicating soft (S) or hard (H) and the second letter indicating particle size, large (L) or small (S). Numbers following the two-letter codes indicate weight percentage in the blend. One of the more favorable blends was SL70/HS30 (Soft, Large, 70 wt. % / Hard, Small, 30 wt. %). Both latices were prepared from styrene, butyl acrylate and methacrylic acid, but at different ratios. The soft latex was designed to have a low minimum film forming temperature (MFFT); St/BA/MA = 37/61/2, T_g = 9 °C, MFFT = 1 +/- 1 °C. Particles of the hard latex are not expected to coalesce, and styrene content is much higher; St/BA/MA = 70/28/2, T_g = 62 °C. The latex blend had much higher resistance to blocking. (The term "blocking" means sticking together of two coated pieces with coating film surfaces in contact.)

Shear storage modulus plots from three films are shown in Figure 4. The film prepared from the soft polymer in the form of large particles without any hard particle blending (SL Alone), shows a single step drop in G' centered at the T_g of 9 °C. The rubbery plateau at a G' level just above 1 x 10^6 dynes/cm^2 is characteristic of uncrosslinked polymers. The plateau is attributed to entanglements (*1*). For the film prepared from the 70/30 weight % blend (SL70/HS30), G' drops in two steps with a large contribution from the hard particles in the 40 °C to 80 °C range. This large contribution is attributed to a network of uncoalesced hard particles throughout the sample. Hard particle contact and spatial arrangement in the softer continuous matrix from large particles was analyzed in terms of percolation theory (*21*). If hard particles were not in contact, a much smaller G' contribution would be expected at 30 wt. % hard particles. The control film represented in Figure 4, was prepared from a single latex that had the same composition as the 70/30 blend. The control has a single step drop in G' but at a higher T_g than SL Alone as expected from the higher styrene content of the control copolymer. It is obvious that blending of particles of the size and hardness selected (*21*) gives films of much higher G' in the 40 °C to 60 °C range than is obtained from the same composition (control film) without blending. The observed improvement in block resistance is consistent with this control of G' values (*21*).

Films from Latex with Carboxyl Groups in the Shell

Kan and Blackson (*22*) carried out DMA on films prepared from styrene/butadiene latex that contained 10 wt. % acrylic acid. Transmission electron microscopy was used to characterize coalescence at various levels of neutralization. Micrographs indicated that films formed under more basic conditions did not coalesce completely. A shell of material, more or less hexagonal in cross-section, was observed where latex particles had come together and deformed during film formation. This hexagonal pattern was interpreted as evidence of honeycomb structure in which the walls were made up of polar material of higher T_g than is present in the center portion. Figure 5 shows Tan δ plots for films prepared following addition of sodium hydroxide to the latex before application. The film prepared at a pH of 6.3 shows a Tan δ peak at 30 °C which is attributed to the softer central portion of the honeycomb structure containing relatively few acrylic acid units. The shoulder that is evident at higher temperatures is attributed to the harder shell portion of the honeycomb, believed to be richer in acrylic acid.

The film prepared at a pH of 9.3 shows two peaks. The lower temperature peak remains at 30 °C which is interpreted as indicating that the central portion contains few acidic units that can be altered by neutralization. A strong peak is noted at higher temperature, and it is attributed to a high level of neutralized acid groups (i.e. sodium acrylate units) in the shell portion of the honeycomb structure. Storage modulus plots (not shown) also depend on pH of the latex before film formation with G' being higher for films prepared at higher pH. New and possibly improved film properties may result from generating honeycomb structure in a purposeful and

Downloaded by UNIV MASSACHUSETTS AMHERST on September 17, 2012 | http://pubs.acs.org
Publication Date: July 26, 2001 | doi: 10.1021/bk-2001-0790.ch006

Downloaded by UNIV MASSACHUSETTS AMHERST on September 17, 2012 | http://pubs.acs.org
Publication Date: July 26, 2001 | doi: 10.1021/bk-2001-0790.ch006

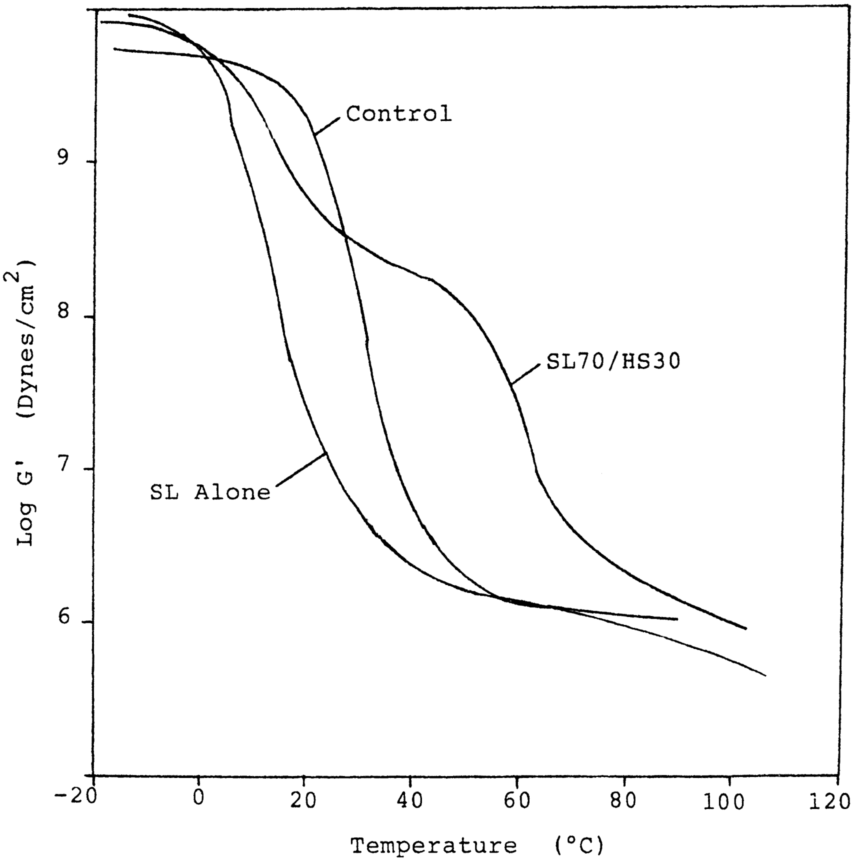

Figure 4. Shear storage modulus (G') plot for a film prepared from a blend of soft latex with large particles (SL) and hard latex with small particles (HS), [SL70)/HS30]. Plots are also shown for films from the soft latex alone (SL alone) and from a latex that has the same monomer composition as the blend (Control). (Reproduced from reference 21. Copyright 1997 Federation of Societies for Coating Technology.)

Downloaded by UNIV MASSACHUSETTS AMHERST on September 17, 2012 | http://pubs.acs.org
Publication Date: July 26, 2001 | doi: 10.1021/bk-2001-0790.ch006

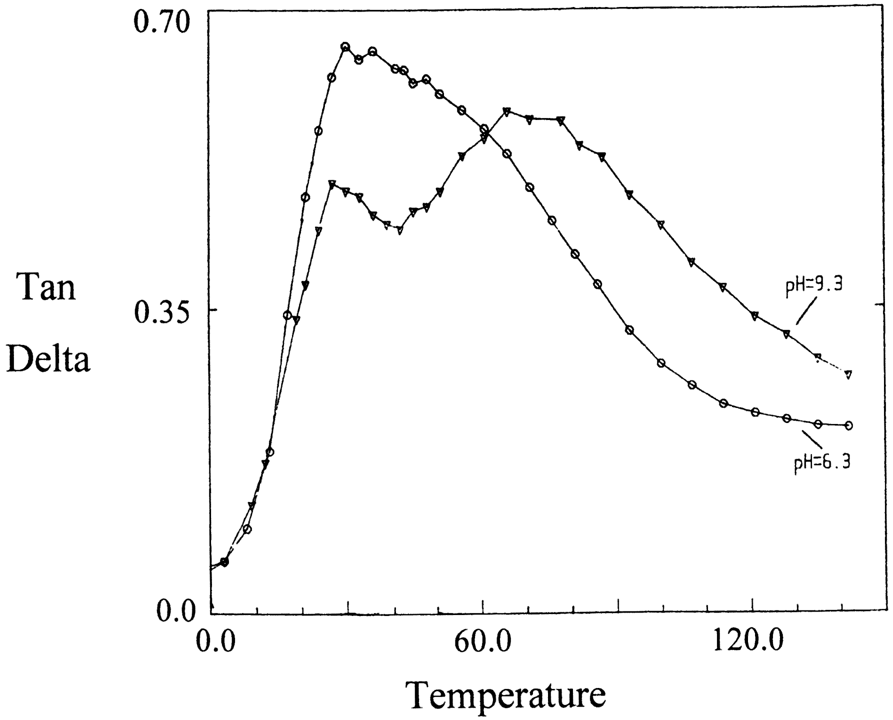

Figure 5. Loss tangent (Tan Delta) plots for films prepared from latex containing carboxylic acid groups neutralized to the indicated pH values: pH = 6.3 [-o-], PH = 9.3 [-▿-]. (Reproduced from reference 22. Copyright 1996 American Chemical Society.)

Downloaded by UNIV MASSACHUSETTS AMHERST on September 17, 2012 | http://pubs.acs.org
Publication Date: July 26, 2001 | doi: 10.1021/bk-2001-0790.ch006

controlled manner. Such control has not yet been demonstrated, and usually the goal in latex film formation is to get complete coalescence.

Heat treatment (annealing) of coalesced films often causes changes in dynamic properties (*23)* and dielectric properties (*24*). These changes have been attributed to alteration in the extent of phase mixing of the softer central portion and the harder honeycomb portion of the partially coalesced latex particles. The harder portion is found to make a disproportionately high contribution to properties when it forms a continuous network throughout the softer matrix. The continuous network is sometimes referred to as honeycomb structure and sometimes as co-continuous structure. If the harder material collapses to unconnected hard particles within the continuous soft matrix, the contribution to properties is reduced. The ACS Symposium Series book edited by Provder et al (*25*) includes several papers that describe the effects of annealing on film structure and properties.

Crosslinking by Butadiene in Latex Films

Richard (*26, 27*) added various levels of chain transfer agent (CTA) during emulsion polymerization of styrene and butadiene monomers and used DMA to determine the effect of CTA on films formed from the latices. Figure 6 shows E' plots for 2 wt. % (A), 0.8 wt. % (C) and 0.0 wt. % (E) of CTA. Values of E' in the rubbery plateau (T > 110 °C) indicate that film A has few chemical crosslinks whereas film E is highly crosslinked. Butadiene contains two double bonds which permits it to participate in chain branching and crosslinking during copolymerization. CTA reduces the concentration of free radical sites on existing polymer chains and favors initiation of new chains. The results are reduction of molecular weight, reduction in extent of branching and reduction in extent of crosslinking. In Figure 6, the variation in temperature of the sharp E' drop is likely an indication of the effect of molecular weight on T_g. Film E has the highest T_g and it is expected to have the highest molecular weight because no CTA was added. Film E also has the highest crosslink density. Observation of a rather typical crosslinking effect for latex film formation may be misleading based on other characterization methods discussed below (*27*).

Incomplete coalescence results in a honeycomb or membrane structure, but this structure may or may not be brittle. The level of crosslinking associated with brittleness following film formation is quite high according to Zozel and Ley (*28*). They discuss brittle behavior in terms of comparison of the molecular weight between crosslinks and the entanglement length of the copolymer under study.

Richard combined DMA work with small angle neutron scattering (SANS) and transmission electron microscopy (TEM) for characterization of the interfacial membranes in cellular structures of styrene/butadiene films (*27*). The role of carboxylic acid groups in the membranes was emphasized, and interpretations were similar to those described above from Kan and Blackson (*22*). The effect of varying CTA is shown once again in Figure 7, but in this case frequency is scanned while temperature is held constant. With this approach, the rubbery plateau region is on the left and the glassy region on the right, which is just the opposite of Figure 6.

Downloaded by UNIV MASSACHUSETTS AMHERST on September 17, 2012 | http://pubs.acs.org
Publication Date: July 26, 2001 | doi: 10.1021/bk-2001-0790.ch006

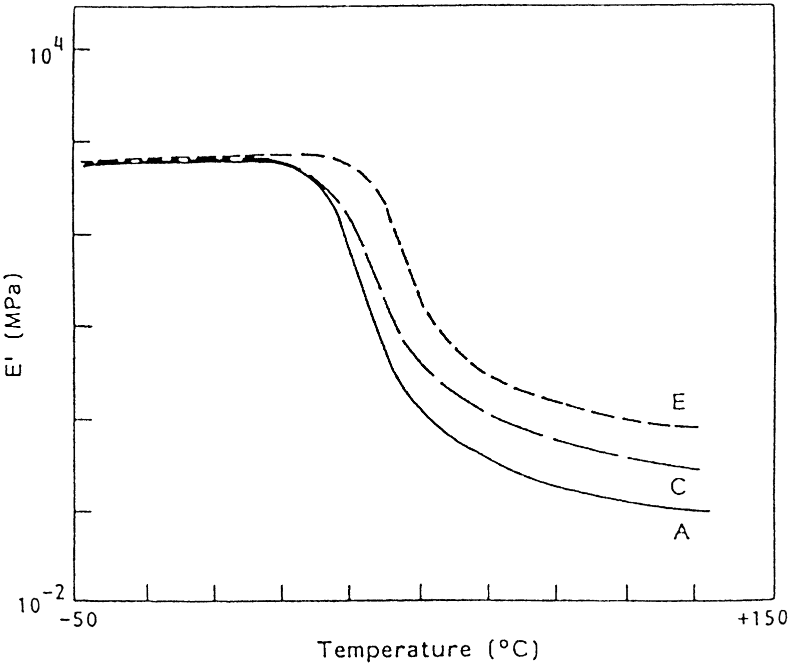

Figure 6. Storage modulus (E') plots for films prepared from styrene/butadiene latex that contained various levels of chain transfer agent (CTA): Plot A, CTA at 2.0 wt. %; Plot C, CTA at 0.8 wt. %; Plot E, CTA at 0.0 wt. %. (Reproduced from reference 26. Copyright 1992 Polymer Journal.)

Downloaded by UNIV MASSACHUSETTS AMHERST on September 17, 2012 | http://pubs.acs.org
Publication Date: July 26, 2001 | doi: 10.1021/bk-2001-0790.ch006

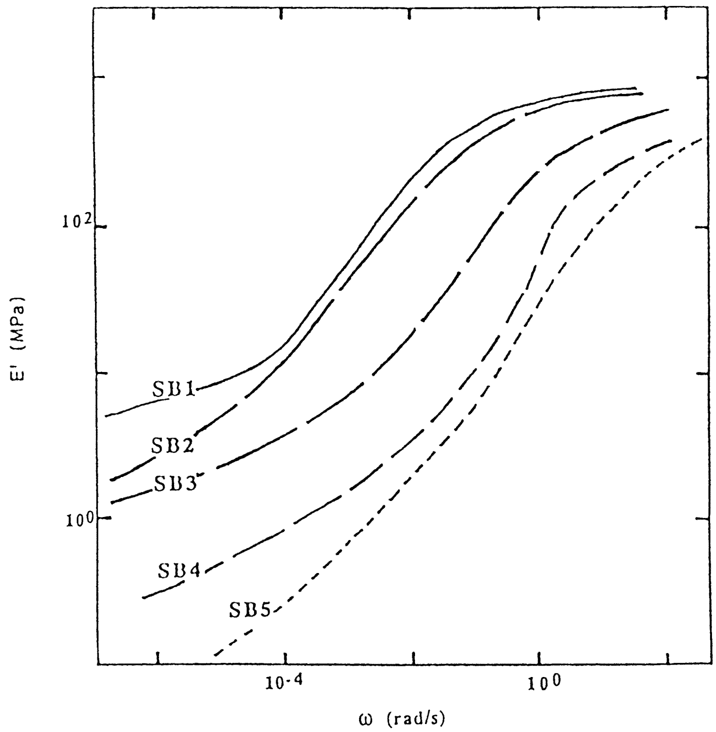

Figure 7. Tensile storage modulus, E', versus frequency of oscillation, ω, for films prepared from styrene/butadiene latex that contained various weigth percentages of chain transfer agent: SB1 0.0 % CTA; SB2 0.4 %; SB3 0.8 %; SB4 1.25 %; SB5 2.0 %. (Reproduced from reference 27. Copyright 1996 American Chemical Society.)

Once again it can be seen that absence of CTA (film SB1) results in a highly crosslinked film whereas 2.0 wt. % CTA (film SB5) exhibits little or no chemical crosslinking. SANS plots for SB1 showed two strong scattering intensity peaks that were interpreted as indicating a highly ordered array of non-fully coalesced latex particles. The height of these scattering intensity peaks decreased steadily as CTA was increased until for SB5 the peaks almost vanished. In summary, the crosslinking in SB1 has prevented complete of coalescence, but the E' plot (Figure 6) shows no evidence of the cellular structure revealed by SANS.

Sequential Coalescence and Crosslinking

Film formation from latex particles that already contain crosslinks is quite different from the commercially important approach of designing systems to coalesce first and then to crosslink next. Taylor (*29*) has reviewed crosslinking technology for films from acrylic copolymer latices. Winnick et al (*30, 31*) have described the use of fluorescence decay measurements to obtain polymer diffusion rates. Diffusion rates are considered to be important because a tenet of sequential coalescence and crosslinking is that good film properties require extensive coalescence before crosslinking takes place. It is believed that crosslinking inside individual particles will prevent coalescence and that resulting films will be brittle. This is currently a very active area of research and development, but reports of use of DMA to confirm crosslinking and property development were not found.

Downloaded by UNIV MASSACHUSETTS AMHERST on September 17, 2012 | http://pubs.acs.org
Publication Date: July 26, 2001 | doi: 10.1021/bk-2001-0790.ch006

Conclusion

Dynamic mechanical analysis has been widely used for determination of crosslink density of films prepared from solvent borne thermoset formulations. Such determinations indicate whether or not the intended network forming cure reactions have occurred as designed. More recent work with films from waterborne systems indicates that there is still a relationship between storage modulus and crosslink density for WB films, but chain entanglements also play a larger role in property development.

DMA is also useful for determining film morphology. If separate domains have distinct, sharp boundaries and widely differing T_g values, Tan δ and storage modulus plots will show separate glass transitions. If domain boundaries are diffuse and/or the separate domains have only moderately different T_g values, the DMA plots will not show separate transitions, but the Tan δ peak width (PW) will be much larger than for homogeneous samples. Peak width data, though available, are not often compiled or used effectively in film morphology determination. The best examples of determination of film structure involve combination of DMA with other methods such as advanced electron microscopy methods (SEM and TEM), small angle neutron scattering (SANS) and atomic force microscopy (AFM). When carboxylic acid groups, especially in anionic form, are present in the shell portion of particles of film forming latex systems, coalescence is often incomplete and a hard domain, called membranes or honeycomb, persists in network form throughout the film.

Literature Cited

1. Murayam, T. *Dynamic Mechanical Analysis of Polymeric Material*; Material Science Monographs 1; Elsevier: NY, 1978.
2. Hill, L.W. In *Paint and Coating Testing Manual*; Koelske, J.V., Ed.; 14th Edition; ASTM Manual Series: MNL 17; American Society for Testing Materials: Philadelphia, PA, 1995; pp 534-546.
3. Skrovanek, D.J. *Prog. Org. Coat.* 1990, *18*, 89-101.
4. Hill, L.W.; Kozlowski, K. *J. Coat. Technol.* 1987, *59*, No.751, 63-71.
5. Hill, L.W. *J. Coat. Technol.* 1992, *64*, No. 808, 29-42.
6. Hill, L.W. *ACS PMSE Proceedings* 1997, *77*, 387-388.
7. Frey, Th.; Groβe-Brinkhaus, K.-H.; Rockrath, U. *Prog. Org. Coat.* 1996, *27*, 59-66.
8. Rockrath, U; Brockkotter, K., Frey, Th.; Poth, U.; Wigger, G. *Prog. Org. Coat.* 1997, *32*, 173-182.
9. Higginbottom, H.P.; Bowers, G.R.; Hill, L.W.; Courtier, J.F. *Prog. Org. Coat.* 1998, *34*, 27-38.
10. Matsuoka, S.; Quan, X.; Bair, H.E.; Boyle, D.J. *Macromolecules* 1989, *22*, 4093-4097.
11. Lange, J.; Manson, J.-A. E.; Hult, A. *Polymer* 1996, *37*, 5859-5868.
12. Kalfoglou, N.K.; Williams, H.L. *J. Appl. Poly. Sci.* 1973, *17*, 1377-1386.
13. Varley, R.J.; Hodgkin, J.H.; Hawthorne, D.G.; Simon, G.P. *J. Poly. Sci.: Part B; Poly Physics* 1997, *35*, 153-163.
14. Provder, T. *J. Coat. Technol.* 1989, *61*, No. 770, 33-50.
15. Palmese, G.R.; Gillham, J.K. *J. Appl. Poly. Sci.* 1987, *34*, 1925-1939.
16. Gillham, J.K. *Poly. International Journal* 1997, *44*, 262-276.
17. Hill, L.W.; Ferrell, P.E.; Gummeson, J.J. In *Film Formation in Waterborne Coatings;* Provder, T.; Winnik, M.A.; Urban, M.W. , Edts., ACS Symposium Series 648, Am. Chem. Soc.: Washington, DC 1996, pp. 235-242.
18. Ferrell, P.E.; Gummeson, J.J.; Hill, L.W. *J. Coat. Technol.* 1995, *67*, No. 851, 63-69.
19. Sartguru, R.; McMahon, J.; Padget, J.C.; Coogan, R.G *J. Coat. Technol.* 1994, *66*, No. 830, 47-55.
20. Van Bogart, J.W.C.; Lilaonitkul, A.; Cooper, S.L., In *Multiphase Polymers,* Cooper, S.L.; Estes, G.M., Edts. Advances in Chemistry Series 176, Am. Chem. Soc.: Washington, DC 1979, pp. 1-23.
21. Eckersley, S.T.; Helmer, B.J. *J. Coat. Technol.* 1997, *69*, No. 864, 97-107.
22. Kan, C.S.; Blackson, J.H. *Macromolecules* 1996, *29*, 6853-6864.
23. Richard, J.; Maquet, J. *Polymer* 1992, *33*, 4164-4173.
24. Pochan, D., *Proceedings of the Waterborne and Higher Solids Coatings Symposium,* New Orleans, *1987,* p.155-166.
25. Provder, T.; Winnik, M.A.; Urban, M.W., Edts., *Film Formation in Waterborne Coatings*, ACS Symposium Series 648, Am. Chem. Soc.: Washington, DC 1996.

Downloaded by UNIV MASSACHUSETTS AMHERST on September 17, 2012 | http://pubs.acs.org
Publication Date: July 26, 2001 | doi: 10.1021/bk-2001-0790.ch006

26. Richard, J., *Polymer* 1992, *33*, 562-571.
27. Richard, J., In *Film Formation in Waterborne Coatings;* Provder, T.; Winnik, M.A.; Urban, M.W. , Edts., ACS Symposium Series 648, Am. Chem. Soc.: Washington, DC 1996, pp. 118-153.
28. Zosel, A.; Ley, G. *Macromolecules* 1993, *26*, 2222-2227.
29. Taylor, J.W., *ACS PMSE Proceedings* 1999, *80*, 309-310.
30. Feng, J.; Pham, H.; MacDonald, P. Winnik, M.A.; Geurts, J.M., Zirkzee, H.; van Es, S; German, A.L. *J. Coat. Technol.* 1998, *70*, No. 881, 57-67.
31. Winnik, M.A.; Pinenq, P.; Kruger, C.; Zhang, J. *J. Coat. Technol.* 1999, *71*, No. 892, 47-60.

Downloaded by UNIV MASSACHUSETTS AMHERST on September 17, 2012 | http://pubs.acs.org
Publication Date: July 26, 2001 | doi: 10.1021/bk-2001-0790.ch006

Downloaded by OHIO STATE UNIV LIBRARIES on September 17, 2012 | http://pubs.acs.org
Publication Date: July 26, 2001 | doi: 10.1021/bk-2001-0790.ch007

Chapter 7

Property Development during Film Formation of Two Component Waterborne Polyurethane Using Dielectric Spectroscopy

John E. Dewhurst, Ava S. Drayton-Elder, Xiaoping Gao*, Thomas M. Santosusso, Chao-fong Tien, and Tracy L. Wickmann

Air Products and Chemicals, Inc., 7201 Hamilton Boulevard, Allentown, PA 18195–1501

A dynamic dielectric analysis (DEA), coupled with infrared spectroscopy (IR), Persoz hardness and dynamic mechanical analysis (DMA) were used to correlate the film formation, curing, and final property development of a two component (2K) waterborne urethane coating. The 2K waterborne urethane coating is based on Air Products' novel zero volatile organic compound (VOC) Adura™ polyol technology. The coating is cured at ambient temperature. The change in capacitance and resistance (which is directly proportional to ionic viscosity before gelation) was studied using DEA. The water evaporation, the consumption of isocyanate groups and appearance of urethane and urea groups were monitored by IR. The hardness development and final Tg of the coating under various conditions were studied by Pendulum Persoz hardness tester and DMA. A correlation among those observations was attempted, and the curing and film formation process of this system is rationalized based on the experimental data.

In conventional industrial maintenance coating systems, organic solvents are commonly used to adjust application viscosity, control sagging, improve surface leveling, and help control other properties. However, the paints and coatings markets-

In Film Formation in Coatings; Provder, T., et al.;
ACS Symposium Series; American Chemical Society: Washington, DC, 2001.

most recently in addition to being strongly competitive have been strongly impacted by environmental concerns. In recent years, VOC (volatile organic compounds) regulations have had a significant impact on coatings technology. VOC reduction has refocused industrial coatings from traditional solvent borne technology to alternative technologies such as waterborne, high solids, and powder coatings. Two component waterborne urethanes were developed with an intent to meet the VOC challenge. They first emerged in the late 1980's and were based on water dispersible isocyanate (through hydrophilic modification of the conventional isocyanate). Over the years, the technology has advanced significantly both in performance and VOC reduction. However, up until relatively recently, completely VOC--free systems having superior performance to solvent borne coatings have not been achieved. Furthermore, the film formation of 2K waterborne urethanes has been studied in very few cases. An understanding of the film formation should significantly assist future development in 2K waterborne urethanes by allowing the elements affecting that critical process to be optimized. Dielectric analysis is a well-known technique for studying epoxies and latex[1,6,8,10,11], its non-destructive nature and sensitivity to minor environmental and compositional changes at the molecular level should make it applicable for studying the film formation of 2K waterborne systems. A few years ago, Air Products introdued a novel zero VOC waterborne urethane technology - Adura technology, which employs conventional isocyanates and performs similarly to solvent borne urethane coatings. This report is aimed at exploring the film formation of Adura coatings through DEA, IR, and DMA studies.

Experimental

Materials: Coatings were prepared by adding HDI trimer isocyanate (Desmodur N-3300 from Bayer) to an Air Products' Adura© aqueous polyol dispersion (equivalent weight = 275) with stirring. The NCO/OH ratio is ~1.5. After mixing (1~2 minutes), the material is diluted with DI water to form a ~67% solid dispersion. Unless otherwise specified, the coatings were applied to a dry film thickness of 70 ± 5 microns (3 ± 0.2 mils) using a #60 wire wound rod or 5 mil drawing bar onto the substrate surface.

Analytical Measurements: Dielectric measurements were performed by coating a sample of the polymer dispersion onto a dielectric sensor (comb electrode), applying a sinusoidal voltage and measuring the resulting current. The sensor is planar, 1 inch by ½ inch in size with 25 um spacing between the electrodes from Micromet Inc. The instrumentation used consisted of a Solartron 1260 Frequency Response Analyzer with commercial ZPLOT and ZVIEW software (supplied by Solarton Inc.). Samples were prepared a few minutes before they were coated onto the comb electrode and tested under ambient conditions (at 70°F and 50% humidity) or in a nitrogen chamber.

Downloaded by OHIO STATE UNIV LIBRARIES on September 17, 2012 | http://pubs.acs.org
Publication Date: July 26, 2001 | doi: 10.1021/bk-2001-0790.ch007

Downloaded by OHIO STATE UNIV LIBRARIES on September 17, 2012 | http://pubs.acs.org
Publication Date: July 26, 2001 | doi: 10.1021/bk-2001-0790.ch007

Dielectric measurements were recorded every minute during the first 50 to 90 hours cure of the sample with a typical frequency of 100 Hz.

Attenuated Total Reflectance (ATR) Infrared Spectroscopy was used to monitor changes in the spectra of the coating during cure which can give information on the isocyanate consumption and cross-linking reactions. The spectra were collected on a Nicolet 860 interferometer. Films were spread onto the crystal to obtain a dry film thickness of 2.0 ± 0.2 mils. Experiments were performed using two different environmental conditions - (1) film is left exposed to ambient air or (2) film was exposed to dry nitrogen.

Dry time of the coated film was monitored by a dry time recorder. The Persoz hardness was measured by a Pendulum hardness tester. Both instruments are commercialized by Paul H. Gardner Co., Inc.

Results and Discussion

Adura coating technology (Preparation and Performance) The preparation of Adura coatings is illustrated schematically in Figure 1. Adura polyol is a mixture of various isocyanate-reactive ingredients (which include the amine neutralized polyol) with water (~30%). Just before coating application, poly-isocyanate (such as HDI trimer) is added to Adura polyol as described above before applying to the substrate surface.

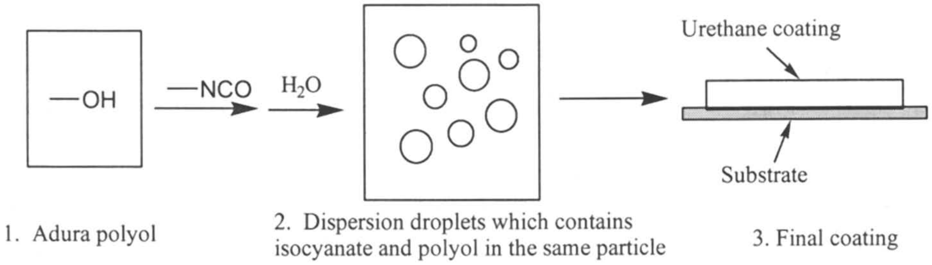
—OH
—NCO
H_2O
Urethane coating
Substrate
1. Adura polyol
2. Dispersion droplets which contains isocyanate and polyol in the same particle
3. Final coating

***Figure1.** Adura coating technology*

The Adura coatings are usually evaluated after curing under ambient conditions for two weeks. The general clear coat performance is summarized in Table 1.

Downloaded by OHIO STATE UNIV LIBRARIES on September 17, 2012 | http://pubs.acs.org
Publication Date: July 26, 2001 | doi: 10.1021/bk-2001-0790.ch007

Table 1 Adura Coating Performance

Set to Touch	~1 hours		***Solvent Resistance*** **(Double Rub)**	
Tack Free	~1 hr 15 min		MEK	>200
Dry Hard	~7 hours		Toluene	>200
Gloss	20°	78	IPA	>200
	60°	98	***Impact***	
	80°	96	Direct	> 160 in-lbs
Adhesion			Reverse	> 150 in-lbs
Dry Tape	5A		***Hardness***	
Wet Tape	5A		Pendulum	~224

The set to touch time is about one hour and the tack free time is around 75 minutes. It takes six to seven hours for the film to be dry hard.

Film formation for waterborne coatings A background discussion of film formation form latexes may be helpful. The general mechanism for latex film formation includes three main steps and is shown in Figure 2[2, 3, 13].

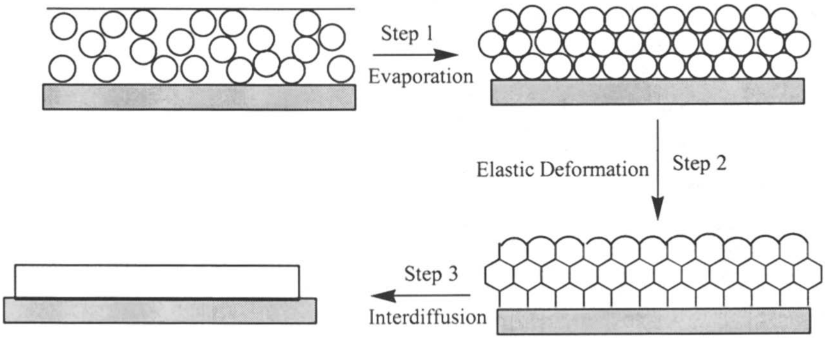

Figure 2. *Film formation Mechanism for Latex System*

During step 1, water evaporates rapidly and latex particles start to contact each other but water still fills the interstices among particles. Step 2 involves the final water evaporation, particles deform and contact each other intimately but each particle still maintains its individuality. The system is essentially dry. In fact, a honey comb structure can be seen through electron microscopy for latex systems with high minimum film formation temperature.[4] In step 3, material diffuses across the particle-particle boundary, the film surface levels, and a homogeneous film forms.

For a latex with a Tg much lower than film formation temperature, step 3 may be quite fast and may begin to occur before evaporation of all the bulk water is complete. The water closest to the coating surface evaporates faster. If step 3 is fast, a continuous film may be formed at surface with a small amount of water trapped inside the coating as isolated dispersed domains. The final water loss will therefore occur by diffusion through the solid phase instead of evaporating from particle-particle interstices. For those low Tg systems, the occurrence of each step is not as clear cut when compared with high Tg latex systems.[5]

In the simplest sense, the latex film formation involves the changes of the continuous phase from water to organic through water evaporation and concomitant formation of a continuous solid film by inter-diffusion of latex particles. In the current study, differences in the dielectric properties of the organic and water phases are exploited in order to explore the film formation mechanism. Even after the loss of the mobile water phase and the onset of gellation, the drying/curing film will still yield information on the progression toward the limiting film properties because of its residual ion content and changes in the chemical nature and orientation of the dipoles, although distinguishing among DEA changes due to water loss, coalescence and chemical reaction is not straightforward.[6]

For 2K waterborne urethanes based on lower molecular weight components, one can speculate that since the internal viscosity of dispersion particles is relatively low, the particle-particle deformation, coalescence and leveling should be relatively fast and the coating should have good leveling and homogeneous cross-linking. The life-time of honey-comb structure after step 2 may be very short at ambient temperature for those systems. This is consistent with the very high gloss and excellent film-forming properties of Adura coatings.

Curing and film composition (IR analysis) The 2K waterborne urethane film composition is sensitive to the curing conditions[7], such as temperature, humidity and catalyst used. This is because water can react with isocyanate leading to urea formation. For ambient curing, the major possible reactions are listed in Figure 3. The water reaction with isocyanate is an important reaction competing with isocyanate-polyol reaction and leads to amine and carbon dioxide formation. This is a slow process but it is followed by fast urea formation from amine and isocyanate. Thus, in 2K waterborne urethane, a larger than stoichiometric amount of isocyanate is used (NCO/OH = 1.5 for this study) to compensate for the water/isocyanate reaction.

To assess the relative amounts of urethane and urea formed during film formation in air and dry nitrogen, Infrared (IR) absorbance is used to monitor isocyanate consumption and urethane and urea formation. Figure 4 shows the rate of isocyanate consumption during cure is apparently faster in air than dry nitrogen.

Downloaded by OHIO STATE UNIV LIBRARIES on September 17, 2012 | http://pubs.acs.org
Publication Date: July 26, 2001 | doi: 10.1021/bk-2001-0790.ch007

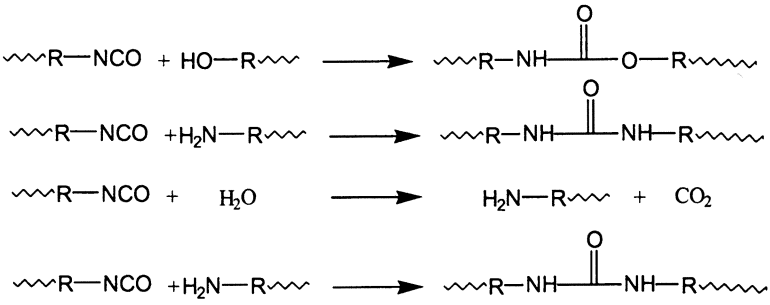
~R—NCO + HO—R~ → ~R—NH—C(=O)—O—R~
~R—NCO + H2N—R~ → ~R—NH—C(=O)—NH—R~
~R—NCO + H2O → H2N—R~ + CO2
~R—NCO + H2N—R~ → ~R—NH—C(=O)—NH—R~

Figure 3. Possible reactions for 2K waterborne urethanes

In the dry nitrogen atmosphere, urethane formation is faster than in moist air, and it is the principal product of the curing reaction, with a negligible amount of urea formation being observed. In air, the rate of isocyanate consumption (also the curing rate) is faster than in nitrogen, since in this case, in addition to urethane formation, the reaction of isocyanate with water and concomitant urea formation becomes significant, which is not the case in dry nitrogen. These results are somewhat surprising, since one might expect the presumed equilibrium amount of water remaining in the curing film to be sufficient to effect the water reaction with isocyanate. This is clearly not the

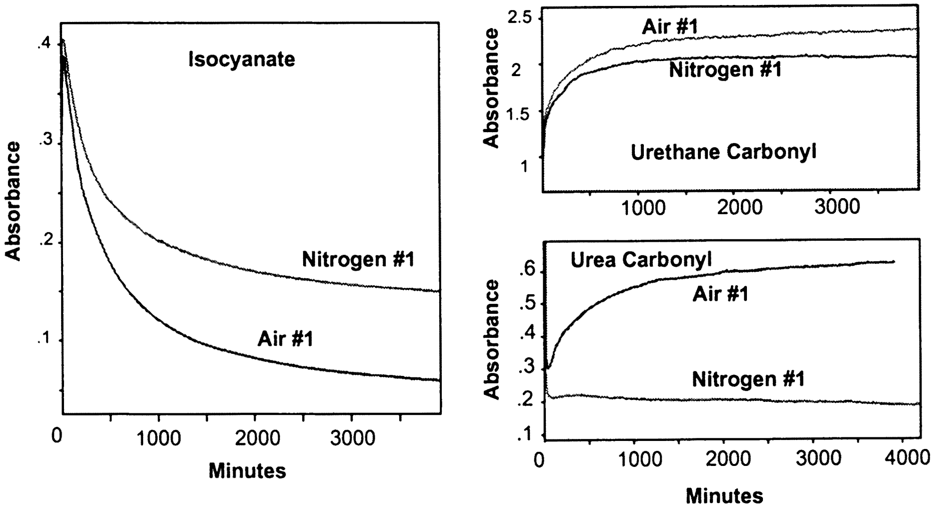

Figure 4. IR absorbance vs. time for isocyanate, urethane and urea during film formation

Downloaded by OHIO STATE UNIV LIBRARIES on September 17, 2012 | http://pubs.acs.org
Publication Date: July 26, 2001 | doi: 10.1021/bk-2001-0790.ch007

case, however, and one must conclude that the isocyanate-water reaction depends heavily on the water content of the atmosphere. Given the difference in rates, the general shape of the plots of isocyanate loss and appearance of urethane with time are similar for both air and nitrogen, that is the rates for both reactions are faster in the first 500 minutes, then slow down but keep progressing even after 7 days.

Table 2 indicates that, in air, the hardness and Tg of the film achieve their limiting value within 3 days. The film has higher Tg and Persoz hardness than the film formed in dry nitrogen. This is consistent with the spectroscopic evidence which suggests that there is significantly less of unreacted isocyanate present under dry nitrogen than in air, along with a much larger amount of urea.

Downloaded by OHIO STATE UNIV LIBRARIES on September 17, 2012 | http://pubs.acs.org
Publication Date: July 26, 2001 | doi: 10.1021/bk-2001-0790.ch007

Table 2 Tg and Hardness for Curing in Air and Nitrogen

Days	Condition	Tg	Persoz Hardness
1	Ambient Air	36	
3	Ambient Air	54	220
7	Ambient Air	55	218
14	Ambient Air	55	224
1	Nitrogen	26	
3	Nitrogen	36	136
7	Nitrogen	48	195
14	Nitrogen	52	206

DEA analysis DEA can measure changes in conductance and capacitance simultaneously in a coating system. Conductance is sensitive to the ion concentration and its mobility (viscosity of the medium) while capacitance is sensitive to the dipole moments in the system and the ease of dipole reorientation under the electric field. Thus, capacitance can provide information of chemical composition changes such as concentration changes and new bond formation while conductance, if the ion content is constant, can probe the physical property variations such as viscosity changes in the medium as curing reactions progress.

DEA has been used to study curing in solvent-borne epoxy systems for several decades.[8]. A in situ frequency dependent electrical measurement sensor (FDEMS) had been used to monitor the cure process, buildup in hardness and the effects of environmental conditions of epoxy and latex paints[1]. In latex systems, water is present in large concentration. Water has a large dielectric constant compared to most organic materials, so DEA should be quite sensitive to changes in the capacitance

Downloaded by OHIO STATE UNIV LIBRARIES on September 17, 2012 | http://pubs.acs.org
Publication Date: July 26, 2001 | doi: 10.1021/bk-2001-0790.ch007

during the drying process.[8] In earlier DEA studies on latex film formation,[1, 6, 10, 11] the drying process was followed by changes in conductance. The shortcoming of conductance measurements for aqueous systems is the presence of a blocking effect due to electrode polarization. The blocking effect makes it difficult to analyze the data for bulk changes during the first 20 to 30 minutes[6, 12] for waterborne systems at low frequencies range. As indicated previously[6] and observed in this study, at the earliest stage of film formation for waterborne coatings the low bulk resistance makes it easy for the mobile ions to pile-up at the interfaces. The accumulation of the ions near the electrode compares to the electron screen effect at metal surfaces. The electric field is blocked by the screen effect and its intensity in the bulk phase is near zero. As a result, the dielectric properties at the interface dominate the contribution of DEA measurements at frequencies lower than 10KHz (see figure 6 and the text). This effect is called the "blocking effect". In order to study water evaporation during the film formation of waterborne systems, an alternative approach other than the conductance measurement has to be sought.

For waterborne coatings, the circuit model for the systems should include a parallel interfacial capacitance (C_i) and resistance (R_i) in series with a parallel bulk resistance (R_b) and capacitance (C_b) as shown in Figure 5(a). The capacitance C_i is the interfacial capacitance at metal/solution interface.[9] C_i is about 10 to 100 $\mu F/cm^2$ in an aqueous solution,[9] and it is about 1 $\mu F/cm^2$ at the very beginning of Adura coating. R_i is an interfacial resistance which depends on the free electron transfer (Faraday) current. If there is no Faraday current, R_i will be infinite. Based on our experimental results after drying, the bulk capacitance C_b is about $\varepsilon \times 10^{-11}$ F depending on the dielectric constant ε of the film. Finally, the bulk resistance R_b depends on the viscosity and the ionic concentration of the coating. The value was varied from 10 ohm to 10^{10} ohm or higher. Figure 5(b) is a complex impedance plot based on the circuit model in Figure 5(a), where X axis is the real part of impedance and Y is the imaginary part of impedance. There are two semicircles corresponding to two parallel CR circuits. As discussed above, at the earlier stage of drying, R_b is small, so the small semicircle represents the impedance of the bulk phase and the big semicircle is caused by the interfacial capacitance and resistance. As water evaporates, the small semicircle will get larger because R_b gets larger.

Theoretically, C_i depends on the dielectric properties at the interface.[9] For waterborne systems, the interfacial dielectric properties are dominated by water concentration due to its higher dielectric constant. Water evaporation will reduce the water concentration in the bulk and at the interface. As a consequence, water evaporation also decreases C_i. In this study, we found that C_i was very sensitive to water evaporation. Based on the experimental results and theoretical considerations, we believe that the interfacial capacitance can be used to monitor the water evaporation process for these coatings. To verify the usefulness of this approach, in this study, C_i measurements are also compared with water loss and IR spectroscopy measurements.

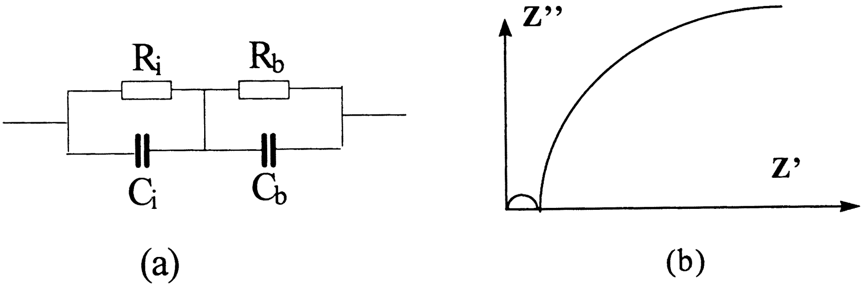

Figure 5. (a) Circuit model of a dielectric sensor. (b) Complex plots of impedance based on the figure 5(a) model.

In this initial work, even though the electrode was calibrated, the sample was not. The data shows the qualitative pattern rather than quantitative pattern of drying and curing profile. An attempt is made to qualitatively correlate dielectric properties, physical testing, and ATR IR spectroscopy during the film formation process.

Figure 6(a) and 6(b) show two complex plots of impedance during the first 21 minutes of drying. The applied frequencies were from 1 Hz to 10 MHz for each curve. Figure 6(b) is a blowup of Figure 6(a) where a small semicircle was observed in the high frequency range from 10 KHz to 10 MHz. Thirteen curves were generated in 1.6 minute intervals in the order that labeled 1, 2, 3, .. in the figure 6. In Figure 6(b), the left curves were collected earlier than the right curves. It was observed that the smaller semicircle becomes larger with time. As discussed previously, this set of semicircles is due to the parallel capacitance and resistance of the bulk film. The large semicircles in Figure 6(a) are due to the interfacial capacitance and resistance. The experimental results show that in order to obtain the bulk dielectric properties such as in the Figure 6(b), the applied frequency should be higher than 10 KHz.

Bulk conductance, σ_b, can be calculated from the small semicircles in Figure 6(b) at about 10 KHz, while C_i can be obtained from Figure 6(a) at 100Hz. As shown in Figure 7(a), σ_b (rectangular) and C_i (triangular) were normalized to the same scale for comparison.

A plot of water evaporation vs time for the Adura coating is shown in Figure 7(b). The sample was coated on a glass slide with a 5 mil draw down bar (the same as that used in DEA experiments), and the weight change was measured every one or two minutes. The coated surface area of the glass slide was 16 cm^2 and the sample

Downloaded by OHIO STATE UNIV LIBRARIES on September 17, 2012 | http://pubs.acs.org
Publication Date: July 26, 2001 | doi: 10.1021/bk-2001-0790.ch007

Downloaded by OHIO STATE UNIV LIBRARIES on September 17, 2012 | http://pubs.acs.org
Publication Date: July 26, 2001 | doi: 10.1021/bk-2001-0790.ch007

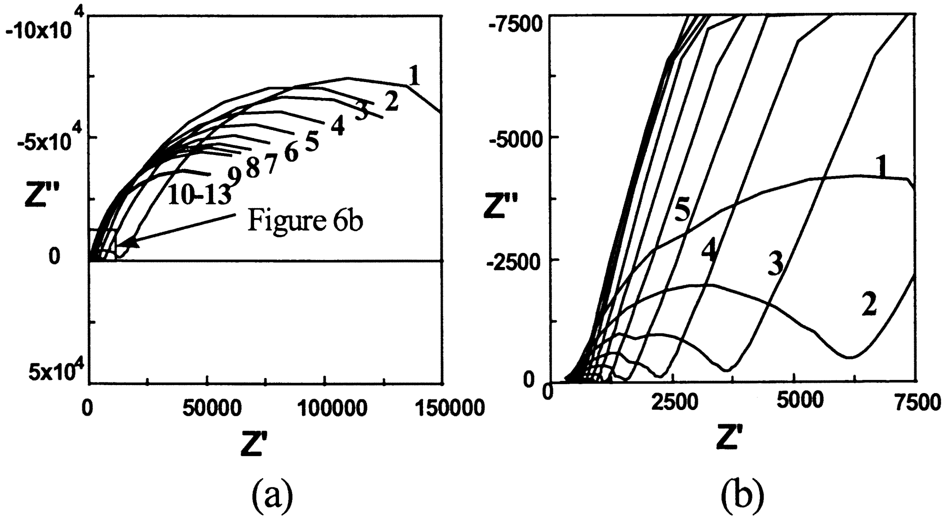

Figure 6. (a) Complex plots of Adura during the first 21 minutes of drying, (b) complex plots of Adura in the high frequency range of figure 6(a).

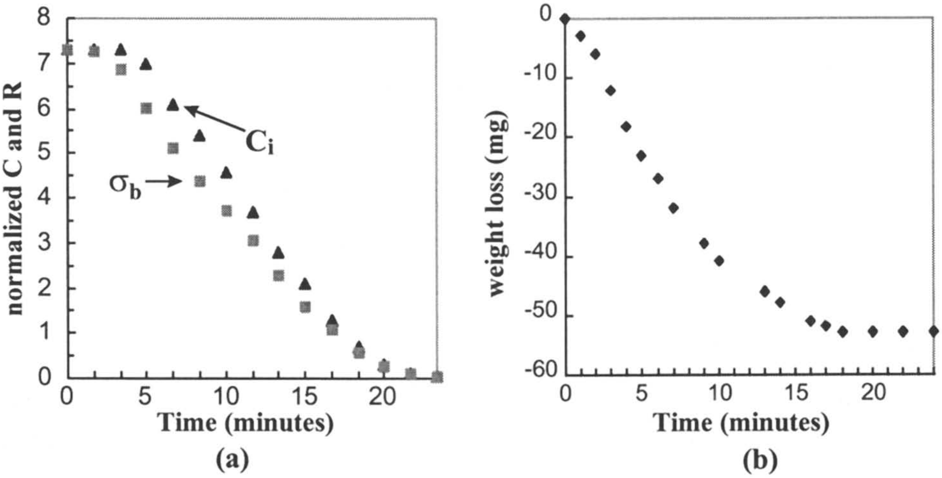

Figure 7. (a) Interfacial capacitance and bulk conductance vs. time (recorded every 1.67 minutes), based on a parallel capacitance and resistance model. (b) Weight loss vs. time.

thickness was about 5 mil or 100 μm. The weight of sample was 163 mg at the beginning (time = 0). It took about 18 minutes to evaporate 53 mg of water (32% of

Downloaded by OHIO STATE UNIV LIBRARIES on September 17, 2012 | http://pubs.acs.org
Publication Date: July 26, 2001 | doi: 10.1021/bk-2001-0790.ch007

total weight) and level off. The uncertainty of the weight is about 1mg and the uncertainty of time is 5 seconds. The conditions used in this experiment is similar to the conditions in the DEA experiments. The evaporation time (18 minutes) by weight loss is close to the time from DEA measurements (about 20 minutes). The two to three minutes delay in the dielectric data is attributed to the fact that the dielectric sensor is located at the bottom of the film.

ATR IR spectroscopy can detect water evaporation and chemical composition in the film. It should be informative to compare IR (water absorbance at 3168 cm^{-1}) and DEA measurement on water evaporation during film formation. One has to bear in mind that the 3168 cm^{-1} region of water absorbance is coincident with the hydroxyl, amino, urethane and urea absorbances. However, water dominates the IR region during the beginning of film formation. The IR measurement was taken every 10 minutes for 72 hours. Figure 8 (a) shows that a sharp decrease in water IR absorbance occured in the first ~20 minutes and the change leveled off immediately. In the next 72 hours, the water IR absorbance was essentially constant.

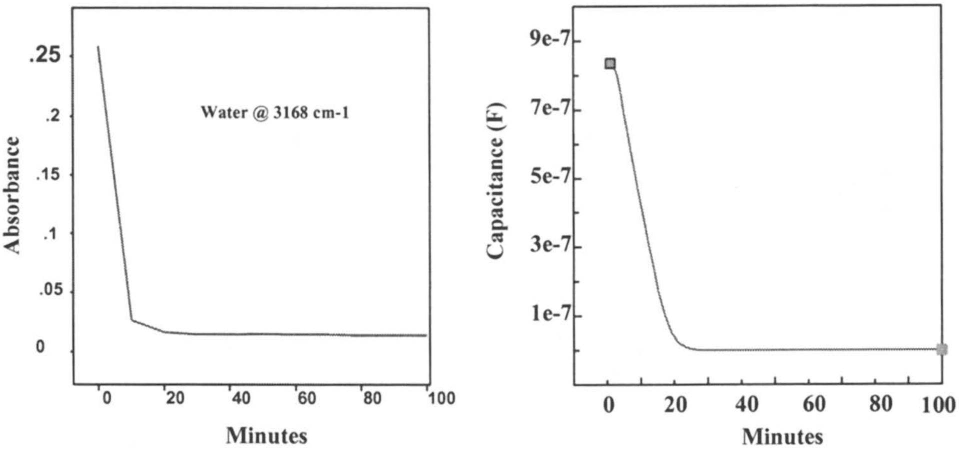

(a)

(b)

Figure 8. *(a) Water IR absorbance vs. time (recorded every 10 minutes); (b) Capacitance vs. time based on a parallel capacitance and resistance model (recorded every minute)*

In the DEA measurements, the linear plot of capacitance vs. time exhibits a similar but slower trend. Figure 8(b) shows an order of magnitude decrease in capacitance (from $11.4x10^{-7}$ F to $3.5x10^{-8}$ F) occurs within a similar time period as the decrease in IR absorbance is observed. The change appears to level off when the Y axis scale unit is 10^{-7} Faraday. We suggest that the change in capacitance is slower than the change in IR because the capacitance does not depend only on the water concentration, but also on the ionic concentration near the interface.

To explore the Adura coating during film formation in more detail, Figure 9 is a log-log plot for capacitance vs. time based on the same data in Figure 8(b). A rapid decrease in capacitance is observed for the first ~20 minute. However, a break region is observed between 20 to ~40 minutes which is followed by a slower decrease in capacitance.

Downloaded by OHIO STATE UNIV LIBRARIES on September 17, 2012 | http://pubs.acs.org
Publication Date: July 26, 2001 | doi: 10.1021/bk-2001-0790.ch007

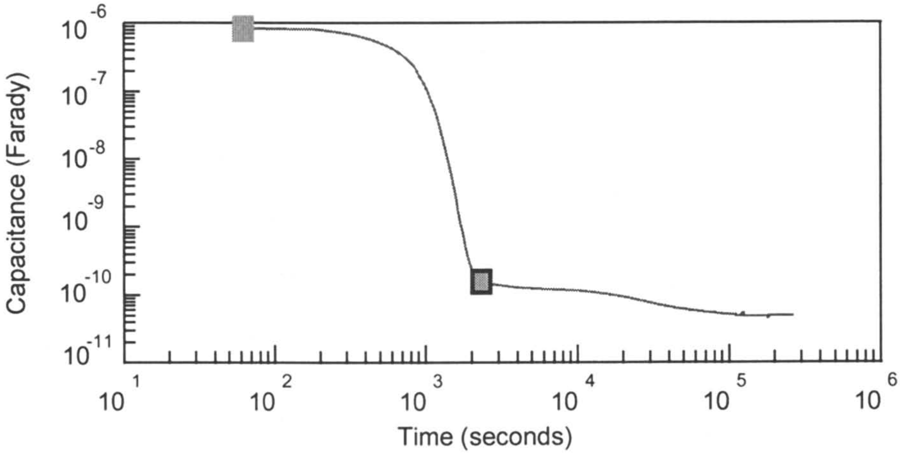

Figure 9. *Capacitance changes with Time*

This observation agrees with previous studies on latex drying that concluded that there are probably two different processes for water evaporation. This is also consistent with the general latex film formation mechanism. However, the Adura coating is complicated by the fact that curing proceeds concurrently with film formation. For simplification of discussion, we have assumed that curing of the Adura coating will a have negligible effect on the dielectric properties of the system before water evaporation is completed. Figure 10 to Figure 13 show more detailed changes in capacitance vs. time.

During the first 20 minutes, water evaporates rapidly and a linear relationship is observed between capacitance decrease and time (Figure 10). As proposed, in step 1 of latex film formation, the water evaporation rate is only proportional to the water vapor pressure. Approximately 96% of total water is evaporated.

After 20 minutes, a steep, two orders of magnitude change in capacitance is observed within 15 minutes (from 3.5×10^{-8} F to 1.74×10^{-10} F) , as seen in Figure 11. The capacitance change vs. time follows an exponential relationship instead of a

Downloaded by OHIO STATE UNIV LIBRARIES on September 17, 2012 | http://pubs.acs.org
Publication Date: July 26, 2001 | doi: 10.1021/bk-2001-0790.ch007

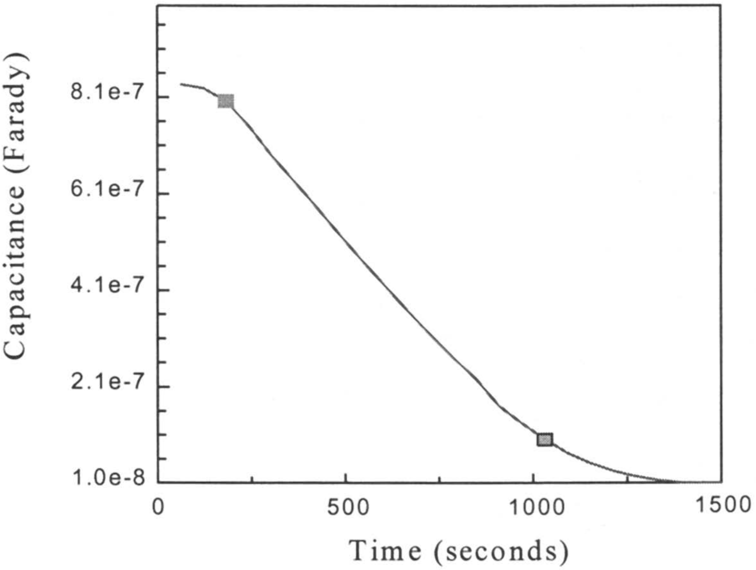

Figure 10. *Capacitance vs. time for the first 20 minutes*

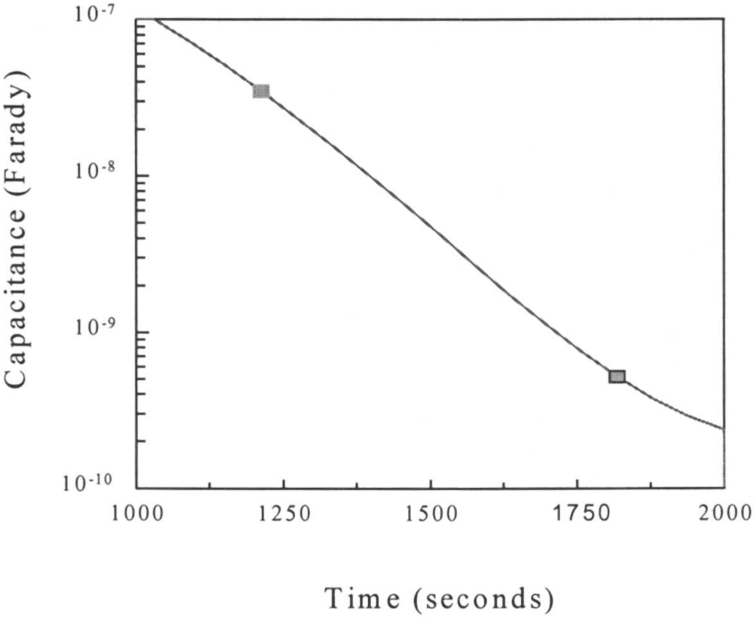

Figure 11. *Capacitance vs. time between 20~35 minutes*

linear relationship. The rate of change is slower. Assuming that this stage of film formation follows what is known about the first stages of non-reactive latex film formation, this is probably due to water evaporation from particle-particle interstices during particle deformation (step 2) and before particles coalescence (step 3). It is proposed that water evaporation is slower in step 2 and depends on other factors in addition to the water vapor pressure.

Once particles coalesce, cross-linking can take place within the whole film and this involves molecular electronic structure changes and the beginning of network formation. This process, in common with other crosslinking reactions, presumably will increase the viscosity and restrict the dipole reorientation. This appears to be reflected in the appearance of a transition zone (35-73 minutes) at the beginning of film formation which does not show any correlation between capacitance change with time (Figure 12).

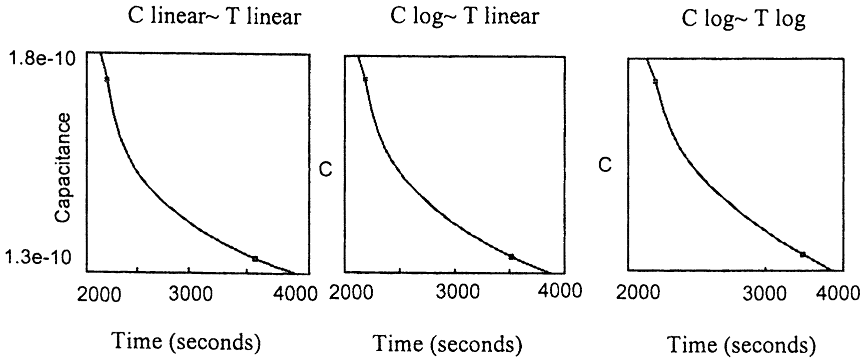

Figure 12. Capacitance vs. time (35-73 minutes)

Reaction between the isocyanate groups and the co-reactants is required to build up the molecular weight (viscosity) from low to infinity through the curing process. It seems reasonable that once the main structure is established, the change in capacitance should again be much slower and more or less linear with time, as is observed (Figure 13). It takes about 75 minutes for the film to become tack free. At this stage, a weak but cross-linked film is formed. The Tg of the film is lower than ambient temperature.

Besides water molecules, the other high dipole entities, before curing, are the hydroxyl groups of the polyols and quaternary amine salts of acids. After cure, polar urethane and urea groups are formed at the expense of these initial polar groups. Presumably, the dipole reorientations of urethane and urea are more restricted due to the strong association among themselves, in combination with effects of network

Downloaded by OHIO STATE UNIV LIBRARIES on September 17, 2012 | http://pubs.acs.org
Publication Date: July 26, 2001 | doi: 10.1021/bk-2001-0790.ch007

Downloaded by OHIO STATE UNIV LIBRARIES on September 17, 2012 | http://pubs.acs.org
Publication Date: July 26, 2001 | doi: 10.1021/bk-2001-0790.ch007

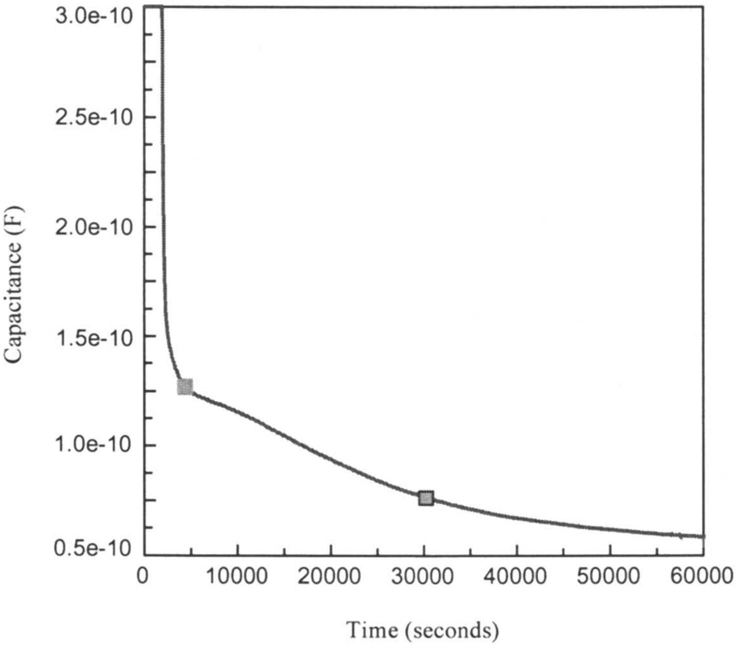

Figure 13. *Capacitance vs. time (73 min. to 500 min.)*

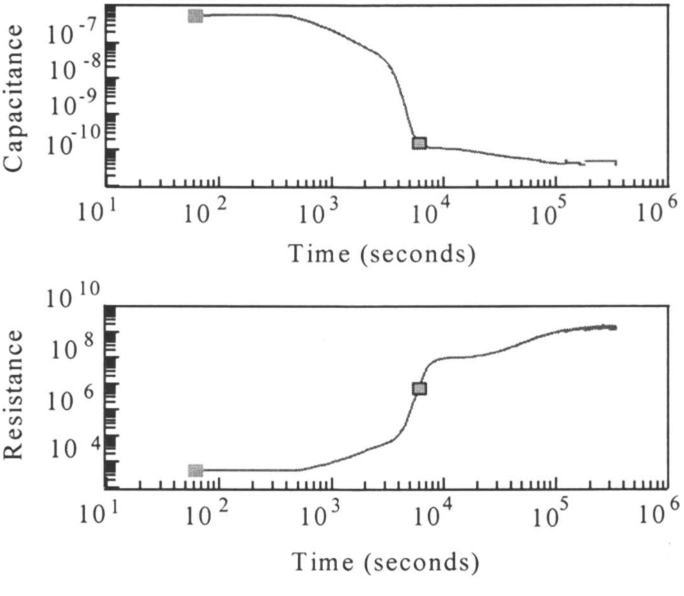

Figure 14. *Capacitance & resistance vs, time*

formation. After 500 minutes, the decrease in capacitance is even slower. When the dry process is monitored by the dry tester, it take approximately 8 hours for the film to become dry hard. This suggests that the whole system has vitrified at this stage.

After 83 hours, both capacitance and resistance changes have leveled off (Figure 14). This is consistent with the Persoz hardness and DMA measurement; after 3 days, both Persoz hardness and Tg are constant (Table 2).

Downloaded by OHIO STATE UNIV LIBRARIES on September 17, 2012 | http://pubs.acs.org
Publication Date: July 26, 2001 | doi: 10.1021/bk-2001-0790.ch007

Summary

DEA has been used to characterize the film formation process of 2K waterborne urethane through capacitance change with time and it is coupled with measurements of film composition change and property development which were followed by IR, dry time tester, Persoz hardness and DMA. Agreements was observed among those measurement. A new method was developed to overcome blocking effect for monitoring water evaporation and the results were in good agreement with weight loss measurements. DEA was especially sensitive in exploring the subtle change during the drying and film formation process. The film formation of 2K waterborne urethane follows a very similar path as conventional latex film formation form casting to coalescence. However, final property development depends on the curing rate which becomes very slow once the film is vitrified.

Acknowledgements

We would like to acknowledge the infrared analysis work of Dr. Gary Johnson, Dr. C. B. Walsh for valuable comments, and Air Products and Chemicals, Inc. for permission to publish this work.

Reference

1. D. E. Kranbuekl, D. Hood, C. Kellam, and J. Yang, *Film Formation in Waterbone Coatings,* **1996**, 646, 96.
2. G. L. Brown, *J. Polym. Sci.*, **1956**, 22, 423.

3. J. W. Vanderhoff, H. L. Tarkowski, M. C. Jenkins and E. B. Bradford, *J. Macromol. Chem.*, **1966**, 1, 361.
4. S. T. Eckersley and A. Rudin, *J. Appl. Polym. Sci.*, **1994**, 53, 1139.
5. S. T. Eckersley and A. Rudin in Film Formation in Waterborne Coatings; Editors, T. Provder, M. A. Winnik and M. W. Urban; ACS Symposium Series 648; 1996; p. 2.
6. J. W. Schultz and R. P. Chartoff, *J. Coat. Tech.*, **1996**, 68 (no. 861), 97.
7. M. W. Urban, C. L. Allison, C. C. Finch and B. A. Tatro, *J. Coat. Tech.*, **1999**, 77 (no. 888), 75.
8. Stephen D. Senturia and Norman F. Sheppard, *J. Advances in Polym. Sci.* Springer-Verlag Berlin Heidelberg **1986** (80), p. 1-47.
9. X. Gao and H.S. White, *J. Electroanal. Chem.*, **1995**, 389, 13.
10. D. D. Shepard, *J. Coat. Tech.*, **1996**, 68 (no. 857), 99.
11. D. R. Dissado, P. W. Green, R. M. Hill and T. A. Strivens, *J. Phys. D: Appl. Phys.*, **1989**, 22, 713.
12. D. R. Day, T. J. Lewis, H. L. Lee and S. D. Senturia J. Adhesion, **1985**, 18, 73
13. W. E. Dillon, D. A. Matheson and E. B. Bradford, *J. Coll. Sci.*, **1951**, 6, 108.

Downloaded by OHIO STATE UNIV LIBRARIES on September 17, 2012 | http://pubs.acs.org
Publication Date: July 26, 2001 | doi: 10.1021/bk-2001-0790.ch007

Chapter 8

On-Line In Situ Sensor Monitoring of Rapidly Curing Coatings-Films

D. Kranbuehl[1], J. Rogozinski[1], A. Meyer[1], L. Hoipkemeier[1], and N. Nikolic[2]

[1]Department of Chemistry and Applied Science, College of William and Mary, P.O. Box 8795. Williamsburg, VA 23187-8795
[2]Corporate Research Center, National Starch and Chemical Company at ICI Company, 10 Finderne Avenue, Bridgewater, NJ 08807

Frequency dependent dielectric measurements(FDEMS) have been used to monitor the extremely rapid polymerization of UV irradiated coatings-adhesives in situ in a representative coating fabrication environment. In one second, the FDEMS system can take 32 measurements, 8 data points each, an average of 4 measurements. Measurement of the cure processing properties of films is itself difficult because one side is exposed. Equally challenging the material goes from a thin layer of liquid to a rubbery or even hard state while changing its thickness. Monitoring the cure process of a coating when it occurs over periods of seconds adds even more difficulties to laboratory measurement. This paper will describe a dielectric technique involving an inert sensor which can be used both in the laboratory, during processing in a production environment and during use in the field to monitor the cure process during application and degradation during use.

An in situ frequency dependent electrical measurement sensor (FDEMS) has been successfully used to monitor cure and the buildup in properties during film formation. The planar micro-sensor is able to make continuous uninterrupted measurements of the film while it cures as a coating with only one side exposed. It is able to monitor reaction onset, cure rate, viscosity, buildup in hardness, cure completion and related processes such as latex coalescence and evolution of volatiles.[1-5] Effects of storage, temperature, humidity, thickness and variations in composition on the cure process can readily be detected. The sensor monitors the changes in the rate of translational motion of ions and rotational motion of dipoles through frequency dependent complex permittivity measurements.

Downloaded by PENNSYLVANIA STATE UNIV on September 17, 2012 | http://pubs.acs.org
Publication Date: July 26, 2001 | doi: 10.1021/bk-2001-0790.ch008

In Film Formation in Coatings; Provder, T., et al.;
ACS Symposium Series; American Chemical Society: Washington, DC, 2001.

Background

Frequency dependent dielectric measurements, made over many decades of frequency, Hz-MHz, have already been shown to be a sensitive, convenient automated means for characterizing the processing properties of thermosets and thermoplastics.[1-15] Using a planar wafer thin sensor, measurements can be made in situ in almost any environment. Through the frequency dependence of the impedance, this sensing technique is able to monitor changes in the molecular mobility of ions and dipoles. These changes in molecular mobility are then related to chemical and physical changes which occur during use or during processing. The FDEMS techniques have the advantage that measurements can be made both in the laboratory, in situ in the fabrication tool and in situ during use. Few laboratory measurement techniques have the advantage of being able to make measurements in a processing tool and in the field during use of a thin film or a coating. It can be used at temperatures exceeding 400°C and at pressures of 100 atm, with an accuracy of 0.1% and a range in magnitude of over 10 decades. It is difficult for most other in the field techniques to attain this level of sensitivity in harsh processing environments.

At the heart of dielectric sensing is the ability to measure the changes at the molecular level in the translational mobility of ions and changes in the rotational mobility of dipoles in the presence of a force created by an electric field. Mechanical properties reflect the response in displacement on a macroscopic level due to a mechanical force acting on the whole sample. The reason why dielectric sensing is quite sensitive is rooted in the fact that changes on the macroscopic level originate from changes in force displacement relationships on a molecular level. Indeed, it is these molecular changes in force-displacement relationships which dielectric sensing measures as the resin cures and ages. They are the origin of the resin's macroscopic changes in mechanical performance properties during processing and during use.

Instrumentation

Frequency dependent complex dielectric measurements are made using an Impedance Analyzer controlled by a microcomputer.[1-3] In the work discussed here, measurements at frequencies from Hz to MHz are taken continuously throughout the entire cure process at regular intervals and converted to the complex permittivity, $\epsilon^*=\epsilon'-i\epsilon''$. The measurements are made with a geometry independent DekDyne micro sensor which has been patented and is now commercially available and a DekDyne automated dielectric measurement system. This system is used with either commercially available impedance bridges or specially built marine environmental bridges for use on offshore oil platforms. The system permits multiplexed measurement of several sensors. The sensor itself is planar, 2.5 cm x 1.25 cm area and 5 mm thick. This single sensor-bridge microcomputer assembly is able to make continuous uninterrupted measurements of both ϵ' and ϵ'' over decades in magnitude at all frequencies. The sensor is inert and has been used at temperatures exceeding 400°C and over 60 atm pressure.

The UV cure light source was manufactured by Novacure. The UV lamp had a spectral range of 320-390 nm with a maximum intensity of 3,000 mW/cm^2. Unless otherwise specified the radiation sequence lasted 5 seconds, at 1000 mW/cm^2 representing a total dose of 5 J.

Downloaded by PENNSYLVANIA STATE UNIV on September 17, 2012 | http://pubs.acs.org
Publication Date: July 26, 2001 | doi: 10.1021/bk-2001-0790.ch008

Downloaded by PENNSYLVANIA STATE UNIV on September 17, 2012 | http://pubs.acs.org
Publication Date: July 26, 2001 | doi: 10.1021/bk-2001-0790.ch008

Chemistry of UV Cure Expoxies

The chemistry of the UV cure epoxies examined in this project is based on the use of a triaryl sullfonium hexafluoro anitimonate catalyst which is added to an often nonstoichiometric mixture cycloaliphatic diepoxides and diol monomers. When exposed to UV radiation the catalyst photocleaves to liberate an exceptionally strong acid, hydrogen hexafluoro antimonate which initiates the rapid cure.

Theory

Frequency dependent measurements of the materials' dielectric impedance as characterized by its equivalent capacitance, *C*, and conductance, *G*, are used to calculate the complex permittivity, $\epsilon^*=\epsilon'-i\epsilon''$, where $\omega=2\pi f$, f is the measurement frequency and C_o is the equivalent air replacement capacitance of the sensor.

$$\epsilon'(\omega) = \frac{C(\omega)\ \mathit{material}}{C_o} \qquad \epsilon''(\omega) = \frac{G(\omega)\ \mathit{material}}{\omega C_o} \tag{1}$$

This calculation is possible when using the sensor whose geometry is invariant over all measurement conditions. Both the real and the imaginary parts of ϵ^* can have a dipolar and ionic-charge polarization components.

$$\epsilon' = \epsilon'_d + \epsilon'_i \qquad \epsilon'' = \epsilon''_d + \epsilon''_i \tag{2}$$

Plots of the product of frequency (ω) multiplied by the imaginary component of the complex permittivity $\epsilon''(\omega)$ make it relatively easy to visually determine when the low frequency magnitude of ϵ'' is dominated by the mobility of ions in the resin and when at higher frequencies the rotational mobility of bound charge dominates ϵ''. Generally, the magnitude of the low frequency overlapping values of $\omega\epsilon''(\omega)$ can be used to measure the change with time of the ionic mobility through the parameter σ where

$$\sigma(ohm^{-1}cm^{-1} = \epsilon_o\omega\epsilon''_i(\omega) \qquad \epsilon_o = 8.854 \times 10^{-14}C^2J^{-1}cm^{-1} \tag{3}$$

The changing value of the ionic mobility is a molecular probe which can be used to quantitatively monitor the viscosity of the resin during cure. The dipolar component of the loss at higher frequencies can then be determined by subtracting the ionic component.

$$\epsilon_d''(\omega)\ \textit{dipolar} = \epsilon''(\omega) - \frac{\sigma}{\omega\epsilon_o} \qquad (4)$$

Peaks in ϵ''_d dipolar (which are usually close to the peaks in ϵ'') can be used to determine the time or point in the cure process when the *mean* dipolar relaxation time has attained a specific value $\tau = 1/\omega$, where $\omega = 2\pi f$ is the frequency of measurement. The dipolar mobility as measured by the mean relaxation time τ can be used as a molecular probe of the changing value of the glass transition temperature T_g. The time of occurrence of a given dipolar relaxation time as measured by a peak in a particular high frequency value of $\epsilon''(\omega)$ can be quantitatively related to the attainment of a specific value of the polymer's T_g. Finally, the changing value of $\frac{d\epsilon''}{dt}/\epsilon''$ can be used to monitor in situ during processing the buildup in degree of cure and related end-use properties such as modulus, hardness, etc., during the final stages of cure or post cure in situ in fabrication environment. Once cured and in the use environment the changes in or $\frac{d\epsilon'}{dt}/\epsilon'$ can be related to aging of the performance properties during use, that is life monitoring of polymeric structures while in use in the field.

Relation of Dielectric Properties to Changes in Macroscopic Performance Properties

The time of occurrence and values of τ, σ, $\frac{d\epsilon''}{dt}/\epsilon''$ and $\frac{d\epsilon'}{dt}/\epsilon'$ can be used to monitor changes in macroscopic performance properties through laboratory calibrations which relate these changes in molecular translational mobility of charge, σ, to the macroscopic performance property of interest. Once this relation is established in the laboratory, in situ dielectric measurements of ϵ'' and thereby σ and τ can be used to monitor with the calibration, changes in the macroscopic performance property during fabrication or during use in the field.

The general relation between conductivity σ and viscosity η is also well established in the fluid state where σ is monitoring a molecular viscosity and is proportional, in general, to the macroscopic viscosity as $\sigma \propto \eta^{-b}$. In the gel-glass transition region, it is well documented τ monitors changes in the glass transition temperature, T_g. Exact determinations of T_g from τ can be made using a VTF or WLF type molecular model. Again once the calibration constants relating τ and T_g are made from laboratory measurements, in the field measurements of ϵ'' dipolar and thereby τ can be used to monitor changes in T_g during cure or during use.

Finally the simple absence of change in $\epsilon''(\omega)$ indicates no change in either

Downloaded by PENNSYLVANIA STATE UNIV on September 17, 2012 | http://pubs.acs.org
Publication Date: July 26, 2001 | doi: 10.1021/bk-2001-0790.ch008

Downloaded by PENNSYLVANIA STATE UNIV on September 17, 2012 | http://pubs.acs.org
Publication Date: July 26, 2001 | doi: 10.1021/bk-2001-0790.ch008

translational mobility of charge and rotational mobility of dipoles. This is a very strong indicator that there is no change in the performance properties of the material.

Similarly, the rate of change in the magnitude of ϵ'' and ϵ' of a material indicates change in the molecular mobility and hence change in the performance properties. The relation between these changes in molecular mobility and performance properties does not follow a single universal relationship as the molecular structure of amorphous materials is complex and theories of the structure of amorphous gel-solid materials are far from complete. Nevertheless careful laboratory measurement of the relationship between changes in molecular ϵ'' and ϵ' are due to changes at the molecular level in translational mobility of charge and rotational mobility of dipoles. These changes in ϵ'' and ϵ' due to changes in molecular mobility can be quantitatively related to changes in other macroscopic force-displacement properties such as modulus, hardness, dry-to-touch and other ASTM states of reaction advancement during processing-cure and over time during use for polymer materials and within given defined environments.

In summary, dielectric measurements are an extremely sensitive means to monitor changes in the state of a polymer material or resin both as it ages and during synthesis, processing and cure. The reason dielectric sensing is extremely sensitive is the fact that changes in macroscopic force-displacement properties such as modulus, elasticity, viscosity, T_g, etc. originate from changes in mobility at the molecular level. Dielectric measurements of ϵ^* monitor molecular mobility and equally important they can be made over many orders of magnitude, in harsh environments, continuously and in situ for polymeric composites, coatings, adhesives, in virtually any environment.

In Situ On Line Monitoring of a Curing Film

First to help understand the dielectric FDEMS sensor monitored cure of a film, Figure 1 shows the changing value of log ($\epsilon''*\omega$) with time of a representative commercial epoxy-amine coating during the first 12 hours after application under normal environmental conditions 24°C and 45% relative humidity. The cure is dominated by ionic diffusion for the first 100 minutes at the lower frequencies as indicated by the overlapping $2\pi f\epsilon''$ lines are proportioned to the inverse of the macroscopic viscosity where, $2\pi f\epsilon'' = A(\frac{1}{\eta})^x$. At the time of application the coating is in the 'wet' stage. In this stage the viscosity is in very low and solvent evaporation occurs rapidly. Solvent loss from the coating was measured by thermogravimetric analysis (TGA) in a pan of approximately the same film thickness. The 'wet' stage of solvent loss was seen in the rapid weight loss in the first 144 minutes. The evaporation slows down markedly after six hours when the change in weight is barely noticeable. Thus a combination of solvent loss and cross-linking of the resin rapidly increase the viscosity of the film which is monitored in the lowering of the value of $2\pi f\epsilon''$ in Figure 1. At 100 minutes into the run the coating reaches it set-to-touch point as defined by ASTM D1640-83 guidelines when the sensor output is log ($2\pi f\epsilon''$) = 4.2. Using the 50Hz line to monitor the initial cure, one observes again by ASTM inspection that the calibration value of log ($2\pi f\epsilon''$) = 2.8 occurs at dry-to-hard. Achievement of these values by the sensor can be used as in situ means of detecting and monitoring when dry-to-touch and dry-to-hard have occurred in any environment.

Downloaded by PENNSYLVANIA STATE UNIV on September 17, 2012 | http://pubs.acs.org
Publication Date: July 26, 2001 | doi: 10.1021/bk-2001-0790.ch008

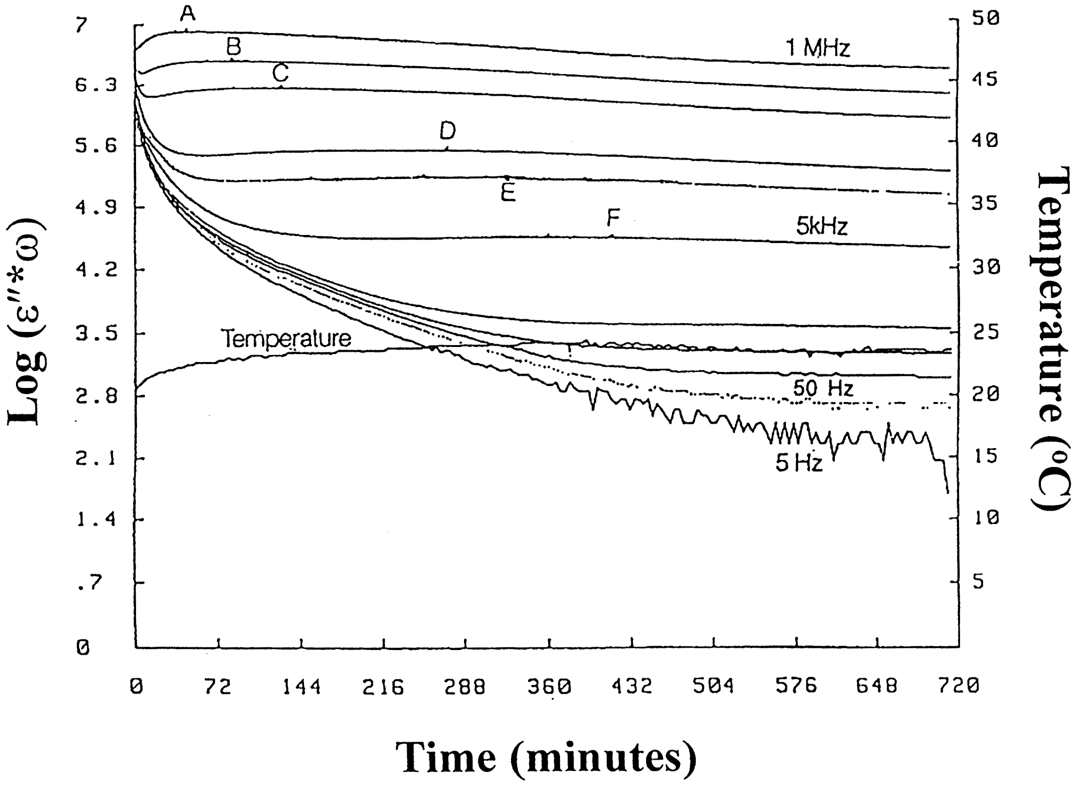

Figure 1. Changing value of $\epsilon'' * \omega$, $\omega = 2\pi f$, with time of a commercial epoxy-amine coating during first 12 hours after application. The letters A through F indicate the time at which the value of ϵ'' peaks for each frequency.

To monitor the long term properties of the coating it is best to examine $2\pi f\epsilon''$ on a non-log scale due to the decreasing change in the signal. A continual decrease in the signal showed that the sample was still curing. There was no further detectable change in ϵ'' 68 hours after application. Therefore the sample, as seen by frequency dependent impedance measurements, has obtained the fullest cure possible after 3 days under 24°C and 45% RH conditions.

The high frequency values of ϵ'' show peaks in Figure 1. They monitor the α relaxation process which can be quantitatively correlated with the buildup in Tg during cure. This is a cooperative relaxation process involving many molecules. It is seen both in dielectric relaxation and dynamical mechanical measurements. The occurrence of this peak monitors the buildup in Tg as well as the corresponding final use properties of the curing coating. The peaks in the 5 kHz to 1 MHz $2\pi f\epsilon''$ lines, points, A,B,C,D,E and F, indicate the time when the characteristic relaxation time for dipolar relaxation $\tau = 1/2\pi f$ has occurred. Thus, point A, 15 minutes, marks the cure time when $\tau = (2\pi x10^6)^{-1}$ sec. and the point F, at 400 minutes, marks the time when the rotational relaxation time has slowed to $\tau = 1(2\pi * 5x10^3)$ sec. The relationship between the value of τ and the value of Tg or any other use property can be quantitatively determined by correlating measurements of τ with measurements of Tg or the use property of interest. Using a correlation plot of a mathematical WLF type fit where $\ln \tau \,\alpha\, A/(B-T(T-Tg))$, the FDEMS output can be used to continuously monitor the buildup in an end-use property such as Tg in situ under the actual cure conditions.

FDEMS output similar to Figure 1 can be used to monitor the variation in cure rate with temperature, humidity, airflow, pigment loading, catalyst concentration, thickness, age, batch, etc.

In Situ, On-Line Monitoring of Rapid Cure

Figure 2 displays the output of a FDEMS sensor monitored UV cure of a specially formulated epoxy coating. The data is taken at 1 kHz, one frequency, to give the maximum number of data points per minute. The sensor output clearly shows the point of the UV flash onset of cure about one minute into the display. The output clearly shows the rapid drop in molecular mobility as monitored by ϵ'', of over 3 decades in about 30 seconds.

Figure 3 is another cure run on the same resin. The FDEMS output measured at 5 frequencies, 100 Hz, 120 Hz, 1 kHz, 10 kHz and 100 kHz with a 0.2 minute time interval between each measurement at the same frequency shows that during the approximate 1 minute time interval required for cure, the 100 Hz, 120 Hz and 1 kHz output of $\epsilon'' * \omega$, $\omega = 2\pi f$, overlaps. This indicates as discussed using equation 3 that at these frequencies the changing value of ϵ'' is monitoring ionic conductivity. Ionic conductivity is determined by both the mobility of the charged particles which monitors buildup in viscosity and by the number of charge carriers. The number of ions is usually approximately constant in epoxy cure. However it can change significantly in UV catalyst initiated cure during the formation of the hydrogen hexafluoro antimonate acid.

Figure 4 displays the output during a third cure run on the same epoxy. In this run, the 10 second interval during which the 5 second UV pulse occurs is emphasized. This 10 second picture clearly shows the UV pulse was initiated at 7.5 seconds. There

Downloaded by PENNSYLVANIA STATE UNIV on September 17, 2012 | http://pubs.acs.org
Publication Date: July 26, 2001 | doi: 10.1021/bk-2001-0790.ch008

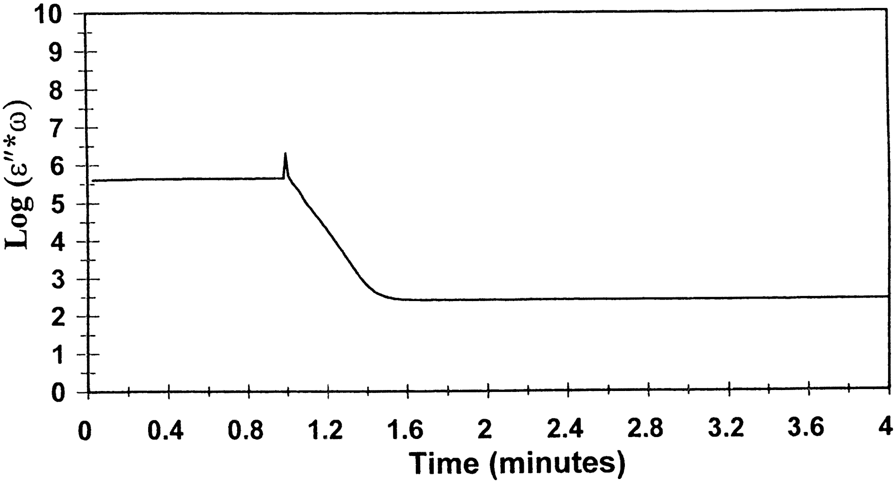

Figure 2. Changing value of ε″ ω at 1 kHz of a uv curing epoxy resin during the initial 4 minutes. The 5 second uv pulse was applied at the time of the spike in ε″, at approximately 1 minute.*

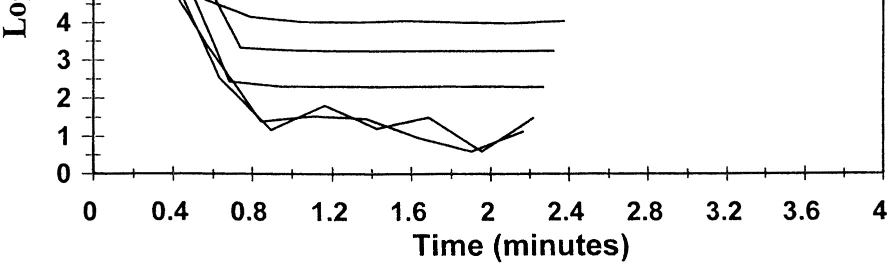

Figure 3. Changing values of ε″ ω monitored at 5 frequencies, 100, 10, 1, 0.120 and 0.100 kHz from top to bottom.*

Downloaded by PENNSYLVANIA STATE UNIV on September 17, 2012 | http://pubs.acs.org
Publication Date: July 26, 2001 | doi: 10.1021/bk-2001-0790.ch008

Downloaded by PENNSYLVANIA STATE UNIV on September 17, 2012 | http://pubs.acs.org
Publication Date: July 26, 2001 | doi: 10.1021/bk-2001-0790.ch008

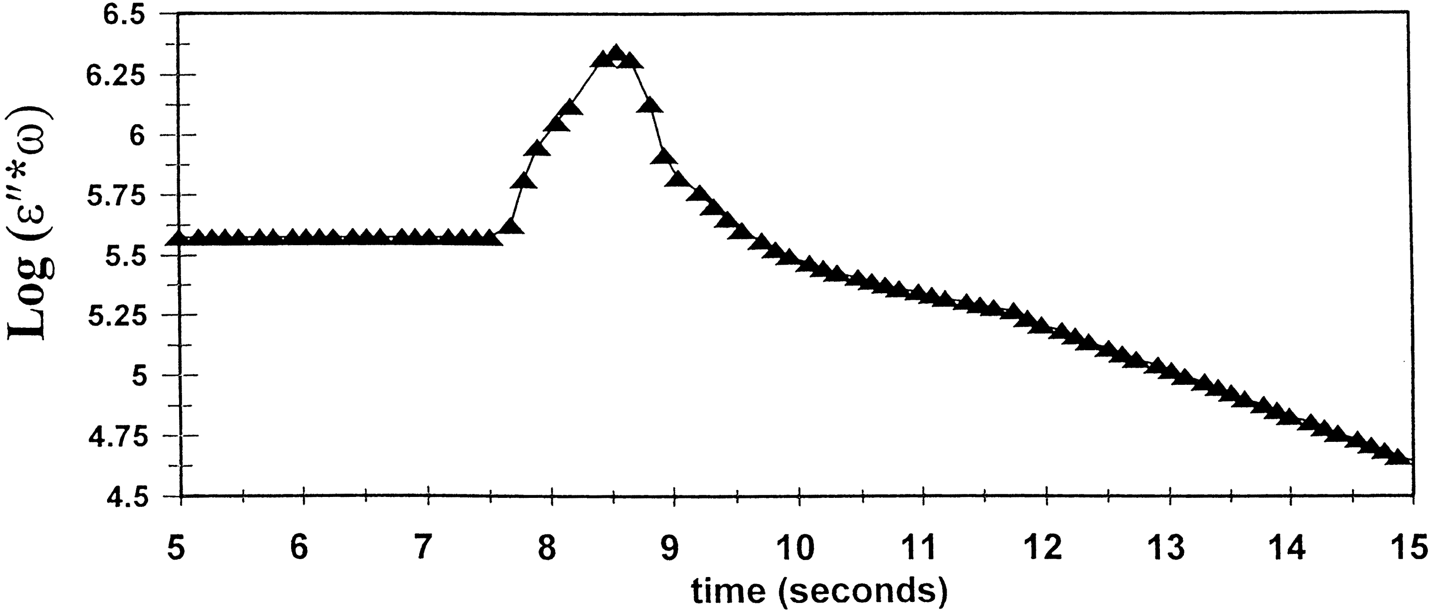

*Figure 4. Blowup of changing value of ε″ * ω at 1 kHz due to a 5 second pulse over a 10 second interval.*

is a 10 fold increase in the conductivity in the next second due to the formation of the protons generated by formation of the acid catalyst. One second later at 8.5 seconds, the reaction is initiated driving the viscosity down. The one second delay may reflect either the diffusion kinetics and/or the fact that the FDEMS sensor sees the bottom portion of the epoxy bead. Throughout the 5 second pulse more catalyst is activated while the viscosity is building up. At 12 seconds the rate of decrease in conductivity increases and follows a log decay. This marks the end of the pulse, actually 4.5 seconds as monitored by the FDEMS system. At this point the sensor is tracking the buildup in viscosity as it decreases the translational mobility of the ions.

Figure 5, a blowup of Figure 2 displays the sensitivity of the FDEMS signal to monitor cure completion over the 0.5 minute to 2.5 minute time period. This blowup of Figure 2 on a non log scale demonstrates how the output can be used to monitor the approach to full cure as monitored by the approach to a constant quenched value of the mobility, ie., $\frac{d\epsilon''}{dt} = 0$. Figures 2 and 5 show the major portion of cure is over after about 30 seconds, between 1.0 minute and 1.5 minutes.

The magnitude of ϵ'' and/or the corresponding values of the ionic mobility can be directly correlated with macroscopic performance properties of viscosity, buildup in Tg, dry to touch, dry to hard as well as durability as discussed previously.

Figure 6 displays the output of a 10 second UV pulse of 40 Joules. This figure suggests 40 Joules is too much energy. The exothermic reaction appear to release so much heat that the viscosity is decreased due to an increase in temperature at 1.2 minutes resulting in a brief increase in the conductivity during the polymerization reaction.

Figure 7 displays the cure of a thick 5mm coating using the standard 5 Joule 5 second pulse. The planar sensors rests at the bottom of the layer and is sensitive to the lower 1 mm portion of the coating. This output suggests that the UV pulse is not able to activate enough catalyst to fully cure the epoxy resin on the lower surface. Visual inspection of this thick film confirmed it was fully cured on the top but tacky on the lower surface.

Finally, Figure 8 a, b, c and 9 a, b, c display the ability of the FDEMS output to monitor and compare the cure properties of three different formulations. The 3 formulations were based on the cycloaliphatic epoxide ERL-4221 sold by Union Carbide. They contained different types and compositions of diols along with the triaryl sulfonium hexaflouro antiminate. Figure 8 displays the complete FDEMS output for full cure of each formulation. Figure 9 displays a non log blowup of the time interval needed to approach full cure. Clearly formulation 2 cures the most rapidly and formulation 1 is the slowest.

Conclusions

- In situ on-line dielectric sensor measurements can be used to monitor the cure process in very rapid UV initiated cure of coatings and films;

Downloaded by PENNSYLVANIA STATE UNIV on September 17, 2012 | http://pubs.acs.org
Publication Date: July 26, 2001 | doi: 10.1021/bk-2001-0790.ch008

Downloaded by PENNSYLVANIA STATE UNIV on September 17, 2012 | http://pubs.acs.org
Publication Date: July 26, 2001 | doi: 10.1021/bk-2001-0790.ch008

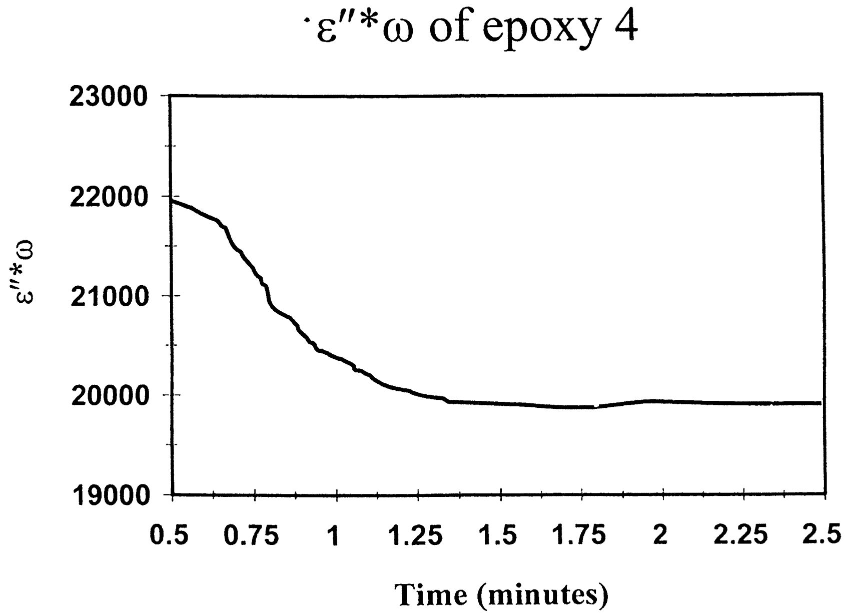

Figure 5. Blowup of the changing value of $\epsilon''* \omega$ on a non log scale between 0.5 and 2.5 minutes as the resin approaches full cure.

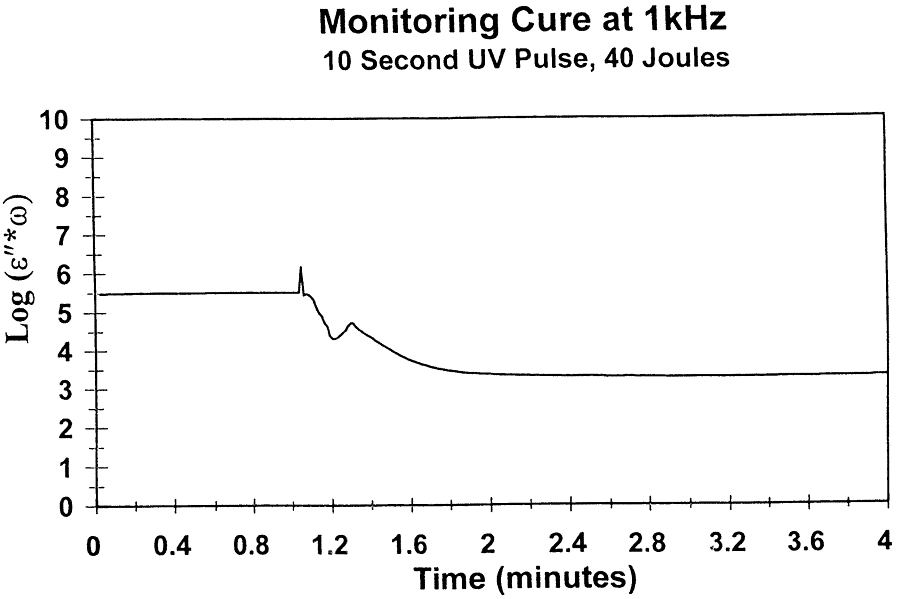

Figure 6. Changing value of $\epsilon''* \omega$ at 1 kHz during uv cure using a 10 second 40 Joule pulse.

Downloaded by PENNSYLVANIA STATE UNIV on September 17, 2012 | http://pubs.acs.org
Publication Date: July 26, 2001 | doi: 10.1021/bk-2001-0790.ch008

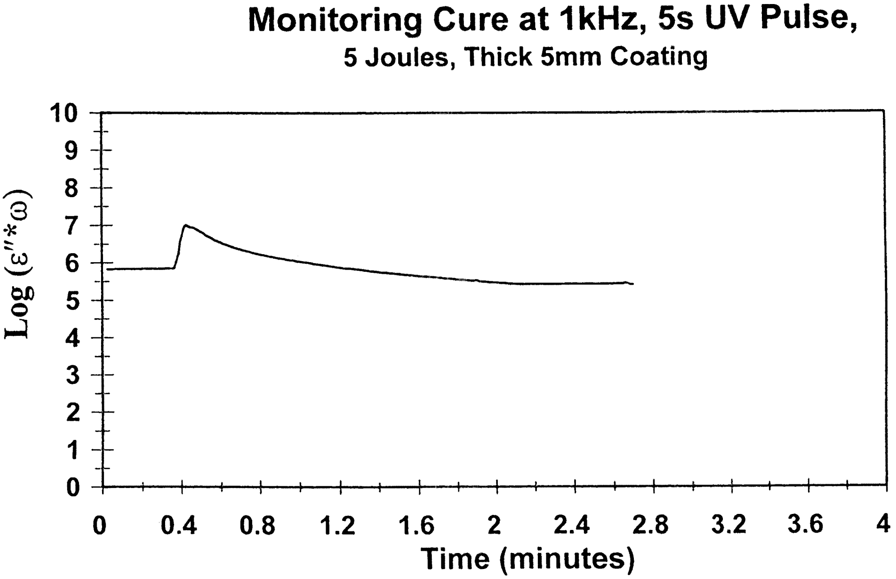

Figure 7. Changing value of $\epsilon''* \omega$ at 1 kHz of a thick 5 mm coating and a 5 second, 5 Joule pulse. Sensor is monitoring cure of resin at bottom 1 mm of coating.

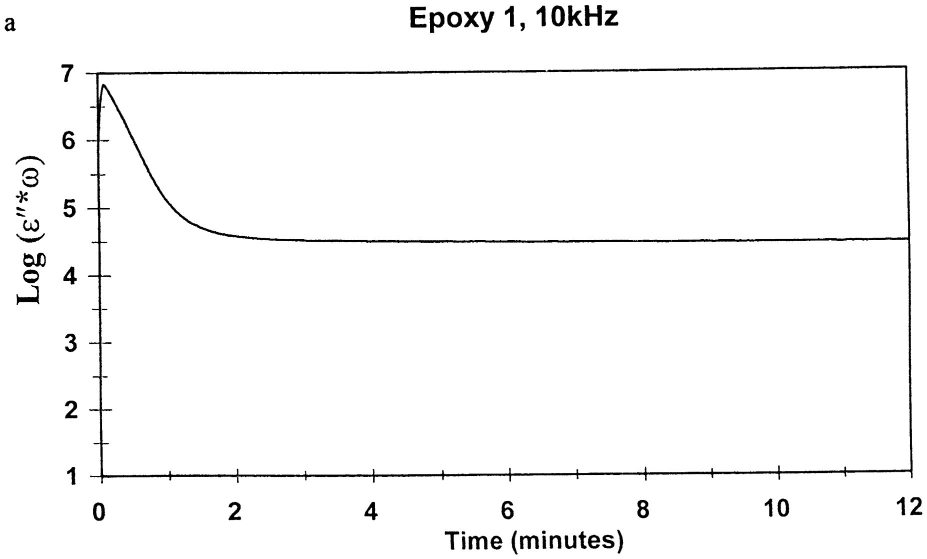

Figure 8. Figures 8a, 8b and 8c emphasize the differences in the rate of rapid cure during the initial 1 to 3 minutes of 3 different formulations of the uv curing epoxy resin under a 5 second, 5 Joule pulse.

b

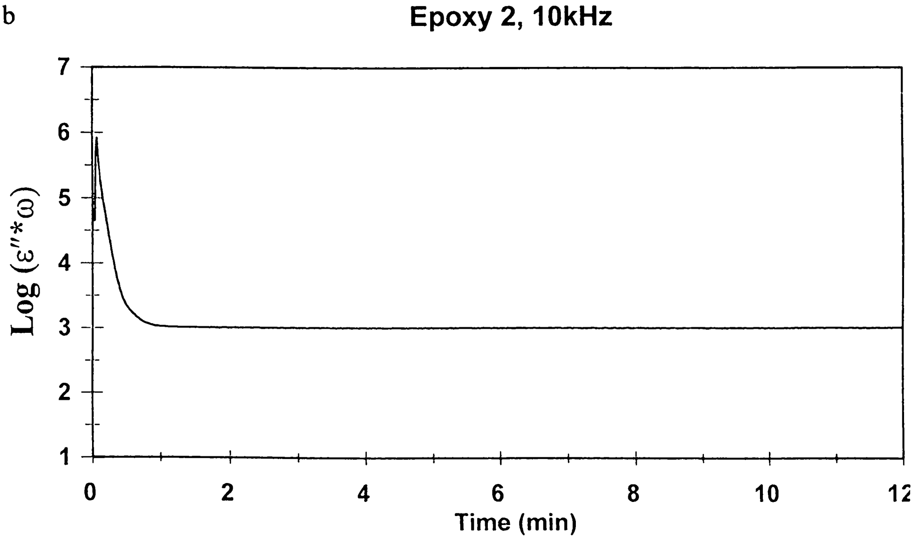

c

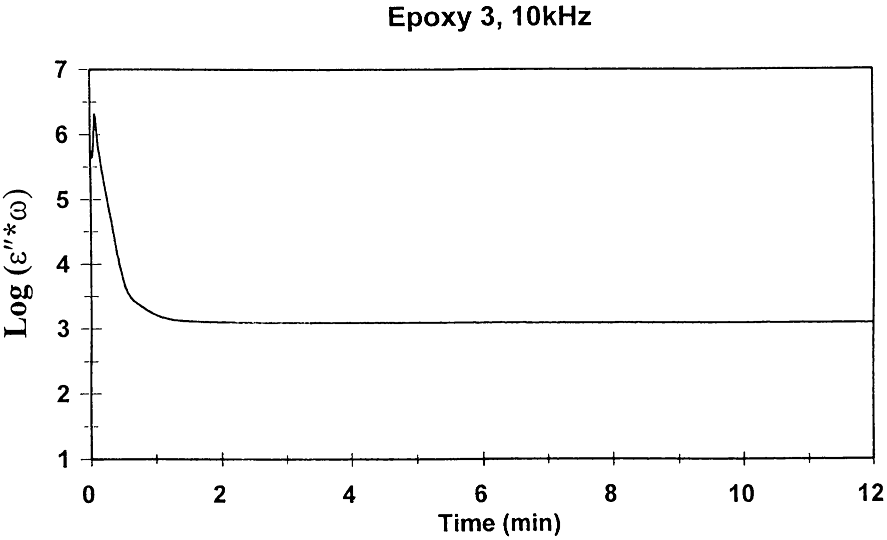

Figure 8. *Continued.*

Downloaded by PENNSYLVANIA STATE UNIV on September 17, 2012 | http://pubs.acs.org
Publication Date: July 26, 2001 | doi: 10.1021/bk-2001-0790.ch008

Downloaded by PENNSYLVANIA STATE UNIV on September 17, 2012 | http://pubs.acs.org
Publication Date: July 26, 2001 | doi: 10.1021/bk-2001-0790.ch008

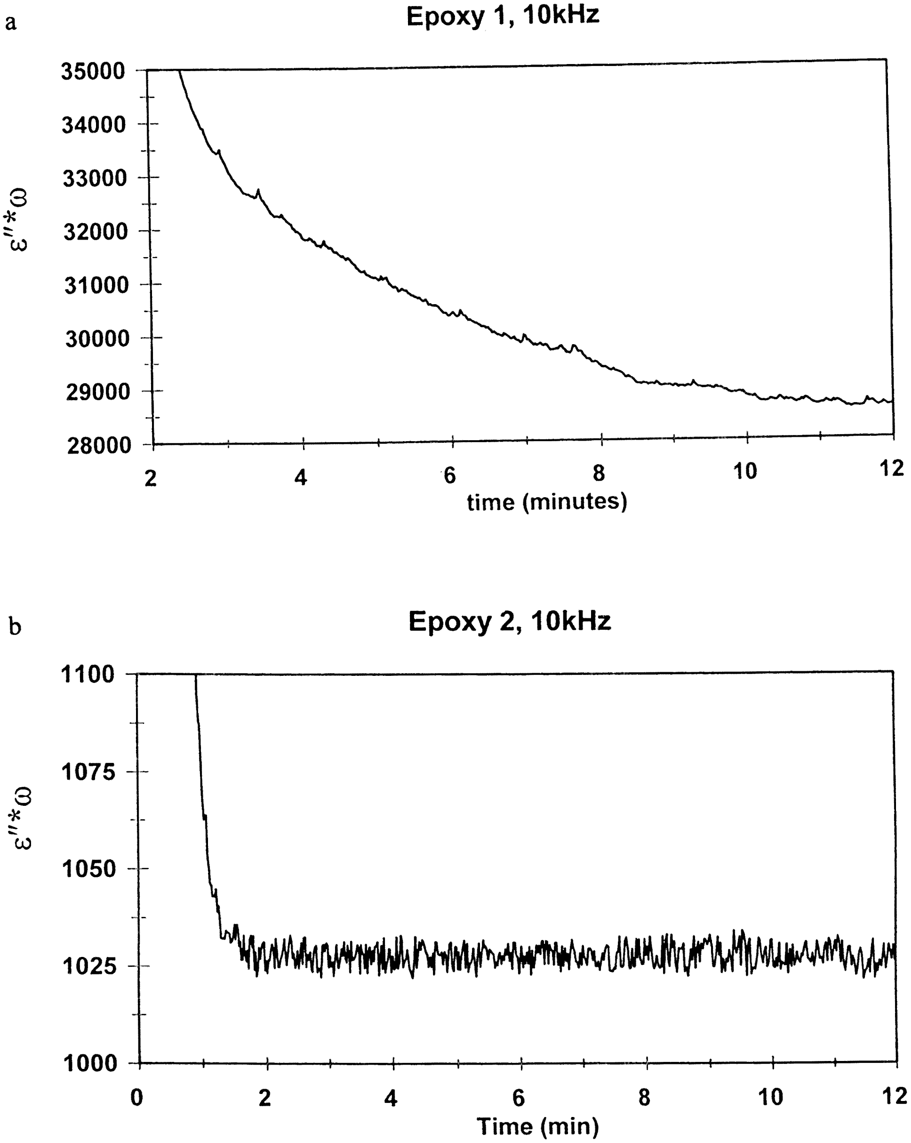

Figure 9. Figures 9a, 9b and 9c emphasize the differences of the long time approach to full cure of these same 3 formulations using a non log blowup of the changing value of $\epsilon'' * \omega$.

Downloaded by PENNSYLVANIA STATE UNIV on September 17, 2012 | http://pubs.acs.org
Publication Date: July 26, 2001 | doi: 10.1021/bk-2001-0790.ch008

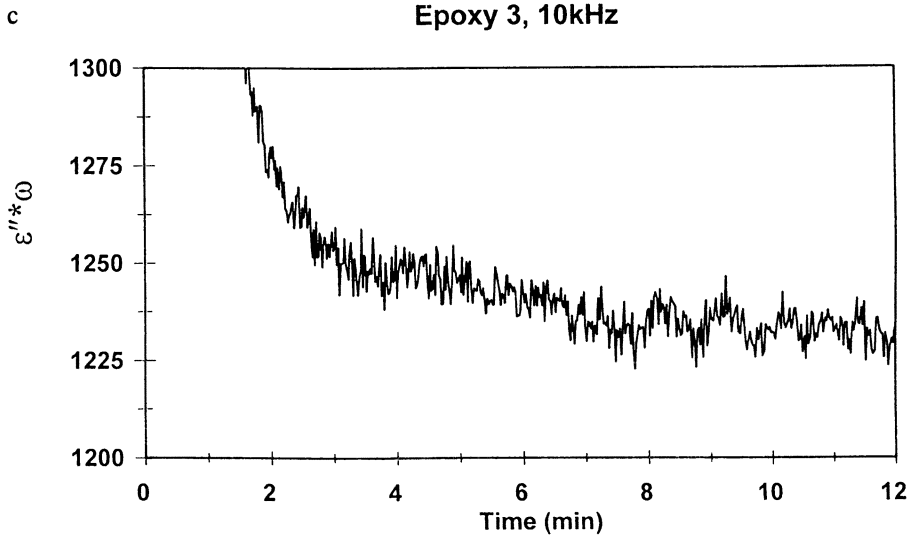

Figure 9. *Continued.*

- The dielectric sensor system can take up to 32 measurements, 8 data points each on average of 4 measurements in one second;
- UV light is able to cure thick coatings up to 5 mm thick at the same rate as thine coatings;
- The dielectric sensor system can be used to monitor the coating cure time in both a laboratory or a production-fabrication environment.

Acknowledgment

Support from ICI World Wide Industries, National Starch, ICI Paints, the NSF Center of Excellence in Polymeric Adhesives and Composites NSF #MR912004 at Virginia Tech, Blacksburg, Virginia, and from NSF grant Int. 9726207 is greatly acknowledged.

Downloaded by PENNSYLVANIA STATE UNIV on September 17, 2012 | http://pubs.acs.org
Publication Date: July 26, 2001 | doi: 10.1021/bk-2001-0790.ch008

References

1. Kranbuehl, D., D. Hood, C. Kellam, J. Kang, *Film Formation in Waterborne Coatings* ed. T. Provder, M. Winnik, M. Urban ACS Sym Ser, 648 Am Chem Soc. Washington, DC 96-117 (1996).
2. Kranbuehl, D., *Dielectric Spectroscopy of Polymeric Materials* ed. J. Runt, J. Fitzgerald, Am. Chem. Soc., Washington, DC 1997 pp. 303-328.
3. Kranbuehl, D., *Developments in Reinforced Plastics,* Vol. 5, Elsevier Applied Science Publishers, New York, pp. 181-204 (1986).
4. Kranbuehl, D., *Encyclopedia of Composites,* ed., Stuart M. Lee. VCH Publishers, New York, pp. 531-43 (1989).
5. Kranbuehl, D., *Structural Health Monitoring,* ed. Fu-Kuo Chang Int. Workshop, Stanford Univ., Sept. 1997, sponsored by Air Force Scientific Research, Army Research Office, Nat. Sci. Foundation, Technomic 1997
6. Senturia, S.: Sheppard, S. *J. Appl. Polym. Sci.* **1986**, *80*, 1-48.
7. Polymer Materials Science and Engineering, May, C. ed ACS Symposium Series 27, Americna Chemical Society, Washington, DC **1983**.
8. Hedvig, P. *Dielectric Spectroscopy of Polymers,* Wiley, New York **1977**.
9. Mijovic, J., Belluci, F.; Nicolais, L. Electrochem Soc. **1995**, *142(4)*, 1176-1182.
10. Mijovic, J.; Winnie Tee, C.F. *Macromolecules* **1994**, *27*, 7287-7293.
11. Parthun, M.B.; Johari, G. *Maacromolecules* **1992**, *25*, 3254-3263.
12. Mathieu, C.; Boiteux, G.; Seytre, G.; Villain, R.; Dublineau, P. *J. Non-Cryst. Solids* **1994**, *172-174*, 1012-1016.
13. Gallone, G.; Levita, G.; Mijovic, J.; Andejellics, Rolla, P. *Polymer* **1998**, *39*, 2095.
14. Deng, Y.; Martin, G. *Macromolecules* **1994**, *27*, 5141-5146.
15. Companik, J.; Bidstrup, S. *Polymer* **1994**, *35*, 4823-4840.

Downloaded by STANFORD UNIV GREEN LIBR on September 17, 2012 | http://pubs.acs.org
Publication Date: July 26, 2001 | doi: 10.1021/bk-2001-0790.ch009

Chapter 9

Acetal Functionalized Latex Films Capable of Cross-Linking at Ambient Temperatures

C. Soares[1], B. Charleux[1,*], J.-P. Vairon[1], C. Vergé[2], and K. Loyen[2]

[1]Laboratoire de Chimie Macromoléculaire, UMR 7610, Université Pierre et Marie Curie, T44, E1 4, Place Jussieu, 75252 Cedex 05, France
[2]Elf-Atochem, CERDATO, 27470 Serquigny, France

Crosslinked films were obtained at room temperature from acetal functionalized latexes. Crosslinking was induced by acidification of the latex serum prior to film formation. Final crosslink density was shown to be a function of the initial concentration of functional monomer as well as a function of pH. Solvent resistance and mechanical properties were highly improved.

The use of aqueous polymer latexes as binders represents one of the best alternatives to reduce the emission of volatile organic compounds (V.O.C.) in coating applications (1,2). However, the ultimate mechanical properties and solvent resistance of the films do not usually match the level of performance of solvent-borne coatings. To improve the properties of those water-borne films, a current strategy is based on the use of post-crosslinkable latexes (3). Crosslinking is accomplished via reactive groups which are covalently incorporated into the latex particles using functional comonomers (3). Among those systems one can distinguish between the addition of an external crosslinker into a functionalized latex (two-pack system) the blend of co-reactive latexes (two-pack-in-one-pot system) and self-crosslinkable latexes. For many of those systems, the formation of chemical crosslinks is performed at elevated temperature. Nevertheless, some examples of functionalized latex films for which

---

* Corresponding author (E-mail address : charleux@ccr.jussieu.fr)

In Film Formation in Coatings; Provder, T., et al.;
ACS Symposium Series; American Chemical Society: Washington, DC, 2001.

Downloaded by STANFORD UNIV GREEN LIBR on September 17, 2012 | http://pubs.acs.org
Publication Date: July 26, 2001 | doi: 10.1021/bk-2001-0790.ch009

post-crosslinking reaction operates at room temperature can be found in the literature (4-18). The main requirement is that the system should be chemically stable during polymerization and storage in order to avoid either the loss of reactive groups by potential hydrolysis or premature crosslinking reactions. The chemical reaction leading to crosslink formation should only take place during the film formation process. This contradiction is usually overcome in the case of a two-pack system with addition of the crosslinker just prior to film formation and with a two-pack-in-one-pot system for which repulsion between the particles prevents premature mixing of the two different functionalized polymers. In order to avoid early crosslinking in self-crosslinkable latex, the chemical reaction is usually induced by an external parameter such as temperature, UV light, or a change in pH. In all cases, the ultimate properties will be directly related to the competition between the chain interdiffusion and the chemical reaction (12,19).

In this context, the present work describes a one-component self-curable latex system, undergoing crosslinking at room temperature. This system is stable during storage and becomes reactive during film formation at a selected pH value. The incorporated functional monomer, the methacrylamido acetaldehyde dimethyl acetal (MAAMA, Scheme 1), contains an acetal group stable at alkaline pH, which can be hydrolyzed into the corresponding reactive aldehyde counterpart under acidic conditions. Acetal-bearing monomers have already been used in the past to promote crosslinking reactions in polymers (20,21). The most studied one was the acrylamidobutyraldehyde dialkyl acetal. Upon acid catalysis, this monomer cyclizes into a hemiamidal intermediate which was shown to play a key role in the chemistry of crosslinking. Monomers with a shorter connecting chain between the amide and the acetal, such as MAAMA, have not been studied. Regarding the crosslinking reactions, the impossibility to form an intramolecular hemiamidal cycle should lead to a completely different behavior. This assumption prompted us to carefully examine the chemistry of self-crosslinking induced by MAAMA under acidic conditions. The present work is focused on the effect of the amount of functional monomer in the latex particles and on the effect of pH on kinetics of the crosslinking reaction and on the properties of the films.

Scheme 1

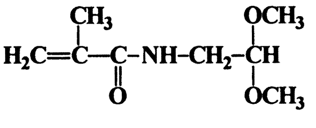

$$H_2C{=}C(CH_3){-}C({=}O){-}NH{-}CH_2{-}CH(OCH_3)_2$$

Experimental

Synthesis of the Functional Monomer

The MAAMA was synthesized by reacting aminoacetaldehyde dimethyl acetal (98% purity, from Aldrich) with methacryloyl chloride (90 % purity, from Aldrich) in dried chloroform at 0 °C in the presence of potassium carbonate (22). Purification was performed by vacuum distillation (boiling point is 97 °C under 0.01 mm Hg). Proton NMR characteristics (200 MHz ; FT AC200 Bruker) are the following : δ (ppm) ($CDCl_3$) = 6.01 (s, 1 H, NH), 5.66 and 5.31 (m, 2 H, CH_2 double bond), 4.34 (t, 1 H, CH), 3.38 (d, 2 H, N-CH_2), 3.32 (s, 6 H, CH_3 acetal), 1.89 (s, 3 H, CH_3 methacrylamide). Both the monomer and the homopolymer are highly water-soluble. The homopolymer has a glass transition temperature of 122 °C (DSC7 from Perkin-Elmer). A non polymerizable model of MAAMA was also prepared by reacting aminoacetaldehyde dimethyl acetal with propanoyl chloride.

Downloaded by STANFORD UNIV GREEN LIBR on September 17, 2012 | http://pubs.acs.org
Publication Date: July 26, 2001 | doi: 10.1021/bk-2001-0790.ch009

Synthesis and Characterization of the Latexes

Emulsion polymerizations were carried out in a conventional 3 L thermostated glass reactor using a semi-continuous addition of a stable emulsion of the monomers n-butylacrylate (BA), methyl methacrylate (MMA) and MAAMA. Starve-feed conditions were applied in order to maintain a constant copolymer composition leading to a homogeneous functionalization in the whole particle volume. For some experiments, a chain transfer agent (dodecanethiol) was also added in order to reduce the molar masses and to suppress the formation of microgels due to chain transfer reactions to poly(n-butylacrylate) (23). To prevent hydrolysis of the acetal groups during the polymerization process, sodium hydrogen carbonate buffer was used in order to maintain the pH above 7 in the reaction medium. Amounts of the incorporated functional monomer and stability of the acetal groups under polymerization conditions were verified by ^1H NMR analyses of the dried copolymers. For that purpose, the latexes were thoroughly washed by dialysis against an aqueous solution containing the same concentration of $NaHCO_3$ as the latex ; they were subsequently dried by lyophilization and the resulting copolymer was solubilized in deuterated chloroform. Accurate NMR analysis could only be performed for series LTx, because the obtained polymers do not contain more than 5 % microgel and thus could be perfectly solubilized in the deuterated solvent. Typical recipe for latex synthesis is reported in Table I and characterization results are listed in Table II.

Film Formation and Characterization

Adjustement of latex pH was performed by the addition of a given amount of 1 N hydrochloric acid solution just before film formation. Then, films were formed in an oven at 30 °C under normal pressure and a high degree of relative humidity. In order to follow the evolution of the crosslink density with time, swelling experiments were carried out periodically. For that purpose, film samples were weighed (W_0) and swollen for 48 hours in acetone at room temperature. W_1 represents the weight of the sample swollen at equilibrium. Acetone was then eliminated by drying the film at 100 °C during 24 hours and W_2 represents the weight of the dried film. Gel content ($\varphi_i = W_2/W_0$) and swelling ratio ($\tau_s = W_1/W_2$) were calculated and these values give an indication of the crosslink density of the films, the higher φ_i and the lower τ_s, the higher the crosslink density. After a period of 40 days, the tensile properties were determined using an Instron 4301 universal tensile testing machine at 25 °C under 75 % relative humidity at a crosshead speed of 50 $mm.min^{-1}$.

Table I. Experimental Conditions for Latex Synthesis.

Components	*Initial load in the reactor (g)*	*Added emulsion of the monomers (g)* [(a)]	*Added solution of the initiator (g)* [(b)]
Water	216	257	27
$Na_2S_2O_8$	0	0	2.0
NOS25® [(c)]	0.18	5.3	0
HV25® [(d)]	0.16	2.0	0
$NaHCO_3$	0.2	1.5	0
Dodecanethiol	0	0 or 0.8	0
Monomers	0	400[(e)]	0

Polymerization temperature : 70 °C ;

(a) Rate of addition = 167 g/h (addition time = 4 hours) ;

(b) Rate of addition = 7 g/h ;

(c) C_9H_{19}-C_6H_4-$(OCH_2CH_2)_{25}$-$OSO_3^-Na^+$ (cmc = 1 g/L)

(d) C_9H_{19}-C_6H_4-$(OCH_2CH_2)_{25}$-OH (cmc = 0.115 g/L)

(e) MAAMA = X g ; MMA = 0.35.(400 - X) g ; BA = 0.65.(400 - X) g

Results and Discussion

Latex and Copolymer Characterization

Using the polymerization technique described in the experimental part, the obtained latexes were stable without coagulum. Solid content was 45 % and the particle diameter was in the range of 220 to 240 nm. The introduction of a functional monomer in various proportions (2.5, 5.0 and 10 wt.% with respect to the overall monomer weight) did not change the colloidal characteristics of the latexes (Table II). The main objective of this work was to obtain film forming latexes able to undergo post-crosslinking at room temperature. Therefore, the comonomers MMA and BA

Downloaded by STANFORD UNIV GREEN LIBR on September 17, 2012 | http://pubs.acs.org
Publication Date: July 26, 2001 | doi: 10.1021/bk-2001-0790.ch009

have been chosen because the glass transition temperature of the resulting copolymer can be easily adjusted over a wide temperature range by varying the composition. For this study, a T_g close to 0 °C has been targeted on the basis of a 65/35 wt/wt proportion of BA and MMA, respectively. The addition of a small amount of the functional monomer led to a slight increase of the measured T_g from – 4.8 °C for the non-functionalized copolymer to – 0.5 °C for the copolymer with 10 wt.% of MAAMA units (Table II).

Downloaded by STANFORD UNIV GREEN LIBR on September 17, 2012 | http://pubs.acs.org
Publication Date: July 26, 2001 | doi: 10.1021/bk-2001-0790.ch009

Table II. Characterization of the Acetal-Functionalized Latexes.

Latex	*MAAMA content (mol.%)* (a)		*Diameter* (c) *(nm)*	M_n *(kg/mol)*	M_w *(kg/mol)*	T_g *(°C)*
	Introduced	*NMR* (b)				
LR0(d)	0	-	246	-	-	- 4.8
LR1	1.7	-	230	-	-	- 4.5
LR2	3.4	-	215	-	-	- 2.6
LR3	7.0	-	231	-	-	- 0.5
LT0(e)	0	0	232	67	215	-
LT1	1.7	1.6	222	64	230	-
LT2	3.4	3.2	221	69	250	-
LT3	7.0	6.5	230	64	260	-

Final solid content = 45 % ; final pH = 8

(a) With respect to monomers

(b) Based on integration of the CH, CH_2 and OCH_3 protons of the acetal group of the poly(MAAMA), of the OCH_2 protons of the poly(BA) and of the OCH_3 protons of the poly(MMA) (see Figure 1)

(c) Dynamic light scattering (Zetasizer4 from Malvern)

(d) Series LRx : no chain transfer agent (microgel content ≈ 75 %)

(e) Series LTx : 0.8 g of dodecanethiol (microgel content < 5 %)

In order to quantify the true fraction of insoluble material resulting only from the post-crosslinking reaction, it is preferable to have a latex with a soluble copolymer. However, the transfer reactions to poly(n-butylacrylate) lead to the formation of microgels (23). In series LRx (Table II) that was prepared without any chain transfer agent, polymers contained more than 75 % of microgels. In contrast, for series LTx prepared in the presence of dodecanethiol, the obtained copolymers were soluble in organic solvents and did not contain more than 5 % microgel ; the number average molecular weight was comprised between 64000 and 69000 g/mol.

The first requirement to obtain homogeneously crosslinked films, is that the reactive functions are randomly incorporated into the polymer chains. For that purpose, the polymer synthesis was carried out using a semi-continuous process under starve-feed conditions as described in the experimental part. This process prevents copolymer composition drift that may be caused by differences in reactivity and in water-solubility between the various comonomers. This is particularly useful for the MAAMA which is highly soluble in water and leads to hydrophilic homopolymer under batch copolymerization conditions. Nevertheless, with the selected procedure, proton NMR analyses pointed out that the functional monomer was well incorporated into latex particles via radical copolymerization with MMA and BA (see Figure 1). Indeed, as shown in Table II, the measured proportions after polymerization matched reasonably well those of the initial mixture of monomers. Moreover, a constant composition of the copolymer was measured throughout the reaction indicating homogeneous functionalization. Less than 10 % of poly(MAAMA) could be recovered in the latex serum after separation from the polymer particles.

Another important observation is the stability of the functional group during and after polymerization. As acetal functions are prone to hydrolysis in acidic medium, polymerizations were performed at a pH of 8, which was maintained throughout the reaction by addition of an adequate concentration of $NaHCO_3$. The NMR spectra showed that the acetal groups were quantitatively recovered after polymerization and that no aldehyde function could be observed (Figure 1).

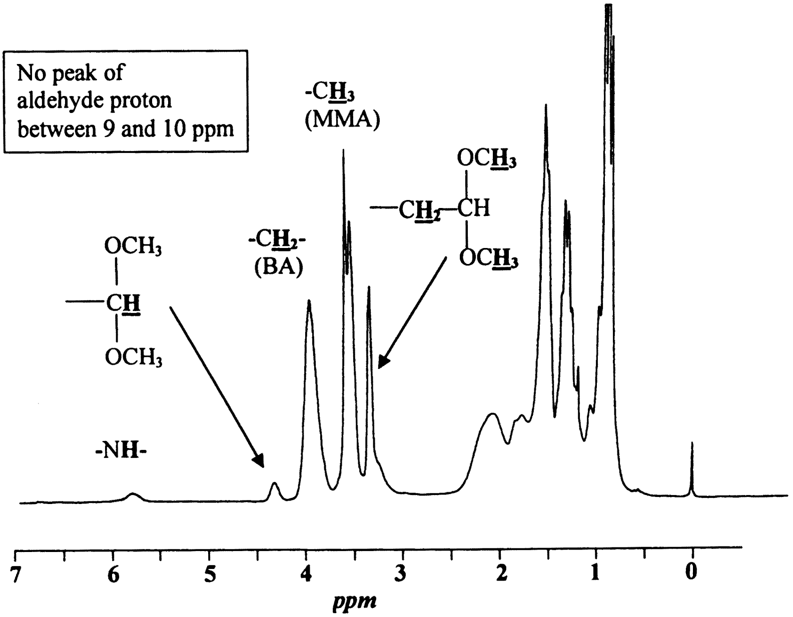

Figure 1. Proton NMR spectrum (200 MHz) in $CDCl_3$ solution of the poly(MMA-co-BA-co-MAAMA) copolymer from latex LT3 (after dialysis and lyophilization).

Downloaded by STANFORD UNIV GREEN LIBR on September 17, 2012 | http://pubs.acs.org
Publication Date: July 26, 2001 | doi: 10.1021/bk-2001-0790.ch009

Downloaded by STANFORD UNIV GREEN LIBR on September 17, 2012 | http://pubs.acs.org
Publication Date: July 26, 2001 | doi: 10.1021/bk-2001-0790.ch009

Swelling Properties of the Films

For series LTx prepared in the presence of a chain transfer agent, films formed at alkaline pH (pH = 8) were found to be fully soluble in acetone, whatever the initial concentration of MAAMA. For series LRx, although polymer particles contained approximately 75 % of microgel, films totally disintegrated into fragments after being immersed in acetone during 48 hours. Those results indicate that under alkaline conditions films did not undergo post-crosslinking reactions. In contrast, adjusting the pH of the latexes to a value of 2 just before film formation, led to crosslinked films with very good solvent resistance, as indicated by the final values of φ_i and τ_s reported in Table III. These final swelling ratio and gel content values appeared to significantly depend upon the initial concentration of MAAMA introduced into the latex particles. Values of φ_i increased and values of τ_s decreased when the concentration was increased. The increase of crosslink density was however accompanied by a more pronounced discoloration of the films. For a given concentration of MAAMA, the initial molar mass of the polymer had also a significant effect on the final crosslink density. Indeed, for series LRx, an uncontrolled slight pre-crosslinking of the polymer led to an enhanced solvent resistance of the final films.

Table III. φ_i and τ_s after 35 days for the films formed at pH = 2 and pH = 8 as a function of MAAMA concentration.

Latex	*pH at film formation*	*Gel content (a) (%)*	*Swelling ratio*
LR0	2	"0"	∞
	8	"0"	∞
LR1	2	92	5.0
	8	"0"	∞
LR2	2	95	3.9
	8	"0"	∞
LR3	2	97	2.5
	8	"0"	∞
LT0	2	0	∞
	8	0	∞
LT1	2	80	8.5
	8	0	∞
LT2	2	92	4.3
	8	0	∞
LT3	2	95	2.9
	8	0	∞

(a) A gel content noted "0" indicates that the films disintegrate in acetone although containing microgels.

Downloaded by STANFORD UNIV GREEN LIBR on September 17, 2012 | http://pubs.acs.org
Publication Date: July 26, 2001 | doi: 10.1021/bk-2001-0790.ch009

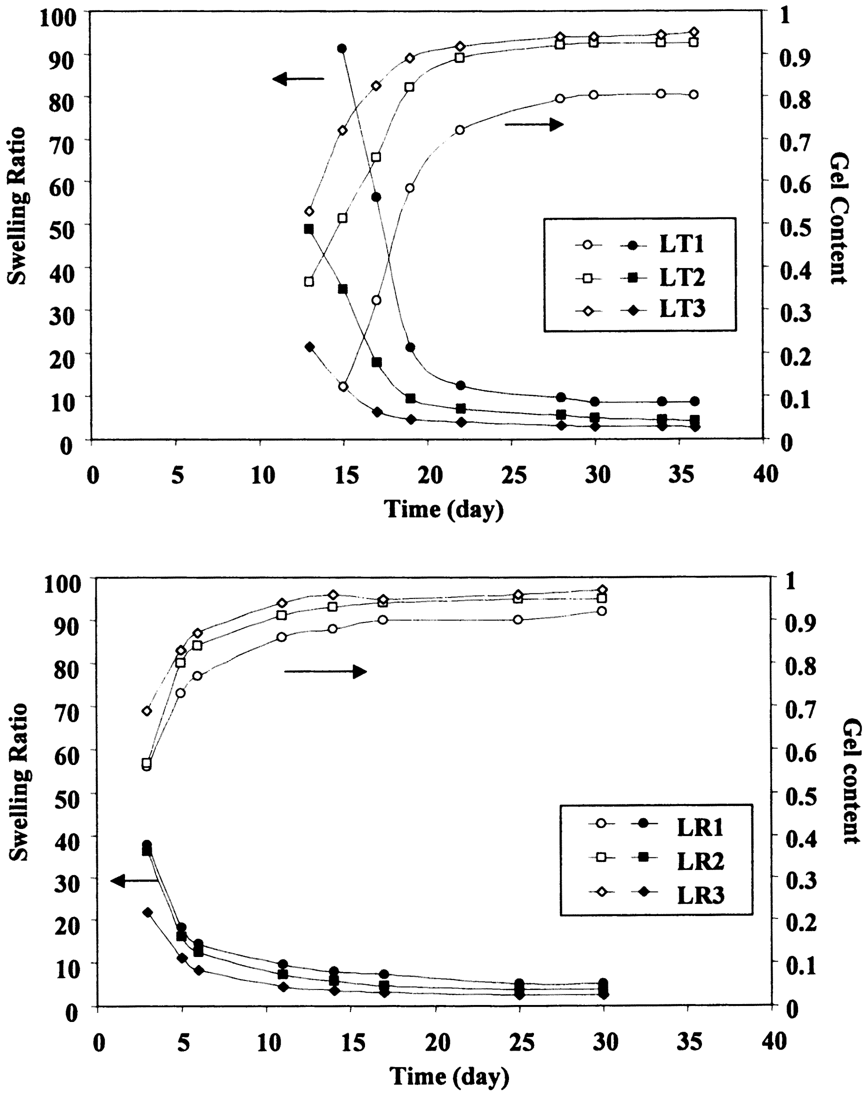

Figure 2. Gel content (φ_i) and swelling ratio (τ_s) as a function of time for the films formed at pH = 2. Series LTx : latexes prepared with a transfer agent ; Series LRx : latexes prepared without transfer agent.

The evolution of gel content and swelling ratio were followed as a function of films ageing time and values are plotted in Figure 2. First, an induction period can be observed, during which films have lost their cohesion in acetone indicating that the systems have not reached the gel point. Owing to the effect of molar mass (and thus, of average functionality of the polymer chains which is lower for shorter chains at a given proportion of MAAMA), duration of this period was much shorter for series LRx than for series LTx. Actually, gelation occurred after 3 days for series LRx and after 12 days for series LTx. Afterward, crosslink densities increased with time but rate of the crosslinking reaction remained relatively slow, as several days (typically more than 10) were needed to reach the ultimate crosslink density.

The effect of pH was also carefully examined. As illustrated in Figure 3 for a constant MAAMA concentration, when pH was increased, the gel point was reached later, the time evolution was slower and the final crosslink density of the film decreased. Particularly, when pH = 6, no crosslink formation could be evidenced as films were totally soluble in acetone at any time. Another important feature for practical application is that latexes can be stored under acidic conditions for weeks before film formation without affecting the swelling and mechanical properties of the films.

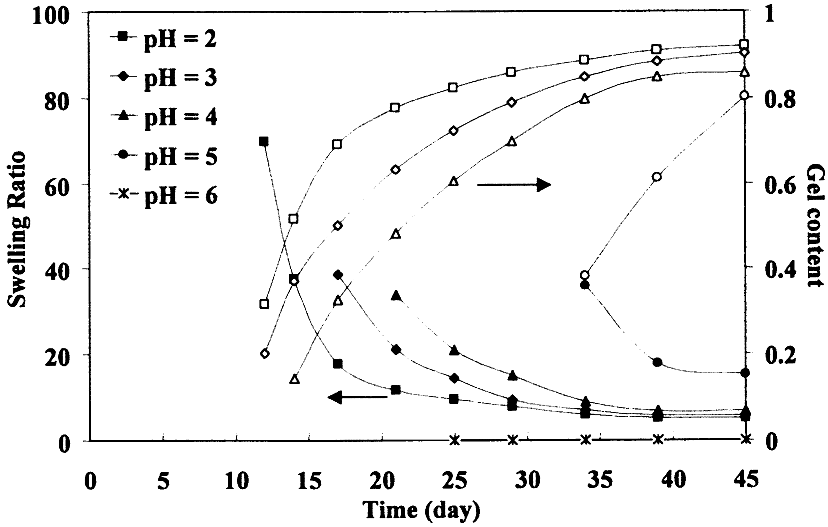

Figure 3. φ_i and τ_s as a function of the initial pH for the films formed from latex LT2.

Mechanical Properties

After a period of 40 days, the tensile properties of the films were tested. The stress-strain curves are displayed in Figure 4 for the two series as a function of MAAMA concentration. Non functionalized films and films obtained at alkaline pH behaved as uncrosslinked rubbers. In contrast, for films formed at pH = 2, tensile strength increased with the initial concentration of MAAMA and elongation at break significantly decreased. This is typical of films with increasing crosslink densities. Interestingly, the films of series LRx which contained slightly pre-crosslinked polymer

Downloaded by STANFORD UNIV GREEN LIBR on September 17, 2012 | http://pubs.acs.org
Publication Date: July 26, 2001 | doi: 10.1021/bk-2001-0790.ch009

exhibited enhanced tensile strength when compared with their counterparts from series LTx, elongation at break being unchanged. Decreasing tensile strength and increasing elongation at break were also observed when pH of the films was increased (Figure 5). This confirms the trend observed with swelling measurements : films had lower final crosslink density when pH was increased.

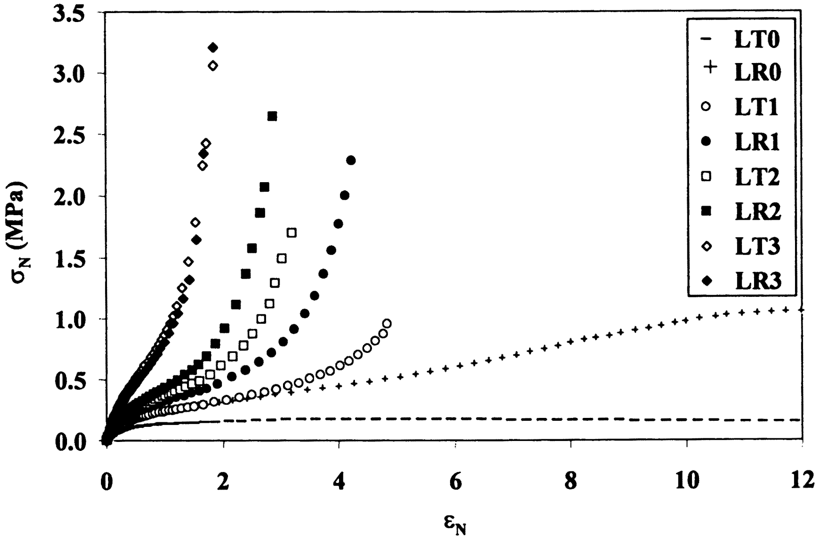

Figure 4. Effect of the amount of MAAMA on tensile properties of poly(MMA-co-BA-co-MAAMA) films formed at pH = 2.

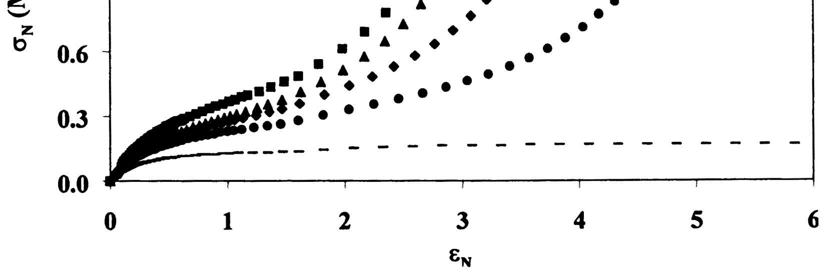

Figure 5. Effect of the pH on tensile properties of poly(MMA-co-BA-co-MAAMA) films from Latex LT2.

Downloaded by STANFORD UNIV GREEN LIBR on September 17, 2012 | http://pubs.acs.org
Publication Date: July 26, 2001 | doi: 10.1021/bk-2001-0790.ch009

Chemical Aspect of Crosslinks Formation

As already mentioned above, the acetal functionality of the MAAMA is stable and chemically inert under alkaline conditions. This is the reason why the functionalized films formed at pH = 8 did not undergo crosslinking reaction and behaved like the non functionalized latexes. In contrast, under acidic conditions, it is known that the acetal group is hydrolyzed into an aldehyde group which is a potentially self-reactive function. In order to study the involved reactions, a non polymerizable model of the MAAMA was synthesized. The kinetics of hydrolysis was first followed at room temperature by ^{1}H NMR in D_2O at different pH values. For that purpose, intensity of the peak at 4.34 ppm corresponding to the CH of the acetal group was measured periodically. The results are displayed in Figure 6 which shows the semilogarithmic plot of the decrease of the acetal group concentration as a function of time. One can see that reaction follows a pseudo first order kinetics with an apparent rate constant value k_{app} depending upon pH. The plot of $\log(k_{app})$ versus pH follows a straight line with slope = -1 indicating a first order dependence with respect to protons concentration. Moreover, with extrapolation at pH = 0, an absolute second order rate constant of $9.0\ 10^{-4}$ $L.mol^{-1}.s^{-1}$ at room temperature was calculated (Figure 7).

A thorough analysis of the ^{1}H and ^{13}C NMR spectra of the model molecule in a mixture of D_2O (pH = 0.8) and d6 DMSO, showed that hydrolysis of the acetal groups led to three products in different proportions : the hemiacetal, the hydrate (geminal diol) and the aldehyde. After complete consumption of the acetal functions, when methanol was allowed to evaporate, the hemiacetal disappeared and the final composition of the medium was approximately 20 mol.% of aldehyde and 80 mol.% of hydrated aldehyde. A very important feature is that, even after 40 days, no other species could be identified in aqueous solution, which would correspond to the product of a condensation reaction. The favored formation of hydrated aldehyde in the presence of water probably slows down the rate of any other reaction. This result probably explains the stability of the functional groups when latexes were stored under acidic conditions.

Kinetics of hydrolysis of the acetal groups incorporated into latex particles was also studied. Latex LT3 was thoroughly washed as described above. Then, for three aliquots, pH was adjusted at 1, 1.5 and 2, respectively, by the addition of a D_2O solution of sulfuric acid. The non functionalized latex LT0 was treated the same way and the pH was fixed at a value of 1 in order to check the possible hydrolysis of the ester groups of the main monomers BA and MMA. The amount of methanol released by the hydrolysis reaction performed at room temperature was monitored by ^{1}H NMR spectroscopy as a function of time. Quantitative analysis was allowed by the addition of a known amount of sodium *para*-toluenesulfonate. It was also checked that the addition of this salt had no effect on the kinetics of hydrolysis. The calculated fraction of acetal that has been hydrolyzed is plotted versus time in Figure 8. The first conclusion is that the release of methanol was essentially due to the hydrolysis of the acetal groups and not to the hydrolysis of the methyl ester of MMA. Interestingly, when the pH was lower than 1.5, the reaction of hydrolysis reached completion within 30 days. On the other hand, hydrolysis was significantly slower and incomplete for

Downloaded by STANFORD UNIV GREEN LIBR on September 17, 2012 | http://pubs.acs.org
Publication Date: July 26, 2001 | doi: 10.1021/bk-2001-0790.ch009

higher pH value. As expected, it can be seen that hydrolysis was also slower in the latex than in solution under the same experimental conditions.

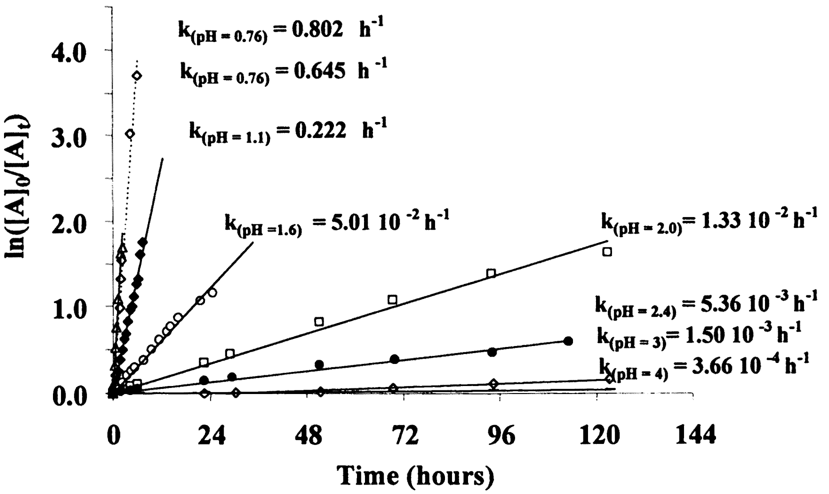

Figure 6. Kinetics of hydrolysis at room temperature of the model of MAAMA in D_2O at different pH, as followed by ^1H NMR analysis ($[A]_0$ and $[A]_t$ represent the concentration of acetal at time zero and time t, respectively).

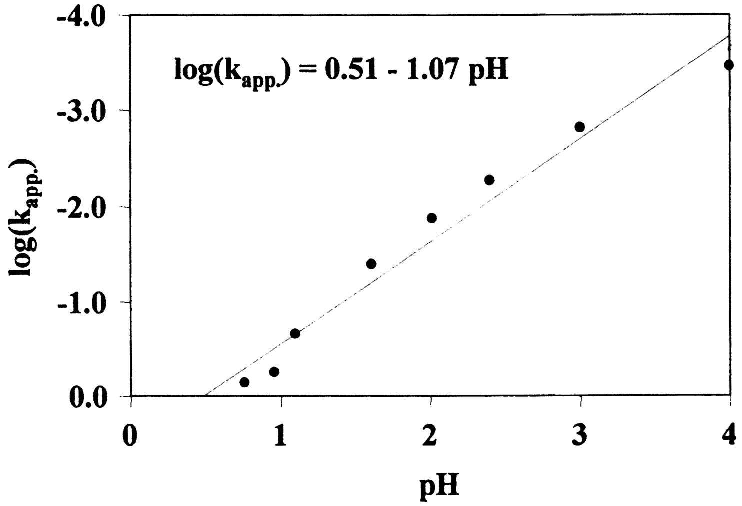

Figure 7. Semilogarithmic plot of the apparent rate constant of hydrolysis as a function of pH (k_{app}, in h^{-1})

Downloaded by STANFORD UNIV GREEN LIBR on September 17, 2012 | http://pubs.acs.org
Publication Date: July 26, 2001 | doi: 10.1021/bk-2001-0790.ch009

Downloaded by STANFORD UNIV GREEN LIBR on September 17, 2012 | http://pubs.acs.org
Publication Date: July 26, 2001 | doi: 10.1021/bk-2001-0790.ch009

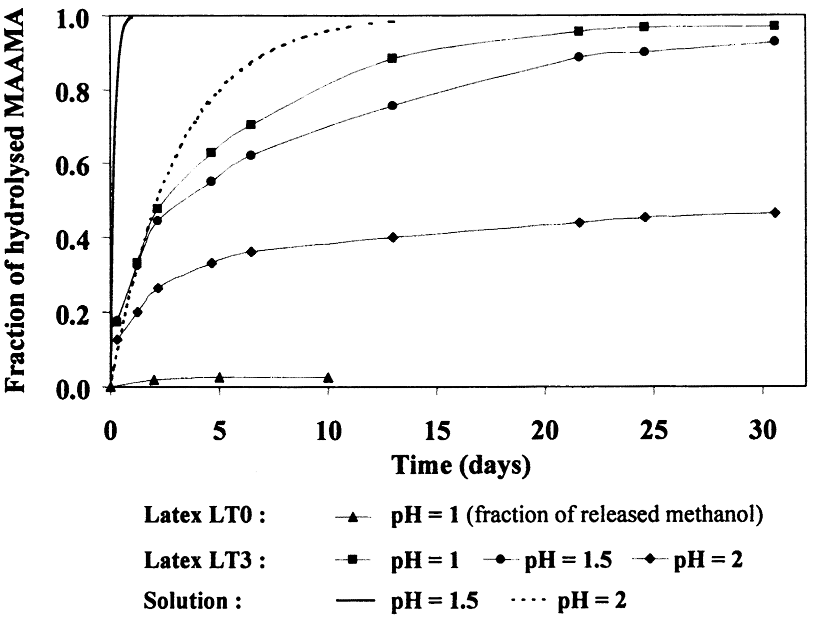

Figure 8. Hydrolysis of the acetal groups in latex LT3, at room temperature and at different pH values, as followed by the amount of released methanol using ^1H NMR spectroscopy.

In order to roughly simulate the conditions of film formation, the above mentioned D_2O / d6 DMSO acidic solution of the model of MAAMA was left open for 30 days in an oven at 30 °C, in order to allow a slow solvent evaporation. After that period of time, a dark brown residue was recovered and analyzed. Mass spectrometry showed the existence of a single species with molar mass of 212 g/mol. The ^1H and ^{13}C NMR analyses in d6 DMSO solvent enabled to identify the structure of the product, which is represented in Scheme 2.

Scheme 2

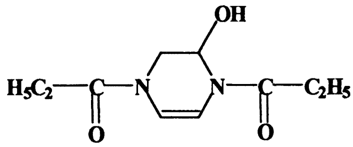

This molecule is formed by the bimolecular reaction between the amide of one molecule and the carbonyl of the other one. The first addition step is followed by a cyclization reaction using the same mechanism, after elimination of one molecule of water. The elimination of a second molecule of water is not favored after cyclization. The expected aldolization-crotonization reaction could not be evidenced.

Unfortunately, identification of the chemical functions responsible for crosslinking in latex films could not be directly performed and further analyses are currently in progress.

The main condition for the formation of crosslinked films is the acidification of the latex serum which is necessary for hydrolysis of the acetal groups. This reaction was shown to be quite slow when the functional groups are incorporated into latex particles and the rate is strongly pH-dependent. This explains the strong effect of the pH on the rate of crosslinks formation as well as on the final crosslink density of the films. When water evaporates, particles concentrate, deformation occurs and chain interdiffusion can proceed across adjacent cell boundaries. Simultaneously, the deprotected functions react with each other to lead to chemical crosslinks. In this system, both hydrolysis and chemical reaction are too slow to lead to premature intra-particle crosslinking which would eventually result in a complete hindrance of the chain interdiffusion process. It is particularly true in the case of series LTx, for which gelation occurred after 12 days. Moreover, if only intra-particle crosslinking occurred and chain interdiffusion was prevented, the mechanical properties and solvent resistance of the films would have been much poorer, according to previous studies (18,24,25). In addition, the experimental results did not give any evidence for purely interfacial crosslinking. Indeed, gel content was always found to be high, and final surface morphology, as studied by atomic force microscopy appeared to be quite homogeneous. Therefore, it is very likely that a large volume fraction of the particles was involved in crosslinking, as a consequence of an extensive mixing of the chains of adjacent particles in conjunction with hydrolysis of a large fraction of the acetal groups (especially at pH = 2).

Downloaded by STANFORD UNIV GREEN LIBR on September 17, 2012 | http://pubs.acs.org
Publication Date: July 26, 2001 | doi: 10.1021/bk-2001-0790.ch009

Conclusion

This work demonstrates that the incorporation of 2.5 to 10 wt.% of the acetal functional monomer MAAMA into low T_g latex particles enabled to form films at room temperature which could post-crosslink at acidic pH. The formation of crosslinks in the films was shown to be a slow process. Kinetics of the crosslinking reaction and final crosslink density are a function of the concentration of the functional monomer, of pH and of the polymer molar mass. Such system led to cohesive films with highly improved solvent resistance and mechanical properties.

Acknowledgments
The authors wish to acknowledge Elf-Atochem for financial support.

References

1. "Film Formation in Water-Borne Coatings" Provder, T.; Winnik, M. A.; Urban, M. W. *Am. Chem. Soc. Symp. Series* **1996**, 648
2. Padget, J. *J. of Coat. Technol.*, **1994**, 66, 839
3. Daniels, E. S.; Klein, A. *Prog. Org. Coat.* **1991**, 19, 359
4. Bufkin, B. G.; Grawe, J. R. *J. Coat. Technol.* **1978**, 50, 65
5. Okubo, M.; Nakamura, Y.; Matsumoto, T. *J. Polym. Sci.: Polym. Chem.* **1980**, 18, 2451
6. O'Brien, R. M.; Brown, S. A.; Bufkin, B. G.; Grawe, J. R. *J. Coat. Technol.* **1981**, 53, 49
7. Clemens, R. J.; Rector, F. D. *J. Coat. Technol.* **1989**, 61, 83
8. Zosel, A.; Hekman, W.; Ley, G.; Mächte, W. *Makromol. Chem. Suppl.* **1990**, 35/36, 423
9. Hidalgo, M.; Guillot, J.; Cavaillé, J.-Y. *J. Appl. Polym. Sci., Appl. Polym. Symp.* **1991**, 49, 103
10. Brown, W. *Surf. Coat. Int.* **1995**, 78, 238
11. Geurink, P. J. A.; Van Dalen, L.; Van der Ven, L. G. J.; Lamping, R. R. *Prog. Org. Coat.* **1996**, 27, 73
12. Guerts, J. M., PhD thesis, Technische Universiteit Eindhoven (1997)
13. "The application of carbodiimide chemistry to coatings", Taylor, J. W.; Basset, D.R., *Am. Chem. Soc. Symp. Series* **1997**, 663, 137
14. Pollano, G. *Polym. Mater. Sci. Eng.* **1997**, 77, 383
15. Mohammed, S.; Daniels, E. S.; Sperling, L. H.; Klein, A.; El-Aasser, M. S. *J. Appl. Polym. Sci.* **1997**, 66, 1869
16. Chen, M. J.; Osterhlotz, F. D.; Pohl, E. R.; Ramdatt, P. E.; Chaves, A.; Bennett, V. *J. Coat. Technol.* **1997**, 68, 43
17. Baumstark, R.; Roser, J.; Portugall, M.; Zosel, A. *Prog. Org. Coat.* **1998**, 34, 245
18. Guinot, P.; Charleux, B.; Vairon, J.-P. *Macromol. Symp.* (in press)
19. Winnik, M. A.; Pinenq, P.; Krüger, C.; Zhang, J.; Yaneff, P. V. *J. Coat. Tech.* **1999**, 71, 47
20. Pinschmidt, R. K. Jr.; Davidowich, G. E.; Burgoyne, W. F.; Dixon, D. D.; Goldstein, J. E.; *in "Crosslinked Polymers : Chemistry, Properties and Applications" Am. Chem. Soc.* **1988**, 467
21. Kjellquist, K.; Rassing, J.; Wesslen, B.; *J. Appl. Polym. Sci.* **1994**, 51, 1063
22. Santos, R. M.; Forcada, J. *Progr. Colloid. Polym. Sci.* **1996**, 100, 87
23. Lovell, P. A.; Shah, T. H.; Heatley, F.; *Polymer Communications* **1991**, 32, 98
24. Zosel, A.; Ley, G. *Macromolecules* **1993**, 26, 2222
25. Tamai, T.; Pinenq, P.; Winnik, M. *Macromolecules* **1999**, 32, 6102

Downloaded by STANFORD UNIV GREEN LIBR on September 17, 2012 | http://pubs.acs.org
Publication Date: July 26, 2001 | doi: 10.1021/bk-2001-0790.ch009

Downloaded by PENNSYLVANIA STATE UNIV on September 17, 2012 | http://pubs.acs.org
Publication Date: July 26, 2001 | doi: 10.1021/bk-2001-0790.ch010

Chapter 10

Cryogenic Scanning Electron Microscopy of Early Stages of Film Formation in Drying Latex Coatings

Erwin Sutanto, Yue Ma, H. T. Davis, and L.E. Scriven*

Coating Process Fundamentals Program, Center for Interfacial Engineering and Department of Chemical Engineering and Materials Science, University of Minnesota, 421 Washington Avenue, S.E., Minneapolis, MN 55455

Cryogenic scanning electron microscopy (Cryo-SEM) was used to examine the distribution of polystyrene (PS) and of poly (butyl methacrylate) (PBMA) latex particles during drying of waterborne suspension coatings. The suspensions were coated on silicon wafer substrates and after different times of drying were rapidly frozen in liquid ethane. Top surfaces and fracture surfaces affording cross-sectional views were examined on the cold stage. The cryo-SEM micrographs demonstrate the presence of abrupt consolidation fronts advancing from the edges of the coatings in the earliest stage of drying of, e.g. suspensions of 10 wt% PS and of 15 wt% PBMA latex. Micrographs successively farther from an edge show that layers of ordered close-packed particles build sequentially downward from the top surface as drying progresses. But depending on the conditions, layered ordering gives way deeper in the coating to inter mixed regions of disordering and ordering. With care about sublimation of frozen water from the surfaces viewed, the cryo-SEM technique is useful for elucidating the compaction process in early stages of drying.

Previous investigators have demonstrated that cryogenic scanning electron microscopy (cryo-SEM) is a useful technique for studying the evolution of the microstructure as polymer latex consolidates and deforms during drying and rehydration in paper and biocatalytic coatings (1,2,3). The cryo-SEM images of the top surfaces (i.e. the air side) of latex coatings are found to be entirely consistent with images by atomic force microscopy (AFM) (3). In the work reported here, latex coatings dried for different times are quickly frozen and then fractured. The cold fracture surfaces are imaged by cryo-SEM to reveal the distribution of polystyrene (PS) and poly (butyl methacrylate)

In Film Formation in Coatings; Provder, T., et al.;
ACS Symposium Series; American Chemical Society: Washington, DC, 2001.

(PBMA) latex particles within the coatings during the early stages of drying. The images locate two consolidation fronts: an edge consolidation front that advances laterally from the perimeter of the coating inward; and, away from the edges, a descending consolidation front that advances from the top surface through the coating to the substrate.

Evidence that an edge consolidation front advances laterally from perimeter inward is followed by a dry-out front has been mentioned frequently in the literature on latex film formation (4,5,6). The front is easily identified visually as the moving boundary at which the turbidity of the original suspension is replaced by a more translucent, slightly cloudy state. The transition is from more strongly light-scattering suspension of latex spheres to less strongly scattering wet packing of consolidated spheres. When the spheres are relatively hard, the second front is distinguished by change to an opaque, white appearance. This transition is to intensely light-scattering moist packing of consolidated spheres; by moist is meant the situation in which most of the is occupied by air that has invaded during drying but pendular rings around the sphere contacts are plentiful.

After these two fronts have passed, the coating with time becomes relatively clear and transparent behind a more diffuse front that also progresses inward from the perimeter. This transition marks the shrinking of the air-filled pore space as the latex particles flatten against one another so that the interstices between them grow smaller and less able to scatter light. Although the clearing is often termed "film-formation" and taken to mean that the latex particles have fully coalesced, it does not necessarily signify that, but only that the pore space has shrunk so much as to lack scattering power. When the original spheres are relatively soft, the "dry-out" front may disappear because it is taken over by the more diffuse "film-formation" front. The lateral progression of these fronts can confound measurements of rates of drying of coatings that are limited in area, because the drying process is spatially non-uniform, varying from the interior to the perimeter (7).

Well away from the perimeter of a coating, the inwardly propagating fronts give way to a more gradual progression in time, from turbid to translucent to opaque to clear as the successive fronts descend through the coating. This distinction between perimeter and interior can be amplified in experiments with coatings of small extent, or with somewhat flattened droplets, because the region around the margin is thinner, dries out faster and enters the film formation stage sooner. In coatings of large extent, a skin may be evident on the surface of a still wet coating (5), depending on the softness of the latex and the drying rate. A skin indicates that the "film formation" front is considerably narrower than the coating, with the consequence that when it is located in the coating, the pore space at the top of the coating is so occluded as effectively to prevent evaporation of water from, and air invasion into, the deeper regions of the coating. In the ultimate of "film formation", the latex particles at the top of the coating coalesce totally and the drying rate becomes limited by diffusion of moisture through the polymer itself, because the pore space has disappeared.

Having compared drying rates (weight loss versus time) of latex paints and pigment slurries coated on 0.1 m^2 substrates, Croll (8) hypothesized that in the early stage of drying of latex paints a dry-out front recedes from the top surface toward the substrate, and that as the particles coalesce more and more in the uppermost layer, the pores between them vanish, cutting off egress of evaporating water and invasion of air. The cryo-SEM images presented below are evidence of the first stage in this sequence of events away from the perimeter, namely a consolidation front moving downward from the coating's top surface to its base at the impermeable substrate.

Downloaded by PENNSYLVANIA STATE UNIV on September 17, 2012 | http://pubs.acs.org
Publication Date: July 26, 2001 | doi: 10.1021/bk-2001-0790.ch010

Materials and Methods

Latex

PS and PBMA latex suspensions were synthesized by batch emulsion polymerization without surfactants in a 1 liter three-neck round bottomed flask equipped with reflux condenser, stirrer, and thermometer. The flask was kept at reaction temperature in a thermostatted water bath and always under an outflow of nitrogen gas. Styrene (Aldrich Chemical Company, Inc., Milwaukee, WI) and butyl methacrylate (Aldrich Chemical Company, Inc., Milwaukee, WI) were washed four times with 0.4 wt% aqueous sodium hydroxide solution in a separatory funnel to remove inhibitor. The monomers were then washed with Millipore water a total of four times to remove residual sodium hydroxide.

At first Millipore water was fed into the flask and allowed to equilibrate at reaction temperature. In PBMA preparation, potassium hydrogen carbonate was added as pH buffer. Washed monomers were then added and the stirrer was brought up to required speed. After the aqueous monomer mixture had been allowed to equilibrate for 30 minutes, the reaction was started with the addition of the potassium persulphate, which had been dissolved in Millipore water at reaction temperature. Table I shows both the recipes for the emulsion polymerization and the reaction conditions.

Table I. Recipe and Reaction Conditions for Emulsion Polymerization

	PS	*PBMA*
Water (g)	515	400
Monomer (g)	51	45
Potassium Hydrogen Carbonate (g)	-	0.20
Potassium Persulphate (g)	0.35	0.85
Reaction Temperature (°C)	70	50
Reaction Time (hour)	8	5

After the reaction times recorded there, the reaction mixtures were cooled to room temperature and the latex suspensions were filtered through 200-mesh screen to remove coagulum. The particles of both latexes were narrowly distributed around 500 nm. The solid content of PS latex particles was 10 wt% whereas that of PBMA was 15 wt%. A portion of the PS latex was deionized with Amberlite MB 3 ion-exchange resin for one day so that the effect of long-ranged repulsive forces could be investigated.

Cryo-SEM of Latex Coatings

The latex suspensions were coated on 5 mm by 8 mm platinum-coated silicon substrates with a No. 36 wire-wound rod (Mayer rods, R. D. Specialties, Webster, NY), air-dried for various periods at 294 to 296 K and 30 to 35% relative humidity, and fast-frozen by hand plunging in liquid ethane at its freezing temperature. The back of each silicon substrate was pre-scratched so that it could be fractured easily. The thickness of the coating before drying was about 250-300 μm and the drying time was from 20 seconds to 6 minutes.

The frozen samples were transferred to a cryo-system developed by Sheehan et al. (1) that was attached to a JEOL JSM-840 SEM (JEOL, Ltd., Akishima, Japan). The

Downloaded by PENNSYLVANIA STATE UNIV on September 17, 2012 | http://pubs.acs.org
Publication Date: July 26, 2001 | doi: 10.1021/bk-2001-0790.ch010

cryo-system consisted of a fracture chamber and a metal coating chamber. Both chambers and the SEM examination chamber were equipped with a liquid nitrogen conduction-cooled sample stage. The samples were fractured in the fracture chamber, sublimed for 5 minutes at 143 K in the metal coating chamber to remove around 0.5 μm of ice from the fracture surface, and sputter-coated to a depth of 7 nm with platinum. The metal-coated samples were then examined on the cold-stage in the JEOL JSM-840 SEM. Because the sample surfaces were sensitive to electron beam damage, the samples were examined at a low electron accelerating voltage of 5 kV and a low probe current of about 10^{-11} A. Except when they were being sublimed, the samples were kept at about 100 K.

Besides fracture surfaces, top surfaces of samples were imaged to reveal particle distributions at the air-water interfaces, particularly at the earliest stage of drying. Subliming some of the ice from the top surface was necessary to reveal latex particles directly beneath the air-water interface.

Room temperature SEM images of dried latex coating were made with a Hitachi S-800 field emission SEM (Nissei Sangyo America, Ltd., Rolling Meadows, IL) to reveal the final microstructure of the coating. The room temperature SEM images provide a reference for assessing the presence of any artifacts in the cryo-SEM images. In the work reported here, the cryo-SEM images of fracture surfaces at different drying time show microstructures that correspond well with the final microstructure revealed by room temperature SEM.

Downloaded by PENNSYLVANIA STATE UNIV on September 17, 2012 | http://pubs.acs.org
Publication Date: July 26, 2001 | doi: 10.1021/bk-2001-0790.ch010

Result and Discussion

Edge consolidation front

Figure 1 establishes that from the earliest stage of drying, an abrupt front of consolidation advances inward from the perimeter of 10 wt% PS latex coatings. These fronts start from where latex particles at the very edge of the coating protrude above the air-water interface as soon as enough water evaporates there that the particles come in contact with the substrate. Around the protruding particles are menisci concave toward the air. Through surface-tension force directly and through capillary-pressure differences that accompany curvature differences induced by particle location and by evaporation, these menisci act locally to draw particles together and consolidate them. Moreover, because the pressure is low beneath the multiplying menisci, it acts regionally to suck suspension from the thicker region farther from the edge. As the water is drawn between emplaced particles, arriving particles lodge in the consolidation front. In this way the front advances, just as filter cake grows in a filtration process.

The fracture surfaces in the suspension region of Figure 1a and 1b run deeper than in the latex consolidation region on the left sides of the figures. The fracture steps between the suspension and the consolidation regions appear as vertical bright stripes because the steps emit more secondary electron signals per unit projected area than do the flat surfaces. Latex particles convected to the front from the suspension appear as bright spots on the right side of the figures. The front moves to the right as the particles arrive and accumulate.

The fracture surfaces shown in Figure 1c and 1d are leafy; torn ice sheets are especially evident in the suspension region. The latex particles in that region of Figure 1c do not appear as clearly as in Figure 1a because no ice was sublimed from the

Downloaded by PENNSYLVANIA STATE UNIV on September 17, 2012 | http://pubs.acs.org
Publication Date: July 26, 2001 | doi: 10.1021/bk-2001-0790.ch010

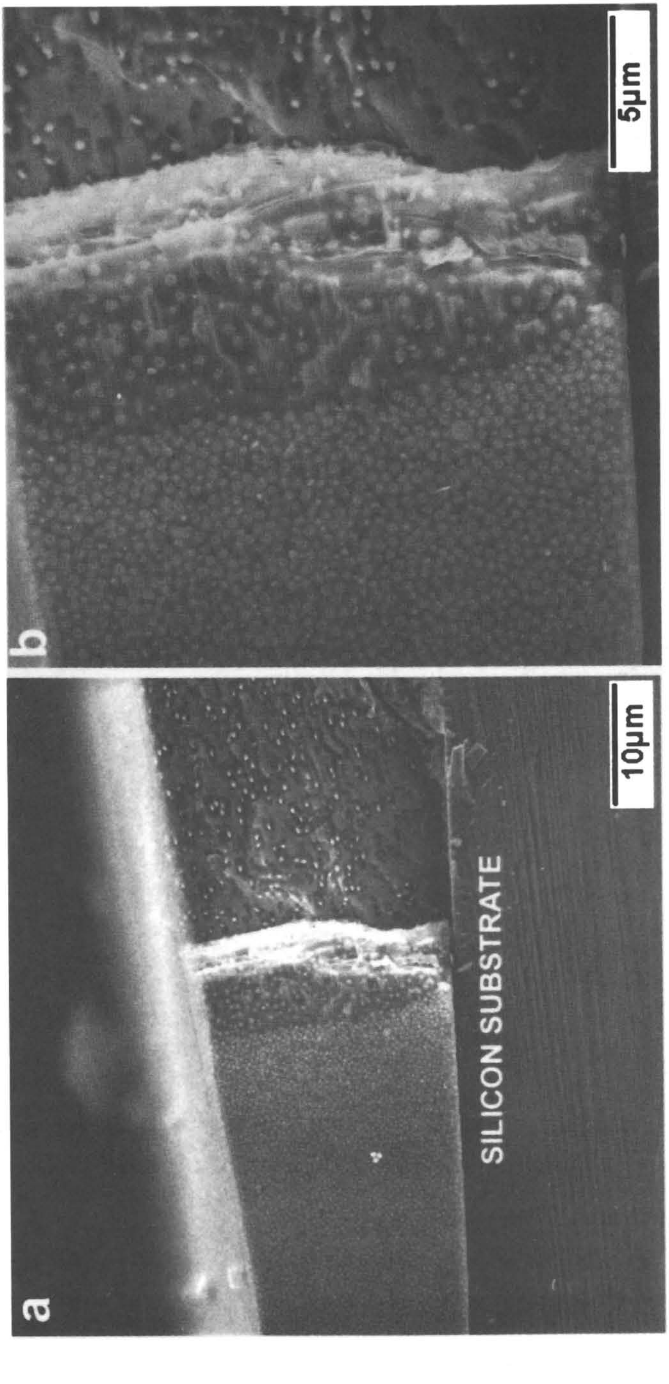
a
b
10µm
5µm
SILICON SUBSTRATE

Downloaded by PENNSYLVANIA STATE UNIV on September 17, 2012 | http://pubs.acs.org
Publication Date: July 26, 2001 | doi: 10.1021/bk-2001-0790.ch010

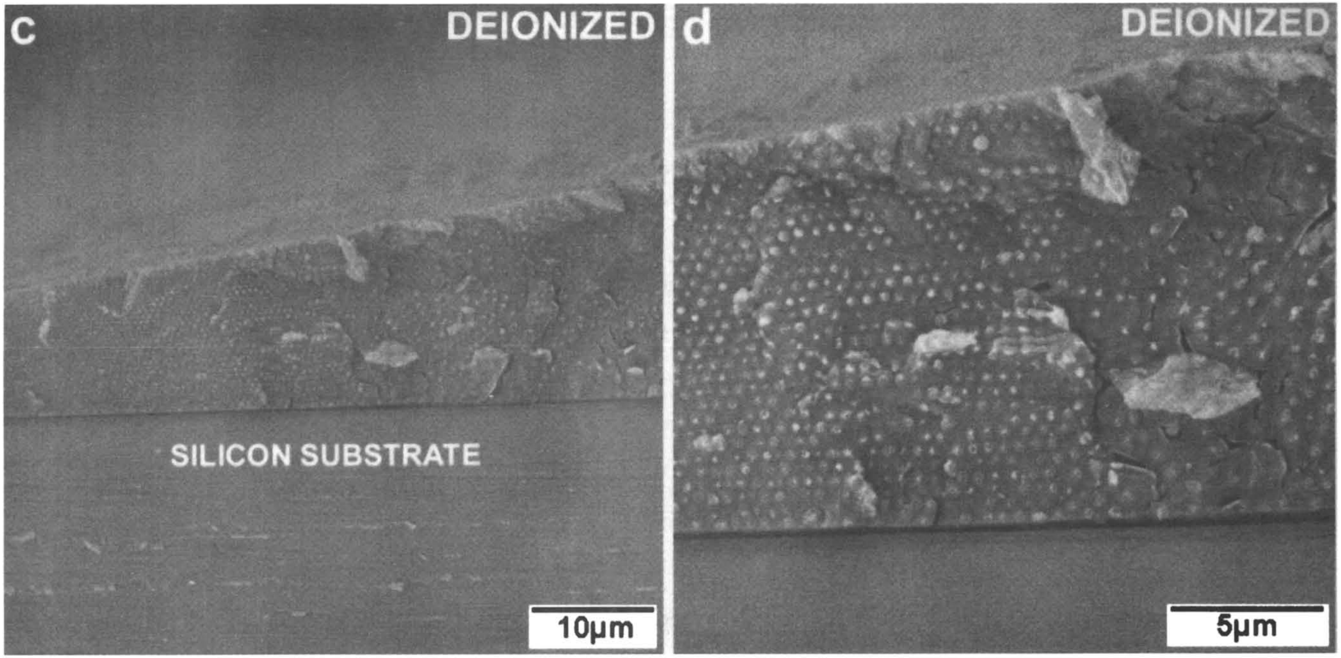

***Figure 1.** (a & b) Edge consolidation front of 10 wt% polystyrene latex suspension after 3 minutes of drying . The fracture surfaces were sublimed for 5 minutes at 143 K before imaging. (c&d) Edge consolidation front of 10 wt% deionized polystyrene latex suspension after 1 minute of drying. The fracture surfaces were not sublimed before imaging.*

fracture surfaces in Figure 1c. Only the middle parts of latex particles that bulge above the fracture surface are evident if no ice is sublimed from the fracture surfaces. Ice masks the edges of the latex particles that are harder to make out. Sublimation that removes less than 1 μm of ice from fracture surfaces before imaging helps to reveal latex particles where they are dilute. However, those on the fracture surfaces in dilute region must fall on top of other latex particles beneath if more than 2 μm of ice is sublimed from the fracture surface. More particles must show up in the suspension region and the consolidation front will become less evident if too much ice is sublimed.

When the suspensions had not been deionized, the PS particles close-packed more or less randomly (Figure 1a and 1b) as they passed through the consolidation front. Evidently the double-layer repulsion between them was short-ranged and weak enough that they adhered and were then locked in place by the next arriving particles. In contrast, when the suspensions had been deionized (Figure 1c and 1d), the particles within the coatings close-packed into highly ordered and therefore more compact packing as they passed through the front. Evidently the longer-ranged double layer repulsion allowed viscous drag and Brownian motion to jiggle, roll, and pack the particles before they were buried by those arriving next. Molecular dynamics simulations of repulsive hard spheres have illustrated this effect of soft, long-ranged, repulsive interaction potential (9).

Figure 2 is a room temperature SEM image of the edge of dried PS latex coating that had not been deionized. Plainly, the packing of consolidated particles at the free surface behind the consolidation front of PS latex coatings is better ordered than the packing inside the coating. Evidently the surface tension and the differential capillary pressure in the menisci between particles on the free surface draw the newly arriving particles to ordered closed-packed before they are locked by the next arriving particles. The viscous drag force at the consolidation front inside the coating is not as strong as the surface tension on the free surface, so that the arriving particles are locked by next arrivals before they roll and jiggle into ordered close packing.

The clusters of straggler particles at the outer edge of the latex coating (top left of Figure 2) are disconnected from the main coating. Evidently the straggler particles are too far behind to be drawn to the main coating by lateral capillary forces in the bridging menisci before water evaporates completely. However, the latex particles within the clusters adhere to each other. The lateral surface tension in the menisci and/or in the pendular rings before water evaporates completely draws the already close particles in a neighborhood together into one cluster.

Particle distribution in the middle of the coating during drying

Away from edges, water evaporates more or less uniformly from the surface of the suspension. As it does so, the particles that were suspended in it are stranded at and then beneath the surface, causing the concentration of particles to rise there. The particles tend to diffuse back toward the bulk of the suspension and raise the concentration there, too. So before long, particles become so concentrated at the surface that they are collided by random thermal fluctuations to overcome any long-ranged repulsive forces and begin the clumping of particles into doublet and triplet clusters. Once three or more particles consolidate into a cluster, further clumping action can be greatly aided by the surface-tension forces and capillary-pressure differences that arise in the increasingly curved menisci in between the particles left protruding at the surface; the reason is that the water evaporating there is not

Downloaded by PENNSYLVANIA STATE UNIV on September 17, 2012 | http://pubs.acs.org
Publication Date: July 26, 2001 | doi: 10.1021/bk-2001-0790.ch010

Downloaded by PENNSYLVANIA STATE UNIV on September 17, 2012 | http://pubs.acs.org
Publication Date: July 26, 2001 | doi: 10.1021/bk-2001-0790.ch010

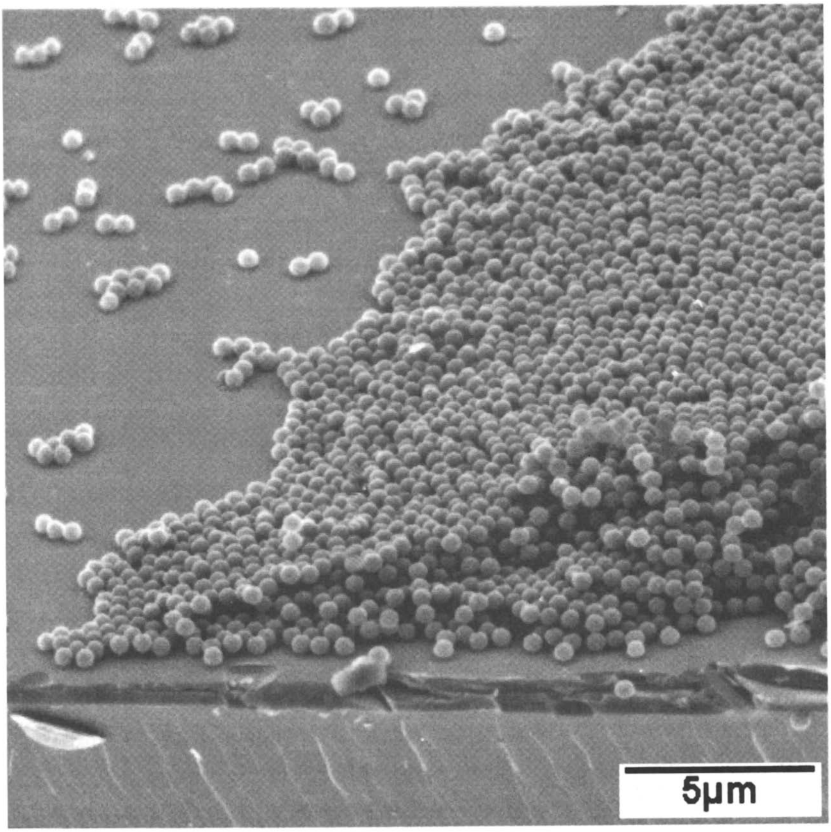

Figure 2. The edge extending away from a fracture of a dried polystyrene latex coating, showing staggler particles at the outer edge disconnected from the main coatings.

replenished fast enough. Replenishment is slowed by the mounting resistance to water flow through the concentrating suspension beneath the surface.

Figure 3 is a top view of clusters that are growing on the free surface at 1 minute of drying. Figure 3a shows that greater parts of the latex particles protrude above the free surface if they crowd together. Apparently, the surface tension force in the menisci between the crowding particles holds the particles on the free surface. If the particles on the free surface are far apart from each other, few are visible: the reason is presumably that the Brownian motion moves the particles in and out of the free surface (10). Sublimation of samples for 5 minutes at 143 K before imaging helped to reveal free particles beneath the free surface (Figure 3b).

The particles within the cluster in the lower right of Figure 3b are packed in a hexagonal array, which of two-dimensional arrays has the highest packing density. Evidently the attractive surface tension force acting on the particles within the cluster is stronger than the repulsive electrostatic force between them, because the particles jiggle and roll into the highest density packing. The cluster grows by attracting free particles that are in its neighborhood; they are attracted to the cluster by two forces: the lateral surface tension force in the menisci at the edge of the cluster, and the viscous drag force induced by low capillary pressure in the menisci between close-packed particles. A spatial transition from square packing to hexagonal packing can be seen at cluster's edge, where the chains of arriving particles merge with the cluster (center of Figure 3b). The growing cluster can be seen merging with another growing cluster at the top right corner of Figure 3b.

In the close-packed surface array of particles, the increasingly curved menisci develop capillary pressure that regionally draws suspension from deeper in the coating. As the water is drawn upward between the already clustered particles at the surface, the particles that the water bore lodge in a consolidation front that is parallel to the surface and advances downward into the coating. This front advances *downward*, not *laterally* along the coating as the front that is nearly perpendicular to the surface does in the thinner edge regions. The underlying mechanism is the same, but the downward pace of the consolidation front throughout the coating (except the edges) is much slower than the lateral pace of the front at the edges, where drying is much faster.

Figure 4 shows how successive layers of highly ordered PS particles form at the moving consolidation front; they are images at 1 minute, 3 minutes, 6 minutes and 1 hour of drying. The high degree of ordering suggests that the rate of arrival of PS particles at the front leaves them enough time to rearrange into ordered close packing before the next arriving particles limit their motion and then lock them into a permanent arrangement. Understanding the self-ordering mechanism during drying of latex suspensions is particularly relevant to synthesizing colloidal crystal as templates of photonic materials (11). Room temperature SEM of fracture surfaces of dried PS latex coatings revealed that the degree of ordering was high in at least the top 20 layers (Figure 4d). Deeper in the coatings the degree of ordering was less and at the very bottom of the coating next to the substrate only random close packing was seen in micrographs.

Figure 4a and 4c indicate that the mechanisms of water loss at 1 and 6 minutes of drying differ. At 1 minute of drying, the air-water interface is covered by a sub-monolayer of latex particles, which have low resistance to the water transport from within the coating to the atmosphere. At 6 minutes of drying, water from the depth of the coatings has to percolate and flow through the pore space between ordered layers

Downloaded by PENNSYLVANIA STATE UNIV on September 17, 2012 | http://pubs.acs.org
Publication Date: July 26, 2001 | doi: 10.1021/bk-2001-0790.ch010

Downloaded by PENNSYLVANIA STATE UNIV on September 17, 2012 | http://pubs.acs.org
Publication Date: July 26, 2001 | doi: 10.1021/bk-2001-0790.ch010

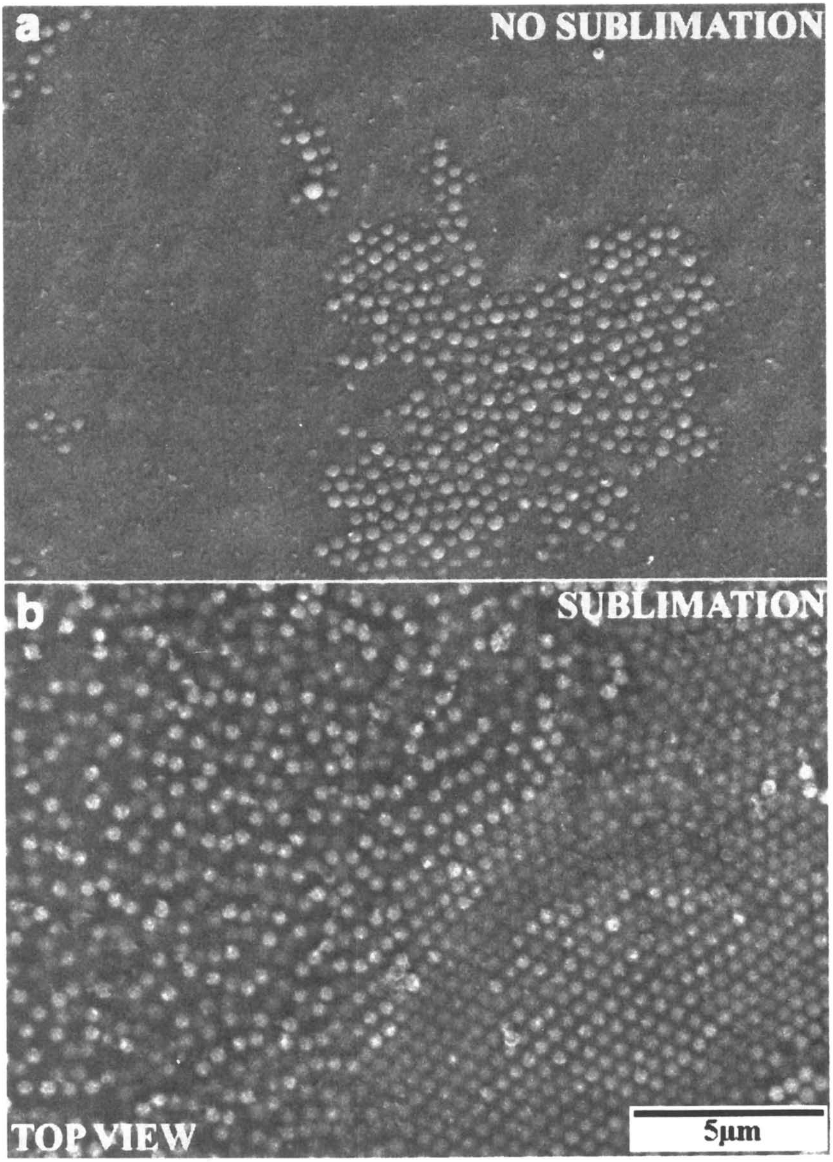

Figure 3. Growth of ordered clusters on the air-water interface away from the edges of the coating at 1 minute of drying of 10 wt% polystyrene latex suspension. (a) Only particles that protrude above the air-water (ice) interface are visible on samples not sublimed before imaging. (b) Particles beneath the air-water (ice) interface are visible on samples sublimed for 5 minutes at 143 K before imaging.

Downloaded by PENNSYLVANIA STATE UNIV on September 17, 2012 | http://pubs.acs.org
Publication Date: July 26, 2001 | doi: 10.1021/bk-2001-0790.ch010

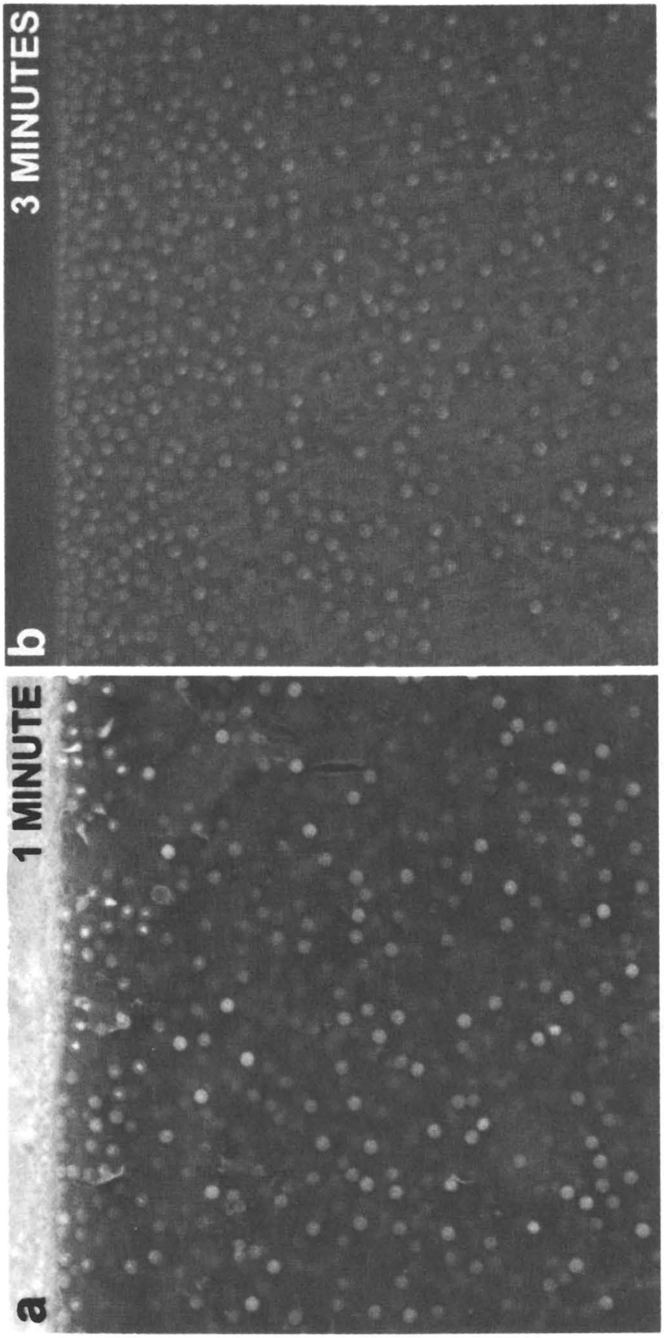

Downloaded by PENNSYLVANIA STATE UNIV on September 17, 2012 | http://pubs.acs.org
Publication Date: July 26, 2001 | doi: 10.1021/bk-2001-0790.ch010

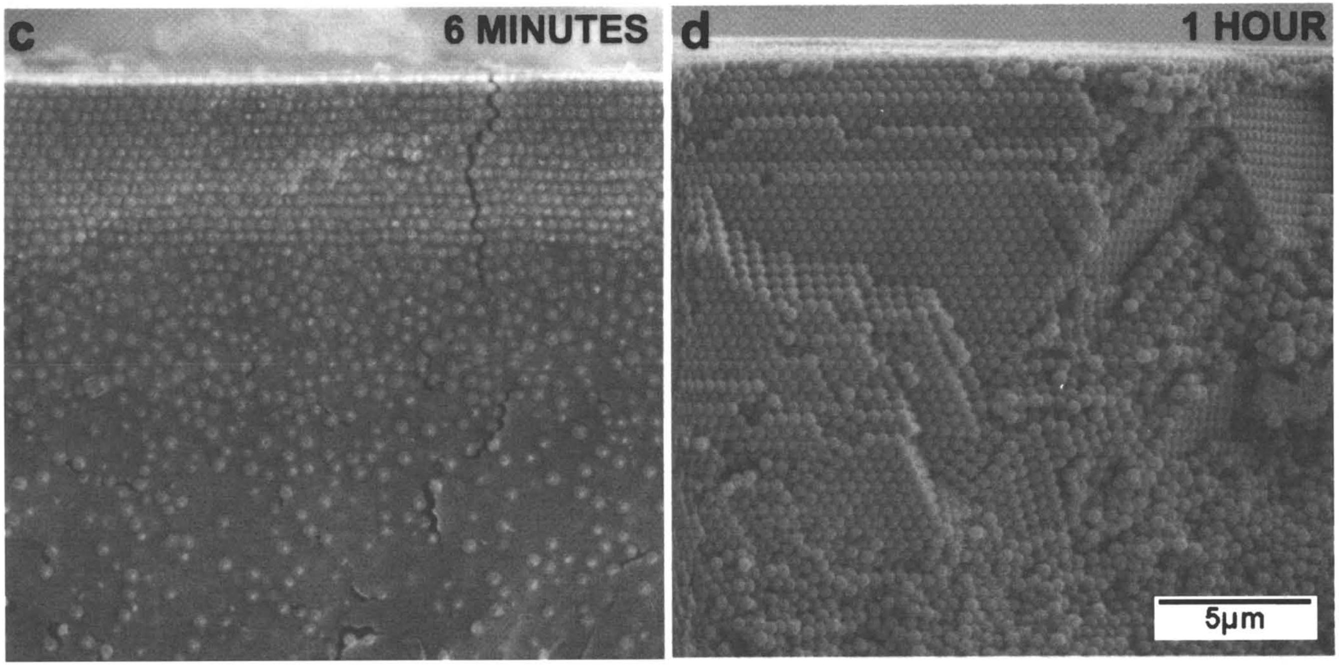

***Figure 4.** Accretion of ordered layers downward from the top surface away from the edges of the coating of 10 wt% polystyrene latex suspension at different periods of drying: (a) 1 minute, (b) 3 minutes, (c) 6 minutes. These images are fracture surfaces that have been sublimed for 5 minutes at 143 K. (d) Fracture surface of a fully dried coating.*

of consolidated latex particles to replenish evaporating water at the free surface of the coatings. The pore space between consolidated latex particles consists of pore enlargements or pore bodies connected by constrictions or pore throats. Drying experiments by Croll (8) and Vanderhoff et al. (12) indicate that the drying rate is constant in the early stages of latex coating before the latex particles in the first top layer start to coalesce.

To maintain the same drying rate, the menisci in the top layer of particles in Figure 4c should curve concave toward the atmosphere to increase the pressure difference available to drive flow between the bulk water in the deeper region and the water directly beneath the menisci. The thicker the ordered latex particle layers, the higher the menisci curvature has to be to maintain a constant drying rate. When the layers become thick enough that the menisci curvature in between particles in the topmost layer is higher than the entry menisci curvature of the largest pore throat in the layer, water menisci jump into a pore body behind the largest pore throat. The water menisci jump further into neighboring pore bodies until all the menisci rested in pore throats whose entry menisci curvature are higher than the attendant water menisci.

Water menisci advance into more pore bodies in the coating as more and more latex layers consolidate beneath the top surface and the pressure difference between the interstitial water in the deeper region of the coating and that directly beneath the menisci grows. As menisci invade the pore space, air replacing water, the flow of water within the coating is altered, particularly that in the neighborhood of pore bodies that have been filled with air. The alteration of the water flow field may be the main reason the latex particles are much less ordered deeper in the coating. In narrow coatings, the edge consolidation front may reach the middle of the coated latex suspension before the descending consolidation front reaches the substrate, and this could also be responsible for less ordering deeper in the coatings.

When the suspension was deionized so that double-layer repulsion between particles (and perhaps between particles and interface) became longer-ranged, the clustering of PS particles in the suspension-air interface was greatly delayed. Figure 5 is a cross-section view of such a sample fast-frozen after 6 minutes of drying (cf. Figure 4a, which is after just 1 minute of drying under similar conditions). Apparently the attractive forces due to surface-tension are weaker at long range than the electrostatic force in deionized PS suspension during the first 6 minutes of drying so that clumping of latex particles at the free surface is delayed.

The SEM micrographs of PBMA latex coatings in Figure 6 show the descending consolidation front that develops away from the edges of the coating; the images were made after 1 minute, 2 minutes, 4 minutes, and 1 hour of drying. The nano-scale cracks in Figure 6a and 6b were probably caused by thermal contraction of ice when the latex suspension was rapidly frozen in liquid ethane. The latex particles in Figure 6c are less evident because the fracture surfaces were not etched by sublimation before they were imaged: however, the accretion of ordered layers of latex particles beneath the free surface is plain. Room temperature SEM of a dried latex coating (Figure 6d) revealed that the first 15 to 20 layers were highly ordered and that the deeper region was much less ordered.

After the samples were put into air at 100% relative humidity for 10 minutes, cryo-SEM images (not shown) revealed that the close-packed PS and PBMA layers at the top surface of samples shown in Figure 4c and 6c had redispersed. Evidently the close-packed particles separated and redispersed after water stopped evaporating

Downloaded by PENNSYLVANIA STATE UNIV on September 17, 2012 | http://pubs.acs.org
Publication Date: July 26, 2001 | doi: 10.1021/bk-2001-0790.ch010

Downloaded by PENNSYLVANIA STATE UNIV on September 17, 2012 | http://pubs.acs.org
Publication Date: July 26, 2001 | doi: 10.1021/bk-2001-0790.ch010

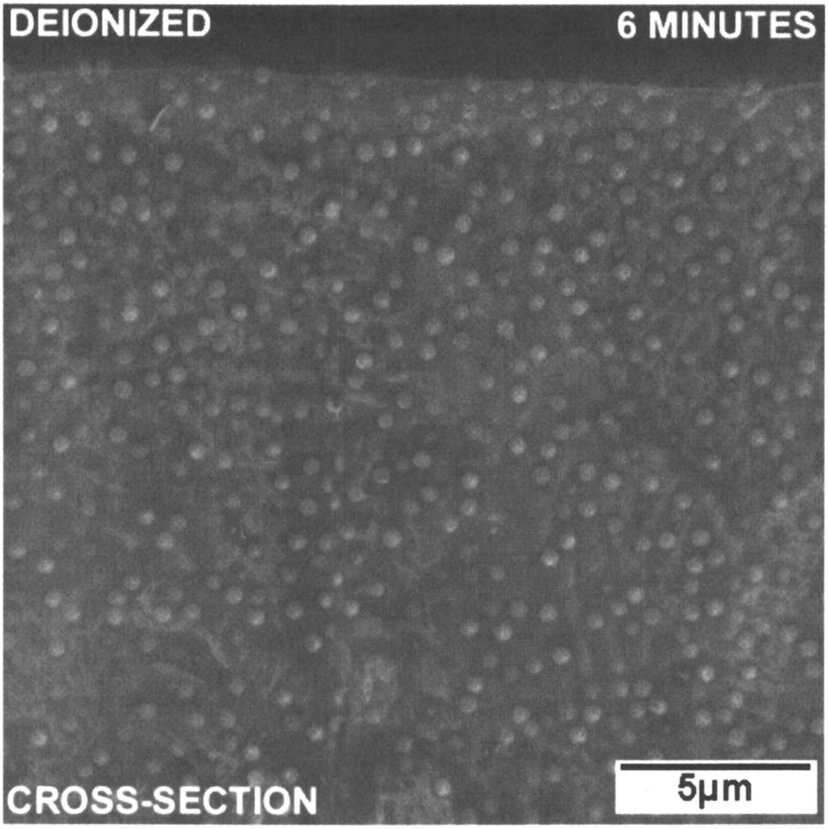

Figure 5. Fracture surface away from the edges of fast-frozen deionized latex suspension coating after six minutes of drying. Absence of ordered layers or clusters at the top surface.

Downloaded by PENNSYLVANIA STATE UNIV on September 17, 2012 | http://pubs.acs.org
Publication Date: July 26, 2001 | doi: 10.1021/bk-2001-0790.ch010

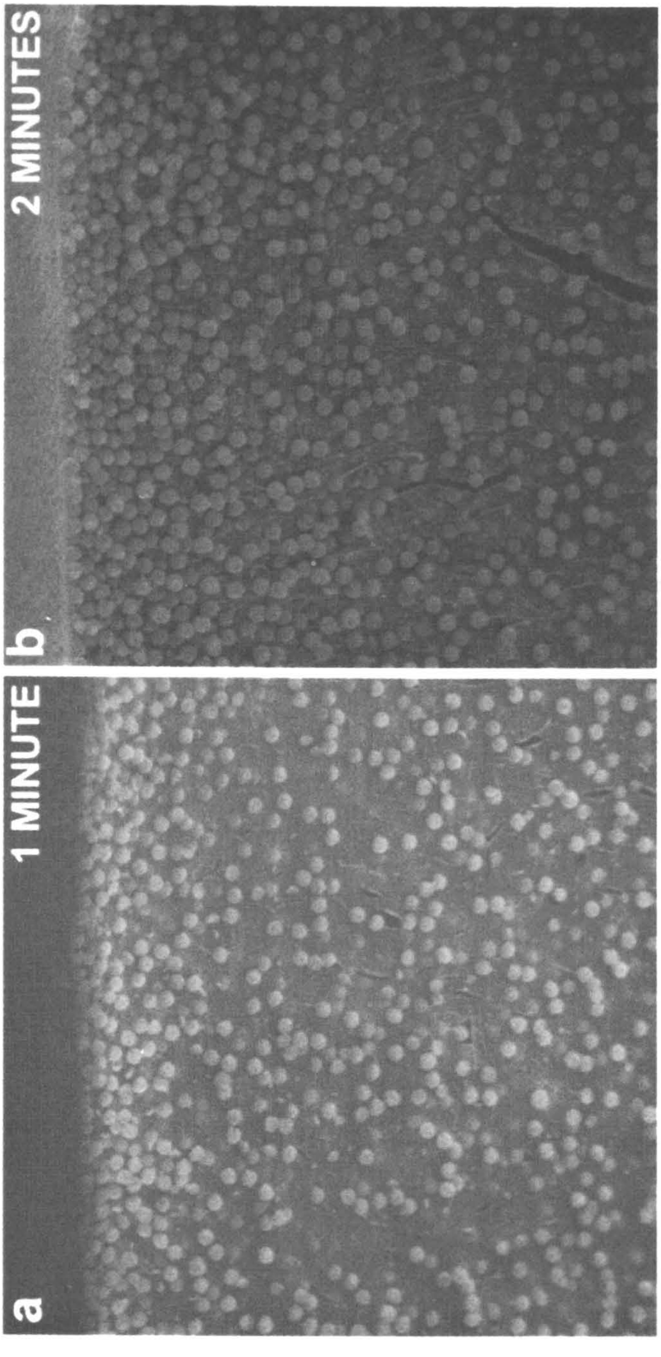

Downloaded by PENNSYLVANIA STATE UNIV on September 17, 2012 | http://pubs.acs.org
Publication Date: July 26, 2001 | doi: 10.1021/bk-2001-0790.ch010

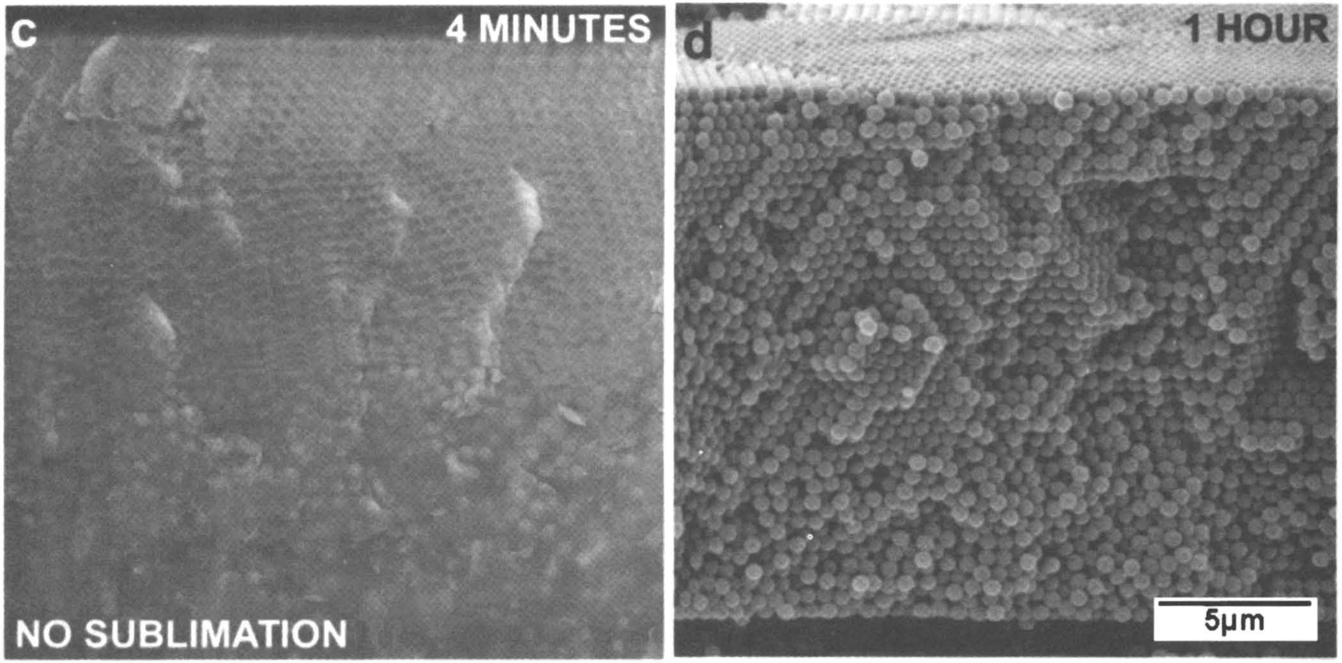

***Figure 6.** Accretion of ordered layers downward from the top surface away from the edges of the coating of 15 wt% PBMA latex suspension after different periods of drying: (a) 1 minute, (b) 2 minutes, (c) 4 minutes. The images in (a) and (b) are fracture surfaces that have been sublimed for 5 minutes at 143 K. (d) Fracture surface of a fully dried coating.*

because water diffused between the particles, the menisci there relaxed to flat states, and the net surface-tension forces and capillary-pressure differences that had drawn particles together disappeared.

Figure 7 show representative sizes of the colloidal crystals that grew beneath the top surface of PBMA latex coating as it dried. The largest crystal that is visible is around 10 to 20 μm in size. This is much smaller than the size of colloidal crystal desired for templates of photonic materials, for example. Perhaps larger crystals can be produced in drying latex coatings by controlling the rate of water evaporation during drying and eliminating the stray air currents above the drying sample.

Downloaded by PENNSYLVANIA STATE UNIV on September 17, 2012 | http://pubs.acs.org
Publication Date: July 26, 2001 | doi: 10.1021/bk-2001-0790.ch010

Conclusions

Cryo-SEM micrographs of drying latex coatings presented here confirm the presence of edge consolidation fronts that advance inward from the coating's perimeter, and descending consolidation fronts that advance from the free surface to the substrate in the region distant from the edges. In experiments with coatings that are small in area (e.g. 1 cm^2) and made with solvent or solution of low viscosity (e.g. 1 cp), the edge consolidation fronts are prominent and make the drying rate non-uniform across the area. However, in industrial and commercial applications the surface area of latex coatings are generally large and thickeners are usually added that elevate the viscosity, so that the descending consolidation fronts dominate and the drying rate is more or less uniform across the coating — except at its very edge.

The latex particles that are consolidated at the relatively slower moving descending consolidation fronts tend to be better ordered than those consolidated at the faster moving edge fronts because there is more time for arriving particles to roll and jiggle into close ordered packing before they are buried by the next arrivals. The latex particles are better ordered even at the fast-moving edge consolidation fronts when the latex suspension is deionized. Presumably the softer and longer-range of repulsive electrostatic force allows particles arriving at the front to roll and jiggle more and thereby pack more closely before they are locked by the next arrival.

The results reported here testify that cryo-SEM is a robust technique for studying microstructure evolution during latex film formation. The technique holds promise for understanding the behavior of more complex latex systems that are formulated for paints, adhesives, and other industrial applications.

Acknowledgements

Our thanks go to Prof. L. F. Francis for platinum-coated silicon substrates, Dr. Ashok Menon for technical discussion of cryo-SEM, and Erin Glaser Arlinghaus and Dianne Miller for help with PBMA synthesis. The research was supported by the Center for Interfacial Engineering at the University of Minnesota.

Downloaded by PENNSYLVANIA STATE UNIV on September 17, 2012 | http://pubs.acs.org
Publication Date: July 26, 2001 | doi: 10.1021/bk-2001-0790.ch010

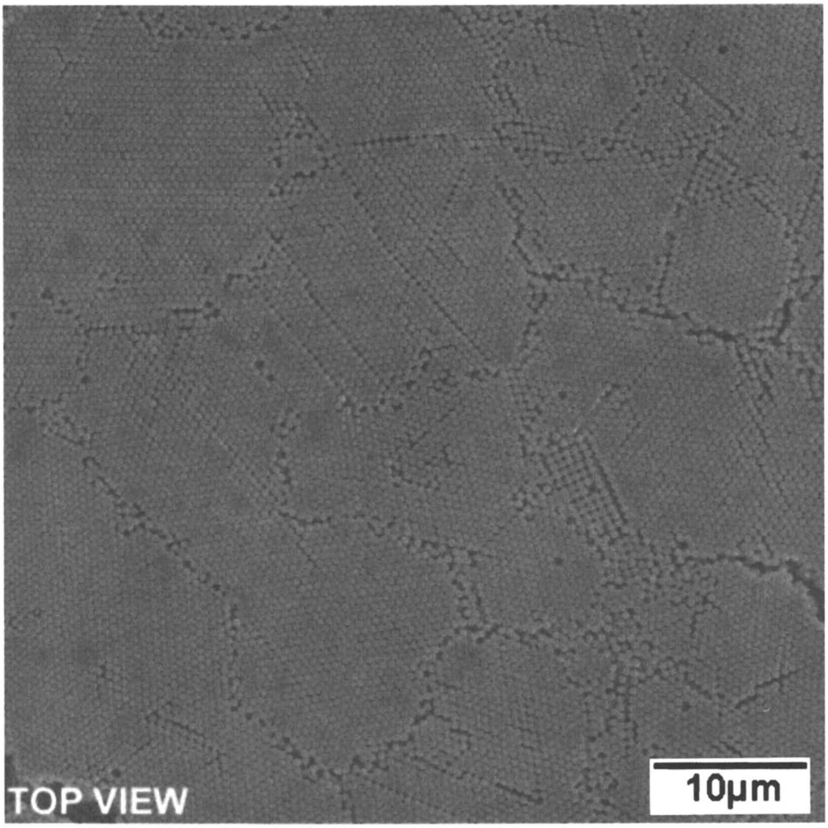

Figure 7. Top view of dried PBMA latex particle away from the edges showing crystals around 10 to 20 micrometers.

Reference

1. J. G. Sheehan, K. Takamura, H. T. Davis, and L. E. Scriven, *TAPPI J.* **1993**, *76(12)*, 93-101.
2. Y. Ming, K. Takamura, H. T. Davis, and L. E. Scriven, TAPPI J. **1995**, *78(11)*, 151-159.
3. Z. Huang, V. S. Thiagarajan, O. K. Lyngberg, L. E. Scriven, and M. C. Flickinger, *J. Coll. and Interface Sci.* **1999**, *215*, 226-243.
4. J. C. H. Hwa, *J. Polym. Sci. A* **1964**, *2*, 785-796.
5. M. Okubo, T. Takeya, Y. Tsusumi, T. Kadooka, and T. Matsumoto, *J. Polym. Sci.: Polym. Chem. Ed.* **1981**, 19, 1-8.
6. M. A. Winnik and J. Feng, *J. Coatings Tech.* **1996**, *68(852)*, 39-50.
7. D. P. Sheetz, *J. Appl. Polym. Sci.* **1965**, *9*, 3759-3773.
8. S. G. Croll, *J. Coatings Tech.* **1986**, *58(734)*, 41-49.
9. R. D. Mountain and A. C. Brown, *J. Chem. Phys.* **1984**, *80(6)*, 2730-2734.
10. G. Y. Onoda, *Phys. Review Letter* **1985**, *55(2)*, 226-229.
11. B. T. Holland, C. F. Blanford, T. Do, and A. Stein, *Science* **1998**, *281*, 538-540.
12. J. W. Vanderhoff, E. B. Bradford, and W. K. Carrington, *J. Polymer Sci.: Polymer Symposia* **1973**, *41*, 155-174.

Downloaded by PENNSYLVANIA STATE UNIV on September 17, 2012 | http://pubs.acs.org
Publication Date: July 26, 2001 | doi: 10.1021/bk-2001-0790.ch010

Downloaded by STANFORD UNIV GREEN LIBR on September 17, 2012 | http://pubs.acs.org
Publication Date: July 26, 2001 | doi: 10.1021/bk-2001-0790.ch011

Chapter 11

Confocal Microscopy and Environmental SEM Applied to Matting Water-Based Lacquers

C. Patrick Royall and Athene M. Donald

Polymers and Colloids Group, Cavendish Laboratory, Department of Physics, University of Cambridge, Madingley Road, Cambridge CB3 0HE, United Kingdom

Two microscopy techniques are used to characterise silica matting agent in water-based lacquers. Environmental SEM permits the resolution of electron microscopy to be applied to insulating and hydrated samples in their natural state. Atomic number contrast enables silica to be readily distinguished from the polymer binder, and surface morphological information can also be obtained.

Images of optical planes within the specimen may be obtained by Confocal Laser Scanning Microscopy (CLSM). Silica is labelled with fluorescein isothiocyanate (FITC) to provide contrast against the surrounding polymer binder. By complementing the surface sensitive technique, Environmental SEM, with bulk studies using CLSM, the relationship between surface and bulk silica occupancies is studied. Maximum surface silica occupancy is reached at a concentration of 2.0% silica by weight, beyond which there is no further increase. The vertical distribution of silica is uniform throughout films of 50 μm in depth, with no tendency for surface segregation.

Introduction

Film formation in polymer latices has been extensively studied, and is at least partially understood *(1)*. The inclusion of microscopic particles of silica

In Film Formation in Coatings; Provder, T., et al.;
ACS Symposium Series; American Chemical Society: Washington, DC, 2001.

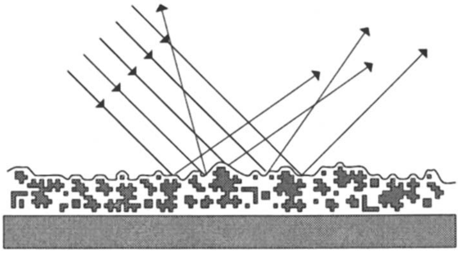

Figure 1: Light scattered by a matting coating

Downloaded by STANFORD UNIV GREEN LIBR on September 17, 2012 | http://pubs.acs.org
Publication Date: July 26, 2001 | doi: 10.1021/bk-2001-0790.ch011

produces an effect known as matting, in which the intensity of specularly reflected light is reduced, figure 1 *(2)*. In this work the microstructure of a clear matting lacquer is accessed by means of two microscopy techniques, in order to understand how the addition of silica particles produces matting. Particular attention is given to the change in structure as a function of silica concentration and a simple model, based on the volume occupied by the silica in the dried lacquer film is able to account for some of the microstructural properties. It appears to go some way towards explaining how a lacquer matts at a microscopic level.

Environmental Scanning Electron Microscopy (ESEM) is a development of SEM, which brings high resolution and depth of field to samples previously inaccessible to electron microscopy. It is distinguished from conventional SEM by the presence of a partial pressure of gas inside the sample chamber *(3)*. ESEM is a surface technique like conventional SEM, and has previously been demonstrated as a unique way to image water-based latices *(4)*, *(5)*.

By elimination of out-of-focus contributions to the signal, confocal microscopy can image optical planes within a thick specimen. The transparent lacquers used are clearly well-suited to this technique. With suitable fluorescent labelling, silica particles are imaged throughout the depth of the lacquer *(6)*, *(7)*.

Image analysis enables numerical data to be extracted from micrographs. Although this process is only *semi-quantitative*, the amount of data available in every image is considerable. This quantitative data from microscopy work can be compared with the amount of silica used in the formulation.

Background

Despite its various benefits, conventional electron microscopy has been limited by the requirement for specimens to be conducting and vacuum resistant, but with ESEM almost any sample can be imaged. A differential pumping system maintains various pressure regimes inside the microscope. These are separated by what are essentially small holes which allow passage of the elec-

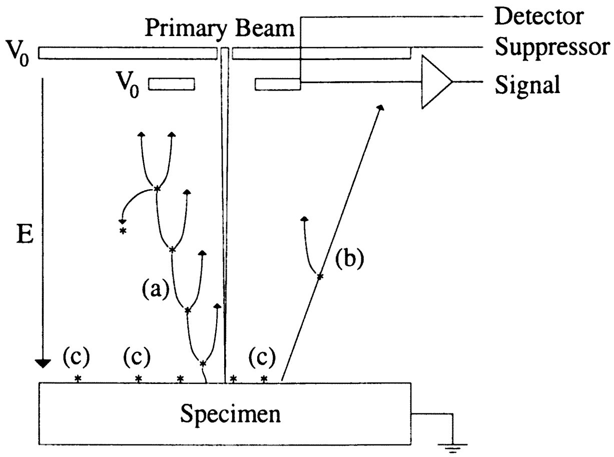

Figure 2: Signal amplification in the ESEM. Secondary electrons emitted by the sample are accelerated in an electric field, and ionise the imaging gas. Successive ionisations initiate a cascade process amplifying the signal (a). Other high-energy backscattered electrons also contribute to the signal, (b). Positive ions (marked as '') then provide charge neutralisation, (c).*

tron beam. Each section is separately pumped, maintaining a pressure gradient throughout the instrument, so the electron gun operates in a relatively high vacuum of 10^{-5} torr ($\sim 10^{-7}$ atm), whereas the sample experiences a pressure of around 5 torr (0.026 atm). At this lower pressure, enough electrons remain unscattered to produce a sharply defined probe so high-resolution images are obtained. *(3)*.

A special detector for non-vacuum operation is required. This is essentially an anode, raised to a few hundred volts, whose electric field produces a cascade from electrons emitted by the sample, figure 2. Each electron emitted from the sample produces up to 200 at the detector. The positive ions produced by this are thought to neutralise the sample surface, so insulating samples can be imaged without the need for a conducting layer *(8)*, *(9)*.

Image contrast in ESEM comes from two routes, secondary electrons and backscattered electrons. Secondary electrons are produced by ionisation events in the sample. These secondary electrons have a low energy and are accelerated by the detector field to produce the cascade (process (a) in figure 2). Secondary electrons have a rather small escape depth, of order a few nanometres. This means that more are emitted from sloping surfaces than from surfaces normal to the incident beam, since the penetration of incident beam electrons is much greater than the escape depth of secondary electrons *(10)*. So secondary electrons are sensitive to surface topography in the matting lacquers.

Backscattered electrons are incident electrons which have scattered strongly in the specimen so that they are ejected, and thus contribute to the signal, pro-

Downloaded by STANFORD UNIV GREEN LIBR on September 17, 2012 | http://pubs.acs.org
Publication Date: July 26, 2001 | doi: 10.1021/bk-2001-0790.ch011

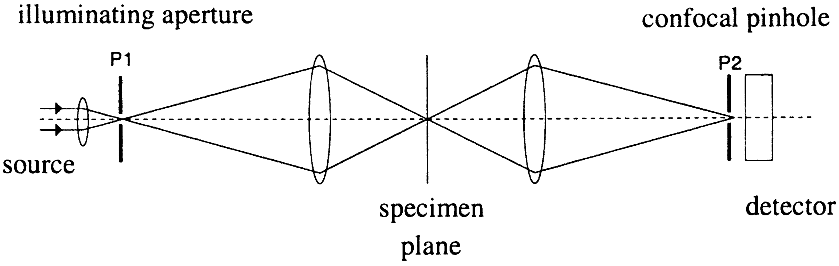

Figure 3: The principle of Confocal Microscopy. Light is focussed into a point in the sample plane by the condenser lens. The confocal pinhole rejects all light except that from the point in focus.

cess (b) in figure 2. Since backscattered electrons have a much higher energy than secondary electrons, they interact more weakly with the gas molecules and the cascade mechanism is suppressed, although the backscattered signal is still considerable *(11)*. Silicon has a higher atomic number than the surrounding polymer matrix. The incident electrons interact more strongly with the greater charge on the larger atomic nuclei, and increase the backscattered signal. So the silica particles are expected to produce bright regions, due to increased backscattering *(10)*. This means that ESEM is able to study the distribution of silica at the surface effectively, but is unable to penetrate the sample significantly.

Although confocal microscopy was originally proposed in 1957, it is only recently that the full potential of the technique has been realised. The confocal principle is shown schematically in figure 3. In conventional light microscopy, a thin planar sample is illuminated, and an image of the entire specimen is produced. This has the disadvantage that only very thin specimens may be studied (often requiring a series of slices to be made), and that out-of-focus contributions to the image degrade resolution *(6)*.

In a confocal microscope, light from only one point in the specimen passes through to the detector. All light from other regions in the sample is rejected by the confocal pinhole (figure 3). This has the advantage that, provided the sample is reasonably transparent, thick specimens may be imaged without the problem of out-of-focus contributions. In practice, in fluorescence mode, one lens may be used as both the condenser and objective, and a half-silvered mirror is used to split the incident and emitted light. This does not alter the confocal optics.

Since only a single point is observed at any one time, the specimen or light beam must be *scanned* in a similar way to a scanning electron microscope. By scanning vertically as well as horizontally, a 3d image may be produced.

The resolution is better than conventional light microscopy, at around 0.1μm in the horizontal plane, and 0.6μm in the vertical direction. As a single point is viewed at any one time, intensity is quite small. A laser source is used to improve this. Such an instrument using a laser light source is referred to as a

Downloaded by STANFORD UNIV GREEN LIBR on September 17, 2012 | http://pubs.acs.org
Publication Date: July 26, 2001 | doi: 10.1021/bk-2001-0790.ch011

confocal laser scanning microscope (CLSM). Selective labelling with a fluorescent dye can enormously enhance contrast, by binding it to a region of interest in the sample. A filter is then used to allow only fluorescent light through to the detector, rejecting reflected light *(6)*. In order to study matting water-based lacquers, it is therefore necessary to label the silica matting agent with a fluorescent dye. Refractive index matching of the polymer binder with the silica matting agent allows light to penetrate up to 50 μm below the sample surface without significant attenuation.

Downloaded by STANFORD UNIV GREEN LIBR on September 17, 2012 | http://pubs.acs.org
Publication Date: July 26, 2001 | doi: 10.1021/bk-2001-0790.ch011

Experiment

The lacquer used is a commercial product. The latex is largely polybutyl methacrylate, with a diameter of 85nm and polydispersity of around 0.05, measured by static light scattering. A number of additives are also used, as shown in the recipe in table 2. The ingredients are added in succession to a Cowles head rotating at 1500rpm. The speed is increased to 3000 rpm following addition of the silica, which is pre-dispersed in an aqueous solution of the fluorescent dye. The silica matting agent is based on a fumed silica, with the appearance of agglomeration. For silica characteristics, see table 1.

For confocal work the silica is labelled with a fluorescent dye, rhodamine 6G, obtained from Sigma. The dye is in the form of a chloride salt and dissolves in water to a concentration of around 0.01 mol. Rhodamine 6G is cationic, and is expected to adsorb onto the negatively charged silica surfaces, when silica is dispersed in solution prior to inclusion in the lacquer formulation *(13)*. This expectation appears to be supported by centrifuge studies, where the dye remains adsorbed onto the silica after six washes in water at 10,000 rpm for 5 minutes. Although there is some leaching out of the dye into the supernatant, the silica remains dyed red. The amount of dye required to label the silica was determined by measuring the relative brightness of the silica particles in

Table 1: Characteristics of fumed silica used in this work.

Bulk density	$0.045 gcm^{-3}$ [a]
True density	$2.2 gcm^{-3}$ [b]
Surface area	$180 m^2 g^{-1}$ [c]
Pore volume	$0.951 cm^3 g^{-1}$ [c]
Mean particle size	$4 \mu m$ [b]
Oil Absorption	$360 g/100 g$ of silica [b]

[a] determined in this work, [b] *(12)*, [c] determined by Crosfield R&D Group with Mercury Porosimetry.

Downloaded by STANFORD UNIV GREEN LIBR on September 17, 2012 | http://pubs.acs.org
Publication Date: July 26, 2001 | doi: 10.1021/bk-2001-0790.ch011

Table 2: Formulation recipe and suppliers. The silica is dispersed in the rhodamine solution prior to mixing.

Component	*Function*	*Supplier*	*% by weight*	*Density* (gcm^{-3})
Glascol C47	Latex Binder	Allied Colloids (UK)	71.4	1.04
Rhodamine 6G Soln.	Fluorescent dye	Sigma	16.8	1.0
Tegofoamex 1488	Defoamer	Tego Chemie (UK)	0.1	
TS100	Matting Agent	Degussa	0-4.0	0.045
Dowanol PnB	Coalescing aid	Dow Chemical Co.	3.81	0.9
Dowanol DPnB	Coalescing aid	Dow Chemical Co.	1.90	0.922
Tegofoamex 1488	Defoamer	Tego Chemie (UK)	0.05	1.0
Troysol LAC	Anti Cratering Agent	Troy Chemical	0.5	1.04-1.07
Glaswax E1	Surface enhancer	Allied Colloids (UK)	2.14	0.995
DSX 1514	Rheology Modifier	Henkel	0.8	1.068

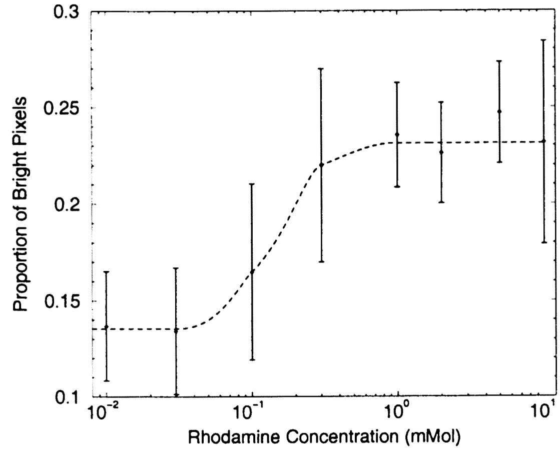

Figure 4: Image contrast is found to increase with greater rhodamine concentration up to a value of 3×10^{-4} *mol. Beyond this, the silica is assumed to be sufficiently labelled that it can all be seen.*

the images produced for various concentrations of rhodamine, holding the silica quantity constant.

The images were analysed such that bright pixels were selected corresponding to silica, and noise eliminated by requiring that the size of a bright region exceeded ten pixels. With insufficient rhodamine, there was little fluorescent signal, and not all the silica was labelled, so fewer bright pixels were observed. When enough rhodamine had been incorporated, all the silica was labelled, and the proportion of bright pixels reaches a maximum at a rhodamine concentration of 3×10^{-4} mol, figure 4. Experiments have been carried out with a 2×10^{-3} mol solution of rhodamine 6G.

Samples were produced as wet films of nominal thickness 100 μm on glass for confocal work or chromated aluminium for ESEM, with a small (20 mm) bar coater. No difference has so far been found between the substrates, as the CLSM can image samples prepared on chromated aluminium as well. These films were then dried in a dessicator with phosphorous pentoxide dessicant for 24 hours before each experiment. A helium-neon laser at 543 nm is used to excite the rhodamine, whose absorption peak is around 525 nm. A bandpass filter of 560-615 nm eliminates light that is simply reflected, but the emission peak of rhodamine 6G is sufficiently close to this range, at 555 nm that a sufficiently strong signal is produced *(14)*.

Downloaded by STANFORD UNIV GREEN LIBR on September 17, 2012 | http://pubs.acs.org
Publication Date: July 26, 2001 | doi: 10.1021/bk-2001-0790.ch011

Downloaded by STANFORD UNIV GREEN LIBR on September 17, 2012 | http://pubs.acs.org
Publication Date: July 26, 2001 | doi: 10.1021/bk-2001-0790.ch011

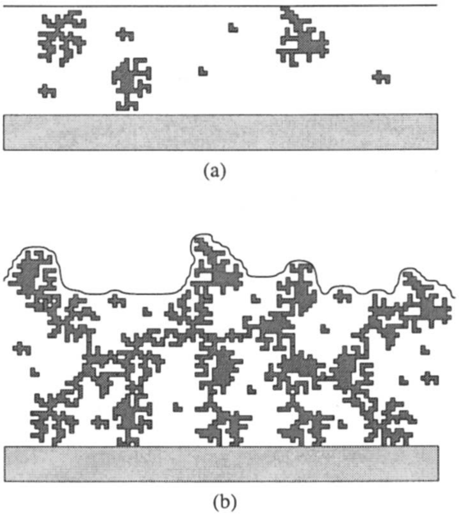

Figure 5: A schematic side-view of the dried film. Small amounts of silica are isolated in the dried film (a) but a sufficiently high concentration can produce a continuous silica structure, producing a roughened surface (b).

Silica Behaviour

Fumed silica is formed by a gas phase reaction at elevated temperature and comprises small ($\sim$20 nm) *ultimate* particles of high purity *(13)*. These are formed into larger *primary* particles in the micron range which are studied in this work. These primary particles are weakly bound *(15)* and highly porous (table 1) with an extremely low bulk density. To find the bulk density, the silica volume was found by filling a $25cm^3$ measuring cylinder, which was then allowed to fall repeatedly through $1cm$ onto a hard surface to encourage settling. This gave a value of 0.045 gcm^{-3} for the bulk dry powder.

The bulk volume occupied by such a low density material is largely air, which is present both in the pores within the particles and in the spaces between the particles. Air in pores and between particles is assumed to be replaced by polymeric material from the latex in the dried lacquer. At the silica concentrations used, table 3, this bulk volume occupied by the silica is a significant proportion of, or may even exceed that of the dried polymer film. Two scenarios are considered, figure 5. In the first case the silica is present in quite small quantities, and the dried lacquer may be regarded as a continuous layer of polymer, in which *isolated* silica particles are embedded figure 5 (a).

At a certain concentration, the silica particles touch, and can rest against one another, figure 5 (b). At this point, the structure formed by the silica is assumed to be the same as the dry powder, and thus to have the same *packing fraction.* So rather than a polymer film with isolated silica particles, we expect a continuous silica structure, similar to the dry powder, but with spaces in between silica particles and pores now occupied by polymer. This structure may be accessed with the microscopy techniques previously described. Varying the amount of silica in the lacquer, the critical concentration required to form a silica structure may be found, by comparing the observed structure with that proposed in figure 5.

A mathematical treatment of the above description is now given. The dry mass of the lacquer is given by

$$m_{dry} = m_{wet} C_{sol} \tag{1}$$

where m_{dry} and m_{wet} are the dry and wet masses of the lacquer, $C_{sol} = 0.35$ is the solids weight fraction of the lacquer, the weight fraction of the lacquer which does not evaporate *(16)*. Since the densities of the lacquer and its components are similar (excluding the silica), table 3,

$$V_{dry} = V_{wet} C_{sol} \tag{2}$$

where V_{dry} and V_{wet} are the dry and wet volumes of the lacquer. The bulk density of dry silica is given as

$$\rho_{sil} = \frac{m_{sil}}{V_{bulk}} \tag{3}$$

where the bulk volume V_{bulk} is the volume occupied by the silica particles *and* the air between them, m_{sil} is the silica mass and ρ_{sil} the bulk density of the silica powder (0.045 gcm^{-3}). Now if the way the silica packs in the dried lacquer is the same as the powder, we expect a packing fraction p_f, which will give the proportion of volume occupied by the silica

$$V_{bulk} p_f = V_{sil} = \frac{m_{sil}}{\rho_{sil}} p_f \tag{4}$$

with V_{sil} the volume of the silica particles and their internal pores only. Assuming that the density measured for the dry powder is valid for the dried lacquer, a continuous silica structure will span the dry lacquer when

$$V_{bulk} = V_{dry} \tag{5}$$

$$\Rightarrow V_{sil} = V_{dry} p_f . \tag{6}$$

Downloaded by STANFORD UNIV GREEN LIBR on September 17, 2012 | http://pubs.acs.org
Publication Date: July 26, 2001 | doi: 10.1021/bk-2001-0790.ch011

Table 3: Silica concentration and $\frac{m_{sil}}{m_0}$ as calculated from equation 9

Silica concentration (% by weight) $\frac{m_{sil}}{m_{wet}} \times 100$	$\frac{m_{sil}}{m_0}$
0	0
0.25	0.16
0.5	0.32
1.0	0.64
1.5	0.96
2.0	1.27
2.5	1.59
3.0	1.91
3.5	2.22
4.0	2.54

This is satisfied at a *critical mass*, m_0 of silica, given by

$$V_{sil} = \frac{m_0}{\rho_{sil}} p_f = V_{wet} C_{sol} p_f \tag{7}$$

$$\Rightarrow m_0 = \rho_{sil} V_{wet} C_{sol} = \frac{\rho_{sil} m_{wet} C_{sol}}{\rho_{wet}} \tag{8}$$

where ρ_{wet} is the density of the wet lacquer (≈ 1 gcm^{-3}). For a given weight fraction of silica, a parameter $\frac{m_{sil}}{m_0}$ can be assigned, such that $\frac{m_{sil}}{m_0} = 1$ when $V_{bulk} = V_{dry}$.

$$\frac{m_{sil}}{m_0} = \frac{m_{sil}}{m_{wet}} \frac{\rho_{wet}}{\rho_{sil} C_{sol}}. \tag{9}$$

where $\frac{m_{sil}}{m_{wet}}$ is the silica mass fraction of the wet lacquer. Values of $\frac{m_{sil}}{m_0}$ are given for various silica concentrations in table 3.

From equations 2, 4 and 9, we can relate $\frac{m_{sil}}{m_0}$ to the volume fraction of silica. This is equal to the fraction of silica expected in two-dimensional micrographs, assuming that the silica is uniformly distributed.

$$\frac{V_{sil}}{V_{dry}} = \frac{m_{sil}}{m_0} p_f = \phi_{sil} \tag{10}$$

Downloaded by STANFORD UNIV GREEN LIBR on September 17, 2012 | http://pubs.acs.org
Publication Date: July 26, 2001 | doi: 10.1021/bk-2001-0790.ch011

where ϕ_{sil} is termed the silica occupancy. So the occupancy is linear in $\frac{m_{sil}}{m_0}$, and is equal to p_f when a continuous silica structure is formed.

Results and Analysis

This section deals with images produced from CLSM and ESEM. Image analysis is then discussed in some detail before numerical results are presented.

The contrast in the ESEM images in figure 6 agrees with expectation. Silica is distinguished as small, white regions around a few μm in size. Figure 6 *(b)* in particular suggests a degree of topographic contrast. There is considerably more silica present in figure 6 *(b)* ($\frac{m_{sil}}{m_0} = 0.95$) than figure 6 *(a)*. ($\frac{m_{sil}}{m_0} = 0.64$). There is little further increase in *surface* silica occupancy in figure 6 *(c)* ($\frac{m_{sil}}{m_0} = 1.91$) compared to the previous image, although the topology appears somewhat different. These images are in agreement with the model discussed above, although they do not conclusively demonstrate it.

Confocal images also reveal silica particles. The images shown in figure 7 are taken around the middle of the dried lacquer and are x-y scans, z being depth. The silica is easily seen from the rhodamine labelling, and the surrounding polymer has a degree of brightness as well. This is presumably the result of some rhodamine leaching out from the silica. The brightness of the polymer matrix reveals some dark regions, such as the one marked as *(i)* in figure 7 *(d)*. These are thought to be air voids.

The silica occupancy increases markedly from figure 7 *(a)* to *(c)*. Figure 7 *(a)* ($\frac{m_{sil}}{m_0} = 0.32$) appears to be in the regime of figure 5 *(a)*, of silica particles isolated in a continuous polymer medium. The same is true of figure 7 *(b)* ($\frac{m_{sil}}{m_0} = 0.64$). This is expected as the $\frac{m_{sil}}{m_0}$ values are less than 1 for both of these images. Increasing the silica concentration further might be expected to produce a continuous silica structure, but since the images are two dimensional and any structure is expected to be three dimensional, the absence of a spanning structure from figure 7 *(c)* and *(d)* ($\frac{m_{sil}}{m_0} = 1.27$ and 1.91 respectively) is not surprising. However there is no apparent increase in silica between figure 7 *(c)* and *(d)*. Like the ESEM images, the increase in silica occupancy with $\frac{m_{sil}}{m_0}$ ceases when $\frac{m_{sil}}{m_0} \gtrapprox 1$.

To go further, it is necessary to extract quantitative information from the images, and indeed to test equation 10, which predicts that at a concentration of $\frac{m_{sil}}{m_0} \approx 1$, the volume of silica is related to the volume of the dry lacquer by the packing fraction. Since a two-dimensional image of the sample is also expected to have a silica occupancy of ϕ_{sil} on average, image analysis may be used to find the silica occupancy.

The brightness of an image may be thought of as a two-dimensional function of position, $I(x,y)$. Noise may be reduced with a Gaussian blur filter *(17)*. Silica particles cause local brightness variation, as the value of $I(x,y)$ changes from a low value (darker, surrounding polymer) to a higher value (brighter silica).

Downloaded by STANFORD UNIV GREEN LIBR on September 17, 2012 | http://pubs.acs.org
Publication Date: July 26, 2001 | doi: 10.1021/bk-2001-0790.ch011

Downloaded by STANFORD UNIV GREEN LIBR on September 17, 2012 | http://pubs.acs.org
Publication Date: July 26, 2001 | doi: 10.1021/bk-2001-0790.ch011

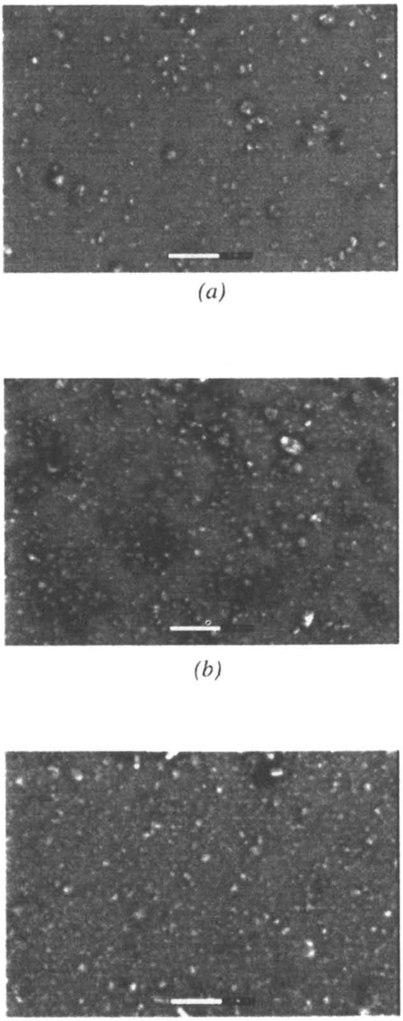

(a)

(b)

(c)

Figure 6: ESEM images of increasing silica concentration, $\frac{m_{sil}}{m_0} = 0.64$ (a), $\frac{m_{sil}}{m_0} = 1.27$ (b), $\frac{m_{sil}}{m_0} = 1.91$ (c), *bars* $= 20\mu m$.

So the gradient of $I(x,y)$ increases in the vicinity of silica particles. This is found numerically by differentiating with respect to x and y, and squaring the differentials to obtain a positive value. A square root is then taken, in an algorithm known as the Sobel operator *(17)*

$$SOBEL(x,y) = \sqrt{\left(\frac{\partial}{\partial x} I(x,y)\right)^2 + \left(\frac{\partial}{\partial y} I(x,y)\right)^2} . \qquad (11)$$

The resulting function, $SOBEL(x,y)$ has peaks in regions of high brightness variation, such as the edges of particles, regardless of the original brightness. Since there is intensity variation within the silica particles, which are in any case quite small, $SOBEL(x,y)$ is greater than zero in the centres of particles as well.

However the polymer background value is close to zero, as there is very little brightness variation there. If the small brightness variation from noise can be excluded by a suitably chosen *threshold*, all other brightness variation may be considered as silica. Such a thresholded image is separated into 'not silica' and 'silica', and this two-level image is termed a binary image, figure 8. The silica occupancy may then be found by dividing the number of white pixels by the total number of pixels.

The choice of threshold is found by using a sample without any silica, as this should be comprised purely from the polymer background. The threshold is then set such that brightness variation in this image is ignored. The silica occupancy is then found for each image, and the results are plotted in figures 9 and 10 for ESEM and confocal images respectively. In the ESEM case, the surface silica occupancy is found, whereas confocal image analysis reveals the bulk silica occupancy from below the surface of the lacquer, equal to ϕ_{sil} in equation 10.

The trend is the same as that in figures 6 and 7, in that silica occupancy increases up to $\frac{m_{sil}}{m_0} \approx 1$, and then levels off. The silica occupancy of the plateau is different between the ESEM and confocal plots (figures 9 and 10), but these numbers have been arrived at via two different techniques. Apart from the two different contrast mechanisms between confocal microscopy and ESEM, confocal images contain contributions from a region around $0.6\mu m$ in depth (the z-resolution), which may contain more silica that a true plane. Alternatively, there may be a difference between the surface and the bulk. Surface tension during drying may result in a thin layer of polymer covering the silica particles, figure 5. This may reduce the amount of silica detected by ESEM.

The point for surface silica occupancy at $\frac{m_{sil}}{m_0} = 0.64$ lies some way from the best fit line, figure 9. This may be the result of a different surface occupancy regime, before a 'jump' at $\frac{m_{sil}}{m_0} \approx 1$, when the surface occupancy increases significantly. More data are required to elucidate this point further. For the present, the first five points are assumed to lie on a straight line, along with the last six. The point at $\frac{m_{sil}}{m_0} = 0.95$ is taken to lie on both lines. Regression fits to these lines are shown in figure 9. As can be seen, the data for $\frac{m_{sil}}{m_0} \lesssim 1$ agree well with a linear oncrease in surface silica with silica concentration. In addition,

Downloaded by STANFORD UNIV GREEN LIBR on September 17, 2012 | http://pubs.acs.org
Publication Date: July 26, 2001 | doi: 10.1021/bk-2001-0790.ch011

Downloaded by STANFORD UNIV GREEN LIBR on September 17, 2012 | http://pubs.acs.org
Publication Date: July 26, 2001 | doi: 10.1021/bk-2001-0790.ch011

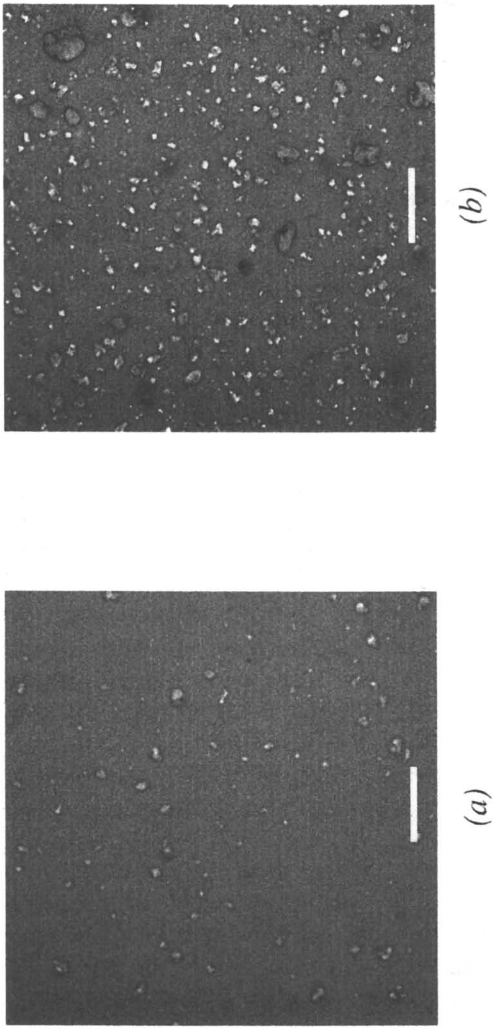

Downloaded by STANFORD UNIV GREEN LIBR on September 17, 2012 | http://pubs.acs.org
Publication Date: July 26, 2001 | doi: 10.1021/bk-2001-0790.ch011

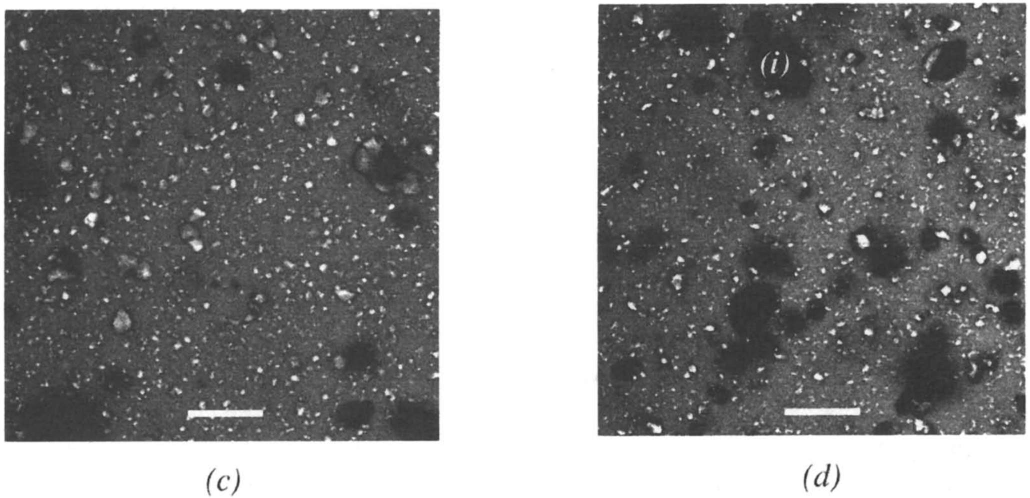

(c) (d)

Figure 7: Confocal images of increasing silica concentration, $\frac{m_{sil}}{m_0} = 0.32$ (a), $\frac{m_{sil}}{m_0} = 0.64$ (b), $\frac{m_{sil}}{m_0} = 1.27$ (c), $\frac{m_{sil}}{m_0} = 1.91$ (d), *bars* $= 20\mu m$, *all images were taken around 10 μm from the substrate*

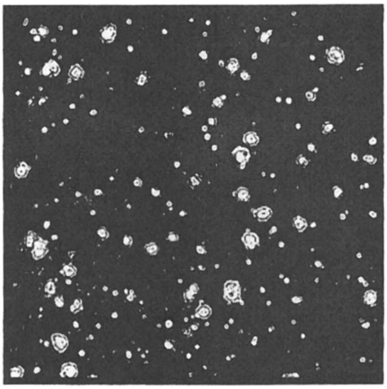

Figure 8: A binary image from figure 7 (a)*. The regions in white are taken to be silica, those in black are identified as polymer. The fraction of white pixels is the silica occupancy.*

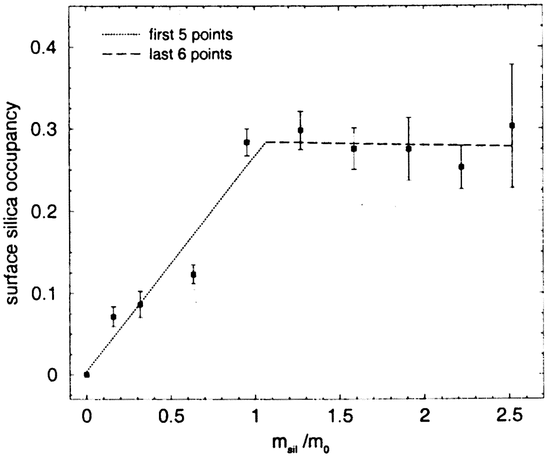

Figure 9: Surface silica occupancy as a function of $\frac{m_{sil}}{m_0}$ *for ESEM images. The increase to* $\frac{m_{sil}}{m_0} = 1$ *and subsequent plateau are clearly seen.*

for $\frac{m_{sil}}{m_0} \gtrsim 1$ the regression fit is almost flat, suggesting that the maximum silica surface occupancy has been reached. The intercept was determined as

Downloaded by STANFORD UNIV GREEN LIBR on September 17, 2012 | http://pubs.acs.org
Publication Date: July 26, 2001 | doi: 10.1021/bk-2001-0790.ch011

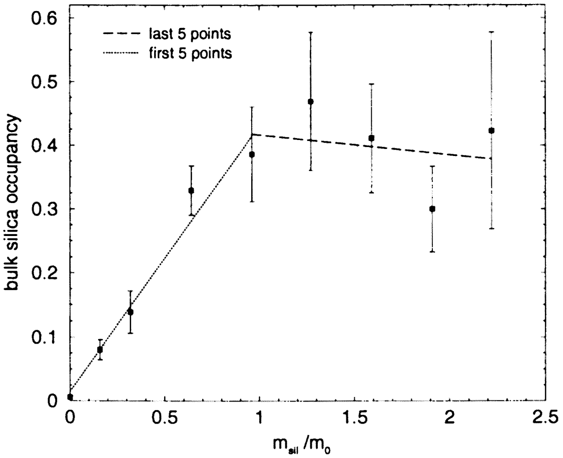

Figure 10: Bulk silica occupancy as a function of $\frac{m_{sil}}{m_0}$*, from confocal images. The rise to* $\frac{m_{sil}}{m_0} = 1$ *appears to lie on a straight line, and the plateau for greater values is also present. The straight line and plateau region have had best fit lines applied to them.*

$\frac{m_{sil}}{m_0} = 1.07 \pm 0.14$, for a silica surface occupancy of 0.281 ± 0.014. These results are in agreement with the model described above, although they do not conclusively confirm it.

Up to a value of $\frac{m_{sil}}{m_0} \approx 1$, the confocal data (figure 10) appears to follow equation 10, so we can determine the value of the packing fraction as $p_f = 0.43 \pm 0.02$ from a regression fit of the first five points. Like the ESEM data for $\frac{m_{sil}}{m_0} \gtrapprox 1$, the last five points in figure 10 show no further increase in silica occupancy. The value for the packing fraction is much less than close-packed systems (0.74 for close-packed spheres *(18)*) and in fact lies closer to that for *percolating* systems. From percolation theory, if sites on a cubic lattice are randomly filled a spanning structure is formed when a proportion of around 0.312 sites are occupied *(19)*. Taking into account the fact that the silica particles have a distribution of sizes, the higher value obtained for p_f is not unreasonable. Since the silica particles are extremely polydisperse, the smaller particles may lie between the larger ones, increasing the packing fraction as well, figure 5 (b). Effects such as gravity and surface tension in the drying lacquer are also expected to increase the packing fraction.

The plots in figures 9 and 10 support the observation from the images that the silica occupancy does not increase beyond $\frac{m_{sil}}{m_0} \approx 1$. This is at odds with equation 10, which predicts a linear increase in silica occupancy as a function of $\frac{m_{sil}}{m_0}$.

There seem to be two possibilities when $\frac{m_{sil}}{m_0} > 1$. First, if the silica structure is rigid, then it should determine the thickness of the dried film. So the film thickness should increase with $\frac{m_{sil}}{m_0}$, for $\frac{m_{sil}}{m_0} > 1$. This is not found to be the

Downloaded by STANFORD UNIV GREEN LIBR on September 17, 2012 | http://pubs.acs.org
Publication Date: July 26, 2001 | doi: 10.1021/bk-2001-0790.ch011

case, as all the dried films are around the same thickness, of $20 - 30\mu m$, with no dependence on $\frac{m_{sil}}{m_0}$, the thickness being found as a by product of confocal microscopy.

Secondly, the silica structure may be crushed by the volume reduction in the drying lacquer. In this case the surface appearance of such a crushed structure may be unaltered by the precise quantity of silica present, so ESEM images will not be sensitive to $\frac{m_{sil}}{m_0}$. Below the lacquer surface, the fragments from crushed silica particles may be extremely small, since the ultimate particles are only $20nm$ in size. This is far below the maximum resolution of the confocal microscope of $0.1\mu m$, so no further increase in silica occupancy is expected for $\frac{m_{sil}}{m_0} > 1$.

Downloaded by STANFORD UNIV GREEN LIBR on September 17, 2012 | http://pubs.acs.org
Publication Date: July 26, 2001 | doi: 10.1021/bk-2001-0790.ch011

Conclusions

A simple model based on volume occupied by silica in matting lacquer is able to predict microstructural properties. Both surface and bulk images and numerical image analysis suggest that at a critical silica concentration, a three dimensional silica structure is formed throughout the dried lacquer. The critical concentration required to form this structure may be predicted by measurement of the bulk density of the dry powder, assuming that the way the silica packs in the dry powder remains unchanged in the dried lacquer film.

Although it is unlikely to fully explain the behaviour of silica in matting lacquers, this simple model demonstrates the applicability of microscopy to such systems.

Acknowledgements

This work was supported by EPSRC and Crosfield Group Ltd, Warrington UK. The Authors would like to thank Dr Ian Hopkinson and Matthew Myatt for all the help with the confocal microscope, Dr Gemma Morea-Swift at Crosfields, and the suppliers of the various ingredients for the formulation.

Literature Cited

1. Keddie, J.L. *Materials Science and Engineering R-Reports*,**1997**, *21*, no 3, pp 101-170.
2. Schneider, H. *Surface Coatings International*, **1994**, *77*, no 9, p376.

3. Danilatos, G.D. *Microscopy Research and Technique*, **1993**, *25*, pp 354-361.
4. Keddie, J.L.; Meredith, P.; Jones, R.A.L.; Donald, A.M.; *Macromolecules*, **1995**, *28* , pp 2673-2682.
5. Keddie, J.L.; Meredith, P.; Jones, R.A.L.; Donald, A.M. In *Film Formation in Waterborne Coatings*; Editors, T. Provder, M. A. Winnik, M.W. Urban; ACS Symposium Series 648; American Chemical Society, 1996, Vol 648, pp 332-348.
6. Sheppard, C.J.R.; Shotton, D.M. *Confocal Laser Scanning Microscopy*, Microscopy Handbooks 38, BIOS Scientific Publishers, Oxford, England, 1997.
7. *Handbook of Biological Confocal Microscopy*, Editor Pawley, J.B.,2nd ed, Plenum Press, New York and London, 1995.
8. Fletcher, A.L. ; Thiel, B.L.; Donald, A.M.; *J. Phys D; Appl. Phys*, **1997**, *30*, pp 2249-2257.
9. Thiel, B.L.; Bache, I.C.; Fletcher, A.L.; Meredith, P.; Donald, A.M.; *J. Microscopy*, **1997**, *187*, Pt 3, pp 143-157
10. Goldstein, J.I.; Newbury, D.E.; Echlin, P.; Joy, D.C.; Romig, A.D. Jr; Lyman, C.E.; Fiori, C.; Lifshin, E. *Scanning Electron Microscopy and X-ray Microanalysis*, 2nd Edition, Plenum Press, New York, 1992.
11. Fletcher, A.L. PhD Thesis, University of Cambridge, Cambridge, England, 1997.
12. Ash, I; Ash, M *Handbook of Paint and Coating Additives*, Gower Publishing Ltd, Aldershot, England, 1996, Vol 1: Raw Materials.
13. Ihler, R.K. *The Chemistry of Silica*, Wiley, New york, 1979.
14. Haughland, R.P. *Handbook of Fluorescent Probes and Research Chemicals*, 6th ed, Molecular Probes Inc., Eugene, OR, 1996.
15. Kleinschmidt, P. *Speciality Inorganic Chemicals*, Royal Society of Chemistry Special Publication no 40, 1981, Vol: 40.
16. Turner, G.P.A. *Introduction to Paint Chemistry*, 3rd ed, Chapman and Hall, London, 1991.
17. Russ, J.C. *The Image Processing Handbook*, 2nd ed, CRC Press, Boca Raton, FL, 1995.
18. Blakemore, J.S. *Solid State Physics*, 2nd ed, Cambridge University Press, Cambridge, England, 1985.
19. Stauffer, D.; Aharony, A, *Introduction to Percolation Theory*, 2nd ed, Taylor and Francis, London, 1991.

Downloaded by STANFORD UNIV GREEN LIBR on September 17, 2012 | http://pubs.acs.org
Publication Date: July 26, 2001 | doi: 10.1021/bk-2001-0790.ch011

Chapter 12

Influence of Carboxyl Groups on the Morphology and Surface Properties of Films Prepared from Model Carboxylated Latex Blends

Jiansheng Tang, Eric S. Daniels, Victoria L. Dimonie, Andrew Klein, and Mohamed S. El-Aasser

Emulsion Polymers Institute and Department of Chemical Engineering, Lehigh University, 111 Research Drive, Bethlehem, PA 18015

Downloaded by COLUMBIA UNIV on September 17, 2012 | http://pubs.acs.org
Publication Date: July 26, 2001 | doi: 10.1021/bk-2001-0790.ch012

Model carboxylated latex blends consisting of cleaned polystyrene (PS) hard and poly(*n*-butyl methacrylate-co-*n*-butyl acrylate) soft latex particles were studied to understand the influence of the presence of carboxyl groups on the morphology and surface properties of the resulting latex blend films. It was found that utilizing PS particles with a low density of carboxyl groups present on particle surfaces (e.g., 13% surface coverage) resulted in an even distribution of these particles in the soft copolymer matrix, and thus, good gloss was achieved, while the use of PS hard particles with a high density of carboxyl groups (e.g., 77.2% coverage) resulted in less uniform distribution and poor gloss. However, the neutralization of the carboxyl groups improved the particle distribution and the gloss. A strong base used for the neutralization showed stronger effects than a weak base on the improvement of the uniformity of the PS hard particle distribution and the gloss. The presence of the carboxyl groups on the latex particles also improved the strength of the interphase between the hard particle and the soft polymer matrix. A cluster model and an interparticle hydrogen bonding mechanism were proposed to explain these phenomena.

The move toward environmentally-friendly products have driven the coatings industries to develop new durable films with strong mechanical properties and with zero volatile organic compounds (VOCs). Latex blending, especially blends of hard

In Film Formation in Coatings; Provder, T., et al.;
ACS Symposium Series; American Chemical Society: Washington, DC, 2001.

Downloaded by COLUMBIA UNIV on September 17, 2012 | http://pubs.acs.org
Publication Date: July 26, 2001 | doi: 10.1021/bk-2001-0790.ch012

and soft latex particles, is an attractive strategy to achieve this goal[1-4]. Therefore, academic research to understand the fundamental parameters governing film formation and their relationships to the properties of zero VOC films was initiated. It is envisioned that the soft latex particles (low T_g) will deform and form a continuous film with embedded hard latex particles (high T_g) whose presence will impart desirable optical or mechanical properties. Polymer latex blends are thus expected to offer a compromise between latexes that have good optical or mechanical properties and those which are good film formers[5]. However, the benefits obtained from the latex blends would be greatly decreased if the hard particles were not uniformly distributed in the soft polymer matrix and the adhesion between the hard particles and the soft matrix were not well developed[1,3]. Thus, how to control the particle packing and strengthen the hard/soft particle interphase are active issues in this area.

This paper focuses on the investigation of the influence of the latex particle surface characteristics on the morphology and surface properties of films obtained from the model latex blends. Carboxyl groups were incorporated into the surface of the particles to alter the surface characteristics of the latex particles in a controlled manner. The model hard/soft latex blend system comprises polystyrene (PS) hard latex particles (T_g = 106 °C) and poly(*n*-butyl methacrylate-co-*n*-butyl acrylate) [P(BMA/BA)] copolymer soft latex particles. The T_g of the soft latex (e.g., 0 °C) can be adjusted by varying the composition of the copolymer.

Experimental

Materials

n-Butyl methacrylate (BMA), *n*-butyl acrylate (BA), styrene (St), and methacrylic acid (MAA) monomers (Aldrich; reagent grade) were purified by passing them through columns filled with an appropriate inhibitor removal packing material (Aldrich). Maleic acid (MA; Aldrich; analytical grade), sodium dodecyl sulfate (SDS; Fisher Scientific; reagent grade), Aerosol MA-80 (Cytec Industries), sodium bicarbonate (Aldrich; reagent grade), ammonium hydroxide (28%; EM Science; reagent grade), sodium hydroxide (NaOH; Fisher; reagent grade), potassium hydroxide (KOH; Aldrich; reagent grade), and cesium hydroxide (CsOH; Aldrich; reagent grade) were used as received without further purification. Cationic ion exchange resin (AG 50W-X4, 20-50 mesh; Bio-Rad Company) was extensively washed with deionized (DI) water before use. Anionic ion exchange resin (AG 1-X4, 20-50 mesh; Bio-Rad Company) was converted from its chloride form to a hydroxide form using a 3N sodium hydroxide solution, followed by complete washing of the resin with DI water to remove the sodium hydroxide just before use. The serum replacement process was also used to pre-clean some of the latexes[6].

Synthesis and Characterization of Model Latex Particles

The detailed methods used for the synthesis, cleaning, and characterization of the model polystyrene (PS; non-carboxylated and carboxylated) and poly(*n*-butyl methacrylate-co-*n*-butyl acrylate) [P(BMA/BA); non-carboxylated and carboxylated] latex particles are reported elsewhere[7]. P(BMA/BA) copolymer model latexes (non-carboxylated and carboxylated) were prepared by conventional semi-continuous emulsion polymerization processes at 80 °C. All syntheses were performed in a 500 ml four-neck flask equipped with a reflux condenser, nitrogen gas inlet tube, PTFE stirrer (~ 230 rpm), and two feed tubes for monomer and surfactant solution, respectively. The initial 1.5 hour period of the polymerization represents the seeding step where 10% of the monomer mixture (weight ratio of BMA/BA = 75/25) was used to prepare an in-situ seed latex. After the seed latex was almost fully formed (~ 95% conversion), the remaining monomer mixture (BMA, BA, and MAA for carboxylated latex particles) and surfactant solution were fed separately into the reactor at constant rates using two syringe pumps (Harvard Apparatus 22). The monomer and surfactant feed rates were carefully calculated to obtain monodisperse latex particles with homogeneous copolymer composition[7]. When the feed process was completed, the reaction was allowed to continue for another two hours and the latex was allowed to cool to room temperature. Each of these carboxylated P(BMA/BA) latex particles obtained in the manner described above contains a tiny P(BMA/BA) copolymer core with a volume fraction of around 0.1 and a thick BMA/BA/MAA copolymer [P(BMA/BA/MAA)] shell (Figure 1A). The copolymers in the core and in the shell have approximately the same glass transition temperature which was achieved by adjusting the copolymer compositions in the core and shell.

Downloaded by COLUMBIA UNIV on September 17, 2012 | http://pubs.acs.org
Publication Date: July 26, 2001 | doi: 10.1021/bk-2001-0790.ch012

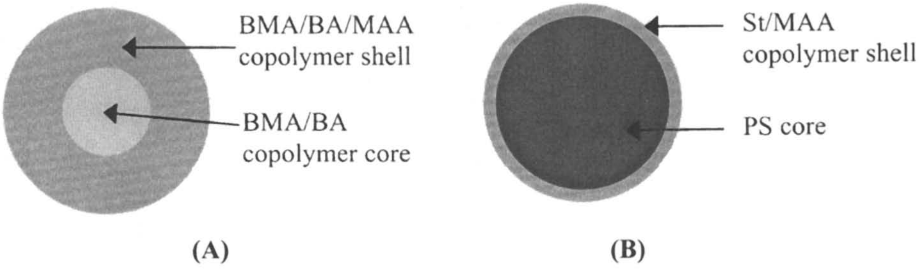

Figure 1. The structures of the carboxylated model latex particles: (A) a carboxylated P(BMA/BA) soft latex particle; and (B) a carboxylated PS hard latex particle.

Most PS latexes (carboxylated and non-carboxylated) were also prepared by a conventional semi-continuous emulsion polymerization process at 80 °C using the same setup mentioned above. The initial 1.5-hour period of the polymerization is the seed stage. After the seed was almost fully formed, styrene and SDS solution were fed separately into the reactor at constant rates (calculated based on SDS surface coverage on particles[7]) using two syringe pumps. Based on the seed particle size, the time of the styrene (monomer I) feed was controlled to build up core latex particles with specific size (i.e., 120 nm). After the core (seed) latex was formed, monomer II (i.e., the mixture of styrene and MAA) was fed into the reactor. The amount fed was adjusted to form a poly(styrene-co-methacrylic acid) [P(S/MAA)] shell with a thickness of about 3 nm. When the feeds were finished, the reaction was continued for another two hours and the latex was allowed to cool to room temperature. Each of these PS particles obtained above contains a large PS homopolymer core with a volume fraction of about 0.93 and a thin layer (~ 3 nm) of P(S/MAA) copolymer shell (Figure 1B).

Some carboxylated PS latex particles were also prepared by a shot growth batch process[7-9]. The polymerizations were carried out in 200 cm^3 pressure bottles. There were two stages for feeding the reactants in this process. In the initial stage, specific amounts of styrene, surfactant (Aerosol MA-80), sodium bicarbonate, and water were charged into the bottles. The contents of each bottle were purged with nitrogen using a hypodermic needle inserted through a rubber gasket in the bottle cap. The required amount of aqueous initiator solution (KPS) was purged with nitrogen and injected into each bottle using a hypodermic syringe. The bottles were placed in cloth jackets and placed in a bottle polymerizer unit and rotated end-over-end in a thermostated bath heated at 70 °C for 1.5 hours. At this time, the conversion of styrene reached 95% according to a conversion vs. time curve which was determined independently. At this point, specific amounts of Aerosol MA-80, sodium bicarbonate, KPS, styrene, maleic acid, and water were injected into each bottle. The polymerization was continued for 13.5 hours.

The PS and P(BMA/BA) latex particles which were obtained in the processes described above were then cleaned using the ion exchange method[10]. The cleaned latex particles were characterized by conductomitric titration (to determine the carboxyl group concentration on the latex particle surfaces or inside the particles), capillary hydrodynamic fractionation (Model 1100, Matec Applied Sciences; for particle size and size distribution), and transmission electron microscopy (Philips EM400T; for particle morphology)[7]. The characterization results for some of the PS and P(BMA/BA) model latexes which have been used in this work are listed in Table 1.

Preparation of Latex Films

Thick latex blend films for the investigation of bulk morphology were cast on clean glass plates covered with a non-sticky Tedlar [poly(vinyl fluoride)] film using latex blends of 4.5% initial solids content and dried under controlled drying conditions (temperature = 22 ± 0.5 °C; relative humidity = 50% ± 0.5%) for ten days in order to achieve full aging. The thickness of these films ranged from 100 to 150 μm. Latex blend films for gloss measurements and surface morphology observations were dried on microglass slides (1" x 3") using the same weight (i.e., 1.0 g) of a latex blend with the same solids contents (i.e., 4.5%) for each sample under controlled drying conditions (the same as those described above). The latex blends were spread over the entire surface of the glass slide. The thickness of these dried films was around 30 μm.

Characterization

TEM observations were performed using a Philips EM400T at an acceleration voltage of 100 kV. Film samples were microtomed at −80 °C using a CY2000 microtoming instrument (RMC, Inc. Microtomy & Cryobiology Products) to obtain thin sections ~ 90 nm in thickness; these sections were then imaged with the TEM.

Downloaded by COLUMBIA UNIV on September 17, 2012 | http://pubs.acs.org
Publication Date: July 26, 2001 | doi: 10.1021/bk-2001-0790.ch012

SEM examinations were carried out on an ETEC SEM instrument at an acceleration voltage of 20 kV. Latex films with a thickness of 0.1 to 0.15 mm were fractured in liquid nitrogen. The fractured surfaces were coated with a thin layer (~ 100 Å) of gold-platinum alloy before being imaged with the SEM.

Table 1. Model latex particles that were used for the investigation of the morphology and surface properties of films prepared from model carboxylated latex blends

Latex polymer	D_n[a] *(nm)*	D_w[b] *(nm)*	*PDI*[c]	*Wt.% MAA*[d]	D_{COOH}[e] *(COOH /nm²)*	σ_{COOH}[f] *(%)*
Hard latex particles						
[PS core and 3 nm thick P(S/MAA) shell]						
PS	130.4	132.9	1.019	0.00	0.00	0.00
PS + P(S/MA)	130.5	134.7	1.032	0.555[g]	0.816	7.34
PS + P(S/MAA)	125.8	128.4	1.021	1.80	1.43	12.9
PS + P(S/MAA)	128.8	131.6	1.022	3.13	2.12	19.1
PS + P(S/MAA)	127.5	129.8	1.018	4.71	3.30	29.7
PS + P(S/MAA)	127.6	130.8	1.025	6.24	7.31	65.8
PS + P(S/MAA)	128.5	131.0	1.019	6.61	8.58	77.2
Soft latex particles						
(MAA almost uniformly distributed throughout latex particles)						
P(BMA/BA)	128.9	131.4	1.019	0.00	0.00	0.00
P(BMA/BA/MAA)	117.3	120.4	1.026	2.75	1.64	14.7
P(BMA/BA/MAA)	116.8	118.1	1.011	5.65	2.43	21.9

[a] Number-average particle diameter

[b] Weight-average particle diameter

[c] Polydispersity index (D_w/D_n)

[d] Weight percentage of MAA (source of carboxyl group) based on total weight of the latex polymers (including the core and shell)

[e] Density of the carboxyl groups on latex particle surface

[f] Percentage of particle surface area covered by the carboxyl groups, using the value of 9 Å² as the cross-sectional area of each COOH group[11]

[g] Weight percentage of MAA (source of carboxyl group) based on total weight of the latex polymer (including the core and shell)

Surface gloss was measured with a Glossmeter (Novo-Gloss, Phopoint). Each sample was measured at two different incident angles (60° and 75°). A blank slide was used as the reference. The relative gloss defined here is the ratio of the gloss of the film sample to the gloss of the blank slide. Three samples were prepared and measured for each latex blend and averaged results were reported.

Surface morphology was observed with an atomic force microscope (AFM; Park Scientific Instruments, BioProbe Electronics Module). An intermittent-contact mode was selected for the film samples cast from the model latex blends.

Downloaded by COLUMBIA UNIV on September 17, 2012 | http://pubs.acs.org
Publication Date: July 26, 2001 | doi: 10.1021/bk-2001-0790.ch012

Results and Discussion

Bulk Morphology of the Films Obtained from Latex Blends

The bulk morphology of the films prepared from the hard/soft model latex blends was investigated using scanning electron microscopy (SEM) and a freeze-fracture technique. The latex blend films with thickness of 100 to 150 μm were frozen and fractured inside liquid nitrogen. A series of SEM micrographs were taken on a fracture surface from the region near the film surface to the region close to the bottom of a latex blend film (Figure 2). The latex blend films cast from the following two types of model latex blends were investigated. They are: (1) a latex blend without any carboxyl groups or surfactant present, and (2) a latex blend with 14.7 % carboxyl group coverage on the P(BMA/BA) soft copolymer particle surface and 7.34% carboxyl group coverage on the PS particle surface. All other parameters, such as particle size, glass transition temperature, and drying conditions are the same for the samples investigated.

Downloaded by COLUMBIA UNIV on September 17, 2012 | http://pubs.acs.org
Publication Date: July 26, 2001 | doi: 10.1021/bk-2001-0790.ch012

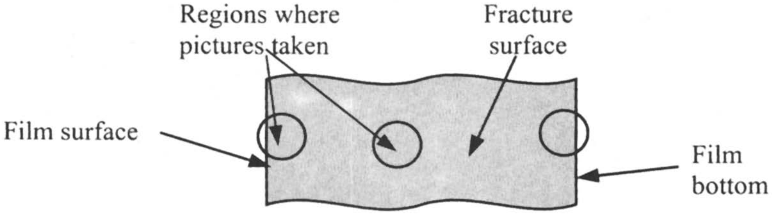

Figure 2. Diagram of the location where the SEM micrographs were taken on the freeze-fracture surface of a model latex blend film.

General characteristics of the SEM micrographs taken on the freeze-fracture surface are the white regions which are distributed in the dark background (Figure 3B). By comparing the TEM micrograph of a cryo-ultramicrotomed section of the same film from a latex blend (Figure 3A; darker spots represents the PS particles), we determined that the white spots on the SEM micrographs are the PS particles which are distributed in the soft P(BMA/BA) copolymer matrix (the dark background in Figure 3B). It could be concluded that most fracture took place at the interface between the PS particles and the P(BMA/BA) copolymer matrix because most of the white regions show fairly clear outlines. This is somewhat like the so-called "inter-granular breaking", meaning that most of the interface regions have the lowest strength. Therefore, PS particles protrude out from the fracture surface, which were imaged by SEM as the spherical spots with fairly clear outlines. Figure 4 shows that the distribution of PS particles in the film prepared from the latex blend without any carboxyl group or surfactant present is obviously uneven from the surface to the bottom of the film. This could be explained by the phase incompatibility of this latex blend system. Because PS is phase incompatible with P(BMA/BA) copolymer, both

PS and P(BMA/BA) particles have a tendency to phase separate during the drying of the latex blend. Thus, P(BMA/BA) particles formed the continuous phase because they had a low T_g and were the major component in the latex blend and PS particles packed together in groups, resulting in clusters of PS particles distributed within the P(BMA/BA) continuous phase. Another feature which is noted in Figure 4 is that for all of the images of this sample, all of the white regions show fairly clear outlines, which is evidence for "inter-granular breaking". The phenomenon that the "inter-granular breaking" is the predominate fracture type indicates that the interphase between the PS hard particles and the P(BMA/BA) soft polymer matrix is the weakest region in the latex blend film. This is because the P(BMA/BA) molecular chains could not interpenetrate into the PS hard particles.

Downloaded by COLUMBIA UNIV on September 17, 2012 | http://pubs.acs.org
Publication Date: July 26, 2001 | doi: 10.1021/bk-2001-0790.ch012

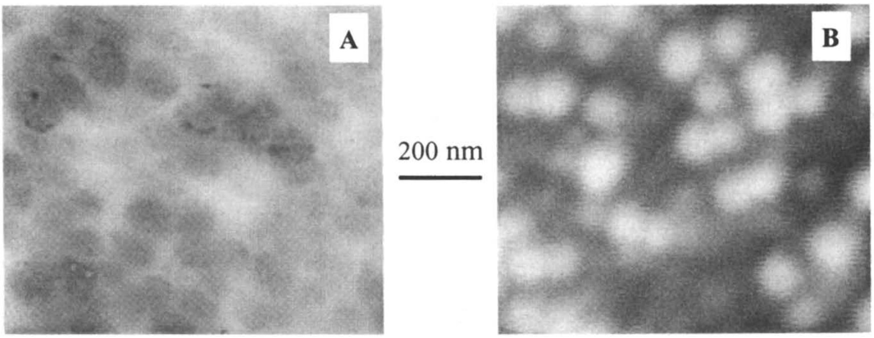

Figure 3. Comparison of TEM and SEM micrographs of the same film from the same latex blend (blended latex contains no COOH and 2.06 wt.% SDS based on the solid weight of polymer): (A) TEM micrograph of an cryo-ultramicrotomed section and (B) SEM micrograph of a freeze-fractured section.

Interesting images were found for the fractured film sample prepared from the latex blend containing carboxyl groups (Figure 5). SEM micrographs were taken from different regions of the 150 µm thick film from the film surface to the area near the bottom of the film. The three micrographs shown in Figure 5 are representative of three different film regions: (A) the film-air interface region; (B) the hackle region located near the surface of the film; and (C) the mirror region consisting of most portions of the fracture surface. It was noted that the hard particles were evenly distributed in the mirror region (Figure 5C). Hard particle clusters were seldom observed. This indicates that the carboxyl groups improved the phase compatibility of the PS and P(BMA/BA) polymers and prevented the formation of the hard particle clusters, which resulted in a uniform distribution of the hard particles in the soft polymer matrix. A very interesting region is found near the surface of the film which corresponds to a hackle region. This area has a dimension of approximately 30 µm in thickness from the surface to the middle of the film. In this region, few clear hard particles can be observed. However, we can observe the hard PS particles buried under the soft matrix (Figure 5B). This indicated that fracture took place in this region inside the soft matrix instead of at the interface between the PS hard particles and the soft polymer matrix. This indicates that the carboxyl groups present on the latex particles strengthened the interface region and made it stronger than the soft polymer matrix, resulting in "intra-granular breaking" (breaking occurring inside one phase) in the hackle region. The strengthening of the interphase by the presence of the carboxyl groups on the particles could be explained by hydrogen bond formation in the interphase. The carboxyl groups on the carboxylated PS latex particles could form hydrogen bonds with the carboxyl groups or carbonyl groups present in the soft copolymer matrix. The hydrogen bonds in the interphase increased the connection between the hard/soft phases, and thus, improved the hard/soft interphase strength.

Downloaded by COLUMBIA UNIV on September 17, 2012 | http://pubs.acs.org
Publication Date: July 26, 2001 | doi: 10.1021/bk-2001-0790.ch012

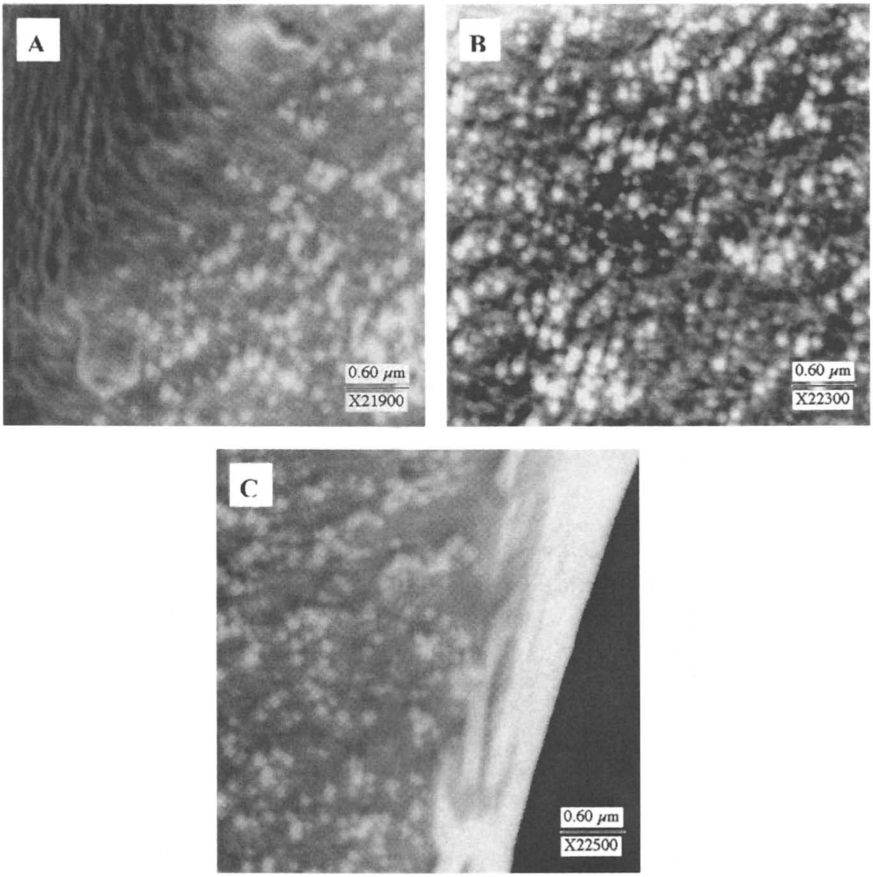

Figure 4. SEM micrographs of a fractured section of a latex film obtained from the latex blend without any carboxyl groups or surfactant present: (A) fracture at the film surface; (B) fracture at the middle position of the film; and (C) fracture at the bottom of the film. The film thickness was 110 μm.

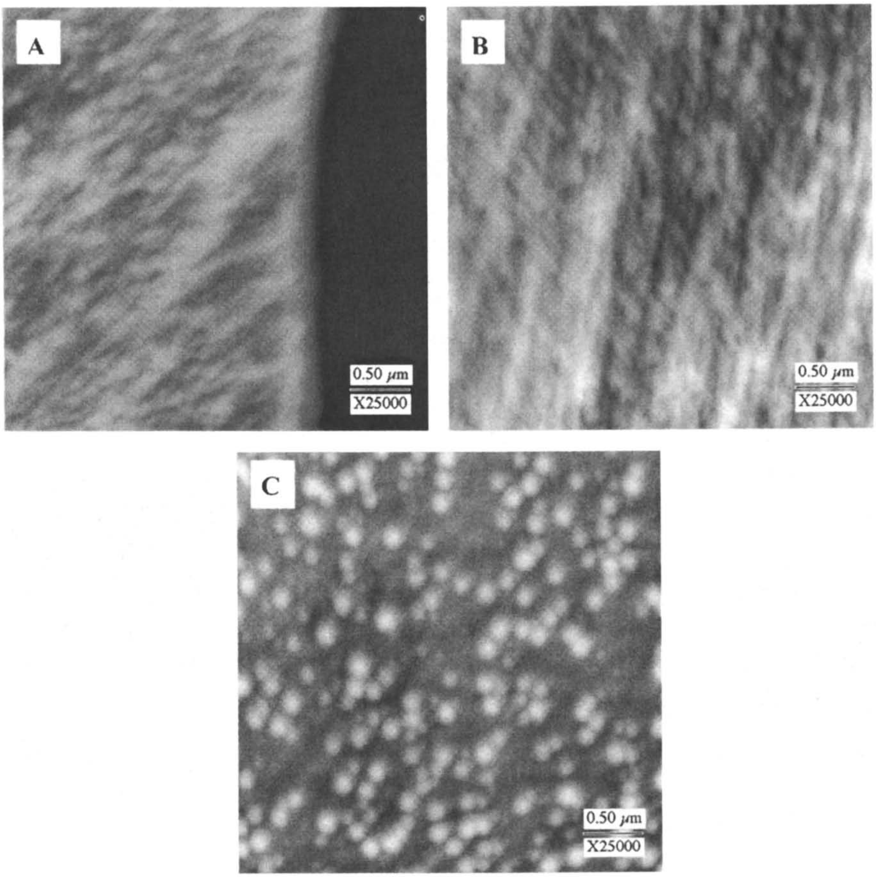

Figure 5. SEM micrographs of a fractured section of the latex film prepared from the latex blend with 14.7% carboxyl group coverage on the soft particles and 7.34% carboxyl group coverage on the PS particles: (A) fracture at the film surface; (B) fracture 20 µm away from the surface of the film; and (C) fracture 40 µm from the bottom of the film. The film thickness was 150 µm.

Influence of Carboxyl Groups on Gloss and Surface Morphology of Latex Blend Films

Gloss is one of the most important contributors to the aesthetics of coated products and must be carefully controlled. The appearance of a surface depends upon the manner in which incident light is reflected, absorbed, or transmitted by the surface. Light reflected at the specular angle (angles of incident and reflected light are equal in magnitude but opposite in direction) is known as specular reflectance and is related to surface gloss. An important premise in reflectance theory is that the flux of

Downloaded by COLUMBIA UNIV on September 17, 2012 | http://pubs.acs.org
Publication Date: July 26, 2001 | doi: 10.1021/bk-2001-0790.ch012

the reflected beam approaches a maximum at the specular angle and that, for a perfect mirror surface, the reflected flux equals the incident flux at every specular angle. In practice, flux per se is not measured but rather the reflectance relative to that of a mirror surface. On this basis, specular gloss may be defined as the degree to which a given surface approaches the reference surface. Gloss is expected to increase with: (a) an increase in the refractive index of the surface; (b) an increase in the specular angle at which the measurement is made; and (c) an increase in the surface micro-smoothness.

Specular gloss (incident angle between 20° and 85°) is influenced primarily by the refractive index and the smoothness of the surface, but the latter has a greater effect if the incident angle is fixed[12]. Micro-defects reduce specular gloss by acting as light scattering centers and produce an actual loss of energy from the specular beam. Rayleigh calculated a tolerable defect height [D; eq. (1)] which, if exceeded, would reduce specular gloss[13]:

$$D = \frac{\lambda}{8\cos i} \tag{1}$$

where λ is the wavelength of incident light and i is the angle of incidence. It was also proved that the shape and height of the irregularities, and not their concentration per unit area, plays a greater role in the reduction of gloss[14]. According to eq. (1), the critical defect height is determined by the wavelength and the angle of incidence. For visible light, the wavelength ranges from 400 to 700 nm. Thus, the minimum and maximum tolerable heights are 193 nm and 338 nm, respectively, if choosing the incident angle as 75°.

Figure 6 shows that the surface gloss of the latex blend films changed as the carboxyl group coverage on the hard PS latex particles was varied. The gloss increased as the carboxyl coverage on the hard particles increased until 13% carboxyl coverage on the hard particles was attained. However, after this point, the gloss decreased with a further increase in the carboxyl coverage on the hard particles. The latex blend system described in Figure 6 yielded a maximum gloss value at around 13% carboxyl coverage on the hard latex particles for both 60° and 75° incident angles.

As mentioned before, at a fixed incident angle, the gloss of the latex blend films is a function of the refractive index and the smoothness of the film surface. Because all of the latex blends used in this study have almost the same polymer composition and were cleaned, the refractive index should basically be the same. Thus, the main parameter that influences the gloss of the latex blend films is the smoothness of the film surface. This implies that as the carboxyl coverage on the hard latex particles increased before attaining the maximum gloss, the surface smoothness of the latex blend films also increased; however, after the maximum gloss point was reached, the surface smoothness decreased as the carboxyl coverage on the hard latex particles was increased further. This hypothesis was confirmed by the AFM (atomic force microscopy) investigation of the surface morphology of the latex blend films (Table 2 and Figure 7).

Downloaded by COLUMBIA UNIV on September 17, 2012 | http://pubs.acs.org
Publication Date: July 26, 2001 | doi: 10.1021/bk-2001-0790.ch012

Downloaded by COLUMBIA UNIV on September 17, 2012 | http://pubs.acs.org
Publication Date: July 26, 2001 | doi: 10.1021/bk-2001-0790.ch012

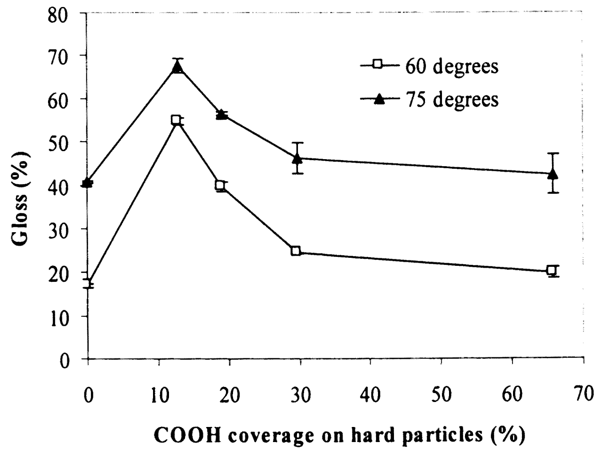

Figure 6. Surface gloss of latex blend films as a function of the carboxyl group coverage on the hard particles: weight fraction of hard PS particles = 0.35; D_n ~ 125 nm; all latexes were cleaned and no carboxyl groups were present in the soft latex particles; the gloss of pure soft latex film is 30.8% ± 2.3% and 62.6 ± 3.3% at incident angles of 60° and 75°, respectively.

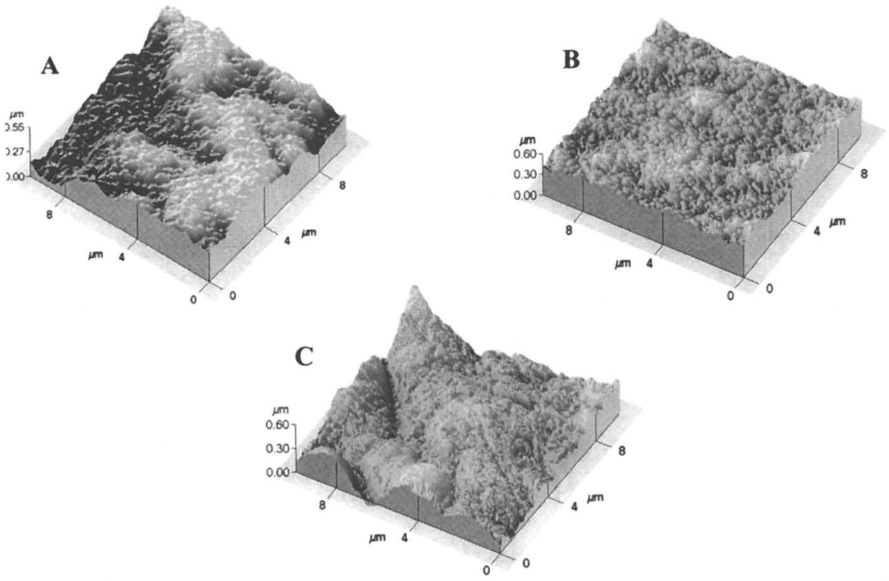

Figure 7. AFM topographic images of the films cast from the latex blends: (A) without any carboxyl groups or surfactants present; (B) with 12.9% carboxyl group coverage on the PS particles; and (C) with 65.8% carboxyl coverage on the hard particles; all samples have no carboxyl groups in the soft particles; weight fraction of hard PS particles = 0.35; D_n ~ 125 nm; all latexes were cleaned.

Table 2. Surface smoothness of the films cast from PS/P(BMA/BA) model latex blends

Latex blend and resulting film	*A*	*B*	*C*
Characterics of latex blends			
σ_{COOH}[a] on hard particles (%)	0.0	12.9	65.8
Wt% MAA[b] in hard particles	0.00	1.80	6.24
σ_{COOH}[a] on soft particles (%)	0.00	0.00	0.00
Wt% MAA[b] in soft particles	0.00	0.00	0.00
Surface roughness of latex blend film			
Average roughness (nm)	75	29	131
Root-mean-square roughness (nm)	95	36	165
Peak-to-valley distance (nm)	466	251	735

weight fraction of hard PS particles = 0.35; $D_n \sim 125$ nm; all latexes were cleaned
[a, b] see Table 1.

The film cast from the latex blend without any carboxyl groups present on either the hard or soft latex particles exhibited a rough surface whose root-mean-square (RMS) roughness is 95 nm with a peak-to-valley distance of 466 nm (Table 2 and Figure 7A). Since the peak-to-valley distance of the non-carboxylated latex blend film is larger than the maximum tolerable defect height which is 338 nm according to eq. (1), the gloss of the film is poor. When carboxyl groups were incorporated into the hard PS latex particles at a low density (i.e., 12.9% coverage on the hard particles), the surface roughness and the peak-to-valley distance dropped substantially (RMS roughness = 36 nm and peak-to-valley distance = 251 nm; Table 2 and Figure 7B). The peak-to-valley distance of this film is lower than the maximum tolerable defect height. Thus, the gloss was improved. However, when carboxyl groups at a high density (i.e., 65.8% coverage on the hard particles) were incorporated, the surface roughness and the peak-to-valley distance of the film increased significantly instead of decreasing. The surface smoothness of the film with high carboxyl coverage on the hard latex particles is even worse than that of the latex blend film prepared without any carboxyl groups present (Table 2 and Figure 7C). These observations indicate that the surface of the latex particles which have been altered by the presence of carboxyl groups play an important role in determining the surface smoothness.

The mechanism by which the carboxyl groups present on the PS hard latex particles influence the hard particle distribution within the soft polymer matrix is depicted by the diagram shown in Figure 8. During drying, due to the poor stability of the cleaned latex particles and phase separation of the hard/soft polymers [PS and P(BMA/BA) are phase-incompatible polymers], the hard latex particles would form clusters if there were no carboxyl groups present on their surface, resulting in a rough film surface and poor gloss. Carboxyl groups present at a low density on the hard latex particles stabilized the hard particles during drying and improved the phase compatibility via hydrogen bond formation between the carboxyl groups on the hard particles and the carbonyl groups or carboxyl groups in the soft polymer matrix, both

Downloaded by COLUMBIA UNIV on September 17, 2012 | http://pubs.acs.org
Publication Date: July 26, 2001 | doi: 10.1021/bk-2001-0790.ch012

of which resulted in a more uniform distribution of hard latex particles in the soft polymer matrix. Consequently, the surface smoothness and gloss were improved. However, when the carboxyl groups were present in high densities (i.e., 65.8%) on the hard particles, it was possible to form hydrogen bonds between the carboxyl groups on different hard particles (i.e., inter-particle hydrogen bonding). Clusters of hard latex particles were then formed via inter-particle hydrogen bonding, resulting in a rough film surface and poor gloss.

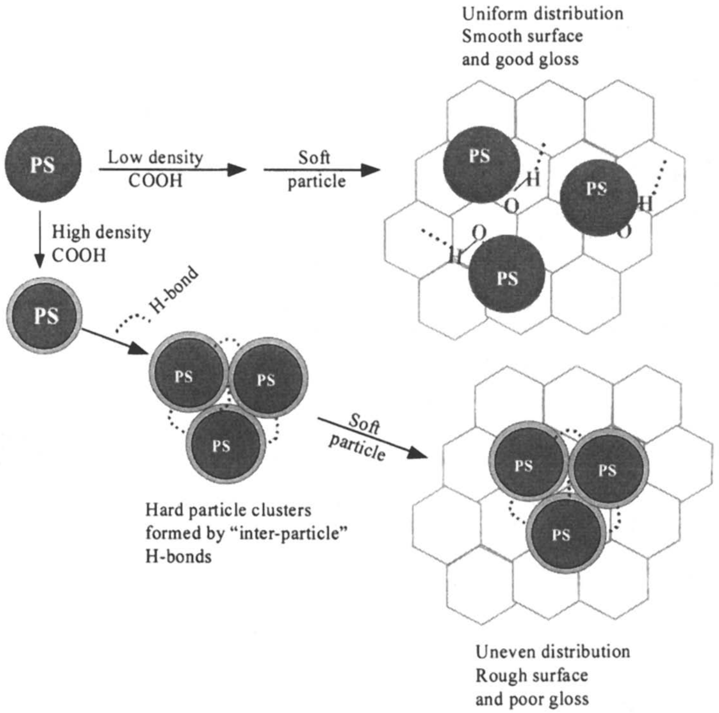
Uniform distribution
Smooth surface
and good gloss
PS
Low density
COOH
Soft
particle
High density
COOH
H-bond
H
O
Soft
Particle
Hard particle clusters
formed by "inter-particle"
H-bonds
Uneven distribution
Rough surface
and poor gloss

Figure 8. Schematic diagram of the manner by which the carboxyl groups present on the PS hard latex particles influence the hard particle distribution within the copolymer films prepared from hard/soft model latex blends.

The clustering of the hard latex particles on the surface of a latex blend film was confirmed by AFM observations (Figure 9). Here, intermittent-contact AFM phase imaging[15] was utilized to investigate the surface morphology of the latex blend films. For heterogeneous samples, AFM phase imaging provides compositional maps because of its sensitivity to variations in local material properties. In AFM phase imaging, the difference between the phase angle of vibration of the free oscillating AFM tip and the phase of the tip as it interacts with the sample surface describes the characteristics of the tip-sample force interactions. Monitoring these phase changes allows one to obtain the compositional maps mentioned above. Compared to AFM

Downloaded by COLUMBIA UNIV on September 17, 2012 | http://pubs.acs.org
Publication Date: July 26, 2001 | doi: 10.1021/bk-2001-0790.ch012

topographic imaging, the detection of phase angle shifts provides enhanced image contrasts, especially for heterogeneous surfaces[16-21]. However, it should be noted that the assignment of the cause of the phase contrast to specific properties differences of the sample components is not fixed[18]. This makes it difficult to assign the features of phase images to different chemical components, unless additional experiments are carried out. Fortunately, in our latex blend films, the separate and continuous phases are already known[22]. Because the soft latex polymer is the major component (i.e., 65 wt%) in the model latex blends, the soft latex particles coalesce into a continuous phase while the PS hard latex particles preserve their original size and spherical shape after drying. Thus, it can be determined that the separated spots and the continuous background in Figure 9 are the PS hard particles and the void-free film formed by the coalesced P(BMA/BA) soft particles, respectively. It is shown in Figure 9A that the PS hard particles on which the carboxyl groups are present in low density (e.g., 12.9% surface carboxyl group coverage) are uniformly distributed among the soft polymer matrix. No large clusters of PS hard particles can be detected on the surface of this latex blend film. This uniform distribution of the PS hard particles resulted in the formation of a smooth surface and good gloss of the latex blend films. However, when the density of the carboxyl groups present on the PS hard particles is high (e.g., 65% carboxyl group coverage), the distribution of the PS hard particles among the soft polymer matrix is not uniform. Large clusters consisting of PS hard particles are clearly observed by AFM phase imaging (Figure 9B). The diameter of these clusters can be up to 835 nm, which is much larger than the maximum tolerable defect height (338 nm) for visible light at 75° according to eq. (1). Consequently, the surface of these latex blend films becomes rough and the gloss becomes poor as the presence of the carboxyl groups in high density on the PS hard particles.

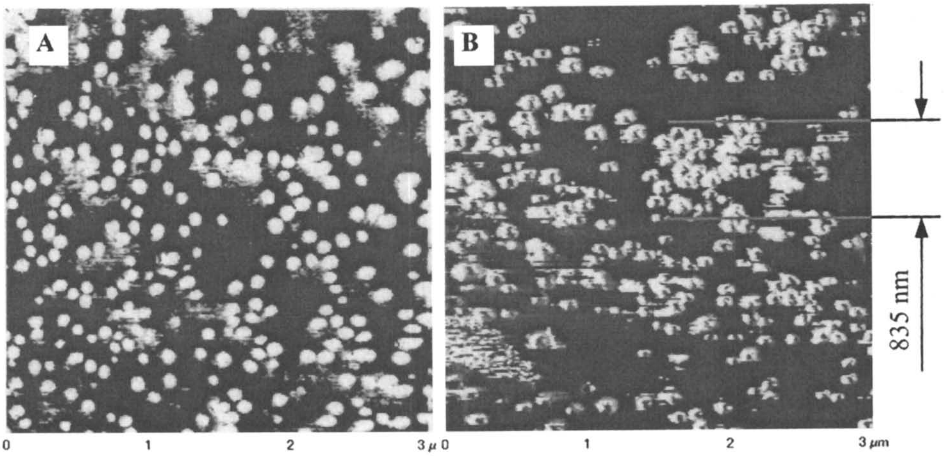

Figure 9. AFM phase images of the surfaces of the latex blend films cast from the high carboxyl group coverage latex blends: (A) % COOH on the hard PS particle = 12.9%, and (B) % COOH on the hard PS particles = 65.8%; no COOH in the soft particles of both samples; weight fraction of hard PS particles = 0.35; D_n ~ 125 nm; all latexes were initially cleaned.

Downloaded by COLUMBIA UNIV on September 17, 2012 | http://pubs.acs.org
Publication Date: July 26, 2001 | doi: 10.1021/bk-2001-0790.ch012

Effect of Neutralization of the Carboxyl Groups on Gloss and Surface Morphology of Latex Blend Films

As mentioned above, when the PS particles in the latex blends were covered by a high density of carboxyl groups, the gloss of the films cast from these latex blends was very low, even lower than that of the films cast from latex blends without any carboxyl groups or surfactant present. However, when the carboxyl groups present in high density on the latex particles were neutralized, the gloss was increased substantially (Figure 10A). Neutralization by both strong and weak bases improves the surface gloss of the films cast from the latex blends with a high density of carboxyl groups present, although strong bases such as NaOH, KOH, and CsOH are more effective in increasing the surface gloss (Figure 10B).

Downloaded by COLUMBIA UNIV on September 17, 2012 | http://pubs.acs.org
Publication Date: July 26, 2001 | doi: 10.1021/bk-2001-0790.ch012

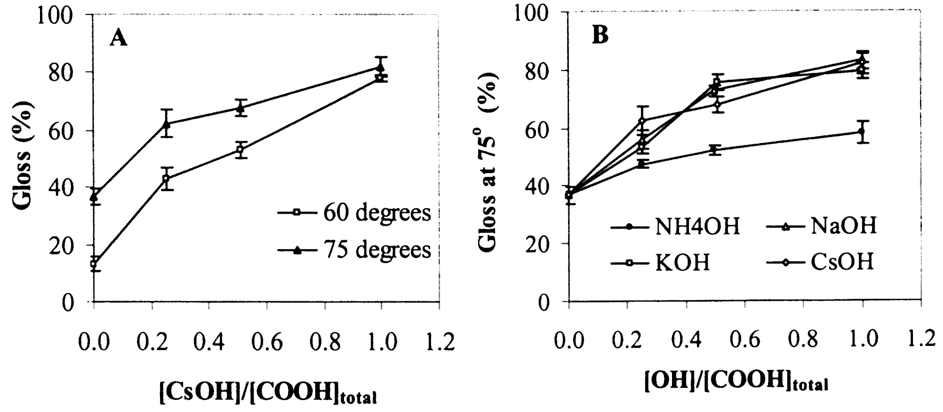

Figure 10. (A) Gloss curves at 60° and 75° vs. the molar ratio of CsOH to the carboxyl groups present on the latex particles; (B) the gloss at 75° as a function of the extent of the neutralization of the carboxyl groups for cleaned latex blends neutralized by NH_4OH, NaOH, KOH, or CsOH: 77.2% carboxyl group coverage on the surface of the PS hard particles; 21.9% carboxyl group coverage on the surface of the P(BMA/BA) soft latex particles; the gloss of pure soft latex film is 30.8% ± 2.3% and 62.6 ± 3.3% at incident angles of 60° and 75°, respectively.

The morphological investigations of these latex blend films also show a quantitative relationship between the surface roughness and the extent of neutralization (with CsOH) of the carboxyl groups (Figure 11). The results show that neutralization by a strong base such as CsOH greatly decreased the surface roughness and peak-to-valley distance of the films cast from the latex blends containing a high density of carboxyl groups residing on the PS particle surface. At the point where the molar ratio of CsOH to the total content of carboxyl groups present on the surface and inside the latex particles is 0.51 (Figure 11), the molar ratio of CsOH to the carboxyl groups which are only located on the surface of the latex particles is 1.00.

Before this point, the surface roughness and the peak-to-valley distance decreased quickly as the extent of neutralization was increased, while after this point, there was only a slight decrease in the surface roughness and peak-to-valley distance, implying that the carboxyl groups present on the surface of the particles played an important role in the improvement of the surface smoothness by the neutralization of these carboxyl groups.

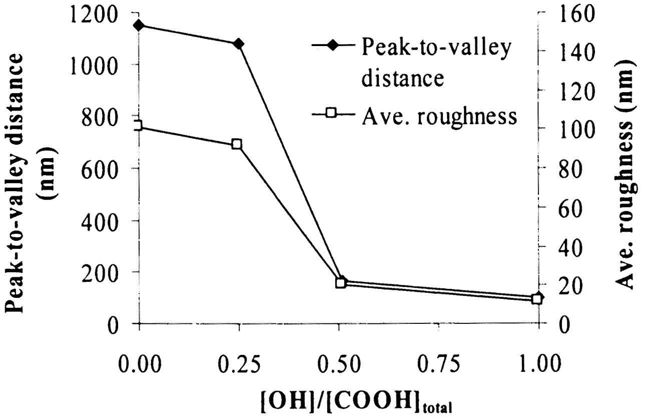

Figure 11. The peak-to-valley distance and surface roughness as a function of the molar ratio of CsOH to the total carboxyl groups on the surface of the particles and inside the particles for carboxylated latex blends consisting of PS hard and P(BMA/BA) soft latex particles.

Questions remain as to the real reasons for the enormous differences in the observed gloss and surface smoothness of the films cast from the model latex blends with different extents of neutralization of the carboxyl groups present at high density on the PS hard latex particles. To answer the question, we have to more closely examine the film surface using high resolution AFM phase imaging. A comparison was made between the film prepared from the hard/soft latex blend with carboxyl groups present at high density (e.g., 77.2% carboxyl group coverage) on the PS hard particles (the AFM phase image is presented in Figure 12A) and the film prepared from the same latex blend, but where the carboxyl groups were neutralized by a strong base such as KOH (the AFM phase image is present in Figure 12B). It is shown in Figure 12A that there are large clusters consisting of PS hard particles within the soft copolymer matrix in the film cast from the hard/soft latex blend with carboxyl groups present at high density on the hard particles. The maximum dimension of the observed clusters is up to 868 nm. The large clusters resulted in large bumps on the surface of these latex blend films, which is the reason that the surface smoothness and gloss becomes poorer as high densities of carboxyl groups were present on the PS hard particles. The driving force for the clustering of the

Downloaded by COLUMBIA UNIV on September 17, 2012 | http://pubs.acs.org
Publication Date: July 26, 2001 | doi: 10.1021/bk-2001-0790.ch012

Downloaded by COLUMBIA UNIV on September 17, 2012 | http://pubs.acs.org
Publication Date: July 26, 2001 | doi: 10.1021/bk-2001-0790.ch012

highly carboxylated PS hard particles may be the inter-particle hydrogen bonding between the carboxyl groups present on different PS hard particles. If this is true, there should be no clusters on the surface of these latex blend films when these carboxyl groups are neutralized. This hypothesis was verified by the AFM phase imaging (Figure 12B). When the carboxyl groups present on the PS hard particles (in the latex blend which was used to cast the film; presented in Figure 12A) were neutralized by KOH, no clusters of PS hard particles were observed on the surface of the film (Figure 12B), indicating that the neutralization of the carboxyl groups with a strong base prevents the formation of inter-particle hydrogen bonding. As illustrated by the diagram in Figure 13, the neutralization of these carboxyl groups eliminates the source to form inter-particle hydrogen bonds, while the formation of anionic charge groups on the particle surface resulted in an increase in the stability of the PS hard particles during drying, both of which improved the uniformity of the PS hard particle distribution within the soft copolymer matrix. The uniform distribution of the PS hard particles, thus, resulted in a smooth surface and good gloss.

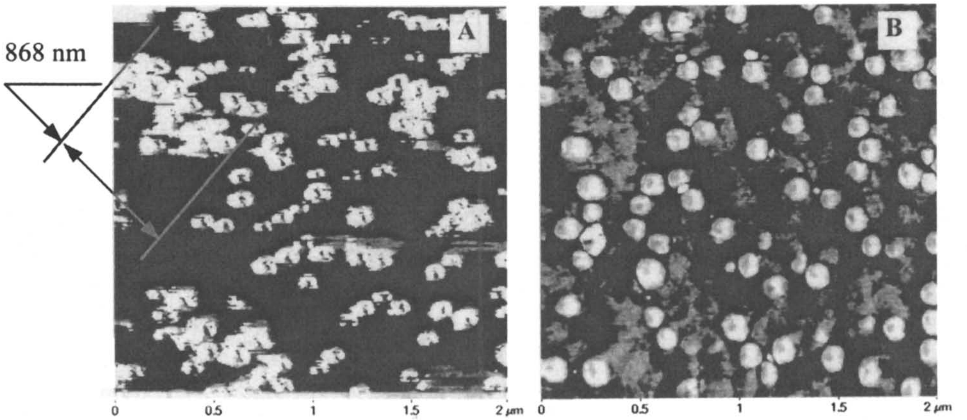

Figure 12. AFM phase images of the surfaces of the films cast from the latex blends with 77.2% and 21.8% COOH coverage on the hard and soft particles, respectively: (A) the carboxyl groups were not neutralized, and (B) the carboxyl groups were 100% neutralized by potassium hydroxide.

However, the effects of the neutralization of the carboxyl groups present on the highly carboxylated PS hard particles on the surface morphology and gloss also depend on the properties of the base used. Weak and strong bases showed completely different effects. Figure 14 shows the dependence of the surface roughness and peak-to-valley distance on the ionic radius of the counterions. When the carboxyl groups present on the latex blend particles were neutralized by NH_4OH, a volatile weak base, the surface roughness and the peak-to-valley distance of the resulting films were much larger than those of the films cast from the carboxylated latex blends (high carboxyl group coverage) whose carboxyl groups were neutralized by a strong base such as NaOH or KOH. This may be due to the evaporation of the ammonia added during drying which would leave the carboxyl groups on the particles unneutralized. The evaporation of the ammonia started before the "freezing" of the PS hard particles because the decrease in the surface roughness and peak-to-valley distance of the films prepared from the latex blends, which resulted from the neutralization by NH_4OH is much less than the decrease that resulted from the neutralization by NaOH or KOH (Figure 14). Once the carboxyl groups present on the PS hard particles at high densities were reconstituted as the ammonia was evaporated, the PS hard particles still have an opportunity to form clusters driven by the inter-particle hydrogen bonding before the "freezing" of the hard particles within the soft copolymer matrix, resulting in a decreased improvement of the surface smoothness by the neutralization with ammonia.

Downloaded by COLUMBIA UNIV on September 17, 2012 | http://pubs.acs.org
Publication Date: July 26, 2001 | doi: 10.1021/bk-2001-0790.ch012

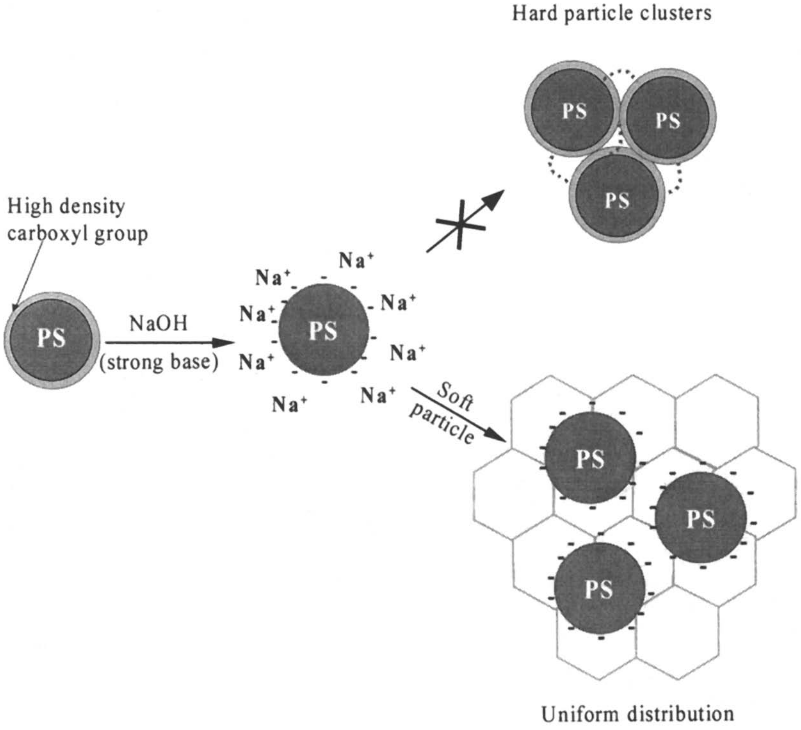

Figure 13. Diagram showing that the neutralization of the carboxyl groups present on the PS hard latex particles present at high density using a strong base prevents the formation of clusters.

Although the surface gloss of these latex blend films was influenced primary by the surface smoothness, the gloss also depends on the properties of the base used to neutralize the carboxyl groups. Neutralization by both strong and weak bases improves the surface gloss of the films cast from the latex blends with a high density of carboxyl groups present. However, strong bases such as NaOH, KOH, and CsOH are more effective in increasing the surface gloss (Figure 15). No obvious difference in surface gloss as a function of the radius of the counterion of a strong base present in the latex blends was detected (Figure 15). This means that the increase in the radius of the counterion of a strong base does not contribute to the improvement of the surface gloss of the films prepared from the model latex blends or it is possible that any improvement resulting from an increase in the radius of the counterion of a strong base can not be detected by the glossometer which was used in these measurements.

Downloaded by COLUMBIA UNIV on September 17, 2012 | http://pubs.acs.org
Publication Date: July 26, 2001 | doi: 10.1021/bk-2001-0790.ch012

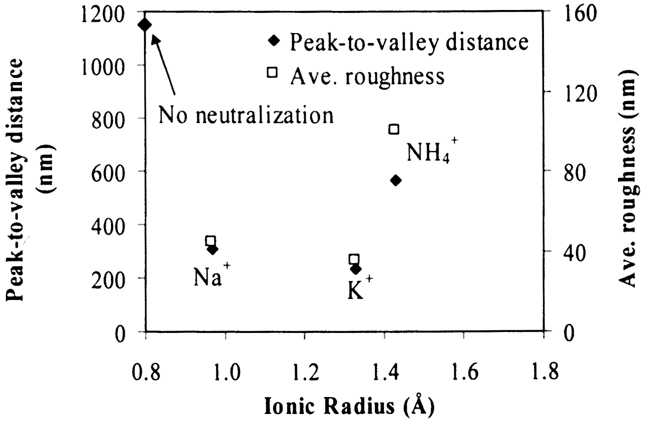

Figure 14. The surface roughness and the peak-to-valley distance as a function of the radius of the counterion present in the carboxylated latex blends with high carboxyl group coverage on the PS hard latex particles: 77.2% carboxyl group coverage on PS hard particles and 21.9% carboxyl group coverage on the P(BMA/BA) soft latex particles; the molar ratio of the base used to the carboxyl groups = 1:1.

Conclusions

In latex blends comprised of cleaned PS hard and P(BMA/BA) soft latex particles, a low density of carboxyl groups present in the PS latex particle surfaces (e.g., 13% surface coverage) results in an even distribution of these particles in the soft copolymer matrix, while a high density of carboxyl groups present in the PS latex particles (e.g., 77.2% coverage) results in less uniform distributions. However, the neutralization of the carboxyl groups improves the hard particle distribution within the soft copolymer matrix. Neutralization using a strong base such as NaOH, KOH, or CsOH is more effective than using a weak base like ammonia in improving the PS hard particle distribution within the soft polymer matrix. Clustering of the PS hard particles plays a very important role in determining the distribution of the hard particles within the soft copolymer matrix. Uneven distribution of the hard particles results from the formation of large hard particle clusters and uniform distribution of the hard particles results from the prevention of the clustering of the hard particles. The clusters of hard particles within the soft copolymer matrix result from phase separation of non-carboxylated PS hard particles from the soft copolymer and also result from inter-particle hydrogen bonding between highly carboxylated PS hard particles (e.g., 65% carboxyl group coverage on the hard particles). Thus, the incorporation of carboxyl groups at low density onto the PS hard particles and the neutralization of the carboxyl groups present on the PS hard latex particles can both prevent the formation of the hard particle clusters. The surface smoothness and gloss depend on the uniformity of the distribution of the PS hard particles within the soft copolymer matrix. The presence of the carboxyl groups on the latex particles also improves the strength of the interphase between the hard particles and the soft copolymer matrix.

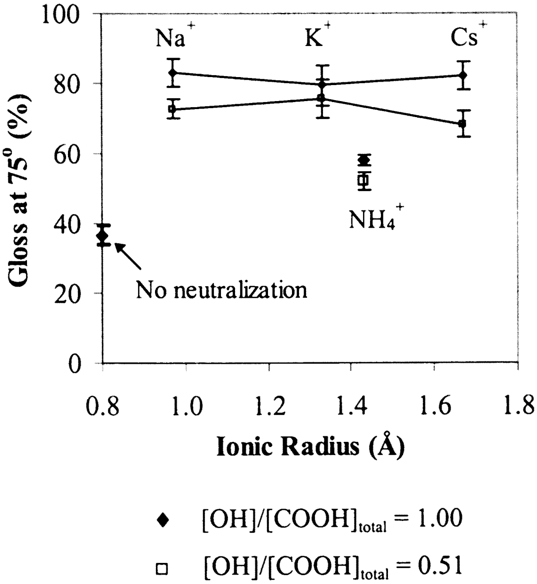

Figure 15. The gloss at 75° as a function of the radius of the counterions present in the latex blends: 77.2% carboxyl group coverage on the surface of the PS hard latex particles; 21.9% carboxyl group coverage on the surface of the P(BMA/BA) soft latex particles.

Acknowledgements

The AFM measurements of some samples by Ms. Olga L. Shaffer and the help of Ms. Jean S. Lavelle and Jo Evelyn Gallagher are greatly appreciated.

Downloaded by COLUMBIA UNIV on September 17, 2012 | http://pubs.acs.org
Publication Date: July 26, 2001 | doi: 10.1021/bk-2001-0790.ch012

References

1. Feng, J.; Winnik, M. A.; Shivers, R.; Clubb, B. *Macromolecules*, 28, **1995**, 7671.
2. Friel, J. European Patent Application No. 0 466 409 A1, 1992.
3. Keddie, J. L.; Meredith, P.; Jones, R. A. L.; Donald, A. M. *Langmuir*, 12, **1996**, 3793.
4. Lepizzera, S.; Lhommeau, C.; Dilger, G.; Pith, T.; Lambla, M. *J. Polym. Sci.: Part B: Polym. Physics*, 35, **1997**, 2093.
5. Rynders, R. M.; Hegedus, C. R.; Gilicinski, A. G. *J. Coat. Tech.*, 67(845), **1995**, 59.
6. Ahmed, S. M.; El-Aasser, M. S.; Pauli, G. H.; Poehlein, G. W.; Vanderhoff, J. W. *J. Colloid Interface Sci.*, 73(2), **1980**, 388.
7. Tang, J.; Dimonie, V. L.; Daniels, E. S.; Klein, A.; El-Aasser, M. S. *J. Appl. Polym. Sci.*, v.77, **2000**.
8. Kim, J. Ph.D. Dissertation, Lehigh University, Bethlehem, PA, 1986.
9. Sakota, K.; Okaya, T. *J. Appl. Polym. Sci.*, 20, **1976**, 1735.
10. Van den Hul, H. J.; Vanderhoff, J. W. *J. Electroanal. Chem.*, 37, **1972**, 161.
11. Huheey, J. E. *Inorganic Chemistry*; Harper and Row: New York, NY, 1978, pp. 846.
12. Simpson, L. A. *Proc. Org. Coat.*, 6, **1978**, 31.
13. Hiemenz, P. C. *Principles of Colloid and Surface Chemistry*, Marcel Dekker, Inc.: New York, NY, 1977.
14. Tilleard, D. L.; Bullett T. R. *JOCCA*, 36, **1953**, 545.
15. Chernoff, D. A. *Proceedings Microscopy and Microanalysis*, San Francisco Press: San Francisco, CA, 1995.
16. Magonov, S. N.; Elings, V.; Papkov, V. S. *Polymer*, 38, **1997**, 297.
17. Leclère, Ph.; Lazzaroni, R.; Brédas, J. L.; Yu, J. M.; Dubois, Ph.; Jèrôme, R. *Langmuir*, 12, **1996**, 4317.
18. Bar, G.; Thomann, Y.; Brandsch, R.; Cantow, H.-J.; Whangbo, M.-H. *Langmuir*, 13, **1997**, 3807.
19. McMaster, T. J.; Hobbs, J. K.; Barham, P. J.; Miles, M. J. *Probe Microscopy*, 1, **1997**, 43.
20. Magonov, S. N.; Elings, V.; Whangbo, M.-H. *Surf. Sci. Lett.*, **1997**, 375, L385.
21. Magonov, S. N.; Cleveland, J.; Elings, V.; Denley, D.; Whangbo, M.-H. *Surf. Sci.*, 389, **1997**, 201.
22. Abhijit, A. P.; Feng, J.; Winnik, M. A.; Vancsot, G. J. *Polymer*, 37(25), **1996**, 5577.

Downloaded by COLUMBIA UNIV on September 17, 2012 | http://pubs.acs.org
Publication Date: July 26, 2001 | doi: 10.1021/bk-2001-0790.ch012

Downloaded by NORTH CAROLINA STATE UNIV on September 17, 2012 | http://pubs.acs.org
Publication Date: July 26, 2001 | doi: 10.1021/bk-2001-0790.ch013

Chapter 13

Studies on Porosity in Polymer Latex Films

Ian C. Hodges, John Hearn, and Michael C. Wilkinson

**Department of Chemistry and Physics, Nottingham Trent University,
Clifton Lane, Nottingham NG11 8NS, United Kingdom**

Mechanisms for preparation of polymer latex films with porosity in the dry state have been investigated. Leaching additives from cast films and exceeding the critical pigment volume fraction of a binder were assessed for their void generating characteristics. Leachable additives successfully used included sucrose, polyvinyl pyrrolidone, sodium diphenyl ether disulphonate, and a pH dependent soluble polymer latex. Specific surface area and porosimeter studies were used to evaluate the effectiveness of each pore generating mechanism.

Initial studies on the transport properties of these porous latex films were evaluated via dynamic adsorption and advantages shown. Samples of a well characterized carbon adsorbent coated in non porous and porous latex films were compared to determine hindrance to vapour sorption.

Porous colloidal particles based on the principles of macroreticular resin synthesis, but utilizing emulsion polymerization, have been produced. Incorporation of these porous particles into porous latex films to enhance surface area was investigated and proved reasonably efficient.

Differences in pore characteristics of porous films where interstitial water is removed by sublimation compared to evaporation were used to illustrate an effect of capillary forces on pore closure.

INTRODUCTION

The best barrier properties are usually obtained in latex films when the particles are well ordered prior to the final stage of film formation, when polymer chains interdiffuse, so as to achieve maximum density without voids or defects[1,2]. Films with low porosity and low surface area have better film qualities such as scrub resistance[3]. The highest degree of packing order within the film is usually

In Film Formation in Coatings; Provder, T., et al.;
ACS Symposium Series; American Chemical Society: Washington, DC, 2001.

achieved when the latex particles have a monolayer coverage of surfactant, with higher levels of addition resulting in an inferior performance[4]. When latex films are used as binders these same barrier properties can be a disadvantage where access to reactive or adsorptive sites is required. Transport pores are then desirable in a latex film[5]. Steward[6] has shown that water leachable materials added to polymer latex films can be used to control solute permeability. This was attributed to water filled pores, but when films having Tg's below room temperature were allowed to dry, porosity was lost as a consequence of further film formation processes.

The aim of this study is to extend this approach to the creation of porosity in dried latex films by additive leaching and to explore other possible routes to pore creation by deliberate reductions in latex stability prior to film formation and by exceeding critical pigment volume fractions (CPVF). The latter is a method used in the coating industry to prepare 'breathable paint'. This involves adding excess pigment or filler so that there is enough binder to glue the particles together, but not enough to completely fill interstitial voids.

For successful production of porous films, leachable additives must neither be too compatible nor too incompatible. If too compatible with the polymer the additive may dissolve into the particles producing a homogenous film, whereas an incompatible additive may be completely exuded from the film during coalescence. Work by Zhao[7] *et al* measured surface concentrations of sodium dodecyl sulphate (SDS) and sodium diphenyl ether disulphonate (SDED) in coalesced acrylic latex films. It was found that SDS readily migrated to the films surfaces (film-air and film-casting substrate) and continued to be exuded to the surface during film maturation. SDED, however, had a much less pronounced surface enrichment that did not change during film aging, indicating better polymer compatibility.

Successful pore generation can be evaluated by nitrogen adsorption and mercury porosimetry. These techniques evaluate the specific surface area and the pore size distribution, respectively.

Barrier characteristics of prepared films can be evaluated via dynamic adsorption. This measures the ability of a packed bed of adsorbent to adsorb a vapour from an inert gas flowing through the bed. If the kinetics of vapour sorption are inhibited by the presence of the latex film then the adsorbent may not be able to utilise its full capacity before vapour breaks-through the packed bed. Comparison of the dynamic adsorption profiles for the coated and uncoated adsorbent would then indicate the degree to which the polymer film hinders access of adsorbate to adsorptive sites.

Also of interest is production of colloidal porous particles, based on production of macroreticular resins, for potential use in reactive films. Macroreticular beads are commonly produced by suspension polymerization of styrene and divinyl benzene in the presence of a porogen (usually an organic solvent) producing millimetre size beads. Previous studies on emulsion polymerization of vinyl and divinyl monomers have been carried out, but without the incorporation of porogens[8]. During macroreticular resin synthesis the growing crosslinked polymers precipitate out of the porogen producing amalgams of polymer.

Downloaded by NORTH CAROLINA STATE UNIV on September 17, 2012 | http://pubs.acs.org
Publication Date: July 26, 2001 | doi: 10.1021/bk-2001-0790.ch013

Removal of porogen after reaction results in a permanent porosity throughout the bead even when dry. Reaction of the monomers without a porogen results in a gel type resin that only has porosity when swollen with solvent. Adaptation of this process to emulsion polymerization was to be evaluated for the production of macroreticular particles with diameters in the nanometre range. This would facilitate their incorporation into a polymer latex film, which could then be utilized for its high surface area.

The aim of this paper is to report preliminary findings from ongoing research into pore development in latex films and in latex particles.

Downloaded by NORTH CAROLINA STATE UNIV on September 17, 2012 | http://pubs.acs.org
Publication Date: July 26, 2001 | doi: 10.1021/bk-2001-0790.ch013

EXPERIMENTAL

Latex films were formed from four main base latices, which were soap free poly(styrene) (PS) (Ø 525nm) and poly(butyl methacrylate) (PBMA) (Ø 320nm) both prepared in-house, and Eudragit® L30D (ethyl acrylate/methacrylic acid), and Eudragit® NE30D (ethyl acrylate/methylmethacrylate) (Röhm Pharma). L30D is water soluble at pH's>7 and NE30D has a Tg below room temperature. Other water soluble additives investigated were, sucrose, hydroxypropyl methyl cellulose (HPMC), sodium dodecyl sulphate, Dowfax 2A1 (SDED), polyvinyl pyrrolidone, and sodium chloride. Films were cast at 40°C in glass rings and plates sealed with silicone grease. In the case of films incorporating water soluble additives the resulting cast films were soaked in distilled water until the additive was no longer detectable in the wash water.

Porous colloidal particle production was based on macroreticular resin preparation with modification of the polymerization type. The organic phase consisted of styrene (Aldrich), divinylbenzene (BDH Chemicals Limited), and toluene (Aldrich), which was emulsified in water containing the surfactant Aerosol OT-100 (Fisher Scientific U.K. Limited). Polymerization was initiated by potassium persulphate at a reaction temperature of 80°C for 6 hrs.

The specific surface areas of the final films were measured by BET nitrogen desorption on a Quantasorb detector (Quantachrome Corporation). Nitrogen in a helium carrier stream is passed over the sample at various partial pressures by varying both gases flow rates. Immersion of the sample in liquid nitrogen promotes adsorption on to the accessible surface of the film until equilibrium is reached. Warming of the sample after equilibrium desorbs the adsorbed nitrogen back into the carrier stream, which passes through a thermal conductivity detector where the amount of nitrogen desorbed is determined. Nitrogen adsorption at five partial pressures, between 0.1 and 0.3, were taken and incorporated into the BET equation[9] and the specific surface area of the sample was calculated. The Quantasorb continuous flow method of surface area determination has a high sensitivity allowing low areas to be determined.

Pore size distributions and pore volumes were determined by mercury porosimetry on a Porosimeter 2000 series mercury porosimeter (Carlo Erba Strumentazione). Films samples were placed in a dilatometer evacuated of air and filled with mercury. Mercury is non-wetting so will not enter pores until a critical pressure is reached relative to the pore diameter, smaller pores require higher pressures for mercury to enter them. The filled dilatometer was placed in an oil filled autoclave were the pressure was increased and the mercury intrusion volume noted for each pressure point. A plot of the pore radius against the change in volume with change in pore radius gives the pore size distribution.

The barrier characteristics of the latex films were evaluated by dynamic adsorption of methanol as a model vapour on a base carbon adsorbent coated in latex film. The methanol capacity of BPL made it the vapour of choice to optimise the duration of the experiment. The dynamic adsorption apparatus has been described previously[10]. 12-30 mesh granules of steam activated coal based carbon BPL (Chemviron) were dip coated in latex. Methanol was carried through a volume activity tube, packed with the granules, by nitrogen carrier gas (1 l/min) at 1 mg/l, 0% relative humidity, and 25°C and the exhaust concentration monitored with time by infrared spectrometry (Miran model 1Acvf).

Downloaded by NORTH CAROLINA STATE UNIV on September 17, 2012 | http://pubs.acs.org
Publication Date: July 26, 2001 | doi: 10.1021/bk-2001-0790.ch013

RESULTS & DISCUSSION

Porous Latex Films

Specific Surface Area

Of the methods tried, the most promising results were for the films obtained by leaching L30D, sucrose, PVP, and SDED from PBMA, and those obtained by exceeding the CPVF of NE30D with PS.

For L30D leaching experiments, PBMA films were cast with varying amounts of L30D based on the dry film weight with subsequent extraction of L30D by washing with 0.2M sodium hydroxide. For sucrose, PVP, and SDED leaching experiments, PBMA films were cast with varying amounts of each additive based on dry film weight with subsequent extraction by washing with distilled water. All films were freeze dried after additive leaching and their specific surface areas evaluated and the results are shown in figure 1. For the CPVF experiments, NE30D was cast with various loads of PS above its CPVF resulting in voids between PS particles. No further treatment was required after casting. The specific surface areas of these films are also shown in figure 1.

Study of the results reveals that L30D leached films show an increase in specific surface area with increasing L30D loading. This indicates that at the lower loadings there are large domains of film formed PBMA with limited access to the surface area of the original particles within the domain. With increasing L30D loadings these domains become smaller so more surface area is available for adsorption.

Downloaded by NORTH CAROLINA STATE UNIV on September 17, 2012 | http://pubs.acs.org
Publication Date: July 26, 2001 | doi: 10.1021/bk-2001-0790.ch013

Films leached of sucrose, PVP, and SDED both show higher specific surface areas with increasing additive loading, in the same way as L30D. For sucrose films containing loadings greater than 35% no films were attainable, due to the washing step redispersing the polymer particles. This suggests that larger amounts of sucrose hinder particle-particle contact restricting coalescence of the film. PBMA films with PVP and SDED loadings greater than 25 and 45% respectively, also suffer from redispersion during the washing step. The film leached of 45% SDED shows no increase in surface area compared to leaching at 29%. This indicates that a certain point can be reached were the polymer domains will not get any smaller and so no extra surface of the original particles can be accessed.

In CPVF experiments, a gradual decrease in specific surface area is seen with increasing NE30D loading. This is in accord with the assumption that larger NE30D loadings cover more of the polystyrene spheres and will begin to block interstices completely.

Visual examination of fracture cross-sections of the films shows opacity running all the way through the film from top to bottom. This indicates that the pores are interconnecting, else leaching additive completely from the film interior would not be possible. Examination of unsuccessful films shows opacity at the top and bottom only, with a transparent interior. This indicates the additives inability to form the continuous network required for leaching, resulting in the final films poor performance.

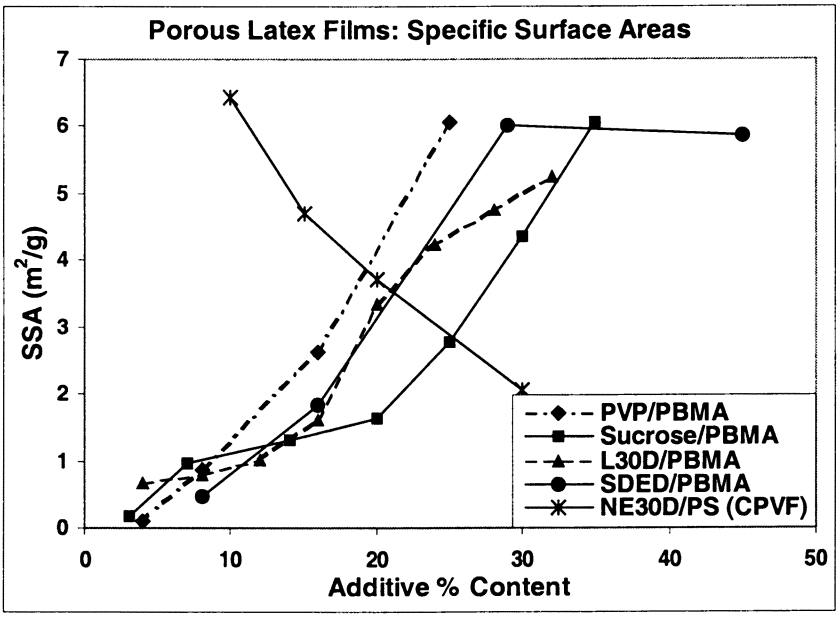

Figure 1. Comparison of specific surface areas for prepared films.

Porosimetry

The porous nature of all films was determined by mercury porosimetry for each pore generating process. Pore size profiles for PBMA films leached of L30D, and CPVF-exceeded NE30D are shown in figures 2 & 3 respectively. The trends in total pore volume for all films are shown in figure 4.

PBMA films leached of L30D show a general increase in pore radius and cumulative pore volume with increasing amount of L30D leached (fig 2 & 4). All films contain relatively the same amount of small pores, but with increasingly larger pores being added with increasing amounts of L30D. This indicates that with more L30D spheres present, larger agglomerates of L30D can be formed in the cast film that will produce larger pores once leached out.

PBMA films leached of sucrose show a decrease in pore radius and total pore volume with increasing amount of sucrose leached. This suggests that with higher sucrose loadings sugar is more easily expelled from the film possibly due to more complete migration channels to the surface formed during drying. This results in more sucrose exuded to the surface and less sucrose inside the dry film.

PBMA films leached of PVP show an increase in total pore volume with increasing amount of PVP leached, while the average pore radius stays relatively unchanged. This indicates that PVP separates out into domains of a single size. Addition of more PVP increases the number of pores while the pore radius stays constant.

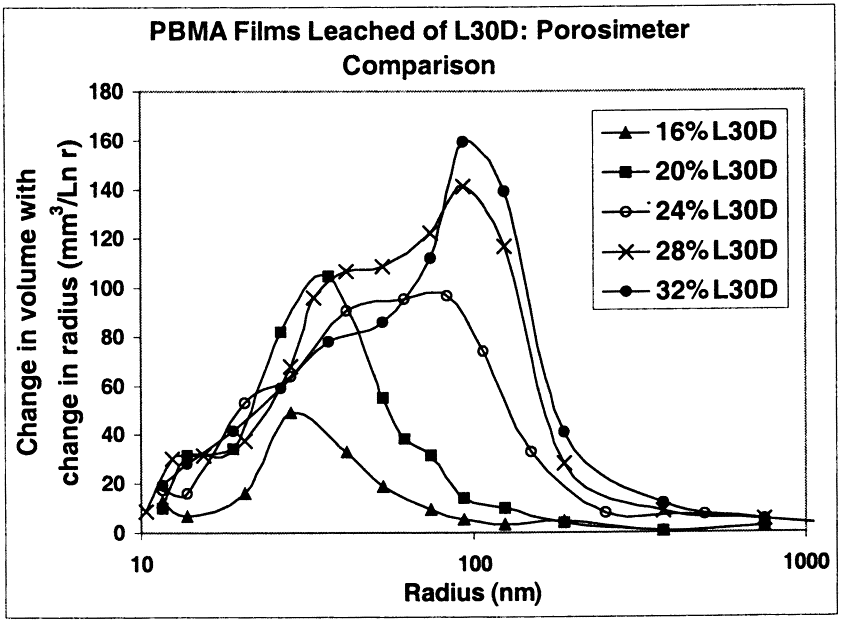

Figure 2. Comparison of pore radius profiles for films leached of L30D.

Downloaded by NORTH CAROLINA STATE UNIV on September 17, 2012 | http://pubs.acs.org
Publication Date: July 26, 2001 | doi: 10.1021/bk-2001-0790.ch013

PBMA films leached of SDED show increasing total pore volume with increased loadings, while the average pore radius stays relatively unchanged. This indicates, like PVP, that SDED forms domains of a similar size and on addition of more additive increases the number of pores.

Films prepared by exceeding the CPVF of NE30D with PS have a relatively narrow pore size distribution and high total pore volumes (fig 3 & 4) compared to the other films. At low amounts of NE30D there are two apparent pore size distributions close together. As NE30D loading is increased, firstly the larger pore distribution is reduced leaving only the smaller, and then, secondly the smaller distribution is reduced until no pores are present. The narrow pore radius distribution is due to the uniform interstices formed from the monodisperse PS latex. The reduction in total pore volume with increasing NE30D content is due to the filling of the interstices with polymer, which is also apparent in the specific surface area loss (fig 1).

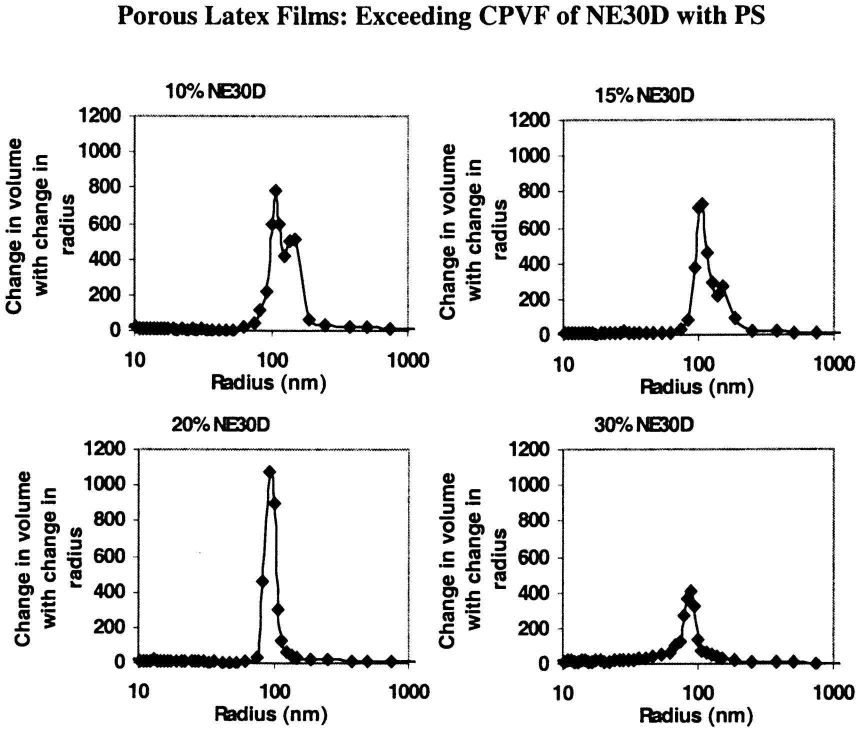

Figure 3. Comparison of pore radius profiles for films prepared by exceeding the CPVF of NE30D with PS.

Downloaded by NORTH CAROLINA STATE UNIV on September 17, 2012 | http://pubs.acs.org
Publication Date: July 26, 2001 | doi: 10.1021/bk-2001-0790.ch013

Downloaded by NORTH CAROLINA STATE UNIV on September 17, 2012 | http://pubs.acs.org
Publication Date: July 26, 2001 | doi: 10.1021/bk-2001-0790.ch013

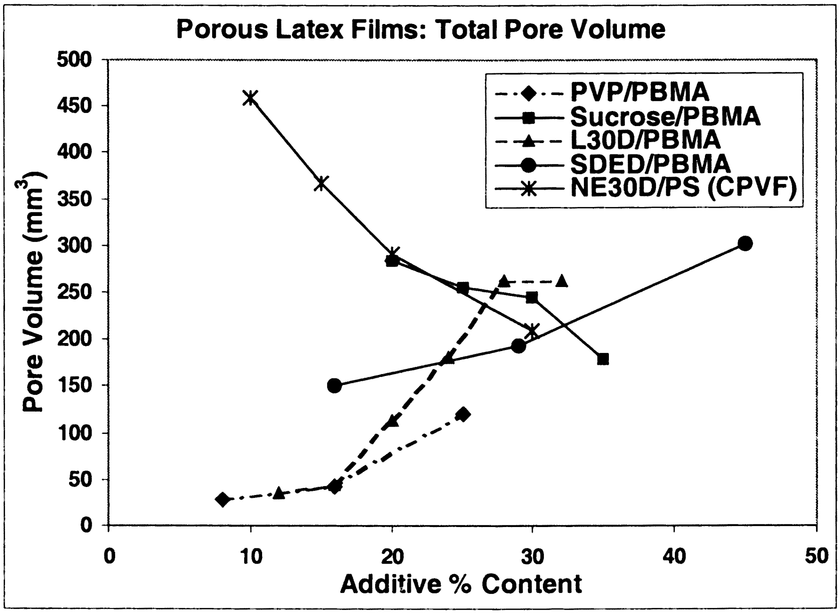

Figure 4. Comparison of total pore volume for prepared films.

Leaching HPMC, sodium dodecyl sulphate, and low concentrations of sodium chloride were ineffective in producing films with detectable specific surface areas under the casting conditions used. Limited solubility of HPMC in water, prevented films being formed with high enough quantities to form a porous film. After leaching only the surface of the film was opaque while the interior was still transparent. The degree of opacity is a good indication of porosity due to light scattering by a large number of small pores (unless the pores are significantly smaller than the wavelength of light).

Only small amounts of sodium chloride could be added to the latex without affecting stability. These small quantities were not effective for pore generation.

Sodium chloride was added to the latex in quantities so that some films were prepared from initially flocculated latex. Other films were cast from stable latex, but flocculation occurred at various stages of casting as the serum ionic strength increases during water evaporation. All films prepared by this method were very opaque and, in the case of higher sodium chloride contents, rough textured. Although pores were present in the film, indicated by the opacity, no surface area could be determined. This suggests that the majority of pores are inaccessible and are in the form of air pockets trapped within the polymer.

Films prepared by leaching SDS showed only surface opacity with a transparent interior. Du Chesne[11] *et al* showed that incompatible stabilizers migrate to the film surfaces and to islets within the polymer film. These islets may not be accessible to leaching so only the surface surfactant will be removed resulting in very little porosity. The successful pore generation by SDED compared to SDS illustrates the importance of partial additive-polymer compatibility for porous film production.

Good reproducibility of the pore radius profiles were found for films prepared under the same set of conditions, but on different dates.

Downloaded by NORTH CAROLINA STATE UNIV on September 17, 2012 | http://pubs.acs.org
Publication Date: July 26, 2001 | doi: 10.1021/bk-2001-0790.ch013

Pore Closure

Films prepared for this study from poly(butyl methacrylate) with various loadings of leachable Eudragit® L30D show a different range of pore sizes between each film. The lower loadings form relatively small pores while higher loadings add larger pores to the profile (fig 2). After casting and leaching of L30D from the film, a porous PBMA film is left with all pores filled with water. These films are effectively at film formation stage two as the particles are already ordered and partly coalesced. These films were divided into two halves, which were dried differently. One half was dried in a nitrogen gas stream at room temperature and the other half freeze dried so that water sublimed rather than evaporated from pores within the film. After freeze drying was complete, it too was kept at room temperature for an equal time to that of the nitrogen dried sample, before both halves being stored at 4°C ready for analysis.

The specific surface area results for freeze dried and nitrogen dried films are shown in figure 5. Nitrogen dried samples with low additive contents show complete loss of surface area compared to their freeze dried counterparts. As additive content increases the difference in surface area between nitrogen dried and freeze dried samples decreases until little difference is noted.

Comparison of the pore radius profiles for films leached of 10% and 30% L30D both freeze and nitrogen dried are shown in figure 6.

Films prepared from 10% L30D show similar pore radii by both methods of drying, but the nitrogen dried sample shows a reduced number of pores suggesting pore closure. This pore closure is responsible for the differing specific surface areas seen for these two films.

Films prepared from 30% L30D by both drying regimes have similar pore radius profiles at similar heights indicating little difference in pore characteristics between the two. This is evident in the similar specific surface area obtained for both these samples. This indicates that films with only small pores further coalesce during nitrogen drying, but if larger pores are present less coalescence is seen. Pore closure can arise through viscoelastic deformation caused either by polymer-water interfacial tension (wet sintering)[12]; polymer-air interfacial tension (dry sintering)[13] or from the water-air interfacial tension (capillarity)[14]. Both film halves experienced a similar period of leaching, so that wet sintering is unlikely to

Downloaded by NORTH CAROLINA STATE UNIV on September 17, 2012 | http://pubs.acs.org
Publication Date: July 26, 2001 | doi: 10.1021/bk-2001-0790.ch013

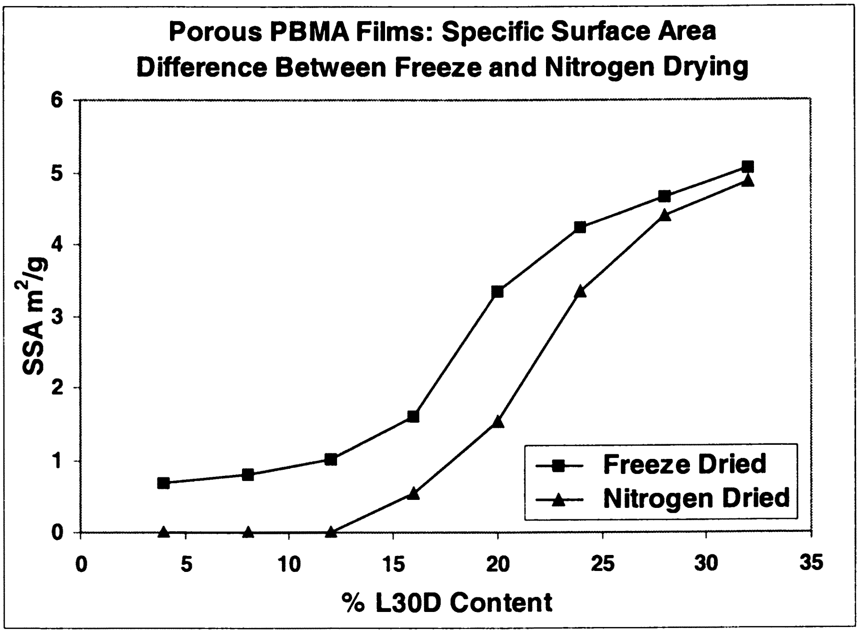

Figure 5. Comparison of the different specific surface areas found between freeze and nitrogen drying.

lead to a difference and both films experienced a similar period in a dry state at room temperature, so that dry sintering is also an unlikely cause. It is thus tentatively suggested, since it is a matter of much debate[15] whether water has a direct role to play in the mechanism of film formation from hydrophobic latex particles, that pore closure is driven by capillary forces as water evaporates from fine pores. These forces being proportional to pore radius, have the greatest effect on the population of small pores. Lin & Meier[16] have also claimed a role for water and capillary forces in film formation from hydrophobic latex particles.

Macroreticular Colloid particles

The preparation of porous particles based on macroreticular resin synthesis, but using emulsion polymerization has resulted in the production of stable colloidal latices with particle diameters of 100nm and specific surface areas of ~200m^2/g. The pore characteristics were evaluated via full nitrogen adsorption/desorption isotherms and two peaks were found between 2 and 4 nanometres radius indicating presence of pores in the mesoporous range.

Downloaded by NORTH CAROLINA STATE UNIV on September 17, 2012 | http://pubs.acs.org
Publication Date: July 26, 2001 | doi: 10.1021/bk-2001-0790.ch013

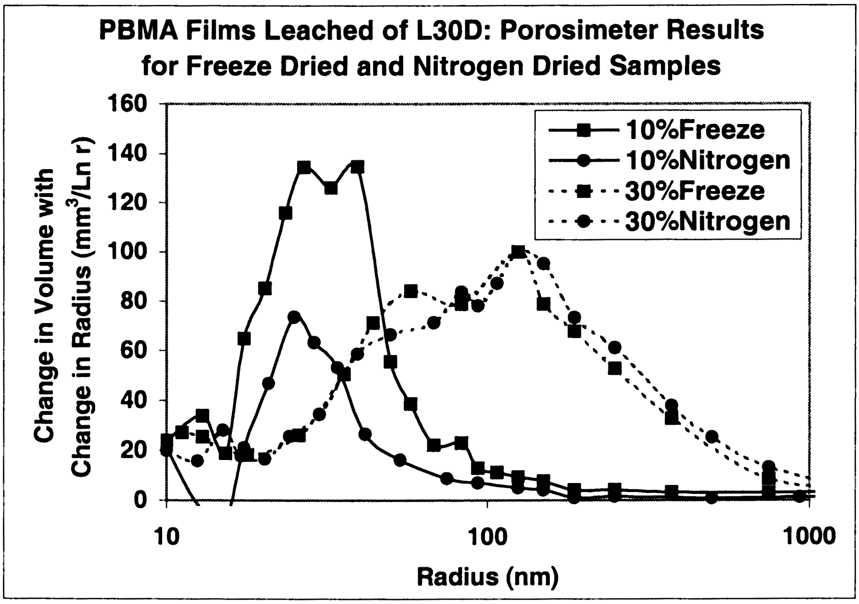

Figure 6. Comparison of the pore radius profiles for films leached of 10% and 30% L30D under different drying regimes.

Addition of this latex into NE30D (25% NE30D loading) above its CPVF resulted in a film with a specific surface area of 95 m^2/g. The relatively high surface area of this film shows potential for development into a reactive film. Approximately half the surface area of the porous particles is lost. Study of the specific surface area graph for NE30D films exceeding CPVF with PS (fig 1) shows that there is scope to increase the surface area further.

Dynamic Adsorption

Dynamic adsorption profiles for plain BPL carbon, non-porous latex coated carbon, and porous latex coated carbon are shown in figure 7.

The latex coat consisted of PBMA and L30D at 50% loading. The non-porous coat involved no leaching and the porous coat required removal of L30D via washing. Plain BPL carbon shows a typical profile[10] with an initial period (~10 minutes) where no vapour passes completely through the bed. The non-porous latex coated sample shows an immediate and rapid increase in methanol exhaust concentration indicating severe loss of performance. The porous latex coated sample has an initial period with no methanol in the exhaust stream (~3 minutes) and a slower rate of adsorption compared to the plain carbon sample. Integration of the area above the curves gives the total amount of methanol adsorbed per sample and shows that the plain and porous coated carbons have adsorbed approximately the same amount. Although the porous coated sample showed poorer dynamic performance than the plain sample the results indicate that the adsorbent sites are still accessible, but at a slower rate.

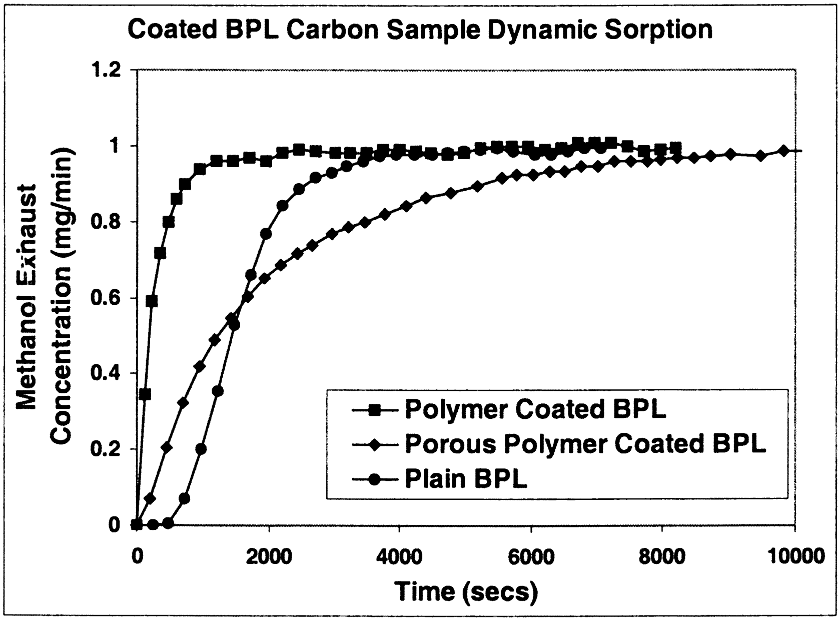

Figure 7. Comparison of dynamic adsorption profiles for polymer coated, porous polymer coated, and plain BPL carbon.

Conclusions

Polymer films prepared from coalescence of polymer binder latex have been formed with porosity in the dry state. Voids have been formed by leaching additives from cast films and by exceeding a binders critical pigment volume concentration. The number of small pores retained depends upon the method of drying used.

Initial studies on the transport properties of these porous latex films have been evaluated via dynamic adsorption. Carbon adsorbents coated in porous latex

Downloaded by NORTH CAROLINA STATE UNIV on September 17, 2012 | http://pubs.acs.org
Publication Date: July 26, 2001 | doi: 10.1021/bk-2001-0790.ch013

show their complete adsorption capacity for a vapour, but at a slower adsorption rate compared to plain carbon performance, whereas with a non porous film their capacity is lost completely.

Production of porous colloidal particles has been achieved based on macroreticular resin synthesis utilizing emulsion polymerization. Incorporation of these porous particles into porous latex films to enhance available surface area has been successful.

The potential functionalization of these porous latex films to produce reactive films, offer the advantages of ready access to a high surface area of colloidal size particles whilst avoiding the difficulty of recovery from the reaction products. Functionalized latices for example are deliberately destabilized and sedimented destroying their potential for further use. Porous binder films offer the prospect of improved adsorbent performance and its complement the potential for sustained release.

Downloaded by NORTH CAROLINA STATE UNIV on September 17, 2012 | http://pubs.acs.org
Publication Date: July 26, 2001 | doi: 10.1021/bk-2001-0790.ch013

References

1. Roulstone B.J., Wilkinson M.C., Hearn J., Polym. Int., 27, p43-50, (1992)
2. Okubo M., Takeya T., Tsutsumi Y., Kadooka T., Matsumoto T., J. Polym. Sci., Polym. Chem. Ed., 19, p1-8, (1981)
3. Isaacs P.K., J. Macromol. Chem., 1 (1), p163-185, (1966)
4. Juhué D., Lang J., Colloids & surfaces A: Physico. Chem. Eng. Aspects, 87 p177-185, (1994).
5. Lyngberg O.K., Scriven N.E., Flickinger M.C., Abstracts of papers of the American Chemical Society, Vol.216, No.Pt3, p35-BTEC, (1998).
6. Steward P.A., Hearn J., Wilkinson M.C., Wilson A.J., Roulstone B.J., Ch.23 in ACS Int. Symp. Ser. No. 648, p359-402, Film Formation in Waterborne Coatings, Eds. Provder, Winnick & Urban, (1996).
7. Zhao C.L., Dobler F., Pith T., Holl Y., Lambla M., J. Colloid and Interface Science, 128, 2, p437-449, (1988).
8. Tobita H., Hamielec A.E., Polym. Int., 30, p195-201, (1993).
9. Brunauer S., Emmet P.H. Teller E., J. Am. Chem. Soc., 60, p309, (1938).
10. Karpowicz F., Hearn J., Wilkinson M.C., Carbon, 33, 11, p1573-1583, (1995).
11. Du Chesne A., Gerharz B., Lieser G., Polym. Int., 43, p187-196, (1997).
12. Vanderhoff J.W., Tarkowski H.L., Jenkins M.C., Bradford E.B., J. Macromol. Chem., 1(2), p361-397, (1966).
13. Dillon R.E., Matheson L.A., Bradford E.B., J. Colloid Sci., 6, p108-117, (1951).
14. Brown G.L., J. Polym. Sci., 22, p423434, (1956).
15. Sperry P.R., Synder B.S., O'Dowd M.L., Lesko P.M., Langmuir, 10, p2619-2628, (1994).
16. Lin F., Meier D.J., Langmuir, 11, p2726-2733, (1995).

Downloaded by COLUMBIA UNIV on September 17, 2012 | http://pubs.acs.org
Publication Date: July 26, 2001 | doi: 10.1021/bk-2001-0790.ch014

Chapter 14

Creation of Polymer Films with Novel Structures and Properties by Processing with Inclusion Compounds

L. Huang, M. Gerber, H. Taylor, J. Lu, E. Tapaszi, M. Wutkowski, M. Hill, F. N. Nunalee, A. Harvey, C. C. Rusa, F. Porbeni, E. Edeki, and A. E. Tonelli

Fiber and Polymer Science Program, North Carolina State University, 2401 Research Drive, Raleigh, NC 27695-8301

We have begun to fabricate polymer films whose compositions, structures, and properties may be developed and controlled during their formation with inclusion compounds (ICs). ICs formed with either urea(U) or cyclodextrin(CD) hosts and containing guest polymers or small-molecule additives are embedded into carrier polymer films either by solution casting or melt pressing methods. Once embedded, the IC crystals are left undisturbed or are disrupted by solvent treatment, which removes the host (U or CD), but not the carrier polymer nor the coalesced IC-guest. In this manner polymer-polymer composite and additive-filled films have been fabricated. Employment of polymer-U or CD-ICs produces composite films containing two different polymers or two populations of the same polymer. In the latter case, the morphologies of the carrier and IC-coalesced chains may differ, because of chain-folded and chain-extended crystallization, respectively. We may, for example, control film permeabilities by either controlling the compositions or the morphologies of the composite films. Dyes, flame retardants, antibacterials, etc. have been delivered to films by processing with their ICs., and, depending on the application, subsequently disrupting the IC crystals to release the additive and remove the IC host. Several examples of both composite and additive-filled polymer films will be presented and discussed, and extension to polymer fiber samples will be mentioned.

Supported by: Army Research Office, The National Textile Center (Dept. of Commerce), ACS-Project SEED, Burroughs-Wellcome Fund

Introduction

Crystalline inclusion compounds (ICs) may be formed between a variety of small-molecule hosts and guests that are either also small-molecules or polymers (1-5). Employing urea (U) and the cyclodextrins (CDs) as hosts we have formed a large number of polymer-U- and polymer-CD-ICs, and more recently several small-molecule-CD-ICs with guests that often serve as polymer additives. These IC crystals may be incorporated into polymer films either by melt processing at temperatures below the melting points of the ICs or by casting the film from a solvent that does not dissolve the ICs. In this manner a number of polymer-polymer molecular composites and additive-filled polymer films have been obtained. This technique is illustrated schematically in Figure 1.

In addition, because it has been observed by us (6,7) and others (8,9) that washing polymer-IC crystals with a solvent for the small-molecule host, but which does not dissolve the included guest polymer, leads to coalescence of the guest polymer into a chain-extended rather than chain-folded morphology when the guest polymer is able to crystallize, we have also embedded polymer films with IC crystals containing the same polymer. The purpose of this procedure was to attempt to induce chain-extended crystallization throughout the film or on the film surface, because the chain- extended crystals generally melt at significantly higher temperatures than the chain-folded crystals. The goal of this fabrication technique is to modify the strengths and/or barrier properties of the IC-processed films.

In Figure 2 both U- (10) and CD-ICs are illustrated. It is apparent that the guests included in these IC crystals are isolated from the environment external to the crystals, and that they may only be released into the surroundings by melting or appropriate solvent treatment. Even if the IC guest is a liquid in its pure phase, once the guest-IC is formed a crystalline solid results. ICs formed with CDs are particularly robust with melting temperatures in the range 275-350°C, and so they may be conveniently melt-processed into a variety of polymer films that melt below this temperature range.

Here we report on several polymer-polymer composites and additive-filled polymer films fabricated by forming films that include polymer- or additive-U- and -CD-ICs. Some preliminary results concerning their morphologies and permeabilities will be presented and discussed. In addition, attempts were made to form composite polymer films directly from IC crystals containing two different polymers, in the hope that washing the polymer-1/polymer2-IC crystals with a solvent/non-solvent for the host/guest polymers would produce a homogeneously mixed, polymer-1/polymer-2 composite film made from normally incompatible polymer pairs. Among the films described will be poly(L-lactic acid)(PLLA) and nylon-6 with poly(ethylene oxide)(PEO) and poly(epsilon-capolactone)(PCL),and PLLA, PCL, nylon-6, and poly(ethylene terphthalate)(PET) films filled with dyes, flame-retardants, and anti-bacterials.

Downloaded by COLUMBIA UNIV on September 17, 2012 | http://pubs.acs.org
Publication Date: July 26, 2001 | doi: 10.1021/bk-2001-0790.ch014

Downloaded by COLUMBIA UNIV on September 17, 2012 | http://pubs.acs.org
Publication Date: July 26, 2001 | doi: 10.1021/bk-2001-0790.ch014

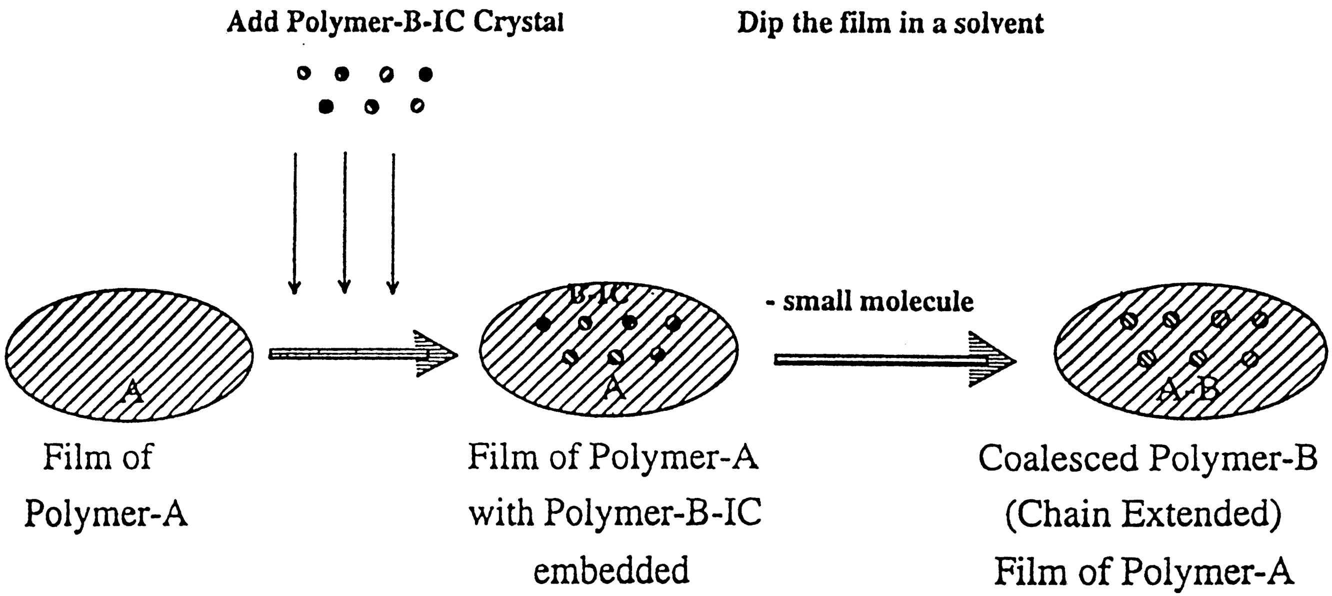
Add Polymer-B-IC Crystal
Dip the film in a solvent
- small molecule
A
B-IC
A
A-B
Film of
Polymer-A
Film of Polymer-A
with Polymer-B-IC
embedded
Coalesced Polymer-B
(Chain Extended)
Film of Polymer-A

Figure 1. Mechanism for the coalescence of polymer-B from its inclusion compound into carrier polymer-A.

Materials and Methods

Urea(U) and cyclodextrins (CDs) were obtained from Aldrich and Cerestar, respectively. PLLA (MW=285,00), PCL (MW=30,000), PEO (MW=100,000), nylon-6 (MW=12,000), and PET (MW=18,000) were obtained from Research Triangle Institute, Aldrich, Sigma, Allied Signal, and Aldrich, respectively. Preparation of the polymer-U- and CD-ICs have been previously described (7,11-14). PCL/PLLA-ß-CD-IC was obtained from a dioxane solution of the two polymers and a saturated solution of ß-CD. Washing this IC with hot water produced a coalesced sample of PCL/PLLA which was compared with a PCL/PLLA film cast directly from their dioxane solution. Films embedded with polymer-U- and -CD-ICs were washed with methanol and water, respectively, in order to coalesce the IC-included polymers into the carrier polymer films.

Downloaded by COLUMBIA UNIV on September 17, 2012 | http://pubs.acs.org
Publication Date: July 26, 2001 | doi: 10.1021/bk-2001-0790.ch014

The dyes used in this study were obtained from Aldrich (10127-02-3 and 34994-50-8) and synthesized by K. Hamada. The antbacterials neomycin- sulfate and Irgasan-DP300r (Trichlosan) were obtained from Calbiochem and Ciba Specialty Chemicals Companies, respectively. The flame retardant was obtained from Albright and Wilson, and the surfactant/spermicide from Jeen International.

The following additive-CD-ICs were formed: 3 dyes whose structures are given in Figure 3, 2 antibacterials shown in Figure 4, and the flame retardant presented in Figure 5. The additive-CD-ICs were formed as described in references 15-17.

X-ray diffractograms of the IC powders observed at wide angles were primarily used to verify successful IC formation. A Siemens type-F X-ray diffractometer with a nickel filtered CuKα radiation source (wavelength= 1.54Å) and voltage and current set to 30kV and 20 mA, respectively, was operated at a scan rate of 2Θ=1°/min, between 2Θ=5-40°, to obtain the powder diffractograms, such as presented in Figures 6 and 7. Note the similarity between the X-ray diffractograms of valeric acid-, PEO-, and PCL-a-CD-ICs in Figure 6. Because single-crystal X-ray diffraction analysis of valeric acid-a-CD-IC (18) has revealed a channel structure (see Figure 2c), it is clear that PEO and PCL also form a-CD-ICs with a channel structure. In Figure 7 the X-ray diffractograms of ß-CD, a red azo-dye, and the dye-ß-CD-IC powders are compared. The diffraction pattern of the dye-ß-CD-IC is significantly different from the patterns exhibited by the crystals of its constituents, and so we conclude that the dye-B-CD-IC has been formed.

Films were formed either by casting from solution or melt pressing. In the former case, just before solvent evaporation went to dryness, the IC powder was sprinkled lightly on top of the drying film. Prior to melt- pressing, the carrier polymer and the IC to be embedded were thoroughly mixed as fine powders. The IC-embedded films were soaked in warm methanol (U-ICs) or hot water (CD-ICs) in order to break up the polymer- or additive- IC crystals, remove the U or CD host, and coalesce the included polymer or additive into the carrier film.

Downloaded by COLUMBIA UNIV on September 17, 2012 | http://pubs.acs.org
Publication Date: July 26, 2001 | doi: 10.1021/bk-2001-0790.ch014

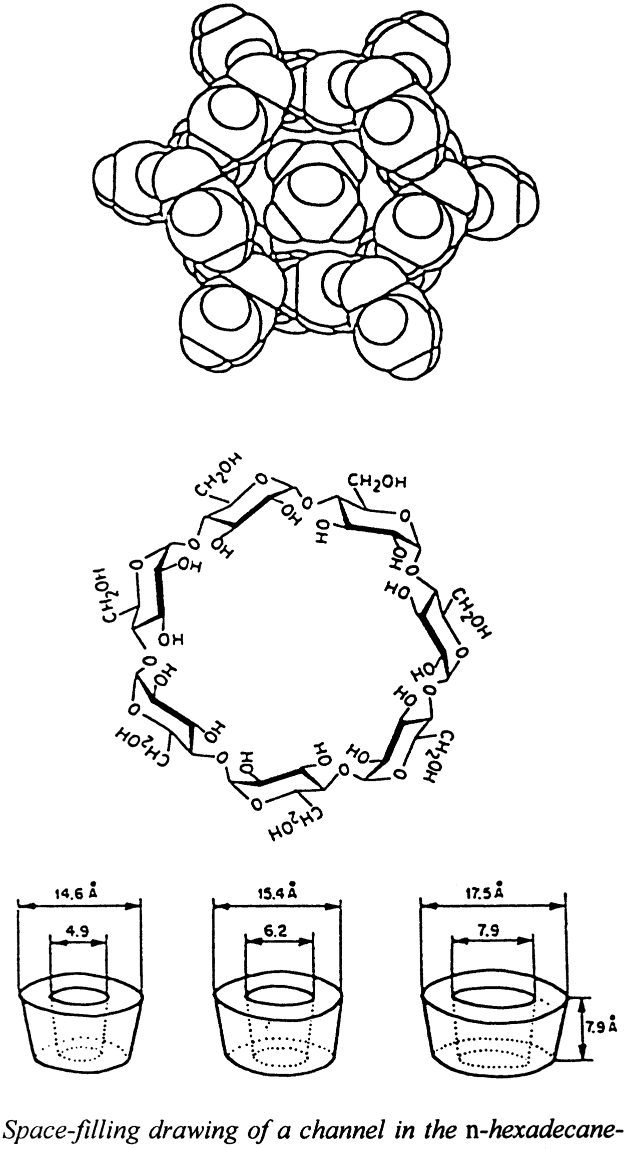

Figure 2. Space-filling drawing of a channel in the n*-hexadecane-U-IC in the top panel. Structure of β-cyclodextrin and molecular dimensions (left to right) of α-, β-, and γ-cyclodextrins in the middle panel, and schematic representation of (a) channel-type, (b) cage herringbone-type, and (c) cage brick-type crystal structures formed by crystalline cyclodextrin inclusion compounds in the lower panel.*

Downloaded by COLUMBIA UNIV on September 17, 2012 | http://pubs.acs.org
Publication Date: July 26, 2001 | doi: 10.1021/bk-2001-0790.ch014

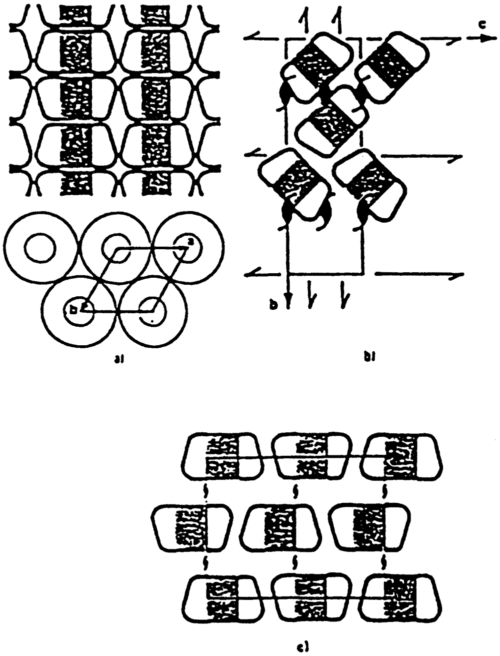

Figure 2. *Continued.*

Downloaded by COLUMBIA UNIV on September 17, 2012 | http://pubs.acs.org
Publication Date: July 26, 2001 | doi: 10.1021/bk-2001-0790.ch014

Dye I (Red Dye-^{19} F labeled) – Organic Azo Acid Dye

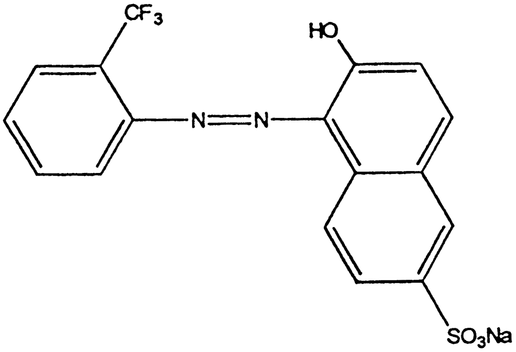

Dye II (Resorufin, sodium salt) – Fluorescent Dye

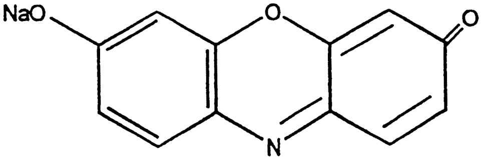

Dye III (Acridine Orange) – Fluorescent Dye

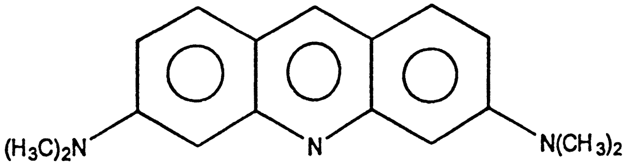

Figure 3. Chemical structures of the dyes used in this study.

Downloaded by COLUMBIA UNIV on September 17, 2012 | http://pubs.acs.org
Publication Date: July 26, 2001 | doi: 10.1021/bk-2001-0790.ch014

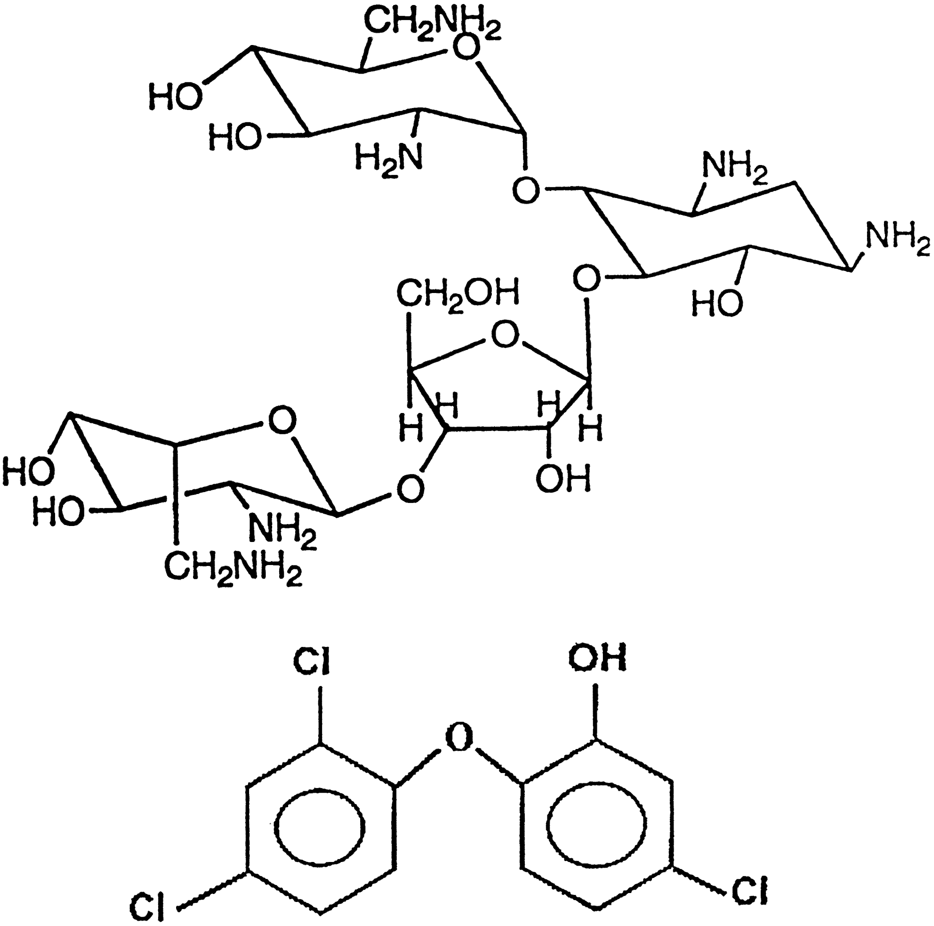

Figure 4. Chemical structure of the antibacterials neomycin (top) and trichlosan (Irgasan-DP300R).

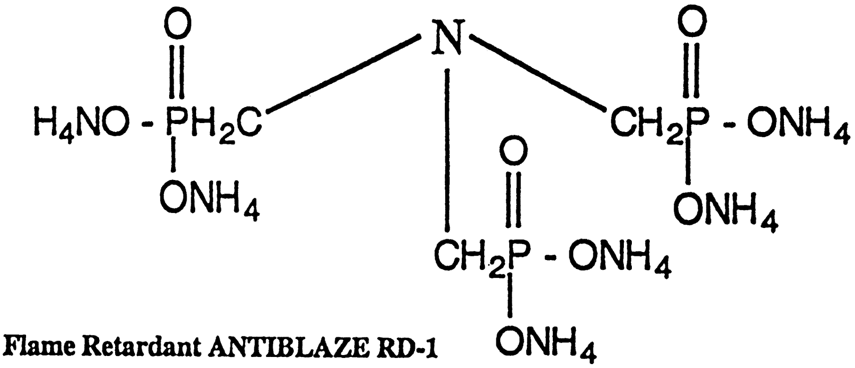

Figure 5. Chemical structure of the flame retardant (ANTIBLAZE RD-1).

Downloaded by COLUMBIA UNIV on September 17, 2012 | http://pubs.acs.org
Publication Date: July 26, 2001 | doi: 10.1021/bk-2001-0790.ch014

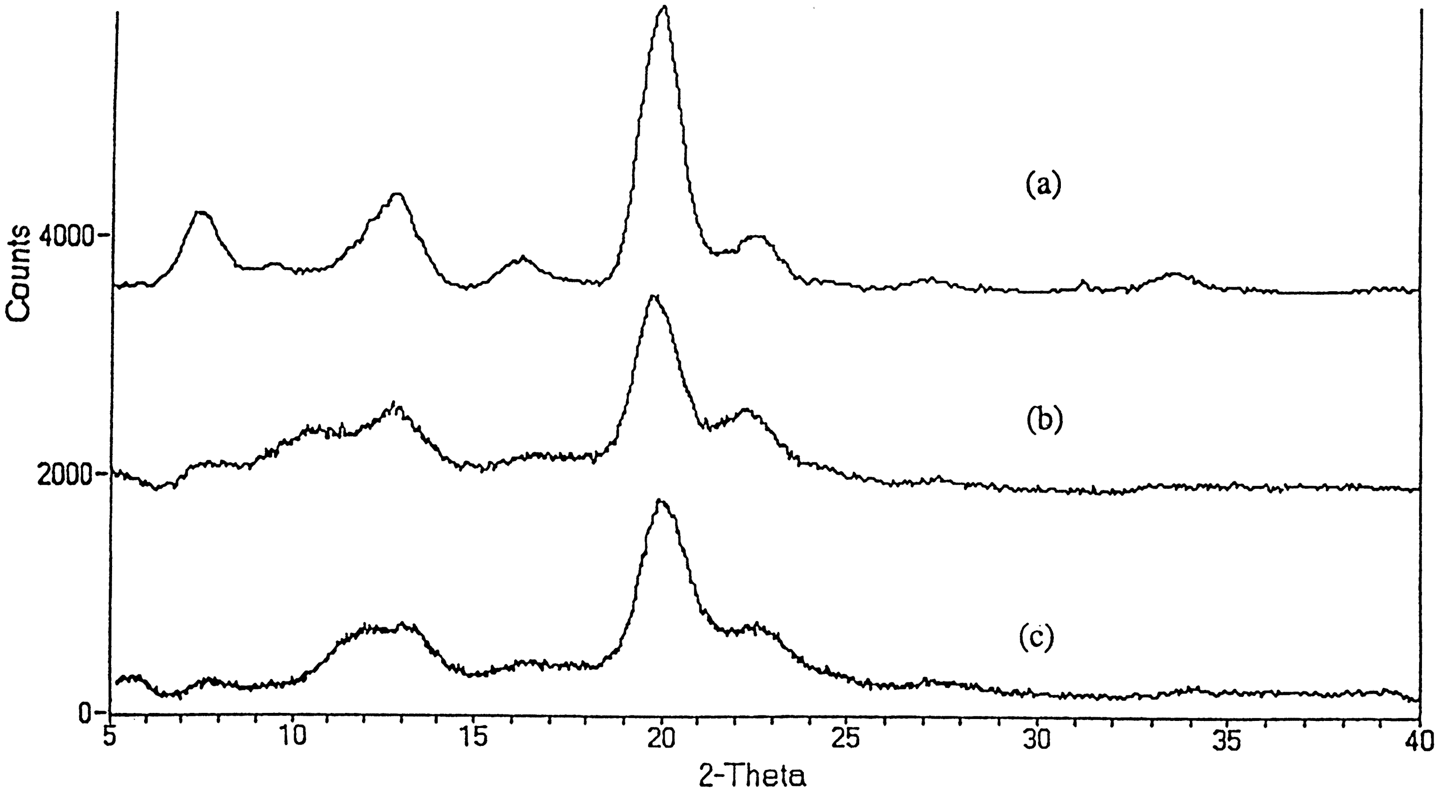

Figure 6. Wide angle X-ray diffractograms of (a) valeric acid-α-CD-IC, (b) PEO-α-CD-IC, and (c) PCL-α-CD-IC.

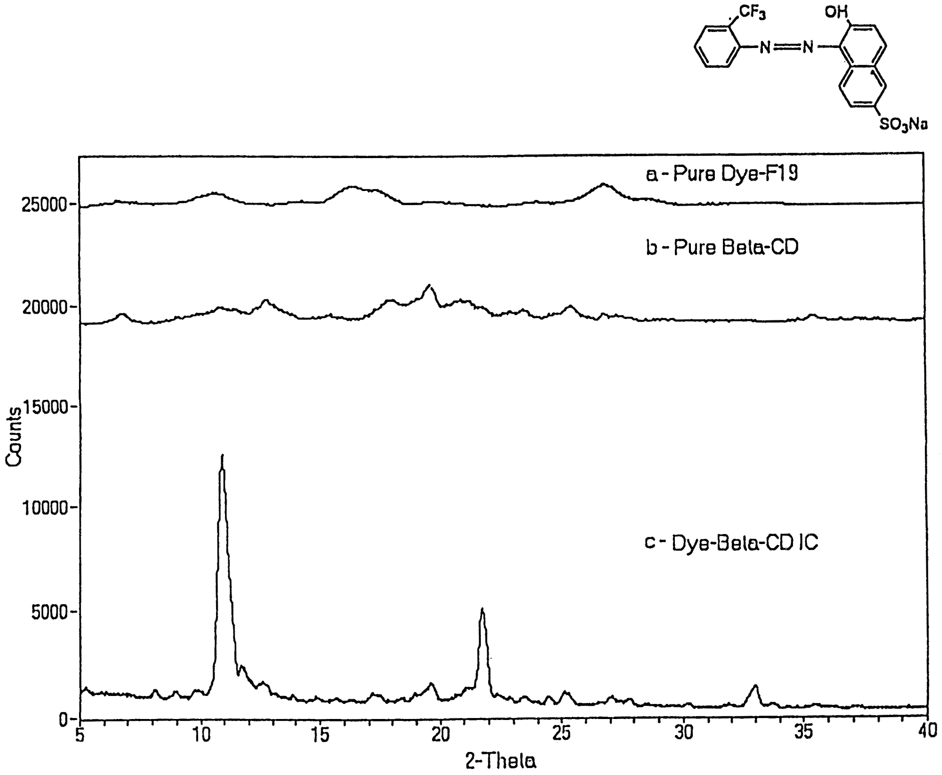

Figure 7. Wide-angle diffractograms of (a) Dye I, (b) β-cyclodextrin, and (c) Dye I-β-CD-IC.

Downloaded by COLUMBIA UNIV on September 17, 2012 | http://pubs.acs.org
Publication Date: July 26, 2001 | doi: 10.1021/bk-2001-0790.ch014

Film thicknesses were obtained with a Thwing-Albert thickness tester (Model II) and rates of water vapor permeation through the films were obtained from weight loss measurements of pans containing water that were covered and sealed with the films (ASTM-E96-80). A Perkin-Elmer DSC-7 was employed to observe calorimetric scans (10°C/min) of the embedded films before and after solvent dipping to coalesce the IC-included guest (polymer or additive) into the carrier film.

Results and Discussion

Polymer-ICs:

Figures 8 and 9 present the DSC scans of PCL-U- and -a-CD-ICs(19) recorded before and after washing with methanol and water, respectively. Note the increase in the melting temperatures of PCL coalesced from its U-IC (64°C) and a-CD-IC (70°C) compared with PCL crystallized from solution or the melt (58°C). This is indicative of a more stable chain-extended crystalline morphology. DSC scans of PCL and PLLA films embedded with PCL-U-IC recorded before and after washing with methanol are shown in Figure 10. It is clear that the PCL-U-IC is removed from both films during their methanol washes. It can also be seen in Table 1 that the PCL and PLLA films containing U-IC coalesced PCL do not exhibit any significant increases in water vapor permeability, so apparently the coalescence of PCL from PCL-U-IC into the PCL and PLLA carrier films proceeds without the formation of holes. Figure 11 presents the DSC scans of PLLA and nylon-6 films embedded with PEO-a-CD-IC after being washed in hot water (20). Note the melting endotherms of PEO at ca. 60°C in both scans, which is indicative of the release and coalescence of PEO chains into the PLLA and nylon-6 carrier films.

Downloaded by COLUMBIA UNIV on September 17, 2012 | http://pubs.acs.org
Publication Date: July 26, 2001 | doi: 10.1021/bk-2001-0790.ch014

The DSC scans of two PCL/PLLA composite films are presented in Figure 12. The film in (a) was cast from a dioxane solution containing both PCL and PLLA, while the film in (b) was obtained by washing a PCL/PLLA-ß-CD-IC sample with hot water. The PCL/PLLA-ß-CD-IC was formed by adding a dioxane solution of PCL and PLLA to a saturated aqueous solution of ß-CD (7). Note the two clearly separated melting endotherms observed for PCL and PLLA in (a) and (b), which indicate phase segregated morphology for both blends. On the other hand, in (b) the melting temperature of PLLA appears elevated compared to the solution-cast film, possibly a consequence of chain-extended crystallization. The fact that the IC-coalesced film also exhibits distinct melting points for PCL and PLLA suggests that PCL and PLLA are not included in the same or neighboring cannels of their ß-CD-IC crystals. If this is confirmed by further observations, then it may prove difficult to achieve intimately compatible polymer blends by coalescence from ICs formed from their common solutions.[More recently intimately mixed blends of the normally incompatible pair PCL/PLLA have been achieved by coalescence of PCL/PLLA from their IC formed with α-CD.]

Figures 13 and 14 present the X-ray diffractograms of PET- and silk-γ- CD-ICs (14,21) and their comparison to the diffractogram of the 1-propanol- γ-CD-IC, which single crystal X-ray diffraction has shown (22) to adopt the channel structure. Clearly

Downloaded by COLUMBIA UNIV on September 17, 2012 | http://pubs.acs.org
Publication Date: July 26, 2001 | doi: 10.1021/bk-2001-0790.ch014

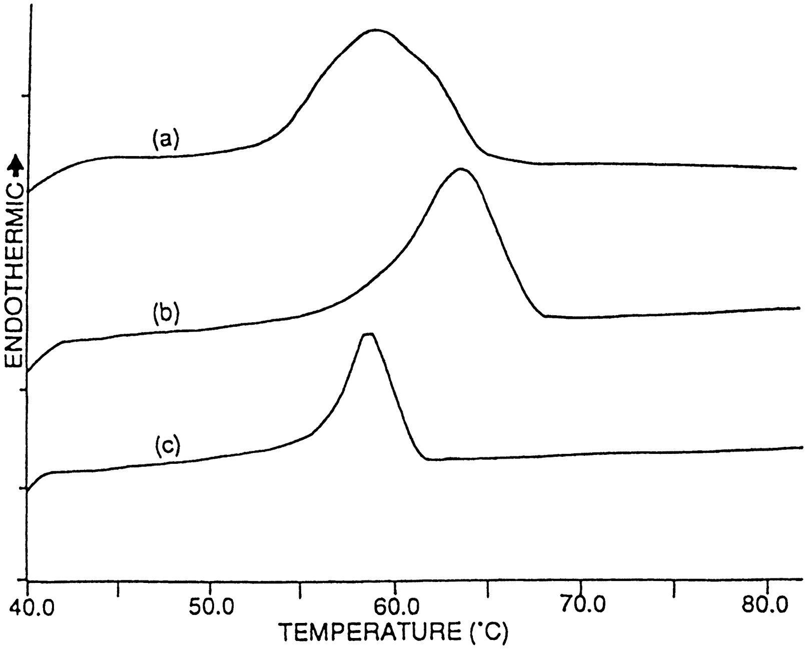

Figure 8. DSC thermograms of PCL: (a) crystallized from solution, (b) coalesced from PCL-U-IC, and (c) crystallized from the melt.

Downloaded by COLUMBIA UNIV on September 17, 2012 | http://pubs.acs.org
Publication Date: July 26, 2001 | doi: 10.1021/bk-2001-0790.ch014

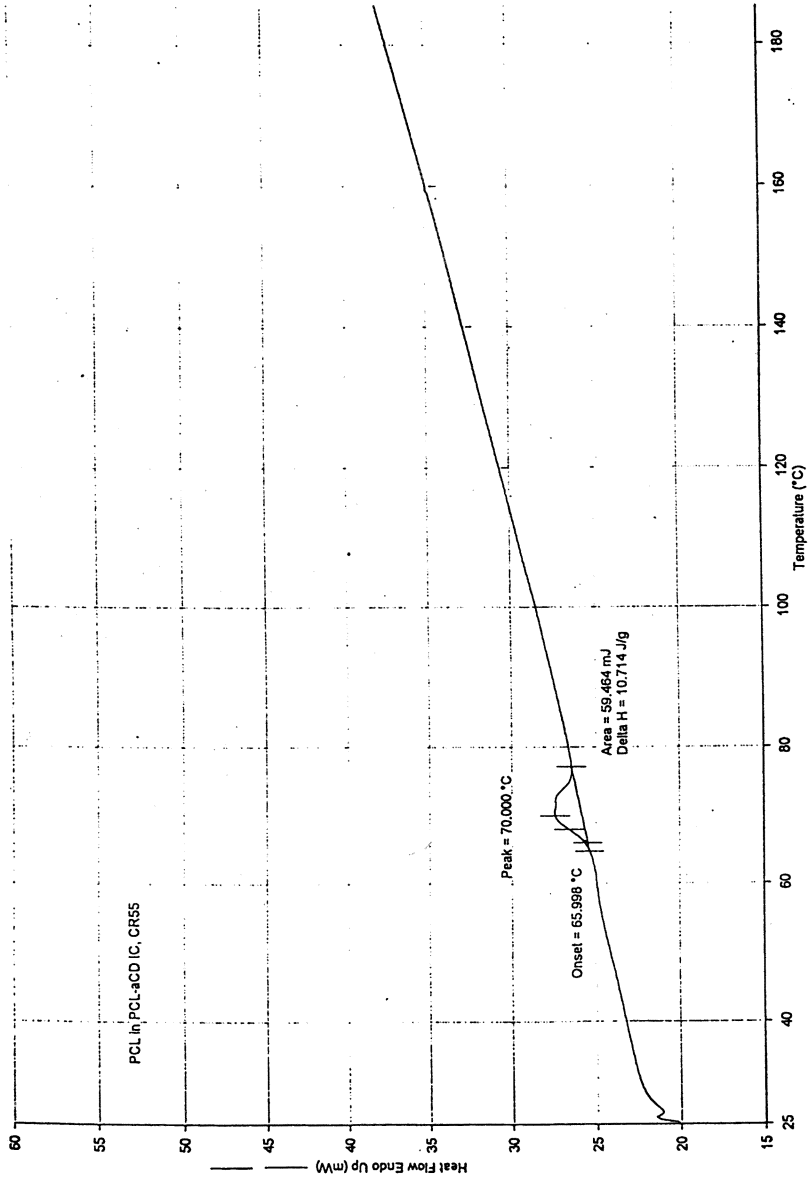

Figure 9. DSC scan of PCL coalesced from PCL-α-CD-IC.

Downloaded by COLUMBIA UNIV on September 17, 2012 | http://pubs.acs.org
Publication Date: July 26, 2001 | doi: 10.1021/bk-2001-0790.ch014

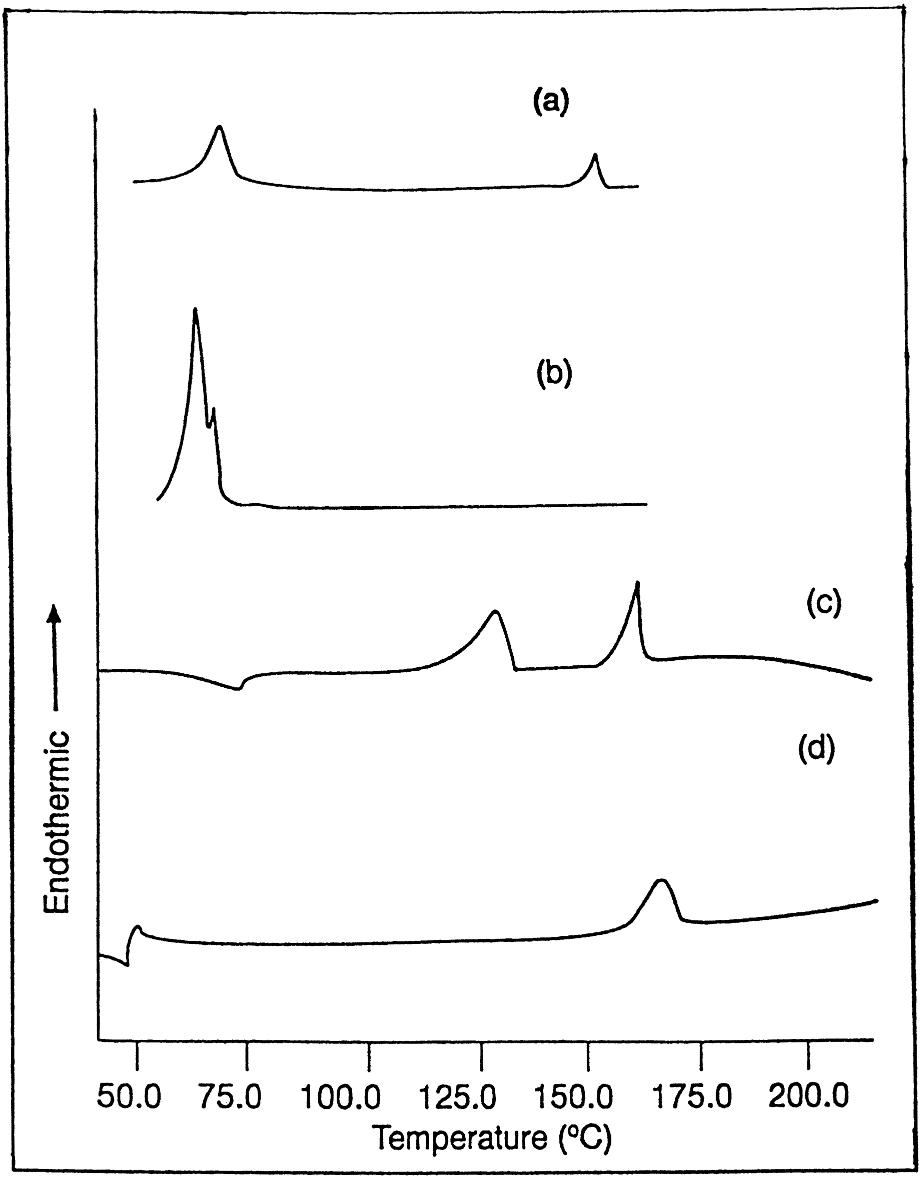

Figure 10. DSC scans of PCL embedded with PCL-U-IC before (a) and after (b) washing in methanol, and DSC scans of PLLA embedded with PCL-U-IC before (c) and after (d) washing in methanol.

Downloaded by COLUMBIA UNIV on September 17, 2012 | http://pubs.acs.org
Publication Date: July 26, 2001 | doi: 10.1021/bk-2001-0790.ch014

Table I Comparison of Thicknesses and Permeabilities of PCL, PCL-Urea, PCL-IC, PLLA, PLLA-Urea, and PLLA-IC Solution-Cast Films Before and After Dipping in Methanol

Sample Name	Average Thickness (mm)	Moisture Vapor Permeability (g/m^2/24 h)
PCL Film	0.022	375
Dipped PCL Film	0.010	440
PCL-Urea Film	0.139	413
Dipped PCL-Urea Film	0.313	747
PCL-IC Film	0.054	418
Dipped PCL-IC Film	0.076	583
PLLA Film	0.024	173
Dipped PLLA Film	0.041	187
PLLA-Urea Film	0.180	207
Dipped PLLA-Urea Film	0.155	540
PLLA-IC Film	0.045	183
Dipped PLLA-IC Film	0.052	236

Downloaded by COLUMBIA UNIV on September 17, 2012 | http://pubs.acs.org
Publication Date: July 26, 2001 | doi: 10.1021/bk-2001-0790.ch014

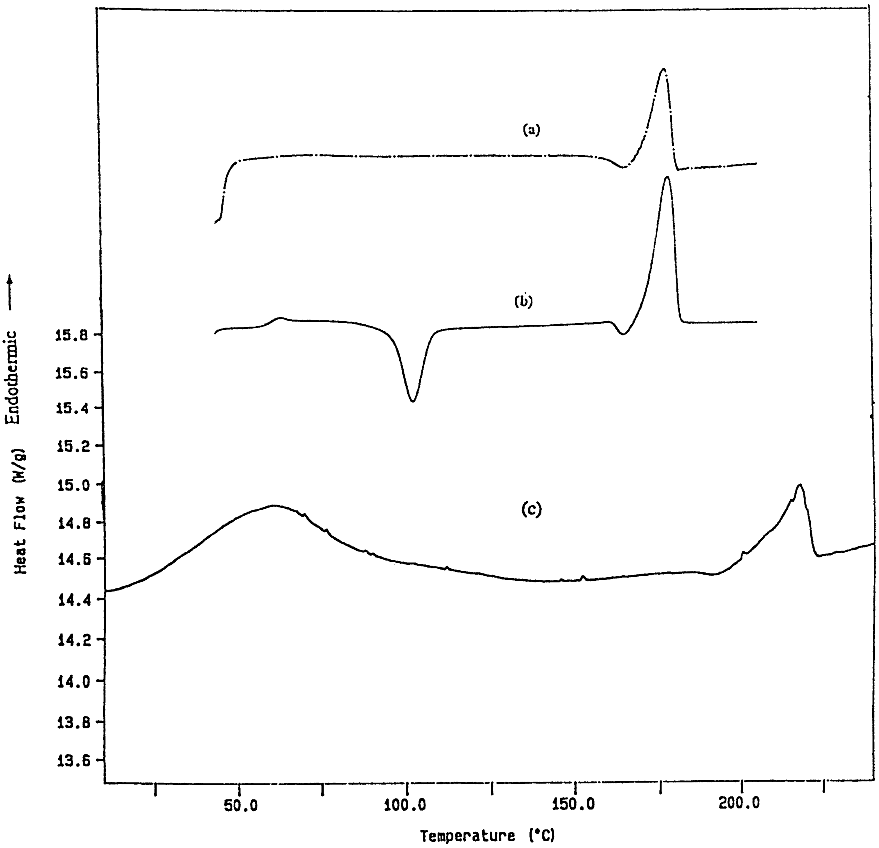

Figure 11. DSC scans of PLLA embedded with PEO-α-CD-IC before (a) and after (b) washing in hot water and DSC scans of nylon-6 embedded with PEO-α-CD-IC after (c) washing with hot water.

Downloaded by COLUMBIA UNIV on September 17, 2012 | http://pubs.acs.org
Publication Date: July 26, 2001 | doi: 10.1021/bk-2001-0790.ch014

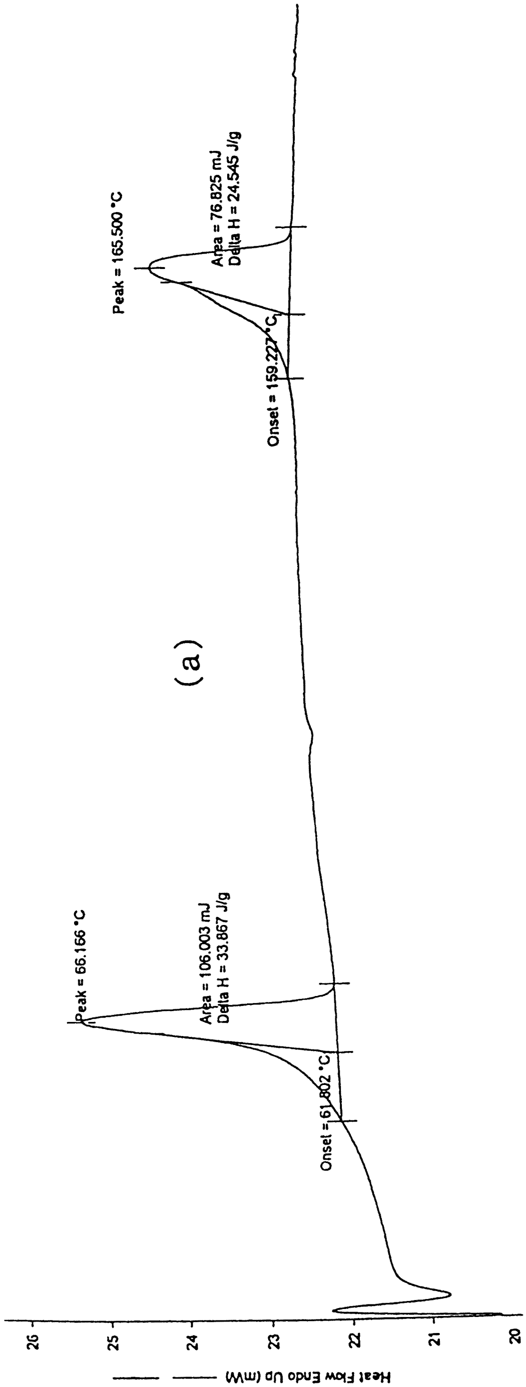

Downloaded by COLUMBIA UNIV on September 17, 2012 | http://pubs.acs.org
Publication Date: July 26, 2001 | doi: 10.1021/bk-2001-0790.ch014

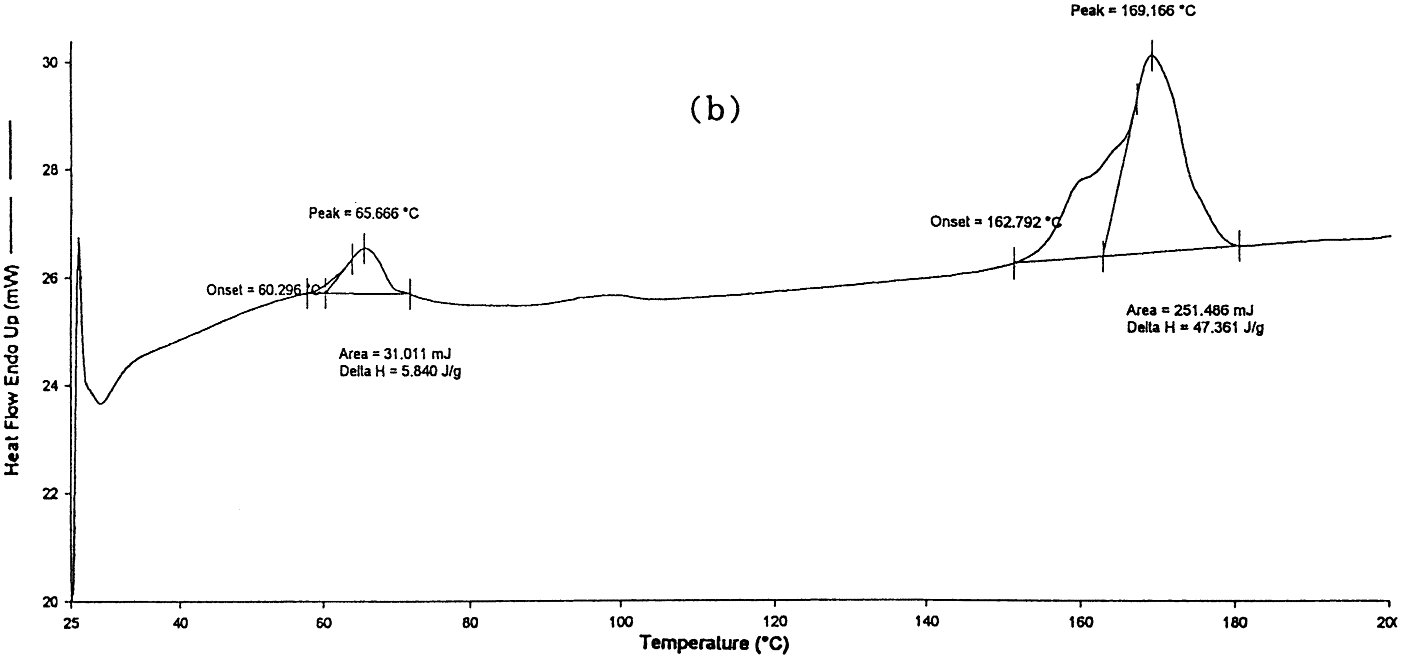

Figure 12. DSC scans of two PCL/PLLA composite films cast from dioxane solution (a) and coalesced from PCL/PLLA-β-CD-IC (b) using hot water.

Downloaded by COLUMBIA UNIV on September 17, 2012 | http://pubs.acs.org
Publication Date: July 26, 2001 | doi: 10.1021/bk-2001-0790.ch014

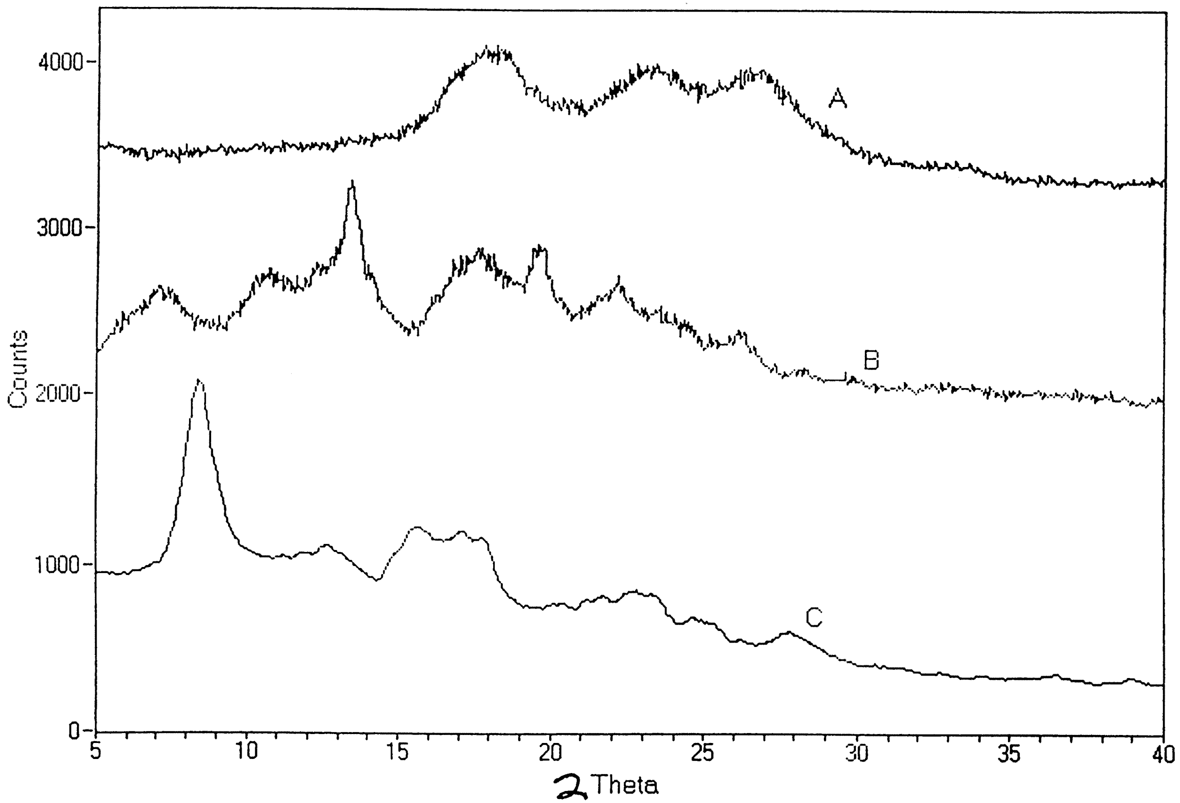

Figure 13. Wide angle X-ray diffractograms of PET (a), γ-CD (b), and PET-γ-CD-IC (c).

In Film Formation in Coatings; Provder, T., et al.;
ACS Symposium Series; American Chemical Society: Washington, DC, 2001.

Downloaded by COLUMBIA UNIV on September 17, 2012 | http://pubs.acs.org
Publication Date: July 26, 2001 | doi: 10.1021/bk-2001-0790.ch014

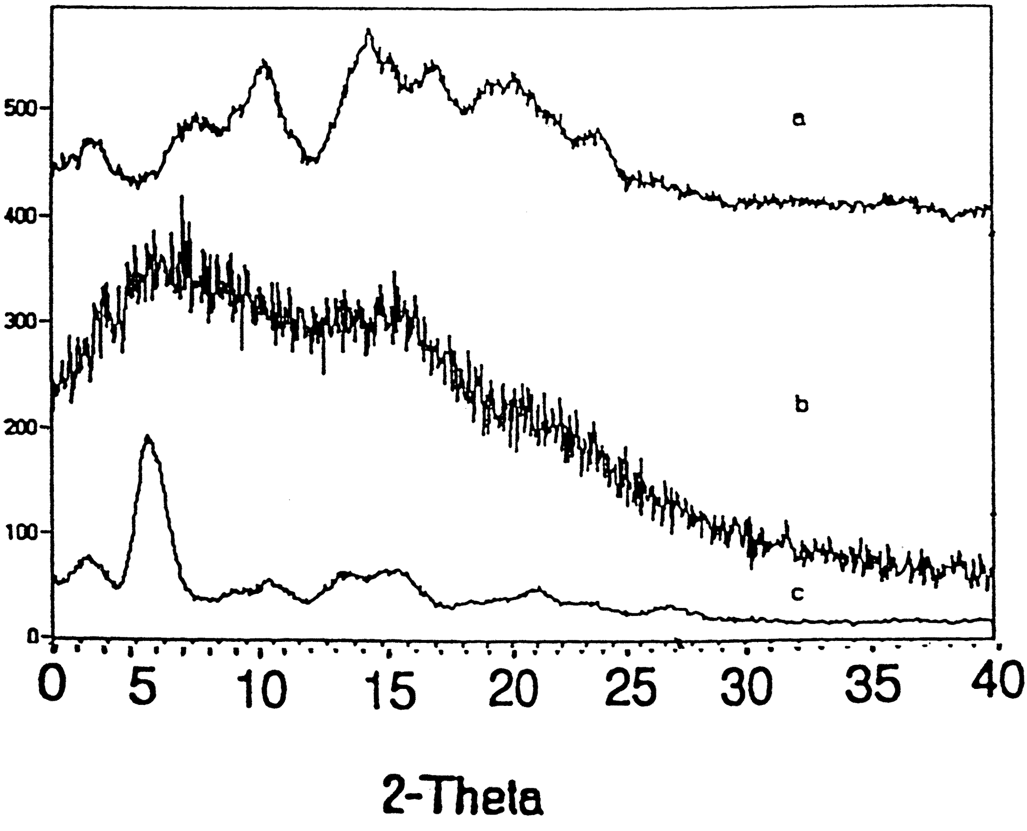

Figure 14. Wide-angle X-ray diffractograms of γ-CD (a), silk-γ-CD-IC (b), and 1-propanol-γ-CD-IC(c).

the γ-CD-IC formed with a silk fibroin solution in $CH_3OH/Ca(NO_3)_2$(23) is also quite suggestive that at least substantial portions of the silk protein chains are included in the narrow channels, ~10Å in diameter, of its γ-CD-IC crystals. In addition to fabricating composite polymer films with either or both PET- and silk-γ-CD-ICs, we are beginning to investigate the behaviors (conformations and motions) of the extended and isolated PET and silk polymer chains occupying the narrow channels of their γ-CD-IC crystals.

Additive ICs:
The three dyes, whose structures are given in Figure 3, were included in ICs formed with both α- and ß-CD (16). Figure 7, for example, presents the wide angle X-ray diffractograms of Dye I, ß-CD, and the Dye I-ß-CD-IC, where it is apparent that the Dye I-ß-CD has a crystal structure distinct from its constituents. When these dye-CD-ICs are embedded in nylon-6 films and then soaked in hot water, the embedded dye-CD-IC is disrupted and the nylon-6 film is eventually dyed from the inside out. Practical considerations aside, this does provide a means for dyeing polymer films and fibers without the necessity of a dye bath, thereby eliminating the environmental concerns attendant with dye bath recovery and/or regeneration. In addition, we may study the diffusion of dyes in polymer films and fibers by observing the migration of dye in these CD-IC-delivered and internally dyed samples, which are free from the usual complications stemming from the dye bath conditions and the interface between the dyebath and the surface of the fiber or film being dyed (23).

Downloaded by COLUMBIA UNIV on September 17, 2012 | http://pubs.acs.org
Publication Date: July 26, 2001 | doi: 10.1021/bk-2001-0790.ch014

The flame retardant (FR) ANTIBLAZE RD-1, whose structure is presented in Figure 5 along with the X-ray diffractogram of its IC with ß-CD in Figure 15, is commercially available as a 40% aqueous solution, which is padded onto cotton-polyester fabric and heated for several minutes at 180°C to provide flame retardancy. Superior flame retardancy may be achieved by embedding small amounts (a few%) of the FR-ß-CD-IC directly into PET films by melt processing (24). PET's hydrophobic nature assures that the embedded FR-ß-CD-IC will not be disrupted during washing, so the FR should be wash- fast unlike PET fabric treated for flame retardancy in the normal manner.

Inclusion compounds have been formed with the two antibacterials shown in Figure 4 and ß-CD (15,17). When the ß-CD-ICs formed with neomycin and trichlosan are embedded in polymer films, such as PC and PLLA, at low levels(< 1% by weight), these films are rendered antibacterial as indicated in Figure 16. Here definite zones of inhibition of E.coli bacterial growth are evidenced in those films embedded with the antibacterial-ß-CD-IC. More recently similar behavior has been observed in fibers of these same polyesters that were spun from their melts containing small amounts of the antibacterial-ß-CD-ICs. Consequently, it would appear feasible to extrude fibers from these biodegradable/bioabsorbable polymers that are also antibacterial, and so obtain sutures that would prevent infections in wounds that they were used to close.

In Figure 17 the structure and X-ray diffractogram of the α-CD-IC of the surfactant/spermicide nonoxynol-9 are presented (25). By comparison to the X-ray

Downloaded by COLUMBIA UNIV on September 17, 2012 | http://pubs.acs.org
Publication Date: July 26, 2001 | doi: 10.1021/bk-2001-0790.ch014

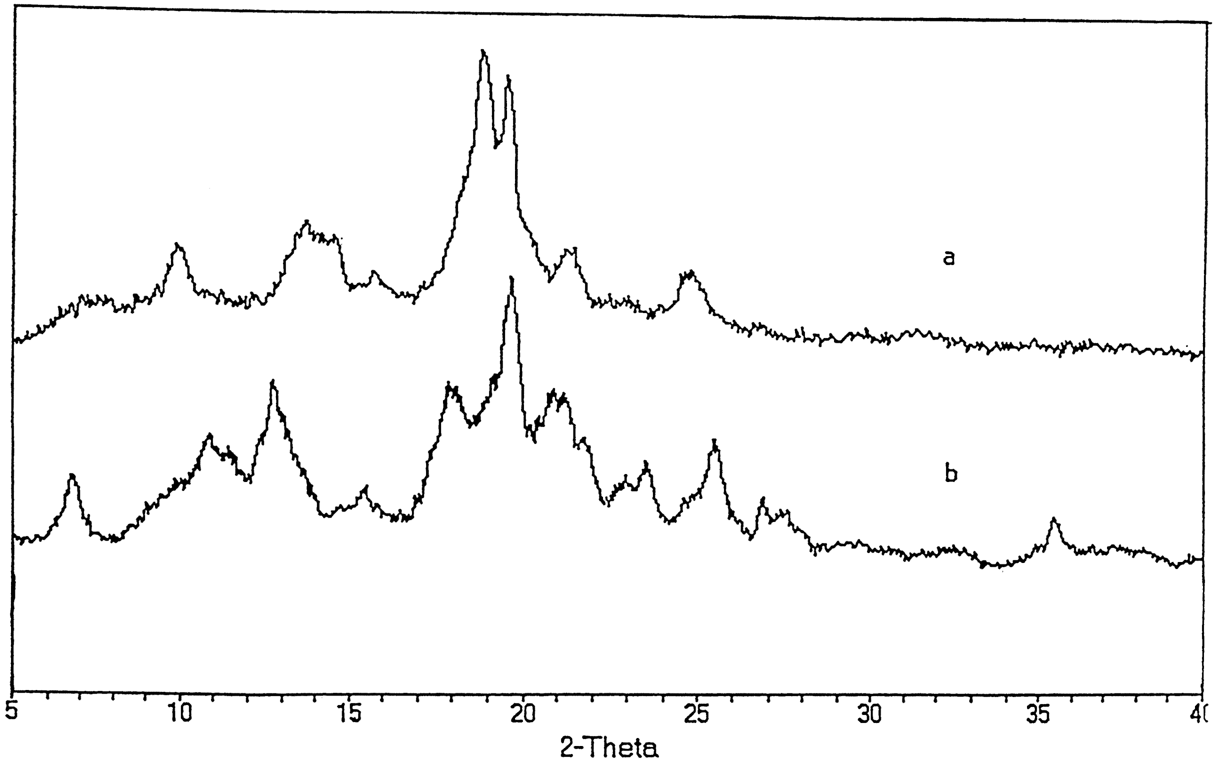

Figure 15. Wide angle X-ray diffractograms of β-CD (a) and FR-β-CD- IC (b).

Downloaded by COLUMBIA UNIV on September 17, 2012 | http://pubs.acs.org
Publication Date: July 26, 2001 | doi: 10.1021/bk-2001-0790.ch014

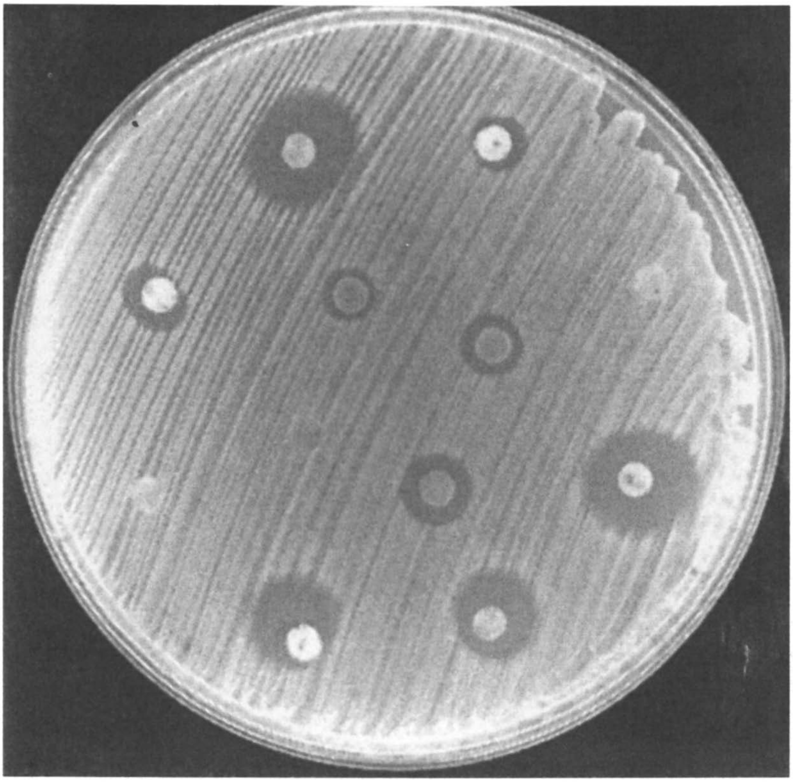

Figure 16. Zones of inhibition of E. coli ***bacterial growth in cultures containing discs cut from PCL and PLLA melt-pressed films embedded with/without 0.01 wt% neomycin or neomycin-ß-CD-IC.***

Downloaded by COLUMBIA UNIV on September 17, 2012 | http://pubs.acs.org
Publication Date: July 26, 2001 | doi: 10.1021/bk-2001-0790.ch014

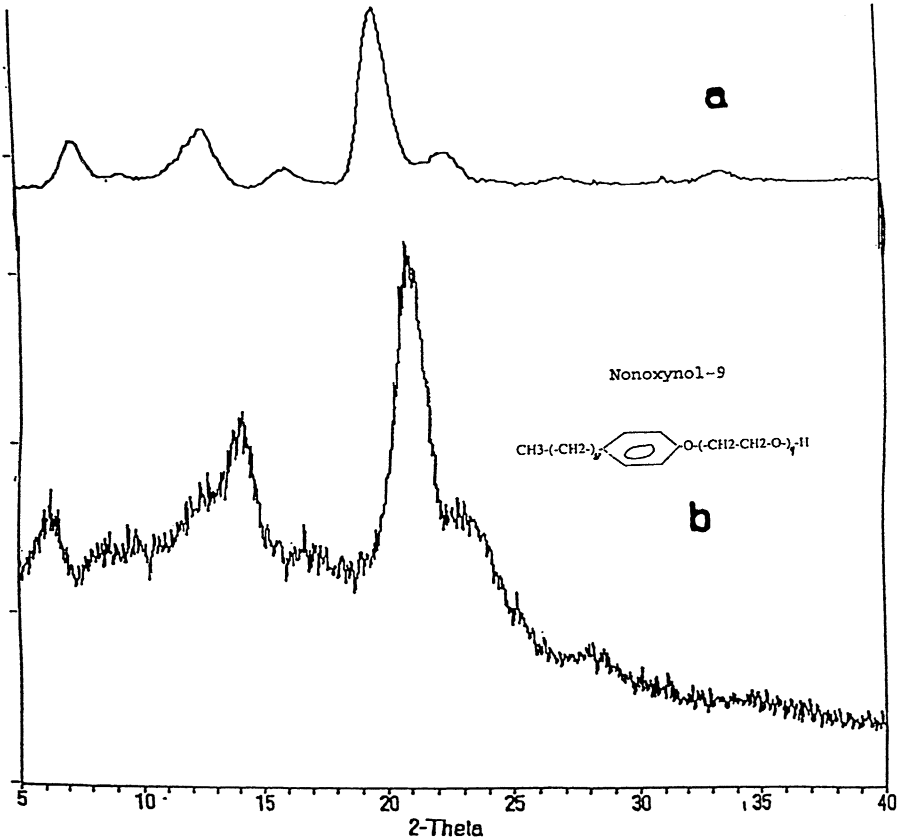

Figure 17. Wide angle X-ray diffractograms of valeric acid-α-CD-IC (a) and nonoxynol-9-α-CD-IC (b).

diffractogram observed for the valeric acid-α-CD-IC (18), it can be concluded that the nonoxynol-9-α-CD-IC is also of the channel variety. It may eventually prove possible to deliver nonoxynol-9 and other surfactants to polymer fibers and films via the embedding of their CD-ICs. This might lead to improvements in the compatibilization of polymer blends, not to mention the possibility of creating spermicidal plastics.

Conclusions

We have described the formation and use of several polymer- and additive-ICs, with emphasis placed on the thermally stable ICs formed with CDs as the host. Creation of polymer films with novel structures and properties has been achieved by embedding these polymer- and additive-CD-ICs into carrier polymers during the melt processing of their films. In addition it was shown possible to create model polymer films containing either more than one polymer or additive which facilitate the investigation of behaviors, such as permeability, diffusivity, and phase separation, that are fundamental to their properties.

Downloaded by COLUMBIA UNIV on September 17, 2012 | http://pubs.acs.org
Publication Date: July 26, 2001 | doi: 10.1021/bk-2001-0790.ch014

References

1. L.C. Fetterly in "Non-Stoichiometric Compounds," L. Mandelcorn, Ed., Academic Press, New York,1965, Ch. 8.
2. M. Farina in "Proceedings of the International Symposium on Macromolecules, Rio de Janeiro, 1974," E. B. Mano, Ed., Elsevier, New York, 1975, p.21.
3. M. Farina in "Inclusion Compounds," J.L. Atwood et al., Eds., Vol. 2, Academic Press, New York 1984, p. 69 and 297.
4. G. DiSilvestro and P. Sozzani in "Comprehensive Polymer Science," G.C. Eastman et al., Eds., Vol. 4, Pergamon, Oxford, England, 1988, Ch. 18.
5. L. Huang and A.E. Tonelli, J. Macromol. Sci., Rev. Macromol. Chem. Phys., *C38(4)*, 781, 1998.
6. N. Vasanthan, I.D. Shin, and A.E. Tonelli, Macromolecules, *27*, 6515, 1994.
7. C.C. Rusa and A.E. Tonelli, Macromolecules, *33*, 1813, 2000.
8. Y Chatani and S. Kuwata, Macromolecules, *8*, 12, 1975.
9. P. Sozzani, F.A. Bovey, and F.C. Schilling, Macromolecules, *22*, 4225, 1989.
10. K.D.M. Harris and P. Joneson, Chem. Phys. Lett., *154*, 593, 1989.
11. C. Choi, D.D. Davis, and A.E. Tonelli, Macromolecules, *26*, 1468, 1993.
12. L. Huang, E. Allen, and A.E. Tonelli, Polymer, *39*, 4857, 1998.
13. L. Huang, E. Allen, and A.E. Tonelli, Polymer, *40*, 3211, 1999.
14. T. A. Bullions, M. Wei, F. E. Porbeni, M. J. Gerber, J. Peet, M. Balik, and A. E. Tonelli, Macromolecules, submitted, 2001.
15. L. Huang, H. Taylor, M. Gerber, P.E. Orndorff, J.R. Horton, and A.E.Tonelli, J. Appl. Polm. Sci., *74*, 937, 1999.
16. L. Huang, PhD Dissertation, North Carolina State University, 1998.
17. J. Lu, M. Hill, M. Hood, D. F. Greeson, Jr., J. R. Horton, P. E. Orndorff, and A. E. Tonelli, J. Appl. Polym. Sci., *XX*, YYYY, 2001.
18. R. K. McMullan, W. Saenger, J. Fayos, and D. Mootz, Carbohydr. Res., *31*, 37, 1973.
19. L. Huang, N. Vasanthan, and A.E. Tonelli, J Appl. Polym. Sci., *64*,281, 1997.

20. L. Huang and A.E. Tonelli, in "Intelligent Materials for Controlled Release," S.M. Dinh, J.D. DeNuzzio, and A.R. Comfort, Eds., Amer. Chem. Soc. Symp. Ser. # *728*, Washington, D.C., 1999, Ch.
10, p. 131.

21. M. A. Hill, J. Lu, J. Pittman, and A. E. Tonelli, in preparation.

22. M. J. Gidley and S.M. Bociek, J. Am. Chem. Soc, *110*, 3820, 1988.

23. Y. Song, M. Srinivasarao, A. E. Tonelli, M. Balik and R. McGregor, Macromolecules, *33*, 4478, 2000.

24. L. Huang, M. J. Gerber, J. Lu, and A. E. Tonelli, Polym. Degrad. & Stabil., *71*, 279, 2001.

25. C. C. Rusa, J. Lu, and A. E. Tonelli, in preparation.

Downloaded by COLUMBIA UNIV on September 17, 2012 | http://pubs.acs.org
Publication Date: July 26, 2001 | doi: 10.1021/bk-2001-0790.ch014

Downloaded by 89.163.34.136 on September 17, 2012 | http://pubs.acs.org
Publication Date: July 26, 2001 | doi: 10.1021/bk-2001-0790.ix001

Author Index

Charleux, B., 157
Daniels, Eric S., 212
Davis, H. T., 174
Dewhurst, John E. , 124
Dimonie, Victoria L., 212
Donald, Athene M., 193
Drayton-Elder, Ava S., 124
Edeki, E., 246
El-Aasser, Mohamed S., 212
Gao, Xiaoping, 124
Gerber, M., 246
Geurts, J. L., 58
Harvey, A., 246
Hearn, John, 233
Hill, Loren W., 104
Hill, M., 246
Hodges, Ian C., 233
Hoipkemeier, L., 141
Holl, Y., 2
Huang, L., 246
Keddie, J. L., 2, 58
Klein, Andrew, 212
Kranbuehl, D., 141
Loyen, K., 157
Lu, J., 246
Ma, Yue, 174
McDonald, P. J., 2
Meyer, A., 141
Mulder, M., 58
Nikolic, N., 141
Nunalee, F. N., 246
Pekurovsky, L. A., 27
Pham, Hung H., 88
Porbeni, F., 246
Rogozinski, J., 141
Royall, C. Patrick, 193
Rusa, C. C., 246
Santosusso, Thomas M., 124
Satguru, R., 58
Scriven, L. E., 27, 174
Soares, C., 157
Sutanto, Erwin, 174
Tang, Jiansheng, 212
Tapaszi, E., 246
Taylor, H., 246
Tien, Chao-fong, 124
Tonelli, A. E., 246
Treacher, E., 58
Tzitzinou, A., 58
Urban, Marek W., 41
Vairon, J.-P., 157
Vergé, C., 157
Wickmann, Tracy L., 124
Wilkinson, Michael C., 233
Winnik, Mitchell A., 88
Winnik, W. A., 2
Wutkowski, M., 246
Zhao, Yaqiu, 41

Subject Index

A

Acetal functionalized latex films
  acetal monomer, methacrylamido acetaldehyde dimethyl acetal (MAAMA), 158
  acidification of latex serum for acetal hydrolysis and crosslink formation, 170
  apparent rate constant of hydrolysis as function of pH, 168*f*
  characterization of latices, 161*t*
  chemical aspect of crosslinks formation, 167–170
  effect of MAAMA content on tensile properties for poly(methyl methacrylate-*co*-*n*-butylacrylate-*co*-MAAMA) [poly(MMA-*co*-BA-*co*-MAAMA)] films formed at pH=2, 166*f*
  effect of pH, 165
  effect of pH on tensile properties of poly(MMA-*co*-BA-*co*-MAAMA) films, 166*f*
  emulsion polymerization of monomers BA, MMA, and MAAMA, 159
  evolution of gel content and swelling ratio, 164–165
  experimental conditions for latex synthesis, 160*t*
  film formation and characterization, 159–160
  gel content and swelling ratio after 35 days for films at pH=2 and pH=8 as function of MAAMA concentration, 163*t*
  gel content and swelling ratio as function of initial pH for films, 165*f*
  gel content and swelling ratio as function of time, 164*f*
  hydrolysis of acetal groups at room temperature and different pH values, 169*f*
  incorporating reactive functions randomly into polymer chains, 161–162
  kinetics of hydrolysis at room temperature of model of MAAMA in D_2O at different pH, 168*f*
  latex and copolymer characterization, 160–162
  MAAMA synthesis, 158–159
  mechanical properties, 165–166
  proton NMR spectrum of poly(MMA-*co*-BA-*co*-MAAMA) copolymer, 162*f*
  simulating film formation conditions and allowing slow solvent evaporation, 169
  sodium hydrogen carbonate buffer, 159
  stability of functional group during and after polymerization, 162
  strong effect of pH on crosslink formation rate, 170
  swelling properties of films, 163–165
  synthesis and characterization of latex, 159
Acrylamidobutyraldehyde dialkyl acetal, promoting crosslinking, 158
Acrylic polyols, binders for thermoset coatings, 111
Additive leaching. *See* Porosity in polymer latex films

Downloaded by 89.163.34.136 on September 17, 2012 | http://pubs.acs.org
Publication Date: July 26, 2001 | doi: 10.1021/bk-2001-0790.ix002

In Film Formation in Coatings; Provder, T., et al.;
ACS Symposium Series; American Chemical Society: Washington, DC, 2001.

Downloaded by 89.163.34.136 on September 17, 2012 | http://pubs.acs.org
Publication Date: July 26, 2001 | doi: 10.1021/bk-2001-0790.ix002

Additives, infrared imaging to determine chemical heterogeneity, 54
Adura™ polyol technology
  log-log plot for capacitance versus time, 135*f*
  materials, 125
  preparation and performance, 126–127
  water evaporation versus time, 132, 133*f*
  See also Polyurethane, two component waterborne
Amount of dryness, user of paint judging, 4
Anthracene
  labeling to study diffusion and miscibility, 93
  See also Carbodiimide- and carboxylic acid-functional latex, blends
Antibacterials
  inclusion compounds, 266, 268*f*
  See also Inclusion compounds (ICs)
Atomic force microscopy (AFM)
  AFM images indicating dome-shaped surfactant features at polymer/air interface of low-MW acrylic latex film (20°C above MFT), 80*f*
  AFM images of polymer/air interface of film from very low MW latex dispersion (5°C above minimum film-formation temperature (MFT)), 77*f*
  AFM images of polymer/air interface of film from low MW latex dispersion, 77*f*
  AFM images of polymer/air interface of film from low MW latex dispersion at 15°C above MFT, 79*f*
  method, studying molecular weight effects on film formation, 61
  ordering in center of laterally drying latices, 18
  pattern of morphologies, 78
  surface morphology and concentration at latex air surface, 76–78
  surfactant at poly(butyl methacrylate) surface after drying, 10
Attenuated total reflectance (ATR)
  allowing surface depth profiling through use of Urban–Huang step-wise approach, 43
  determining surface content changes at interface as function of exposure temperature, 51–52
  distribution of sodium dioctylsulfosuccinate (SDOSS) and interactions across copolymer latex film thickness, 53
  Fourier transform infrared (FT–IR) technique, 42–43
  micro-analysis to determine composition of aggregates, 48–49
  monitoring method for waterborne polyurethanes, 126
  schematic of experiment, 43*f*
  studying under the surface, 53
  water evaporation and chemical composition in polyurethane films, 134–135
  See also Polyurethane, two component waterborne

B

Barrier properties
  well-ordered particles, 233–234
  See also Porosity in polymer latex films
Blend latex films, optical images from film–additive interfaces, 48–49
Blends. *See* Carbodiimide- and carboxylic acid-functional latex, blends; Latex blends, model carboxylated
Blocking effect, conductance measurements for aqueous system, 131

Downloaded by 89.163.34.136 on September 17, 2012 | http://pubs.acs.org
Publication Date: July 26, 2001 | doi: 10.1021/bk-2001-0790.ix002

Boundary, separating dry portion from wet dispersion, 10
Branching
  slowing rate of polymer diffusion, 89–90
  See also Carbodiimide- and carboxylic acid-functional latex, blends
Breathable paint, exceeding critical pigment volume fraction (CPVF), 234
Butadiene, crosslinking by, in latex films, 118, 121
n-Butylacrylate (BA)
  emulsion polymerization with methyl methacrylate (MMA) and methacrylamido acetaldehyde dimethyl acetal (MAAMA), 159
  See also Acetal functionalized latex films

C

Capacitance
  circuit model for waterborne coatings, 131
  dielectric spectroscopy, 130
  frequency dependent dielectric measurement, 143
  interfacial, monitoring water evaporation process, 131
Capillarity, net force of
  moist stage, 33–34
  sphere, 31
  wet stage, 32–33
Capillary pressure
  forces on partly wetted particles, 30*f*
  Laplace pressure, 27
  lateral drying, 14–15
  process of drying latex coating, 27–28
Carbodiimide- and carboxylic acid-functional latex, blends
  carbodiimide- and methacrylic acid (MAA)-containing PEHMA particle preparations, 90
  characterization of labeled poly(2-ethylhexyl methacrylate) (PEHMA) latex, 94, 95*t*
  characterizing diffusion in terms of fraction of mixing, f_m, 92
  chemical reaction necessary for full mixing, 101
  definition of quantum efficiency of energy transfer, ϕ_{ET}, 91–92
  D-MAA-11 + A-tBCEMA-5, 98–99
  D-MAA-11 + A-tBCEMA-5 and A-CCEMA-4.6, 99, 101
  D-MAA-11 and D-MAA-20 + PEHMA-A, 96–98
  energy transfer (ET) experiments, 91–92
  experimental, 90–93
  film preparation method, 90–91
  Fourier transform infrared (FTIR) experiments, 92–93
  latex synthesis, 90
  miscibility of PEHMA copolymers, 94, 96
  packaging reactive groups into separate latex particles, 89
  PEHMA-D + A-tBCEMA-5, 96
  PEHMA-D + PEHMA-A, 96
  percentage carbodiimide remaining under various polymerization conditions, 95*t*
  phenanthrene and anthracene as dyes to study miscibility and diffusion, 93
  plot of ϕ_{ET} vs. annealing time at 60°C for blends of D-MAA-11 + A-tBCEMA-5, 98*f*
  plots of f_m and fraction carbodiimide remaining vs. annealing time at 60°C for three latex films, 100*f*
  plots of ϕ_{ET} vs. annealing time for four pairs of latex films, 97*f*
  polymer diffusion for reaction, 89–90, 93
  polymer interdiffusion vs.

    crosslinking, 99
  stability of –N=C=N– functionality, 93–94
  typical recipes for labeled latex particles, 91*t*
Carbodiimide-functional latex
  requirements to be useful in coatings applications, 93
  stability of functionality, 93–94
  See also Carbodiimide- and carboxylic acid-functional latex, blends
Carboxyl groups. *See* Latex blends, model carboxylated
Carboxylic acid-functional latex. *See* Carbodiimide- and carboxylic acid-functional latex, blends
Coalescence, sequential, and crosslinking in latex films, 121
Coalescence front
  associating collapse with passing of, through the spot irradiated, 8
  latex film formation, 59
Coalescence temperature (T_c)
  sodium dioctylsulfosuccinate (SDOSS) volume concentration as function of T_c for blended latex, 52*f*
  surfactant mobility, 50–51
Coatings, environmentally compliant, goals, 41–42
Coatings manufacturers, environmental and health regulations, 2
Coffee stain, lateral water flux during drying, 10
Colloidal crystal formation, drying, 22
Compaction front, wet side of drying boundary, 12
Conductance
  calculating bulk, 132, 133*f*
  dielectric spectroscopy, 130
  frequency dependent dielectric measurement, 143
  general relation between conductance and viscosity, 144
Confocal microscopy
  bulk silica occupancy as function of m_{sil}/m_o value, 205, 209*f*
  images of increasing silica concentration, 206*f*, 207*f*
  laser source to improve resolution, 196–197
  principle, 196
  resolution, 196–197
  revealing silica particles, 203
  schematic, 196*f*
  See also Matting water-based lacquers
Consolidation fronts
  edge and descending, 175, 190
  See also Cryogenic scanning electron microscopy (cryo–SEM)
Constant angle model, lateral drying, 13
Constant base model, lateral drying, 13
Contact-line pinning, lateral drying shape model, 13
Copolymers
  distribution of tackifier in, by infrared imaging, 54, 55*f*
  latex, and blends, 48–49
  surfactant-copolymer interactions, 45, 47
Critical pigment volume fraction (CPVF)
  exceeding for breathable paint, 234
  macroreticular colloid particles, 242–243
  See also Porosity in polymer latex films
Croll, two-stage drying model, 7
Crosslinking
  acetal-bearing monomers, 158
  butadiene in latex films, 118, 121
  crosslink density determinations by dynamic mechanical analysis (DMA) in thermoset films, 112
  DMA to confirm, in latex films, 121

Downloaded by 89.163.34.136 on September 17, 2012 | http://pubs.acs.org
Publication Date: July 26, 2001 | doi: 10.1021/bk-2001-0790.ix002

improving film properties, 88–89
incorporating reactive groups into latex particles, 157–158
monitoring carboxylic acid and carbodiimide reaction with Fourier transform infrared (FTIR), 92–93
polymer interdiffusion versus, 99
swelling properties of films containing methacrylamido acetaldehyde dimethyl acetal (MAAMA), 163–165
tough elastomeric films, 89
See also Acetal functionalized latex films; Carbodiimide- and carboxylic acid-functional latex, blends

Cryogenic scanning electron microscopy (cryo–SEM)
close-packed polystyrene (PS) particles passing through consolidation front, 180
confirming edge and descending consolidation fronts, 190
consolidation fronts, 175
cryo–SEM method for latex coatings, 176–177
descending consolidation front, 175
dry-out front receding from top to substrate, 175
edge consolidation front, 175, 177, 180
edge consolidation front of 10 wt% deionized PS latex suspension after 1 minute drying, 179*f*
edge consolidation front of 10 wt% PS latex suspension after 3 minutes drying, 178*f*
examining PS and poly(butyl methacrylate) (PBMA) particles during drying, 20
fracture surface away from edges of fast-frozen deionized PS latex coating (6 minutes drying), 186, 187*f*
fracture surfaces of 10 wt% PS latex film, 177, 180
growth of clusters on air-water interface at 1 minute drying of 10 wt% PS latex suspension, 182, 183*f*
indication of skin formation about film formation, 175
maintaining same drying rate, 186
materials and methods, 176–177
mechanisms of water loss differing during drying, 182, 186
particle distribution in middle of coating during drying, 180, 182, 186, 190
PBMA latex particle away from edges showing crystals, 190, 191*f*
PS and PBMA latex suspensions, 176
recipe and reaction conditions for emulsion polymerization of PS and PBMA, 176*t*
room temperature SEM image of edge of dried PS latex coating (not deionized), 180, 181*f*
SEM micrographs of PBMA latex coatings showing descending consolidation front, 186, 188*f*, 189*f*, 190
studying evolution of microstructure during drying and rehydration, 174
successive layers of highly ordered PS particles forming at moving consolidation front, 182, 184*f*, 185*f*, 186

Crystalline inclusion compounds. *See* Inclusion compounds (ICs)

Cure. *See* Epoxy systems

Cyclodextrins (CDs)
host for inclusion compounds, 247
See also Inclusion compounds (ICs)

Downloaded by 89.163.34.136 on September 17, 2012 | http://pubs.acs.org
Publication Date: July 26, 2001 | doi: 10.1021/bk-2001-0790.ix002

D

Datum contact force
  acting on particles, 31
  net elastic reaction force, 32
Descending consolidation front
  cryogenic scanning electron microscopy (cryo–SEM) micrographs confirming, 190
  SEM micrographs of poly(butyl methacrylate) (PBMA) showing, 186, 188*f*, 189*f*, 190
  successive layers of highly ordered polystyrene (PS) particles forming at moving consolidation front, 182, 184*f*, 185*f*, 186
  See also Cryogenic scanning electron microscopy (cryo–SEM); Poly(butyl methacrylate) (PBMA); Polystyrene (PS)
Dielectric spectroscopy
  calculating bulk conductance, 132, 133*f*
  circuit model of dielectric sensor, 131, 132*f*
  measurement method, 125–126
  measuring changes in conductance and capacitance simultaneously, 130
  network formation, beginning for polyurethanes, 137
  nondestructive technique and sensitivity, 125
  relation of dielectric properties to changes in macroscopic performance properties, 144–145
  See also Frequency dependent electrical measurement sensor (FDEMS); Polyurethane, two component waterborne
Diffusion
  drying normal to surface, 5
  three stage drying process model, 6–7
  water molecules through continuous polymer phase, 4
  See also Carbodiimide- and carboxylic acid-functional latex, blends
Dipolar mobility, measurement theory, 144
Disorder-to-order transition, film formation, 3
Dowfax 2A1 (SDED)
  leaching SDED to produce porous films, 237, 239
  total pore volume of SDED/poly(butyl methacrylate), 240*f*
  See also Porous latex films
Drying front
  latex film formation, 59
  See also Cryogenic scanning electron microscopy (cryo–SEM)
Drying modes
  accumulation of sulfate ions in center of film along interface with substrate following mixed, 20*f*
  atomic force microscopy (AFM) for ordering in laterally drying latices, 18
  classical models for normal drying, 5–7
  cryogenic scanning electron microscopy (cryo–SEM) examining polystyrene and poly(butyl methacrylate) latex particles during drying, 20
  diffusion according to Stokes–Einstein equation, 21
  distinguishing three distinct, 4–5
  drying normal to latex dispersion surface, 4
  drying normal to surface, 5–7
  global rate of water loss, 23–24
  homogeneous drying, 4
  importance, 3–4
  lateral drying, 4–5, 8–16

Downloaded by 89.163.34.136 on September 17, 2012 | http://pubs.acs.org
Publication Date: July 26, 2001 | doi: 10.1021/bk-2001-0790.ix002

Downloaded by 89.163.34.136 on September 17, 2012 | http://pubs.acs.org
Publication Date: July 26, 2001 | doi: 10.1021/bk-2001-0790.ix002

  mixed, 16, 18–20
  monitoring turbidity and weight loss, 18
  normal and lateral, occurring simultaneously, 18*f*
  optical micrograph and schematic of unstable acrylic latex dispersion drying on glass plate, 19*f*
  parameters controlling normal versus lateral, 20–24
  polymer particle viscoelasticity, 23
  predicting if drying should be normal to surface, 21
  Routh and Russel gauge for vertical homogeneity during drying, 21, 24
  schematic of normal and lateral drying, 6*f*
  structure and rheology of dispersion, 22–23
  thickness and geometric effects, 21–22
  transport of water in latex dispersion, 4
  water soluble species accumulating in center at film-substrate interface, 20
  water transport in latex dispersion, 4
  See also Lateral drying; Normal drying
Drying normal to latex dispersion surface
  top of latex coating drier than bottom, 4
  See also Normal drying
Dyes
  inclusion compounds, 266
  See also Fluorescent dyes; Inclusion compounds (ICs)
Dynamic adsorption
  barrier characteristics of films, 234
  profiles for plain BPL, non-porous latex coated, and porous latex coated carbon samples, 243–244
  See also Porosity in polymer latex films
Dynamic mechanical analysis (DMA)
  combination with other methods, 121
  crosslinking by butadiene in latex films, 118, 121
  determination of extent of cure for thermoset formulations, 107–110
  determining crosslink density in films, 121
  DMA plots for unpigmented coating from aqueous polyurethane dispersion, 113*f*
  DMA plots for unpigmented, highly crosslinked coating, 108*f*
  film morphology, 121
  films from aqueous polyurethane dispersions, 112–114
  films from latex with carboxyl groups in shell, 115, 118
  films from water reducible binders, 111–112
  following property development during cure, 110–111
  hard/soft latex blends, 114–115
  loss, 105
  loss tangent, 105, 107
  methods and definitions, 104–107
  modulus definitions with shear deformation, 107
  modulus definitions with tensile deformation, 105, 107
  phase lag, 105
  relationship between tensile and shear depending on Poisson's ratio, 107
  relationships between strain, stress, and time, 106*f*
  sequential coalescence and crosslinking, 121
  shear loss modulus, 107
  shear storage modulus, 107
  sine wave plot of applied strain in DMA, 106*f*
  storage, 105
  study of film formation from waterborne latices, 114–121
  tensile loss modulus, 105
  tensile storage modulus, 105

See also Waterborne systems

E

Edge consolidation front
  cryo–SEM micrographs confirming, 190
  See also Cryogenic scanning electron microscopy (cryo–SEM); Polystyrene (PS)
Effective medium approximation (EMA) model, fraction of voids in latex film, 62
Elastic contact force
  acting on particles, 31
  net elastic reaction force, 32
Ellipsometry
  comparing film formation of very-low, low, and medium MW latices, 72, 74*f*
  comparing pseudo-refractive index, <n>, for films from very-low and high MW latices, 72, 75*f*, 76
  dynamic evolution of real component of <n> from very low MW latex films at 5°C, 10°C, and 20°C above minimum film-formation temperature (MFT), 71*f*
  dynamic measurements of film formation, 68, 72, 76
  effect of molecular weight on surface roughness and void content, 66
  effect of surface roughness on ellipsometric angles form simulation of angular scan, 62, 64*f*
  effect of voids on ellipsometric angles, 62, 65*f*
  ellipticity equation, 60
  measurements of surface roughness and void volume fraction by fitting data to model, 66, 67*f*
  <n> and pseudo-extinction coefficient (<k>) dynamic data for low MW latex at three temperatures, 72, 73*f*
  pseudo-extinction coefficient (<k>), 72
  pseudo-refractive index, <N>, from ellipticity, 68
  schematic of model, 63*f*
  surface roughness and void concentration as function of film formation temperature above MFT, 69*f*, 70*f*
  typical dynamic scan of film from low molecular weight latex dispersion (10°C above MFT), 71*f*
  variable-angle method, 60–61
  void content and surface roughness films, 62, 66
Ellipticity, equation, 60
Energy transfer (ET)
  characterizing diffusion in terms of fraction of mixing, f_m, 92
  experiments to characterize miscibility of poly(2-ethylhexyl methacrylate) (PEHMA) copolymers, 91–92
  film preparation for ET experiments, 90–91
  See also Carbodiimide- and carboxylic acid-functional latex, blends
Environmentally compliant polymeric coatings
  goals, 41–42
  latex blending, 212–213
Environmental regulations, waterborne colloidal dispersions of polymers, 2
Environmental scanning electron microscopy (ESEM)
  background, 194–196
  backscattered electrons, 195–196
  image contrast, 195
  images of increasing silica concentration, 203, 204*f*
  signal amplification, 195*f*
  surface silica occupancy as function of m_{sil}/m_o value, 205, 208*f*
  surface technique, 194

Downloaded by 89.163.34.136 on September 17, 2012 | http://pubs.acs.org
Publication Date: July 26, 2001 | doi: 10.1021/bk-2001-0790.ix002

- *See also* Matting water-based lacquers

Epoxy systems
- changing value of log (ε"*ω) with time of commercial epoxy-amine coating, 146*f*
- cure of thick coating using standard 5 Joule 5 second pulse, 150, 152*f*
- dielectric analysis (DEA) studying curing solvent-borne, 130–131
- frequency dependent electrical measurement sensor (FDEMS) to monitor and compare cure properties of three different formulations, 152*f*, 153*f*, 154*f*, 155*f*
- on-line monitoring of curing epoxy-amine coating, 145, 147
- on-line monitoring rapid cure, 147, 150
- output of 10 second UV pulse of 40 Joules, 150, 151*f*
- output of FDEMS sensor monitoring UV cure of rapid cure epoxy coating, 148*f*, 149*f*
- sensitivity of FDEMS signal to cure completion, 150, 151*f*
- *See also* Frequency dependent electrical measurement sensor (FDEMS)

Ethyl acrylate/methacrylic acid (EA/MAA) latices
- effect of substrate surface tension, 47
- surfactant-copolymer interactions, 45, 47
- surfactant stratification in, 48*f*

Ethyl acrylate/methacrylic acid (Eudragit® L30D)
- comparison of pore radius profiles for films leached of L30D under freeze or nitrogen drying, 241–242, 243*f*
- leaching experiments in poly(butyl methacrylate) (PBMA), 236, 237*f*
- specific surface area difference between freeze and nitrogen drying, 241, 242*f*
- total pore volume of L30D/poly(butyl methacrylate), 240*f*
- *See also* Porosity in polymer latex films

Ethyl acrylate/methyl methacrylate (Eudragit® NE30D)
- addition of macroreticular colloid particles into NE30D, 242–243
- exceeding critical pigment volume fraction (CPVF) of NE30D with polystyrene (PS), 239
- total pore volume of NE30D/polystyrene, 240*f*
- *See also* Porosity in polymer latex films

Ethylhexyl acrylate/methyl methacrylate (EHA/MMA), tackifier distribution by infrared imaging, 54, 55*f*

Eudragit® L30D. *See* Ethyl acrylate/methacrylic acid (Eudragit® L30D)

Eudragit® NE30D. *See* Ethyl acrylate/methyl methacrylate (Eudragit® NE30D)

Evaporation
- film formation process, 3, 127–128
- normal rate versus lateral drying, 23–24

Extinction coefficient, pseudo-, latex film formation, 72

F

Film formation
- difference between film formation temperature and T_g, 59
- disorder to order transition, 3
- efficiency in relation to molecular weight of latex, 76

Downloaded by 89.163.34.136 on September 17, 2012 | http://pubs.acs.org
Publication Date: July 26, 2001 | doi: 10.1021/bk-2001-0790.ix002

  evaporation, 3
  factors promoting ordering of dispersion, 3
  inclusion of microscopic particles of silica, 193–194
  latex films, 2–3
  particle deformation, 3
  polymer diffusion, 3
  See also Cryogenic scanning electron microscopy (cryo–SEM); Waterborne systems

Flame retardant
  inclusion compound, 266, 267*f*
  See also Inclusion compounds (ICs)

Fluorescent dyes
  phenanthrene and anthracene labeling to study diffusion and miscibility, 93
  rhodamine for silica labeling, 197, 199
  See also Carbodiimide- and carboxylic acid-functional latex, blends; Rhodamine

Foot, shape models, 13

Force of capillarity, net
  moist stage, 33–34
  sphere, 31
  wet stage, 32–33

Formulation viscosity, role of, in drying, 3

Fourier transform infrared spectroscopy (FTIR)
  attenuated total reflectance (ATR) FTIR technique, 42–43
  carbodiimide remaining by FTIR, 93, 95*t*
  IR imaging, 45
  monitoring reaction between carboxylic acid and carbodiimide groups, 92–93
  photoacoustic spectroscopy, 43
  reflectance-absorbance theory, 43
  schematic of ATR FTIR experiment, 43*f*
  schematic of IR imaging experiment, 46*f*
  schematic of reflectance–absorbance (R–A) experiment, 44*f*
  schematic of step-scan photoacoustic experiment, 44*f*
  surface/interfacial spectroscopic methods, 42–45
  See also Carbodiimide- and carboxylic acid-functional latex, blends

Frequency dependent electrical measurement sensor (FDEMS)
  ability of FDEMS to monitor and compare cure properties of three different formulations, 152*f*, 153*f*, 154*f*, 155*f*
  background, 142
  capacitance, 143
  changing value of log (ε"*ω) with time of commercial epoxy-amine coating, 146*f*
  complex permittivity, 143
  conductance, 143
  cure of thick coating using standard 5 Joule 5 second pulse, 150, 152*f*
  dipolar mobility, 144
  general relation between conductance and viscosity, 144
  instrumentation, 142
  monitoring cure of epoxy systems, 130–131
  on-line monitoring of curing film, 145, 147
  on-line monitoring of rapid cure, 147, 150
  output of 10 second UV pulse of 40 Joules, 151*f*
  output of FDEMS sensor of specially formulated epoxy coating, 148*f*, 149*f*
  parameter for measuring change of ionic mobility with time, 143
  planar micro-sensor for continuous measurements, 141
  relation of dielectric properties to changes in macroscopic performance properties, 144–145

Downloaded by 89.163.34.136 on September 17, 2012 | http://pubs.acs.org
Publication Date: July 26, 2001 | doi: 10.1021/bk-2001-0790.ix002

sensitivity of FDEMS signal monitoring cure completion, 150, 151*f*
theory, 143–144
Fumed silica
characteristics, 197*t*
matting agent, 194, 197
See also Silica
Functionalized latex films. *See* Acetal functionalized latex films

G

Gas pressure force, acting on particles, 31
Gel content
properties of poly(methyl methacrylate-*co*-*n*-butylacrylate-*co*-methacrylamido acetaldehyde dimethyl acetal) films [poly(MMA-*co*-BA-*co*-MAAMA)], 163–165
See also Crosslinking
Gel point, cure of thermoset systems, 110
Geometry, normal versus lateral drying, 21–22
Glass, ethyl acrylate/methacrylic acid (EA/MAA) latex films on, 47
Glass transition temperature (T_g)
cure of thermoset polymers, 111
curing waterborne polyurethanes in air and nitrogen, 130*t*
molecular weight effects, 59
surfactant mobility, 50–51
Gloss
curves versus molar ratio of CsOH to carboxyl groups on latex particles, 226*f*
depending on properties of base for neutralizing carboxyl groups in latex blends, 229–230
effect of neutralization of carboxyl groups, 226–230
influence of carboxyl groups in latex blend films, 220–225
smoothness of film surface influencing, 221
specular gloss, 221
surface gloss of latex blend films as function of carboxyl group coverage on hard particles, 222*f*
tolerable defect height, 221
See also Latex blends, model carboxylated

H

Haines' jumps
evidence in interlayer and intralayer contacts data, 39*f*
particles during drying process, 28
Hardness
curing waterborne polyurethanes in air and nitrogen, 130*t*
method for Persoz, 126
See also Polyurethane, two component waterborne
Hard particles
drying rate of hard versus soft, 12–13
mechanism by which carboxyl groups on polystyrene hard latex influence distribution, 223–224
See also Latex blends, model carboxylated
Hard/soft latex blends, dynamic mechanical analysis (DMA), 114–115, 116*f*
Health regulations, waterborne colloidal dispersions of polymers, 2
Hg (mercury), ethyl acrylate/methacrylic acid (EA/MAA) latex films on, 47
Homogeneity during drying, predictive gauge, 21, 24
Homogeneous drying, uniform water concentration, 4
Hydrogen bonding, inter-particle for

Downloaded by 89.163.34.136 on September 17, 2012 | http://pubs.acs.org
Publication Date: July 26, 2001 | doi: 10.1021/bk-2001-0790.ix002

high density carboxyl groups on hard particles, 224, 228
Hydroxypropyl methyl cellulose (HPMC)
  leaching to produce porous films, 240
  See also Porous latex films

I

Inclusion compounds (ICs)
  additive-ICs, 266, 270
  antibacterials, 266
  attempting to induce chain-extended crystallization throughout film, 247
  chemical structure of flame retardant (ANTIBLAZE RD-1), 253*f*
  chemical structures of antibacterials neomycin and trichlosan, 253*f*
  chemical structures of dyes in study, 252*f*
  differential scanning calorimetry (DSC) scan of poly(ε-caprolactone) (PCL) coalesced from PCL-α-CD-IC, 258*f*
  DSC scans of PCL and poly(L-lactic acid) (PLLA) films embedded with PCL-U-IC before and after washing in methanol, 259*f*
  DSC scans of PLLA and nylon-6 films embedded with poly(ethylene oxide) (PEO)-α-CD-IC after washing with hot water, 261*f*
  DSC scans of two PCL/PLLA composite films, 256, 262*f*, 263*f*
  DSC thermograms of PCL crystallized from solution, coalesced from PCL-U-IC, and crystallized from melt, 257*f*
  dyes, 266
  employing urea (U) and cyclodextrins (CDs) as hosts, 247
  film formation methods, 249
  film thickness measurement method, 256
  flame retardant, 266
  formation, 247
  illustrations of U- and CD-ICs, 250*f*, 251*f*
  materials and methods, 249, 256
  mechanism for coalescence of polymer-B from its IC into carrier polymer-A, 248*f*
  method for X-ray diffractograms of IC powders, 249
  methods for incorporation into polymer films, 247
  nonoxynol-9 spermicide, 266, 270
  PCL/PLLA composite films, 256, 262*f*, 263*f*
  polymer-ICs, 256, 266
  thicknesses and permeabilities of PCL, PCL-U, PCL-IC, PLLA, PLLA-U, and PLLA-IC solution-cast films before and after dipping in methanol, 260*t*
  wide-angle X-ray diffractograms of β-CD and FR-β-CD-IC, 267*f*
  wide-angle X-ray diffractograms of Dye I, β-cyclodextrin, and Dye I-β-CD-IC, 255*f*
  wide-angle X-ray diffractograms of γ-CD, silk-γ-CD-IC, and 1-propanol-γ-CD-IC, 265*f*
  wide-angle X-ray diffractograms of PET, γ-CD, and PET-γ-CD-IC, 264*f*
  wide angle X-ray diffractograms of valeric acid-α-CD-IC, PEO-α-CD-IC, and PCL-α-CD-IC, 254*f*
  wide-angle X-ray diffractograms of valeric acid-α-CD-IC and nonoxynol-9-α-CD-IC, 269*f*
  zones of inhibition of *E. coli* bacterial growth in cultures containing discs cut from PCL and PLLA melt-pressed films embedded with/without neomycin or neomycin-β-CD-IC, 268*f*

Downloaded by 89.163.34.136 on September 17, 2012 | http://pubs.acs.org
Publication Date: July 26, 2001 | doi: 10.1021/bk-2001-0790.ix002

Downloaded by 89.163.34.136 on September 17, 2012 | http://pubs.acs.org
Publication Date: July 26, 2001 | doi: 10.1021/bk-2001-0790.ix002

Infrared imaging
  advanced technique for analysis of surfaces, 45
  chemical heterogeneity and surface/interfacial microstructures, 54, 55*f*
  schematic of experiment, 46*f*
Infrared (IR) spectroscopy
  curing and film composition of waterborne polyurethanes, 128–130
  monitoring isocyanate consumption and urethane and urea formation, 128, 129*f*
  See also Fourier transform infrared spectroscopy (FTIR); Polyurethane, two component waterborne
Interfaces, spectroscopic methods, 42–45
Ionic mobility, parameter for measuring change of ionic mobility with time, 143
Isocyanate groups. *See* Polyurethane, two component waterborne

L

Lacquers, water-based. *See* Matting water-based lacquers
Laplace pressure, capillary pressure difference, 27
Lateral drying
  amount of surfactant by atomic force microscopy (AFM), 10
  appearances of three regions, 8
  boundary region separating dry from wet dispersion, 10
  capillary pressure, 14–15
  coalescence front, 8
  coffee stain, 10
  compaction front, 12
  contact-line pinning, 13
  definition, 8
  drying by gravimetry, 12
  drying first at thinnest portion of wet film, 10
  drying rate of hard versus soft particles, 12–13
  expelling water from drying film to wet area, 8
  experimental studies and modeling, 13–16
  following drying using small angle neutral scattering (SANS) , 8
  general considerations, 9–10
  kinetics of drying process of latex blends, 12
  lateral flow and diffusion models, 14–15
  lateral transport of particles and water soluble species, 10
  lateral transport of water, 9
  magnetic resonance imaging (MRI) experimental studies and modeling, 15–16
  measurements of drying rate versus blend composition, 12
  occurring inward from outer edges, 4–5
  occurring simultaneously with normal, 18*f*
  polystyrene (PS) particles in dilute dispersion in water being driven to edges during evaporation, 11*f*
  pore-emptying front, 12
  recent contributions to understanding of, 10, 12–13
  role of structure and properties of transition region in drying process, 12
  schematic, 6*f*
  schematic of drying front for latex dispersion, 11*f*
  shape models, 8, 13
  thickeners and surfactants influencing open time, 14
  See also Drying modes
Lateral transport
  particles and water soluble species, 10

  water, 9
Latex blending, hard and soft latex particles, 212–213
Latex blends, model carboxylated
  AFM (atomic force microscopy) images of surfaces of films from blends with high density carboxyl groups, neutralized and not neutralized, 228*f*
  AFM images of films from latex blends with and without carboxyl groups, 222*f*
  assigning features of phase images to chemical components, 225
  bulk morphology of films from latex blends, 217–219
  carboxylated polystyrene (PS) latex particles by shot growth batch process, 215
  characterization methods, 215–216
  characterization results for PS and poly(*n*-butylmethacrylate-*co*-*n*-butyl acrylate) [P(BMA/MA)] model latices, 216*t*
  cleaning and characterizing PS and P(BMA/BA) particles, 215
  clustering of hard latex particles on surface of latex blend film by AFM, 224–225
  diagram of location for scanning electron microscopy (SEM) micrographs on freeze-fracture surface of model blend film, 217*f*
  differences in observed gloss and surface roughness of films from blends with high density carboxyl groups and different extents of neutralization, 227–228
  effect of neutralization of carboxyl groups on gloss and surface morphology, 226–230
  effects of neutralization depending on base, 228–229
  experimental materials, 213
  fractured film sample from blend containing carboxyl groups, 218–219, 220*f*
  general characteristics of SEM micrographs, 217–218
  gloss, 220–222
  gloss as function of radius of counterions present in latex blends, 231*f*
  gloss curves versus molar ratio of CsOH to carboxyl groups on latex particles, 226*f*
  gloss depending on properties of base neutralizing carboxyls, 229–230
  hydrogen bond formation in interphase, 219
  incompatibility of PS and P(BMA/BA), 217–218
  influence of carboxyl groups on gloss and surface morphology, 220–225
  inter-granular breaking, 217–218
  inter-particle hydrogen bonding for high density carboxyl groups, 224, 228
  intra-granular breaking, 219
  mechanism by which carboxyl groups influence hard particle distribution, 223–224
  neutralization by strong base, 226–227
  neutralization of carboxyls eliminating ability to form inter-particle hydrogen bonds, 228, 229*f*
  non-carboxylated blend, comparison of TEM and SEM micrographs, 218*f*
  peak-to-valley distance and surface roughness as function of molar ratio of CsOH to total carboxyl groups, 227*f*
  phase angle shifts, 225
  preparation method for latex films, 215
  preparation of carboxylated and non-carboxylated P(BMA/BA) latex particles, 213–214

Downloaded by 89.163.34.136 on September 17, 2012 | http://pubs.acs.org
Publication Date: July 26, 2001 | doi: 10.1021/bk-2001-0790.ix002

Downloaded by 89.163.34.136 on September 17, 2012 | http://pubs.acs.org
Publication Date: July 26, 2001 | doi: 10.1021/bk-2001-0790.ix002

- preparation of carboxylated and non-carboxylated PS latex particles, 214–215
- quantitative relationship between surface roughness and extent of neutralization of carboxyl groups, 227*f*
- reflectance theory, 220–221
- schematic of influence of carboxyl groups on hard particle distribution, 224*f*
- SEM micrographs of fractured section of film from blend without carboxyl groups, 219*f*
- smoothness of surface influencing gloss, 221
- specular gloss, 221
- structures of carboxylated model latex particles, 214*f*
- surface gloss measurement, 216
- surface gloss of blend films as function of carboxyl group coverage on hard particles, 222*f*
- surface morphology method, 216
- surface roughness and peak-to-valley distance as function of radius of counterion in blends with high carboxyl content on PS particles, 230*f*
- surface smoothness of films from model latex blends, 223*t*
- synthesis and characterization of model latex particles, 213–215
- tolerable defect height, 221

Latex coating
- Boussinesq's problem, 35, 37*f*
- capillary force loading of top layer pressing spheres together, 35*f*
- capillary forces, 40
- capillary pressure, 27–28
- cases of axisymmetric elastic contact and crack equilibrium, 37*f*
- datum contact force, 31
- dividing transformation of drying into stages, 27–28, 29*f*
- elastic contact force, 31
- film formation and coalescence by drying, 29*f*
- forces acting on particles, 28, 31–32
- gas pressure force, 31
- liquid pressure force, 28, 31
- moist-stage at interlayer and intralayer contacts, 39*f*
- net elastic reaction force, 32
- net force of capillarity for moist stage, 33–34
- net force of capillarity for wet stage, 32–33
- net force of capillarity on sphere, 31
- pendular rings drawing spheres together in moist stage, 38*f*
- schematic of unit cell from above, 32*f*
- sphere deformation in moist stage, 35, 37–40
- sphere deformation in wet stage, 35
- surface tension force, 31
- wet-stage stresses at interlayer and intralayer contacts, 36*f*

Latex copolymers and blends
- coalescence and glass transition temperatures, 50–51
- optical images, 48–49
- *See also* Latex blends, model carboxylated

Latex dispersions
- addition of diamines to poly(butyl methacrylate) (PBMA), changing drying mode from lateral to normal, 22–23
- following drying using small angle neutron scattering (SANS), 8
- linear water loss, 7
- optical micrograph of unstable acrylic latex dispersion drying on glass plate, 19*f*
- schematic of drying front for, 11*f*
- two-stage drying model, 7

Latex film formation
- additives, 54
- ATR (attenuated total reflection) Fourier transform infrared (FTIR) experiment, 42–43

Downloaded by 89.163.34.136 on September 17, 2012 | http://pubs.acs.org
Publication Date: July 26, 2001 | doi: 10.1021/bk-2001-0790.ix002

ATR FTIR spectra in 1130–960 cm^{-1} region of p-Sty/p-nBA blended latex, 49*f*
ATR FTIR spectra in 1130–960 cm^{-1} region of Sty/nBA copolymer latex, 49*f*
band ratio (1046/1159 cm^{-1}) as function of T_c for copolymer and blended latices, 50*f*
coalescence and glass transition temperature, 50–51
effect of substrate surface tension, 47
FTIR techniques, 42
fraction of voids, 62
general mechanism, 127–128
IR imaging of tactifier distribution in EHA/MMA latex, 55*f*
latex copolymers and blends, 48–49
mathematical model describing drying, 7
optical image of p-Sty/p-nBA blended latex interface, 49*f*
particle size effect, 51–52
photoacoustic spectroscopy, 43
process, 2–3
properties affecting, 45
schematic of ATR experiment, 43*f*
schematic of distribution of surfactant molecules as function of substrate surface tension, 48*f*
schematic of infrared imaging experiment, 46*f*
schematic of relative quantities of sodium dioctylsulfosuccinate (SDOSS) associated with water, COOH, and non-bonded SDOSS as function of depth of penetration from Sty/*n*-BA copolymer interfaces, 53*f*
SDOSS volume concentration as function of Tc for p-Sty/p-nBA blended latex, 52*f*
SDOSS volume concentration changes as function of T_c-T_g for Sty/nBA/MAA core/shell latex, 51*f*
studying underneath the surface, 53
surface/interfacial spectroscopic methods, 42–45
surfactant-copolymer interactions, 45, 47
See also Molecular weight effects on film formation

Leaching, additive. *See* Porosity in polymer latex films
Liquid pressure force, acting on particles, 28, 31
Loss, definition, 105
Loss tangent, definition, 105, 107

M

Macroreticular resin
  colloid particles characteristics, 242–243
  production of colloidal porous particles, 234–235
  See also Porosity in polymer latex films
Macroscopic properties, relation of dielectric properties to changes in, 144–145
Magnetic resonance imaging (MRI)
  experimental studies and modeling of lateral drying, 15–16
  images from drop of latex dispersion with bimodal size distribution, 17*f*
  master equation predicting water concentration, 16
Matting water-based lacquers
  algorithm known as Sobel operator, 205
  binary image of 'silica' and 'not silica', 205, 208*f*
  brightness of image as two-dimensional function of position, 203, 205
  characteristics of fumed silica, 197*t*
  confocal and environmental scanning electron microscopy (ESEM) data for m_{sil}/m_o values ~1, 209

Downloaded by 89.163.34.136 on September 17, 2012 | http://pubs.acs.org
Publication Date: July 26, 2001 | doi: 10.1021/bk-2001-0790.ix002

- confocal images of increasing silica concentration, 206*f*, 207*f*
- confocal microscopy, 196–197
- crushed silica structure by volume reduction in drying lacquer, 210
- ESEM, 194–196
- ESEM images of increasing silica concentration, 204*f*
- experimental, 197–199
- formulation recipe and suppliers, 198*t*
- inclusion of microscopic particles of silica, 193–194
- mathematical treatment, 201–203
- relating m_{sil}/m_o to volume fraction of silica, 202–203
- scattered light by matting coating, 194*f*
- schematic of dried film by two scenarios, 200*f*
- silica behavior, 200–203
- silica concentration by ESEM and confocal images, 203
- silica occupancy differences between ESEM and confocal images, 205, 208, 209*f*
- two possibilities when $m_{sil}/m_o > 1$, 209–210

Mechanical properties
- poly(methyl methacrylate-*co*-*n*-butylacrylate-*co*-methacrylamido acetaldehyde dimethyl acetal) films [poly(MMA-*co*-BA-*co*-MAAMA)], 165–166
- varying molecular weight, 81

Membrane formation, film formation process, 3

Mercury (Hg), ethyl acrylate/methacrylic acid (EA/MAA) latex films on, 47

Mercury porosimetry, pore size distributions and pore volumes, 235–236

Methacrylamido acetaldehyde dimethyl acetal (MAAMA)
- apparent rate constant of hydrolysis as function of pH, 168*f*
- characterization of MAAMA-containing latices, 161*t*
- copolymerization with methyl methacrylate (MMA) and *n*-butylacrylate (BA), 159
- effect of amount of MAAMA on tensile properties for poly(MMA-*co*-BA-*co*-MAAMA) films formed at pH=2, 166*f*
- experimental conditions for latex synthesis, 160*t*
- gel content and swelling ratio for films as function of MAAMA concentration, 163*t*
- kinetics of hydrolysis of model of MAAMA at different pH and room temperature, 168*f*
- nonpolymerizable model of MAAMA for studying reactions, 167
- self-crosslinking under acidic conditions, 158
- simulating film formation conditions for model and allowing slow solvent evaporation, 169
- stability during and after polymerization, 162
- stability under alkaline conditions, 167
- synthesis, 158–159
- *See also* Acetal functionalized latex films

Methacrylic acid (MAA). *See* Carbodiimide- and carboxylic acid-functional latex, blends

Methyl methacrylate/butyl acrylate copolymer, behavior of surfactant, 83

Methyl methacrylate (MMA)
- emulsion polymerization with *n*-butylacrylate (BA) and methacrylamido acetaldehyde dimethyl acetal (MAAMA), 159
- *See also* Acetal functionalized latex films

Downloaded by 89.163.34.136 on September 17, 2012 | http://pubs.acs.org
Publication Date: July 26, 2001 | doi: 10.1021/bk-2001-0790.ix002

Miscibility
  poly(2-ethylhexyl methacrylate) (PEHMA) copolymers, 94, 96
  quantum efficiency of energy transfer, 91–92
  See also Carbodiimide- and carboxylic acid-functional latex, blends
Models, shape models for lateral drying, 13
Modulus definitions
  shear deformation, 107
  tensile deformation, 105, 107
  See also Dynamic mechanical analysis (DMA)
Moist stage
  axisymmetric elastic contact and crack equilibrium, 37*f*
  coating with pore space filled with air except for pendular rings of liquid, 28
  drying latex coating, 28
  forces on particles, 30*f*
  forces on partly wetted particles, 30*f*
  Haines' jumps, 28, 39*f*
  net force of capillarity, 33–34
  pendular rings drawing spheres together, 38*f*
  scenario of film formation and coalescence, 29*f*
  sphere deformation, 35, 37–40
  stresses at interlayer and intralayer contacts, 39*f*
  tensile mean in-plane stress, 38
  See also Latex coating
Molecular weight effects on film formation
  AFM (atomic force microscopy) analysis of low MW latex film, 76, 77*f*, 78
  AFM images indicating dome-shaped surfactant features of polymer/air interface of low-MW acrylic latex film (20°C above minimum film formation temperature (MFT)), 80*f*
  AFM images of latex film from high MW latex dispersion (30°C above MFT), 84*f*
  AFM images of polymer/air interface of film from low MW latex dispersion (15°C above MFT), 79*f*
  AFM images of polymer/air interface of film from very low MW latex (5°C above MFT), 76, 77*f*
  AFM method, 61
  characteristics of MMA/BMA/MAA latex, 82*t*
  comparing film formation of very-low, low, and medium MW latices prepared at 10°C above MFT values, 72, 74*f*
  comparing pseudo-refractive indices <n> for films of very-low and high MW latices (20°C above MFT), 72, 76
  controlling mechanical properties of coating, 59
  dynamic ellipsometry measurements of film formation, 68, 72, 76
  dynamic evolution of <n> and <k> (pseudo-extinction coefficient) for films from low MW latex, 73*f*
  dynamic evolution of <n> and <k> for films of very low and high MW latices prepared at 20°C above MFT values, 75*f*
  dynamic evolution of <n> from very low MW latex films above MFT, 71*f*
  effective medium approximate (EMA) model, 62
  effect of surface roughness on ellipsometric angles from simulation of angular scan, 62, 64*f*
  effect of voids on ellipsometric angles, 62, 65*f*
  efficiency of film formation, 76, 85–86
  elasticity and viscosity of polymer, 59
  evolution of <n> for films from very

low MW latex, 68, 72
film formation 15°C above MFT, 78
film formation 20°C above MFT, 78
film formation for very low, medium, and high MW latices, 81
fraction of voids in latex film, 62
glass transition temperature, 59
interpreting ellipsometry by applying to models, 62
latex polymerization and characteristics, 60
mass loss (thermal gravimetric analysis, TGA) from heating films from high and low MW latex dispersions, 82*f*
measurements of surface roughness and void volume fraction by fitting data to model, 66, 67*f*
mechanical behavior of coating, 59
observations reflecting differences in mechanical properties of polymer with varying MW, 81
pattern of morphologies, 78
pseudo-extinction coefficient <k>, 72
pseudo-refractive index <N> from ellipticity, 68
raw ellipsometry data, 71*f*
real component of pseudo-refractive index <n>, 68
rings of surfactant phase around interparticle voids, 85
schematic of model to fit experimental data from ellipsometry, 63*f*
studying possible effect of water, 81, 83
surface morphologies, 83
surface roughness and bulk void concentration as function of film formation temperature above MFT, 66, 69*f*, 70*f*
surfactant at latex/air surface of low MW latex by AFM study, 83
surfactant morphology and concentration at latex air surface, 76–78
surfactant rings absent at surface of high MW latex films, 85
TGA method, 61–62
variable-angle ellipsometry method, 60–61
varying, to compare efficiency of film formation, 59–60
void content and surface roughness films, 62, 66
water altering latex mechanical properties, 83

Morphology
  AFM (atomic force microscopy) images of films from latex blends with and without carboxyl groups, 222*f*
  AFM images of surfaces of films from high carboxyl group coverage latex blends, 225*f*
  effect of neutralization of carboxyl groups on surface, 226–230
  extent of neutralization of carboxyl groups, 227–228
  influence of carboxyl groups in latex blend films, 220–225
  surface, depending on properties of base for neutralization of carboxyl groups in latex blends, 228–229
  See also Latex blends, model carboxylated

N

Neutralization
  effect on gloss and surface morphology of latex blend films, 226–230
  effects depending on properties of base, 228–229
  See also Latex blends, model carboxylated
Normal drying
  classical models for, 5–7
  model by Sheetz (1965), 6
  occurring simultaneously with

Downloaded by 89.163.34.136 on September 17, 2012 | http://pubs.acs.org
Publication Date: July 26, 2001 | doi: 10.1021/bk-2001-0790.ix002

    lateral, 18*f*
  schematic, 6*f*
  three stage process model by
    Vanderhoff (1973), 6–7
  two-stage process by Croll (1986),
    7
  See also Drying modes
Nylon-6
  polymer-inclusion compounds, 256
  See also Inclusion compounds (ICs)

O

On-line monitoring. *See* Epoxy systems; Frequency dependent electrical measurement sensor (FDEMS)
Open time
  slowing drying process, 3
  thickeners and surfactants
    influencing, 14
Optical images, latex copolymers and blends, 48–49
Optical micrograph, unstable acrylic latex dispersion drying on glass plate, 19*f*

P

Paint, breathable, exceeding critical pigment volume fraction (CPVF), 234
Particle deformation
  effect on drying rate, 23
  elastic and viscous contributions,
    59
  film formation process, 3
  model by Sheetz (1965), 6
Particle front, definition, 14
Particle size effect, migration of surfactant molecules, 51–52
Particle viscoelasticity, normal versus lateral drying, 23
Particles
  datum contact force, 31
  drying rate of hard versus soft, 12–13
  elastic contact force, 31
  forces acting on, 28, 31–32
  gas pressure force, 31
  lateral transport, 10
  liquid pressure force, 28, 31
  net force of capillarity in moist stage,
    33–34
  net force of capillarity in wet stage,
    32–33
  net force of capillarity on sphere, 31
  poly(styrene), in dilute dispersion in
    water being driven to edges during
    evaporation, 11*f*
  surface tension force, 31
Pendular rings
  force of capillarity on sphere by
    single, 34
  geometry, 30*f*
  moist stage, 28
  See also Latex coating
Percolation
  dry top phase in terms of, network of
    voids, 7
  water through interstitial spaces, 4
Permittivity
  frequency dependent dielectric
    measurement, 143
  See also Frequency dependent
    electrical measurement sensor
    (FDEMS)
Persoz hardness
  curing waterborne polyurethanes in
    air and nitrogen, 130*t*
  method, 126
  See also Polyurethane, two
    component waterborne
pH
  acidification of latex serum for
    crosslink formation, 170
  adjustment for film formation from
    poly(methyl methacrylate-*co*-*n*-
    butylacrylate-*co*-methacrylamido
    acetaldehyde dimethyl acetal)
    latex [poly(MMA-*co*-BA-*co*-
    MAAMA)], 159–160

Downloaded by 89.163.34.136 on September 17, 2012 | http://pubs.acs.org
Publication Date: July 26, 2001 | doi: 10.1021/bk-2001-0790.ix002

  effect on crosslink formation rate, 170
  effect on gel content and swelling ratio, 165
  effect on tensile properties of poly(MMA-*co*-BA-*co*-MAAMA) films, 166
  system becoming reactive for crosslinking at selected, 158
  See also Acetal functionalized latex films
Phase lag, definition, 105
Phenanthrene
  labeling to study diffusion and miscibility, 93
  See also Carbodiimide- and carboxylic acid-functional latex, blends
Photoacoustic spectroscopy
  detection of energy absorbed by sample, 43
  distribution of sodium dioctylsulfosuccinate (SDOSS) and interactions across copolymer latex film thickness, 53
  rheo-photoacoustic for detection of work of adhesion, 43
  schematic of step-scan experiment, 44*f*
Pigment suspensions, linear water loss, 7
Pinning, contact-line, shape model for lateral drying, 13
Poisson's ratio, definition, 107
Poly(butyl methacrylate) (PBMA)
  addition of diamines to PBMA latex dispersion changing drying mode, 22–23
  colloidal crystals growing beneath top surface of PBMA latex coating, 190, 191*f*
  comparison of pore radius profiles for films leached of Eudragit® L30D (ethyl acrylate/methacrylic acid) under different drying regimes, 243*f*
  cryo–SEM method for latex coatings, 176–177
  descending consolidation front, 175, 190
  latex coating of carbon and dynamic adsorption profiles, 243–244
  latex suspension synthesis, 176
  latex with fumed silica matting agent, 197
  leaching experiments with L30D, 236, 237*f*
  leaching films of sucrose, poly(vinyl pyrrolidone) (PVP), and Dowfax 2A1 (SDED), 237
  leaching hydroxypropyl methyl cellulose (HPMC), sodium dodecyl sulfate (SDS), and sodium chloride, 240–241
  mixed mode example of polystyrene (PS) and, particles, 20
  pore closure, 241–242
  porous latex films, 236–241
  scanning electron microscopy (SEM) micrographs of PBMA latex coatings showing descending consolidation front, 186, 188*f*, 189*f*, 190
  specific surface area difference between freeze and nitrogen drying, 242*f*
  total pore volume of porous latex films, 240*f*
  See also Cryogenic scanning electron microscopy (cryo–SEM); Matting water-based lacquers; Porosity in polymer latex films
Poly(*n*-butylmethacrylate-*co*-*n*-butyl acrylate) [P(BMA/MA)]
  synthesis and characterization, 213–214, 216*t*
  See also Latex blends, model carboxylated
Poly(ε-caprolactone) (PCL)
  polymer-inclusion compounds (ICs), 256
  See also Inclusion compounds (ICs)

Downloaded by 89.163.34.136 on September 17, 2012 | http://pubs.acs.org
Publication Date: July 26, 2001 | doi: 10.1021/bk-2001-0790.ix002

Polydimethylsiloxane emulsion, drying normal to surface, 5
Polyester polyols, binders for thermoset coatings, 111
Poly(ethylene oxide) (PEO)
  polymer-inclusion compounds (ICs), 256
  See also Inclusion compounds (ICs)
Poly(ethylene terephthalate) (PET)
  polymer-inclusion compounds (ICs), 256, 266
  See also Inclusion compounds (ICs)
Poly(2-ethylhexyl methacrylate) (PEHMA) copolymer. *See* Carbodiimide- and carboxylic acid-functional latex, blends
Poly(L-lactic acid) (PLLA)
  polymer-inclusion compounds (ICs), 256
  See also Inclusion compounds (ICs)
Polymer colloids. *See* Drying modes
Polymer diffusion
  bringing reactive groups together, 89–90
  film formation process, 3
  interdiffusion versus crosslinking, 99
  sequential coalescence and crosslinking, 121
  See also Carbodiimide- and carboxylic acid-functional latex, blends
  Polymer latex blends, importance of uniform distribution and adhesion, 213
Polymer particle viscoelasticity, normal versus lateral drying, 23
Poly(methyl methacrylate-*co*-*n*-butylacrylate-*co*-methacrylamido acetaldehyde dimethyl acetal) [poly(MMA-*co*-BA-*co*-MAAMA)]
  crosslink formation, 167–170
  emulsion polymerization, 159
  film formation and characterization, 159–160
  latex and copolymer characterization, 160–162
  mechanical properties of films, 165–166
  proton NMR spectrum, 162*f*
  stability of acetal-functional group during and after polymerization, 162
  swelling properties of films, 163–165
Polystyrene (PS)
  close-packed particles passing through consolidation front, 180
  cluster growth on air-water surface at 1 minute drying of 10 wt% latex suspension, 182, 183*f*
  cryogenic scanning electron microscopy (cryo–SEM) method for latex coatings, 176–177
  edge consolidation front, 175, 177, 180, 190
  edge consolidation front of 10 wt% deionized PS latex suspension after 1 minute drying, 179*f*
  edge consolidation front of 10 wt% PS latex suspension after 3 minutes drying, 178*f*
  exceeding critical pigment volume fraction (CPVF) of Eudragit® NE30D (ethyl acrylate/methyl methacrylate), 239
  fracture surface away from edges of fast-frozen deionized latex suspension, 186, 187*f*
  fracture surfaces, 177, 180
  lateral transport of particles, 10
  latex suspension synthesis, 176
  mechanisms of water loss during drying, 182, 186
  mixed mode example of PS and poly(butyl methacrylate) (PBMA) particles, 20
  particle distribution in middle of coating during drying, 180, 182, 186
  particles in dilute dispersion in water being driven to edges during evaporation, 11*f*
  room temperature SEM image of

Downloaded by 89.163.34.136 on September 17, 2012 | http://pubs.acs.org
Publication Date: July 26, 2001 | doi: 10.1021/bk-2001-0790.ix002

Downloaded by 89.163.34.136 on September 17, 2012 | http://pubs.acs.org
Publication Date: July 26, 2001 | doi: 10.1021/bk-2001-0790.ix002

    edge of dried PS latex coating (not deionized), 181*f*
  successive layers of highly ordered PS particles forming at moving consolidation front, 182, 184*f*, 185*f*, 186
  synthesis and characterization of carboxylated and non-carboxylated latex, 214–215, 216*t*
  total pore volume of NE30D/PS, 240*f*
  See also Cryogenic scanning electron microscopy (cryo–SEM); Latex blends, model carboxylated; Porosity in polymer latex films
Polytetrafluoroethylene (PTFE), ethyl acrylate/methacrylic acid (EA/MAA) latex films on, 47
Polyurethane, two component waterborne
  Adura™ coating performance, 127*t*
  Adura™ coating technology, 126–127
  analytical measurements, 125–126
  attenuated total reflectance (ATR) infrared method, 126
  beginning of network formation, 137
  blocking effect, 131
  bulk conductance and interfacial capacitance versus time based on parallel capacitance and resistance model, 132, 133*f*
  capacitance and resistance versus time, log-log plots, 138*f*
  capacitance and resistance versus time leveling off, 139
  capacitance changes with time for Adura™ coating, 135*f*
  capacitance versus time based on parallel capacitance and resistance model, 134*f*
  capacitance versus time between 20–35 minutes, 135, 136*f*, 137
  capacitance versus time between 35–73 minutes, 137
  capacitance versus time between 73–500 minutes, 137, 138*f*
  capacitance versus time for first 20 minutes, 135, 136*f*
  circuit model of dielectric sensor, 131, 132*f*
  comparing infrared (ATR–IR) and dielectric analysis (DEA) measurement on water evaporation, 134–135
  complex plots of impedance based on circuit model, 131, 132*f*
  complex plots of impedance during first 21 minutes of drying, 132, 133*f*
  conductance and capacitance, 130
  curing and film composition by IR analysis, 128–130
  DEA measuring changes in conductance and capacitance, 130–139
  dielectric measurement method, 125–126
  dry time monitoring method, 126
  experimental materials, 125
  film formation for waterborne coatings, 127–130
  frequency dependent electrical measurement sensor (FDEMS), 130–131
  general mechanism for latex film formation, 127–128
  infrared (IR) absorbance monitoring isocyanate consumption and urethane and urea formation, 128–130
  interfacial capacitance (C_i) monitoring water evaporation process, 131
  IR absorbance versus time for isocyanate, urethane, and urea during film formation, 129*f*
  overcoming blocking effect for monitoring water evaporation, 139
  Persoz hardness, 130
  Persoz hardness method, 126
  polar entities, 137, 139

- possible reactions for, 129*f*
- preparation of Adura™ coatings, 126*f*
- sensitivity to curing conditions, 128–130
- tack free time, 137
- T_g and hardness for curing in air and nitrogen, 130*t*
- volatile organic compounds (VOC) challenge, 125
- water and DEA, 130–131
- water evaporation processes, 135–137
- water evaporation versus time for Adura™ coating, 132, 134
- water IR absorbance versus time, 134*f*
- weight loss versus time, 133*f*

Polyurethane dispersions
- DMA (dynamic mechanical analysis) of films from aqueous, 112–114
- DMA plots for unpigmented coating from aqueous, 113*f*
- prepolymer mixing process, 112

Poly(vinyl acetate), behavior of surfactant, 83

Poly(vinyl pyrrolidone) (PVP)
- leaching PVP for producing porous films, 237
- total pore volume of PVP/poly(butyl methacrylate), 240*f*
- *See also* Porous latex films

Pore-emptying front, dry side of drying boundary, 12

Porosity in polymer latex films
- additive leaching, 234
- barrier characteristics by dynamic adsorption of methanol, 236
- barrier characteristics of films, 234
- comparison of dynamic adsorption profiles for polymer coated, porous polymer coated, and plain BPL carbon, 244*f*
- comparison of pore radius profiles for films leached of Eudragit® L30D, 238*f*
- comparison of pore radius profiles for films leached of L30D under different drying regimes, 243*f*
- comparison of total pore volume, 240*f*
- critical pigment volume fraction (CPVF) experiments, 237, 239
- dynamic adsorption, 243–244
- experimental, 235–236
- films by exceeding CPVF of Eudragit® NE30D with PS, 239
- films by leaching SDS, 241
- latices for film formation, 235
- leaching experiments, 236–237
- leaching hydroxypropyl methyl cellulose (HPMC), sodium dodecyl sulfate (SDS), and low concentrations of sodium chloride, 240
- macroreticular colloid particles, 242–243
- macroreticular resin synthesis, 234–235
- pore closure, 241–242
- pore creation, 234
- pore size distributions and volumes by mercury porosimetry method, 235–236
- porous colloidal particle production, 235
- production of colloidal porous particles, 234–235
- requirements of leachable additives for successful production of porous films, 234
- specific surface area, 236–241
- specific surface area for freeze dried and nitrogen dried films, 242*f*
- specific surface area measurement method, 235
- specific surface areas of films tested, 237*f*

Post-crosslinking
- improving properties of water-borne films, 157
- requirement of stability during

Downloaded by 89.163.34.136 on September 17, 2012 | http://pubs.acs.org
Publication Date: July 26, 2001 | doi: 10.1021/bk-2001-0790.ix002

polymerization and storage, 158
See also Acetal functionalized latex films
Property development. *See* Dynamic mechanical analysis (DMA)
Pseudo-extinction coefficient
  comparing, for films from very-low and high MW latices, 72, 75*f*, 76
  dynamic data for low MW latex at three different temperatures, 72, 73*f*
  latex film formation, 72
Pseudo-refractive index
  ellipticity leading to, 68
  real component, 68
Pseudo-refractive index, real component
  comparing, for films from very-low and high MW latices, 72, 75*f*, 76
  dynamic data for low MW latex at three different temperatures, 72, 73*f*
  dynamic evolution of, from films of very low, low, and medium MW latices, 72, 74*f*
  evolution from films of very low MW latex at three temperatures, 68, 71*f*
  film formation from varying molecular weight latices, 81

Q

Quantum efficiency of energy transfer, definition, 91–92

R

Rapid drying, need for, 3
Reflectance–absorbance theory
  advantages and disadvantages, 43
  schematic of experiment, 44*f*
Reflectance theory, 220–221
Refractive index. *See* Pseudo-refractive index
Resistance, circuit model for waterborne coatings, 131
Rheology of dispersion, normal versus lateral drying, 22–23
Rhodamine
  fluorescent dye for silica, 197
  fluorescent signal for rhodamine concentration, 199
  image contrast increasing with rhodamine concentration to maximum value, 199*f*
  See also Silica

S

Scanning electron microscopy (SEM). *See* Cryogenic scanning electron microscopy (cryo–SEM); Environmental scanning electron microscopy (ESEM)
Scrub resistance, low porosity and surface area, 233
Shape models, lateral drying, 8, 13
Shear deformation, modulus definitions, 107
Shear loss modulus, definition, 107
Shear storage modulus, definition, 107
Sheetz, particle deformation model, 6
Silica
  behavior, 200–203
  binary image of 'silica' and 'not silica', 205, 208*f*
  bulk density of dried, 201
  bulk occupancy by confocal images, 209*f*
  characteristics of fumed, 197*t*
  continuous structure for roughened surface, 200–201
  critical mass, 202
  crushed structure by volume reduction in drying lacquer, 210
  formation of fumed, 200

Downloaded by 89.163.34.136 on September 17, 2012 | http://pubs.acs.org
Publication Date: July 26, 2001 | doi: 10.1021/bk-2001-0790.ix002

  inclusion of microscopic particles in film, 193–194
  isolated particles in film, 200
  matting, 194
  matting agent, 197
  occupancy in confocal images, 203, 206*f*, 207*f*
  occupancy in environmental scanning microscopy (ESEM) images, 203, 204*f*
  proportion of volume occupied by, 201
  relation m_{sil}/m_o to volume fraction of silica, 202–203
  rhodamine fluorescent dye, 197
  silica concentration and values of m_{sil}/m_o, 202*t*
  surface occupancy by ESEM, 208*f*
  See also Confocal microscopy; Environmental scanning electron microscopy (ESEM); Matting water-based lacquers
Silk
  polymer-inclusion compounds, 256, 265*f*, 266
  See also Inclusion compounds (ICs)
Skin forming systems
  film forming front, 175
  top of latex coating drier than bottom, 4
Small angle neutron scattering (SANS), drying of latex dispersions, 8
Smoothness
  films from model latex blends, 223*t*
  influencing gloss, 221
  See also Latex blends, model carboxylated
Sodium chloride
  leaching low concentrations to produce porous films, 240
  See also Porous latex films
Sodium dioctylsulfosuccinate (SDOSS)
  distribution of SDOSS and interactions across copolymer latex film thickness, 53
  effect of difference between coalescence and glass transition temperatures on migration, 50–51
  mobility in copolymer latexes, 47
  particle size effect on migration, 51–52
  stratification in ethyl acrylate/methacrylic acid (EA/MAA) latexes, 48*f*
  surfactant-copolymer interactions, 45, 47
Sodium dodecyl sulfate (SDS)
  leaching to produce porous films, 240–241
  See also Porous latex films
Soft particles
  drying rate of hard versus soft, 12–13
  See also Latex blends, model carboxylated
Specular gloss, definition, 221
Spermicide nonoxynol-9
  inclusion compound, 266, 269f, 270
  See also Inclusion compounds (ICs)
Sphere deformation
  capillary force loading pressing spheres together in wet stage, 35*f*
  cases of axisymmetric elastic contact and crack equilibrium, 37*f*
  moist stage, 35, 37–40
  moist-stage at interlayer and intralayer contacts, 39*f*
  pendular rings drawing spheres together in moist stage, 38*f*
  wet stage, 35
  wet-stage stresses at interlayer and intralayer contacts, 36*f*
  See also Latex coating
Stokes–Einstein equation, diffusion, 21
Storage, definition, 105
Strain. *See* Dynamic mechanical analysis (DMA)
Stress. *See* Dynamic mechanical analysis (DMA)
Structure of dispersion, normal versus lateral drying, 22–23

Downloaded by 89.163.34.136 on September 17, 2012 | http://pubs.acs.org
Publication Date: July 26, 2001 | doi: 10.1021/bk-2001-0790.ix002

Styrene/butadiene latex
  crosslinking by butadiene, 118, 121
  crosslinking in latex films, 118, 121
  films from latex with carboxyl groups in shell, 115, 118
  latex containing acrylic acid, 115
  loss tangent plots for films containing carboxylic acid groups neutralized to various pH, 117*f*
  storage modulus plots for films with various levels of chain transfer agent (CTA), 119*f*
  tensile storage modulus versus frequency of oscillation for films containing various levels of CTA, 120*f*
Styrene/*n*-butyl acrylate (Sty/nBA) copolymer, optical images from film-additive interfaces, 48–49
Styrene/butyl acrylate/methacrylic acid (St/BA/MAA)
  enrichment of surfactant at interface, 47
  hard/soft latex blends, 114–115
  shear storage modulus plot for film from blend of soft latex with large particles and hard latex with small particles, 116*f*
Substrate surface tension
  effect on migration of components in latexes, 47
  schematic of distribution of surfactant molecules as function of, 48*f*
Sucrose
  leaching to produce porous films, 237
  total pore volume of sucrose/poly(butyl methacrylate), 240*f*
  See also Porous latex films
Sulfate ions, accumulating in center at film-substrate interface, 20
Surface morphology. *See* Morphology
Surface properties. *See* Latex blends, model carboxylated
Surface roughness
  ellipsometry, 62, 66
  function of film formation temperature above minimum film-formation temperature (MFT), 69*f*, 70*f*
  simulated ellipsometry spectra, 62, 64*f*
Surface-tension-driven horizontal flow, lateral drying, 14–15
Surface tension effect
  migration of components in latexes, 47, 48*f*
  normal versus lateral drying, 21–22
Surface tension force, acting on particles, 31
Surfaces, spectroscopic methods, 42–45
Surfactant amount, poly(butyl methacrylate) surface after drying using atomic force microscopy (AFM), 10
Surfactant concentration
  polymer/air interface of latex films of varying molecular weight, 76–78
  See also Atomic force microscopy (AFM)
Surfactant morphology
  atomic force microscopy (AFM) providing evidence for surfactant at latex/air surface, 83
  polymer/air interface of latex films of varying molecular weight, 76–78
  ring-like features for surfactant, 85
  See also Atomic force microscopy (AFM)
Surfactants
  attributing rings due to micelles at particle interstices, 85
  behavior in poly(vinyl acetate) and copolymer of methyl methacrylate and butyl acrylate, 83

Downloaded by 89.163.34.136 on September 17, 2012 | http://pubs.acs.org
Publication Date: July 26, 2001 | doi: 10.1021/bk-2001-0790.ix002

Downloaded by 89.163.34.136 on September 17, 2012 | http://pubs.acs.org
Publication Date: July 26, 2001 | doi: 10.1021/bk-2001-0790.ix002

- distribution of sodium dioctylsulfosuccinate (SDOSS) and interactions across copolymer latex film thickness, 53
- effect of coalescence and glass transition temperatures on mobility, 50–51
- influencing open time, 14
- interactions with copolymer, 45, 47
- particle size effect on migration, 51–52
- presence of surfactant rings dependence on latex molecular weight, 85
- stratification in ethyl acrylate/methacrylic acid (EA/MAA) latexes, 48*f*

Swelling
- properties of poly(methyl methacrylate-*co*-*n*-butylacrylate-*co*-methacrylamido acetaldehyde dimethyl acetal) films [poly(MMA-*co*-BA-*co*-MAAMA)], 163–165
- *See also* Crosslinking

T

Tackifier, distribution in copolymer by infrared imaging, 54, 55*f*

Tensile deformation
- loss tangent, 105
- modulus definitions, 105, 107
- tensile loss modulus, 105
- tensile storage modulus, 105
- *See also* Dynamic mechanical analysis (DMA)

Tensile loss modulus, definition, 105

Tensile properties, poly(methyl methacrylate-*co*-*n*-butylacrylate-*co*-methacrylamido acetaldehyde dimethyl acetal) films [poly(MMA-*co*-BA-*co*-MAAMA)], 165–166

Tensile storage modulus, definition, 105

Thermal conductivity, mathematical model describing drying, 7

Thermal expansivity, mathematical model describing drying, 7

Thermal gravimetry analysis (TGA), method, studying molecular weight effects on film formation, 61–62

Thermoplastic latex polymers, improving film properties with crosslinks, 88–89

Thermoset formulations
- characterizing cure of acrylic and polyester polyols with crosslinkers, 109–110
- determination of extent of cure by dynamic mechanical analysis (DMA), 107–110
- DMA of films from water reducible binders, 111–112
- DMA plots for unpigmented, highly crosslinked coating, 108*f*
- following property development during cure by DMA, 110–111
- importance of glass transition temperature at complete conversion, 111
- polymer network properties, 109
- time-temperature-transformation (TTT) cure diagrams, 110–111

Thickeners, influencing open time, 14

Thickness effects, normal versus lateral drying, 21–22

Time-temperature-transformation (TTT), cure diagrams for thermoset systems, 110–111

Tolerable defect height, equation, 221

Torsional braid analysis (TBA), constructing time-temperature-transformation (TTT) diagrams, 110

Transport, water in latex dispersion, 4

Transport properties. *See* Porosity in polymer latex films

Turbidity, normal and lateral drying modes, 18

U

Ultraviolet cure epoxies. *See* Epoxy systems
Urea (U)
  host for inclusion compounds, 247
  See also Inclusion compounds (ICs)
Urethanes. *See* Polyurethane, two component waterborne

V

Vanderhoff, three stage drying process model, 6–7
Variable-angle ellipsometry
  analysis types, 61
  ellipticity equation, 60
  method, 60–61
  sample preparation, 61
Viscoelasticity, polymer particle, normal versus lateral drying, 23
Viscosity, general relation between conductance and, 144
Viscosity of formulation
  mathematical model describing drying, 7
  normal versus lateral drying, 22–23
  role of, in drying, 3
Vitrification, following cure of thermoset systems, 110–111
Void content
  effective medium approximate (EMA) model, 63*f*
  ellipsometry, 62, 66
  fraction of voids, 62
  function of film formation temperature above minimum film-formation temperature (MFT), 69*f*, 70*f*
  simulated ellipsometry spectra, 62, 65*f*
Volatile organic compounds (VOC), alternative technologies for reduction, 125

W

Water
  altering latex mechanical properties, 83
  lateral transport, 9
  studying possible plasticization effect in latex film formation, 81
Water-based lacquers. *See* Matting water-based lacquers
Waterborne film, film formation process, 2–3
Waterborne systems
  crosslinking by butadiene in latex films, 118, 121
  DMA (dynamic mechanical analysis) from water reducible binders, 111–112
  DMA of films from aqueous polyurethane dispersions, 112–114
  DMA plots for unpigmented coating from aqueous polyurethane dispersion, 113*f*
  DMA study of film formation from waterborne latices, 114–121
  films from latex with carboxyl groups in shell, 115, 118
  hard/soft latex blends, 114–115
  loss tangent plots for films from latex with carboxylic acid groups neutralized to various pH, 117*f*
  sequential coalescence and crosslinking, 121
  shear storage modulus plot for film from blend of soft latex with large particles (SL) and hard latex with small particles (HS), 115, 116*f*

Downloaded by 89.163.34.136 on September 17, 2012 | http://pubs.acs.org
Publication Date: July 26, 2001 | doi: 10.1021/bk-2001-0790.ix002

- storage modulus plots for films from styrene/butadiene latex containing varying amounts of chain transfer agents (CTA), 119*f*
- styrene/butadiene latex containing acrylic acid, 115
- tensile storage modulus versus frequency of oscillation for films from styrene/butadiene latex with varying CTA, 120*f*
- *See also* Polyurethane, two component waterborne

Water concentration, master equation predicting, 16

Water evaporation
- film formation process, 3, 127–128
- latex film formation, 59

Water fluxes, wet regions of drying film, 4

Water loss
- differing mechanisms during drying, 182, 186
- latex dispersions and pigment suspensions, 7
- normal versus lateral drying rate, 23–24

Water reducible binders, dynamic mechanical analysis (DMA) of films from, 111–112

Water soluble species
- accumulating in center at film-substrate interface, 20
- lateral transport, 10

Weight loss, normal and lateral drying modes, 18

Wet stage
- coating with menisci at top surface, 28
- compressive in-plane stress, 35
- drying latex coating, 28
- forces on particles, 30*f*
- forces on partly wetted particles, 30*f*
- net force of capillarity, 32–33
- scenario of film formation and coalescence, 29*f*
- sphere deformation, 35
- stresses at interlayer and intralayer contacts, 36*f*
- *See also* Latex coating

Downloaded by 89.163.34.136 on September 17, 2012 | http://pubs.acs.org
Publication Date: July 26, 2001 | doi: 10.1021/bk-2001-0790.ix002